5-2018

Capturing the role of the co-play of land use and rainfall on water and sediment flux dynamics across different spatiotemporal scales in intensively managed landscapes

Benjamin Kobina Abban
University of Tennessee, babban@vols.utk.edu

To the Graduate Council:

I am submitting herewith a dissertation written by Benjamin Kobina Abban entitled "Capturing the role of the co-play of land use and rainfall on water and sediment flux dynamics across different spatiotemporal scales in intensively managed landscapes." I have examined the final electronic copy of this dissertation for form and content and recommend that it be accepted in partial fulfillment of the requirements for the degree of Doctor of Philosophy, with a major in Civil Engineering.

Athanasios N. Papanicolaou, Major Professor

We have read this dissertation and recommend its acceptance:

Vasilios Alexiades, John S. Schwartz, Daniel C. Yoder, Murugesu Sivapalan

Accepted for the Council:
Dixie L. Thompson

Vice Provost and Dean of the Graduate School

(Original signatures are on file with official student records.)

Capturing the role of the co-play of land use and rainfall on water and sediment flux dynamics across different spatiotemporal scales in intensively managed landscapes

A Dissertation Presented for the
Doctor of Philosophy
Degree
The University of Tennessee, Knoxville

Benjamin Kobina Baah Abban
May 2018

Dedication

To my family – James, Cecilia, Rosemary, Catherine, and Rita – for your undying love and support.

Acknowledgments

I would first and foremost like to express my deep gratitude to my advisor, Prof. Thanos Papanicolaou, for his support and mentorship throughout my PhD journey. His insightful, intellectual discussions and comments have been a constant source of inspiration that has spurred me on to the end. I would also like to thank Prof. Daniel Yoder, Prof. Murugesu Sivapalan, Prof. John Schwartz, and Prof. Vasilios Alexiades for serving on my dissertation committee and providing invaluable feedback at various stages of my research.

I owe a debt of gratitude to my colleagues, who have assisted me in one way or another with data collection, modeling efforts and scholarly discussions related to my research; thank you, Dr. Dimitrios Dermisis, Dr. Kenneth Wacha, Dr. Christopher Wilson, Christos Giannopoulos, Dr. Achilleas Tsakiris, Dr. Tommy Sutarto, Will Ettema, Shengnan Zhou, Micah Wyssmann, Dr. Iordanis Moustakidis, Dr. Filippo Bressan, Dr. Mohamed Elhakeem, and Dr. Ozan Abaci.

I would also like to express a special thank you to my family, for traveling this journey with me and being there for me every step of the way – this degree is as much theirs as it is mine.

Finally, I would like to acknowledge the NSF Integrative Graduate Education and Research Traineeship program, the NSF Critical Zone Observatory for Intensively Managed Landscapes, and the USGS Tennessee Water Resources Center for funding me at various stages of my research.

Abstract

Anthropogenic activities in intensively managed landscapes (IMLs) have significantly modified material travel times and delivery, and have led to more pronounced event-based dynamics compared to undisturbed conditions. Understanding and mitigating human impacts requires the use of both field-based observations and physically-based numerical models to tease out causal relationships and feedbacks between the relevant processes across the cascade of scales, from the plot to the watershed. Unfortunately, there are no event-based numerical models capable of adequately simulating sediment fluxes across scales in IMLs, thus hampering our ability to understand and mitigate anthropogenic impacts.

The goal of this study was to develop a conceptual modeling framework for IMLs that considered all the connections and interactions between terrestrial and in-stream sources on an event basis, and to use the framework to identify a characteristic scale unit (CSU) representative of sediment flux laws within the drainage network. The CSU was considered to be a scale at which local-scale variability in landscape properties ceased to have an effect on mean trends in sediment fluxes and, thus, an appropriate scale for simulating/monitoring sediment fluxes for watershed management purposes.

The framework was developed and tested in the South Amana sub-watershed (SASW), IA. An upland erosion model was coupled with an instream sediment transport model to simulate material fluxes along different pathways in SASW. A sediment fingerprinting model was also utilized to constrain the predicted contributions of terrestrial and instream sources. Modeling advances made included the incorporation of a surface roughness evolution threshold, space/time variant flow resistance representations of landscape attributes, and the stochastic representation of material origins, travel times, and delivery to the watershed outlet. The developed model was validated via an extensive field campaign performed at scales ranging from the plot to the sub-watershed.

The study results revealed thresholds of influence of landscape roughness attributes, and highlighted important intra-seasonal trends in source contributions driven by the co-play of land use and rainfall. A CSU for sediment fluxes and the factors affecting it were identified. Future studies must examine the CSU as dictated by the interplay between event-based and seasonal dynamics, and the implications for watershed management.

Table of Contents

List of Tables

List of Figures

Chapter 1

Introduction

1.1. Overview

Anthropogenic activities related to food production and other life-sustaining services in intensively managed landscapes (IMLs) such as the U.S. Midwest have significantly modified the earth's critical zone over a range of spatial scales, impacting both terrestrial and aquatic ecosystems, and negatively affecting the sustainability of arable lands and stream water quality. This is highlighted in Figure 1.1, which shows a map of cropland in the US experiencing erosion rates above tolerance limits (i.e., limits above which continued sustainable productivity of the land is not guaranteed) as a result of intensive management [*USDA*, 2015]. Changes in the land cover in these landscapes from what were previously grasslands have led to a high degree of spatial heterogeneity and temporal variability in landscape processes that were previously absent. The different practices have led to changes in the percentage of bare soil, soil surface roughness, flow pathways, soil fertilization, and erosion and depositional patterns [*Papanicolaou et al*., 2015; *Van Meter et al*., 2016; *Woo and Kumar*, 2017]. The installation of tile drains and the straightening of channels have modified material travel times and altered the hydrologic regime of the region, with a more pronounced event-based dynamics [*Sloan*, 2013]. These changes and continued human modification are believed to maintaining the system in a state of disequilibrium in which material fluxes over a season are now non-stationary [*Sullivan et al*., 2017].

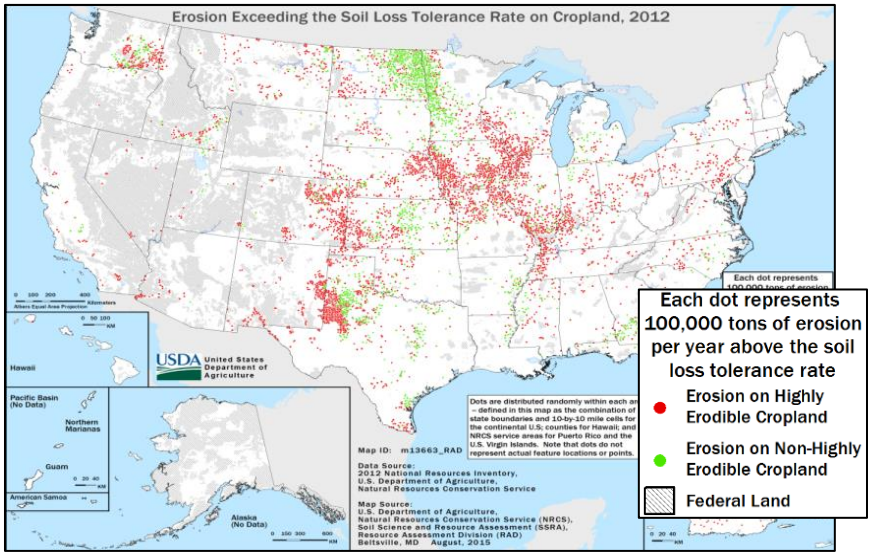

Figure 1.1: Cropland in the U.S. with erosion rates exceeding the soil loss tolerance rate [*USDA*, 2015]

To mitigate these effects, a good understanding of the critical zone processes and how they are affected by anthropogenic activities is needed. Thus, observatories such as the NSF's Critical Zone Observatory for Intensively Managed Landscapes (IML-CZO) have been set up to quantify fluxes and transformations of water, sediment, and nutrients, as well as their interactions, thresholds, and feedbacks, in these landscapes. A central hypothesis is that human modification has resulted in the critical zone exceeding a threshold whereby it has changed from being a transformer of material flux with high residence times and storage of water, sediments, and nutrients to being a transporter with low residence times and storage, thereby threatening the resiliency of the landscape and increasing its vulnerability [*Kumar et al*., 2016].

Understanding these changes and complex interactions within the critical zone requires a two-pronged approach that combines physical observations with numerical modeling to establish the causal relationships between the key variables across the different spatiotemporal scales. Although physical observations can enhance our understanding of critical zone process and reveal some cause-and-effect relationships, there is a limitation on how much inference can be drawn due to limited data in time and/or space [*Michaelides and Wainwright*, 2008; *Brantley and Lebedeva*, 2011]. Physically-based numerical models have the potential to "fill in the blanks" and tease out direct cause-and-effect relationships between the modified land surface and the fluxes across different spatial and temporal scales, thereby providing further insight into the impacts of humans over the broad range of scales and how these can be mitigated appropriately.

However, due to the significantly modified spatiotemporal scales of critical zone processes in IMLs, there is a lack of numerical models that can adequately capture the pronounced event-based dynamics across scales, as well as a lack of understanding of the appropriate spatial and temporal scales at which field observations and modeling efforts need to consider [*Papanicolaou et al*., 2018]. Most existing tools for these landscapes have thus far been developed for spatiotemporal scales corresponding to marginally modified systems, or have focused solely on limited domains within the system (e.g., only on terrestrial processes) [*Papanicolaou et al*., 2015; *Conroy et al*., 2006; *Wu*, 2008].

This dissertation develops a modeling framework for capturing event-based dynamics in IMLs and utilizes the framework to investigate causal relationships and factors affecting water and sediment fluxes from the plot scale to the sub-watershed scale. Emphasis is placed on these scales because natural processes can easily be distinguished from those induced by humans due

to the relatively shorter lag times [*Blöschl et al*., 2007]. The study combines field observations of water and sediment fluxes /travel times, improvements to sediment fingerprinting techniques for IMLs, numerical model development for event-based dynamics, novel model validation techniques, and modeling of representative land cover and storm events in an IML, to provide insight on appropriate scales to consider for field campaigns and modeling efforts in IMLs. It also sheds light on the factors that influence these scales.

1.2. Background and Critical Needs

The co-play of land management and climate dictates the net effects of anthropogenic activities on the critical zone in IMLs [*Papanicolaou et al*., 2015]. Figure 1.2 depicts the degree of heterogeneity and some of the impacts of the combined action of rainfall and human modification observed in these landscapes. During a typical storm event, rain drops falling atop the soil surface break apart soil aggregates giving rise to rain splash erosion. As runoff accumulates during the storm event, the eroded soil particles are transported from interrill areas through concentrated flow channels, such as rills and gullies, downslope and eventually into the stream network. The concentrated flow within rills and gullies also produce erosion due to shear action of the flow, causing the rills and gullies to grow in size and extend horizontally in space. Some of the particles that are being transported within these channels are deposited along the way depending on the runoff conditions, effectively redistributing soil of different sizes across the landscape. Aggregates and larger size particles tend to be deposited on the downslope end of the hillslope due to milder slopes and higher sediment concentrations, as shown in the figure. These highly complex interactions between runoff and sediment processes are further compounded by activities such as tillage, which brings subsurface soil to the surface, exposing it to weathering, thereby increasing the susceptibility of soil aggregates to detachment and thus increasing soil erosion. Redistribution is not limited to abiotic system components alone. Biotic component such as residue are also transported by flow and in soil aggregates. Both the biotic and abiotic interactions ultimately lead to different transformation rates across the landscape due to the different landscape properties.

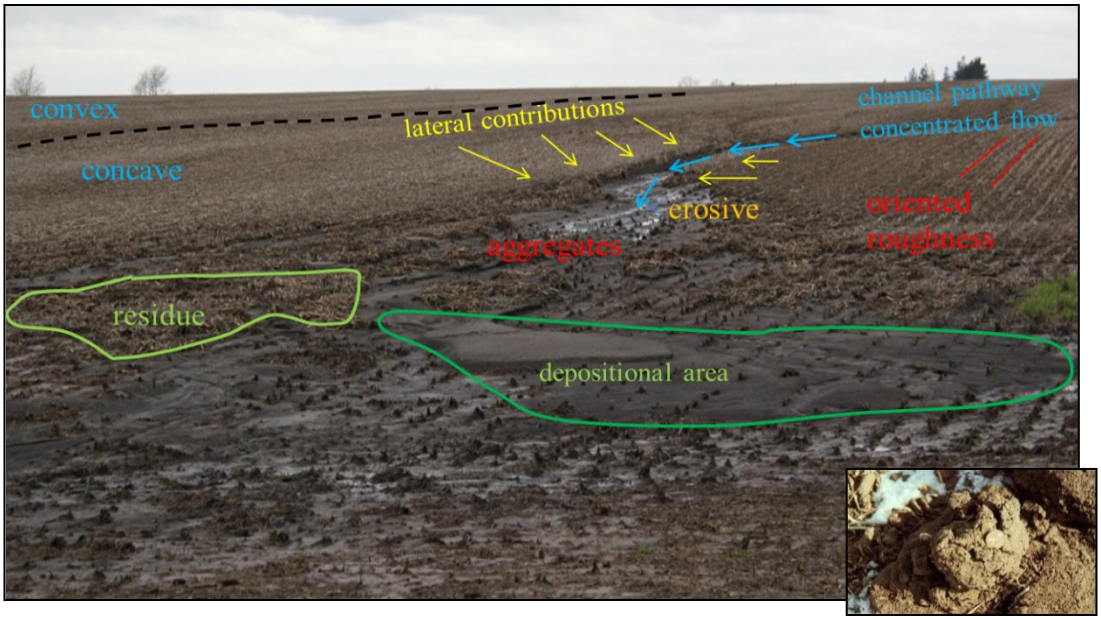

Figure 1.2: Evolving modification of the land through management and rainfall events affects heterogeneity of features and properties (abiotic and biotic) [*Papanicolaou et al*., 2015]

The impact of the co-play of land management and rainfall has also been observed within the stream network, where fluxes originate from both terrestrial and instream sources (

Figure 1.3). Increased water fluxes from the landscape are known to exacerbate instream erosion processes, including sediment entrainment through mining of the stream bed, fluvial erosion of bank material (i.e., particle-by-particle entrainment), and mass failure of the stream bank (i.e., the slumping and collapse of stream banks en masse) [*Sutarto et al*., 2014]. The sediment fluxes from the exacerbated instream erosion processes interact with the increased fluxes from terrestrial sources in a complex fashion to collectively determine the net impact of the co-play on the total fluxes and stream water quality [*Papanicolaou and Abban*, 2016].

Both the terrestrial and in-stream erosion processes vary spatially and temporally as a result of the complex interactions of water, soil/sediment, and crop rotations [*Tayfur and Kavvas*, 1998; *Govers et al*., 2007; *Papanicolaou et al*., 2015]. This results in a high variability in flux characteristics with scale in regards to net amounts and proportions of source contributions [*Wilson et al*., 2012; *Yu*, 2017]. Flux behavior changes from the plot scale to the watershed scale, and over the course of a season. Whereas some events result in highly intermittent fluxes, others result in fluxes that propagate in the form of waves [*Abban et al*., 2016; *Sullivan et al*., 2017].

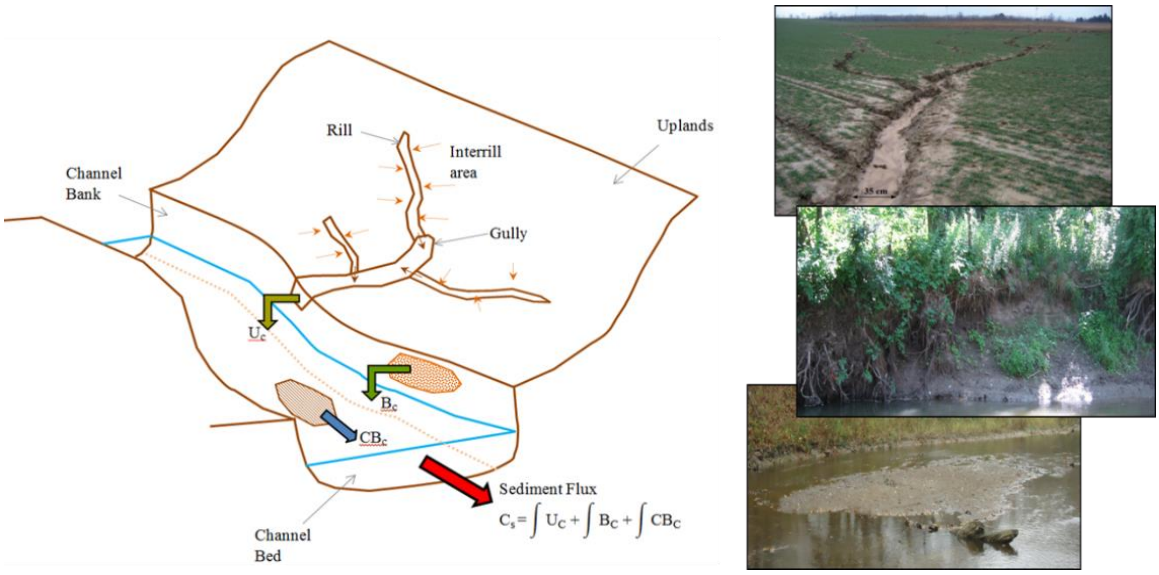

Figure 1.3: Terrestrial and instream sources collectively affect the total sediment budget (Photos: two top photos taken by the Papanicolaou group and third one from the Rhoads group)

Our current ability to predict how water and sediment fluxes transport from the plot scale to the watershed scale in the intensively managed landscapes is questionable. As described above, the modification of the key pathways and connectivity from the plot to the drainage network due to the co-play of land-use and climate has affected the time scale of the processes, driven now more by event-based dynamics rather than seasonal averages. Current watershed models are unable to capture the dynamic connectivity that arises from the co-play at the event scale due to simplistic lumped representations of terrestrial processes that are mostly valid over longer time periods and at larger spatial scales [e.g., SWAT, THREW, VIC, etc.].

The simplistic lumped treatment of hillslopes in watershed scale studies may be warranted when simulating water fluxes at larger spatial scales because of the existence of a characteristic scale unit at which the specific flow discharge does not change with increasing spatial scale and, thus, statistical representation of watershed properties can be used to represent flow dynamics [*Wood et al*., 1988; *Blöschl et al*., 1995]. However, it is uncertain whether or not this lumped treatment is valid for sediment fluxes at the hillslope scale, or at what scale it can be used to assess sediment fluxes with fair accuracy within drainage network where terrestrial and instream contributions interact. Recently, *Dermisis* [2012] has demonstrated that the spatiotemporal evolution of water fluxes in response to spatial variability in landscape attributes

can significantly alter runoff volumes and hydrograph characteristics at the hillslope scale for a storm event, with the potential to significantly alter sediment flux rates and amounts leaving the hillslope into stream networks. In some cases, he found that hillslopes with patchy vegetation on which the spatial variability in landscape attributes was taken into account yielded hydrographs with peaks that were a twice as large as "equivalent" lumped hillslopes that assumed a spatial averaging of the landscape properties (see Figure 1.4). Since sediment flux rates have been shown to correlate with peak runoff rates [*Finkener et al*., 1989], this has implications for the predictive ability lumped models when it comes to sediment fluxes on an event basis.

Another reason why our current ability to predict how sediment fluxes transport from the plot scale to the watershed scale is questionable is that most existing sediment laws assume that the system is in some state of equilibrium. However, as explained above, continued human modification in IMLs are believed to maintaining the system in a state of disequilibrium in which material fluxes over a season may be non-stationary. Sediment fluxes can be intermittent at times, and of different provenance (e.g. terrestrial versus instream sources), while in other instances fluxes can be described in the form of waves [*Abban et al*., 2016]. Further, simplistic assumptions are often made in watershed studies regarding material delivery from terrestrial sources that simply do not hold true for IMLs. Storm sequence, in addition to intensity and frequency, affects soil fluxes and redistribution although it has largely been neglected [*Wilson et al*., 2012] (see Figure 1.5). Also, only a few studies actually consider the exchanges between floodplain and in-stream sediment and the implications that they may have on sediment scaling laws at the watershed scale. All these limitations have so far hampered our ability to identify a characteristic scale unit for sediment fluxes where the specific sediment discharge is not significantly affected by local-scale variability on the landscape (i.e., statistical representation of watershed properties can be used to estimate fluxes) and flux laws representative of the mean watershed response can be established. Such a scale unit is needed for the practical benefits of watershed monitoring and evaluation.

The aforementioned limitations of existing approaches in IMLs are often enshrouded through model calibration, which is usually performed at the outlet of the watershed based on total observed sediment fluxes. However, as *Belmont et al*. [2014] have demonstrated in

FIGURE 1.6 using the SWAT model, different plausible assumptions regarding terrestrial and instream

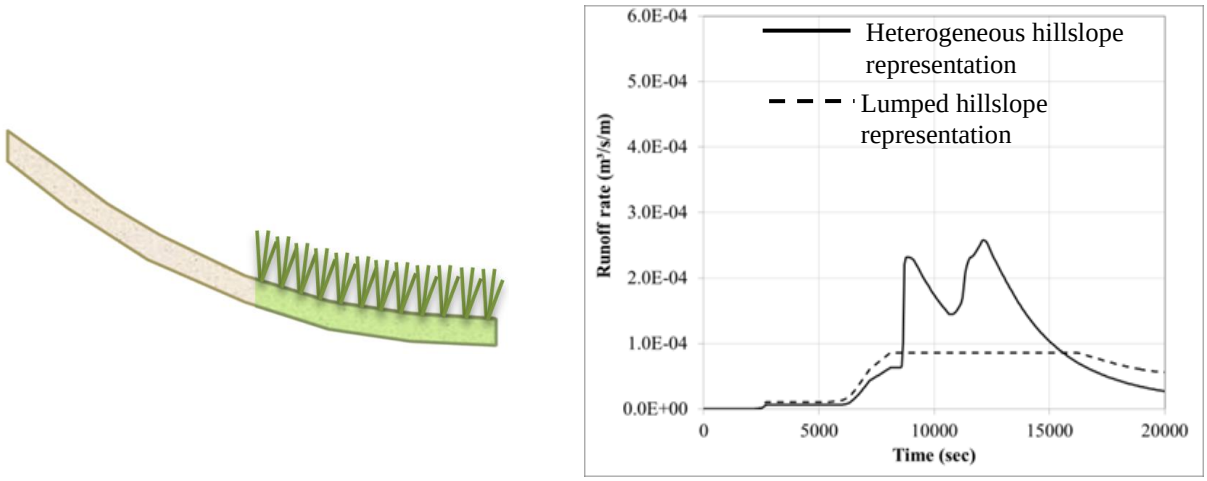

Figure 1.4: Hydrographs predicted on an intensively managed patchy concave hillslope using a model that captures the spatial variability in landscape model and another model that assumes lumped spatially averaged landscape properties [*Dermisis*, 2012].

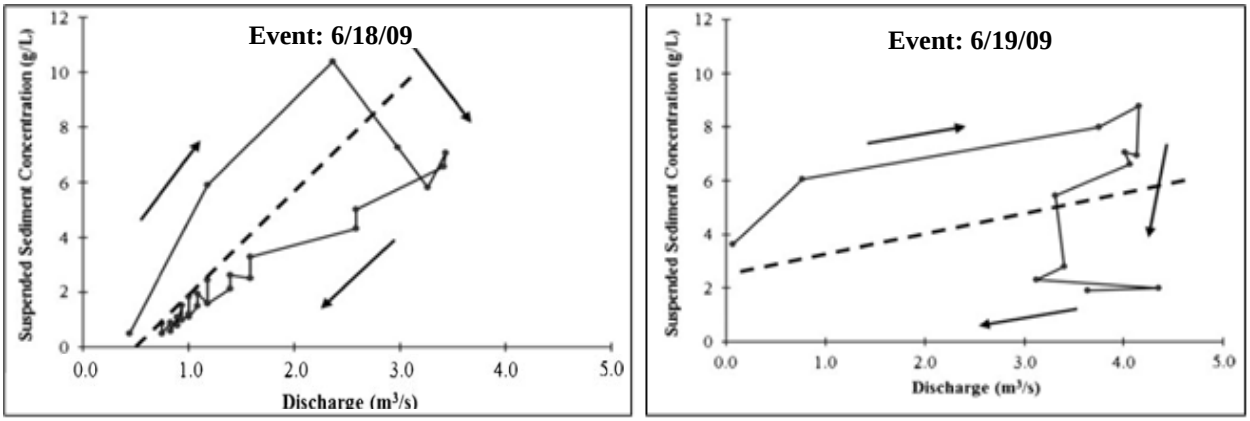

Figure 1.5: Observed sediment rating curves at the same location in an intensively managed for two successive storm events. the hysteresis loops depict exhaustion of material and the change in gradient depict less material available for transport during the second event [*Wilson et al.*, 2012]

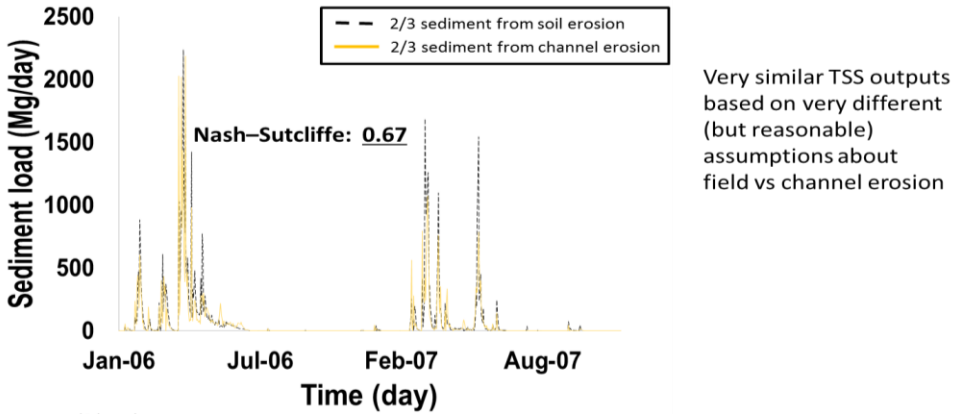

Figure 1.6: Demonstration of the equifinality issue using the SWAT model – different source contributions can lead to very similar net sediment fluxes [*Belmont et al.*, 2014]

sources can yield the same total sediment fluxes despite significantly different contributions from terrestrial and instream sources, raising the issue of equifinality (the case where different conditions lead to the same result) and questions about the true predictive capability of existing models. Evidently, current modeling frameworks that do not consider the dynamic connectivity between terrestrial and instream sources in IMLs, and whose calibration and validation approaches do not capture the relative contributions of the different sources to the total fluxes, are inadequate to ensure that the correct system dynamics are being captured. A modeling framework that is capable of capturing the connectivity between terrestrial and instream processes at the right level of detail is therefore needed to be able to simulate how fluxes of water and sediment propagate from the plot scale to the watershed scale.

Based on the above synthesis, the following two critical needs have been identified for IMLs to enable the understanding of human impact on the landscape across the different scales:

1. There is a need for the development and use of tools that can account for event-based dynamics when predicting fluxes in IMLs. These tools must be able to capture the dynamic connectivity between terrestrial and instream sources, and how it is affected by the co-play of land use and storm events.
2. There is a need for identifying a characteristic scale unit beyond which the specific sediment discharge becomes invariant with increasing spatial scale. Besides offering a parameterization unit where statistical representations of watershed properties can be used to predict mean sediment fluxes, such a scale unit has other practical merits in that is

suited for watershed management and monitoring since it offers a scale at which sediment flux laws can be used dependably to hindcast/forecast mean watershed response.

1.2.1. Overarching Goal and Hypotheses

The overarching goal of this study is, thus, to develop a modeling framework that considers all the connections and interactions between terrestrial and in-stream sources on an event basis, and to use the framework to identify a characteristic parameterization unit that is representative of the sediment flux laws within the drainage network.

Emphasis is placed on scales up to the sub-watershed scale because natural processes at these scales can easily be distinguished from those induced by humans due to the relatively shorter lag times [*Blöschl et al*., 2007]. A much better understanding of the processes and interactions at these scales will serve as a platform for extending the knowledge gained to larger scales. The study focuses on the South Amana Sub-watershed (SASW), located in the headwaters of the Clear Creek Watershed, IA, which is part of the IML-CZO. SASW, which is characterized by corn-soybean rotations on moderately well-drained to somewhat poorly drained soils and a well-integrated drainage network, was selected for the study because it displays features needed to address all the critical needs identified above for IMLs. A more detailed description of the site is provided in Chapters 2, 4, 5, and 6.

This study is premised on the following hypotheses:

1. Continued human modification of the landscape has affected the connectivity between terrestrial and instream domains, significantly altering the travel times and net fluxes of water and sediment through the drainage network, compared to undisturbed conditions. The continued modification is leading the system along a non-stationary path where intra-seasonal patterns in fluxes that are regulated by the collective action of land use and rainfall play an important role on the system state at a given time.
2. There exists a characteristic scale unit where the specific sediment discharge is not significantly affected by local-scale variability in landscape and hydrologic properties, and at which statistical representations of watershed properties may be used to predict sediment fluxes. However, this characteristic scale unit for sediment differs from that for specific flow discharge due to differences in travel times and processes involved.

1.3. Specific Study Objectives

Based on the overarching goal and hypotheses, the following specific objectives are pursued:

1. To use a bottom-up approach to examine and identify the key variables and cause–effect relations affecting water and sediment fluxes from the plot scale to the sub-watershed scale in IMLs. This will include:
   a) The use of state-of-the-art plot scale experiments to examine the interaction between rainfall and land use in modulating soil surface roughness, as well as to examine the fluxes of water and sediment from the different land covers present in IMLs.
   b) The development of an advanced numerical approach for capturing the spatiotemporal effects of roughness related to the different landscape attributes on water and sediment fluxes at the hillslope scale by accounting for the feedbacks between flow and roughness. Then, using the approach, the examination of flux travel times and magnitude, i.e., amplitude and wavelength, at the hillslope scale for IMLs.
   c) The provision of a numerical approach that accounts for the key pathways of transport (i.e., connectivities) between terrestrial and instream domains, and incorporates travel times from the different terrestrial and instream source areas. Then, using the model, the examination of the amplitude and wavelength of fluxes at the sub-watershed scale.
2. To develop a Bayesian statistical sediment sourcing model to validate the numerical treatment of the connectivity between terrestrial and instream sources in space and time outlined in objective 1c. The Bayesian model will utilize prior and current data on land use and rainfall, and will quantify the contributions of the different sources to flux estimates and associated uncertainties.
3. To identify numerically the existence of a scale beyond which the mean sediment discharge per unit area remains reasonably constant with increasing scale, and at which trends in mean sediment fluxes can be monitored. This scale is examined for different rainfall events and land covers that are representative of conditions at different times of the growing season.

1.4. Outline of Dissertation

The modeling framework development and its subsequent use for examining flux propagation in space and time will require a multi-scale approach that addresses key processes from the plot scale to the sub-watershed scale. This approach must necessarily involve a combination of field experiments and numerical modeling exercise to achieve the study goals. A roadmap of the dissertation following the approach is provided in Figure 1.7.

Chapter 2 focuses on the plot scale and addresses a critical component of upland erosion models regarding the evolution of soil surface roughness under raindrop action. The majority of existing models assume a decay in soil surface roughness with continued rainfall, without a limiting threshold for such a decay. The chapter examines roughness evolution under raindrop action on smooth surfaces to determine if such an assumption is always valid, and whether or not there is a threshold length scale at which it becomes invalid.

Chapter 3 deals with flow resistance representation in overland models, focusing specifically on landscapes that display heterogeneity in surface roughness. Although studies suggest that, for a given surface, flow resistance varies both in space and time with changing flow conditions, the common assumption made in many overland models is that flow resistance due surface roughness is invariant with respect to space and/or time during a storm event. The chapter investigates the implications of this assumption on runoff hydrograph peak and shape at the hillslope scale, and any potential implications this may have on sediment transport predictions. Threshold storm magnitudes and hillslope gradients under which the assumption could be valid are also identified for different landscape attributes found in IMLs.

Chapter 4 tackles the issue of connectivity representation between terrestrial and instream sources when modeling IMLs by coupling an established upland erosion model with an established instream sediment transport model. The ability of the model to capture flow-related network dynamics such as backwater effects and sediment fluxes to the watershed outlet are examined and validated using benchmark data and observed rating curves.

Chapter 5 develops a sediment sourcing model for validating the treatment of sediment connectivity between terrestrial and instream sources in IMLs at the sub-watershed scale. Sourcing studies are performed based on previous field campaigns to investigate the intra-seasonal patterns in sediment connectivity between terrestrial and instream sources, and its influence on relative source contributions to sediment fluxes at the sub-watershed scale.

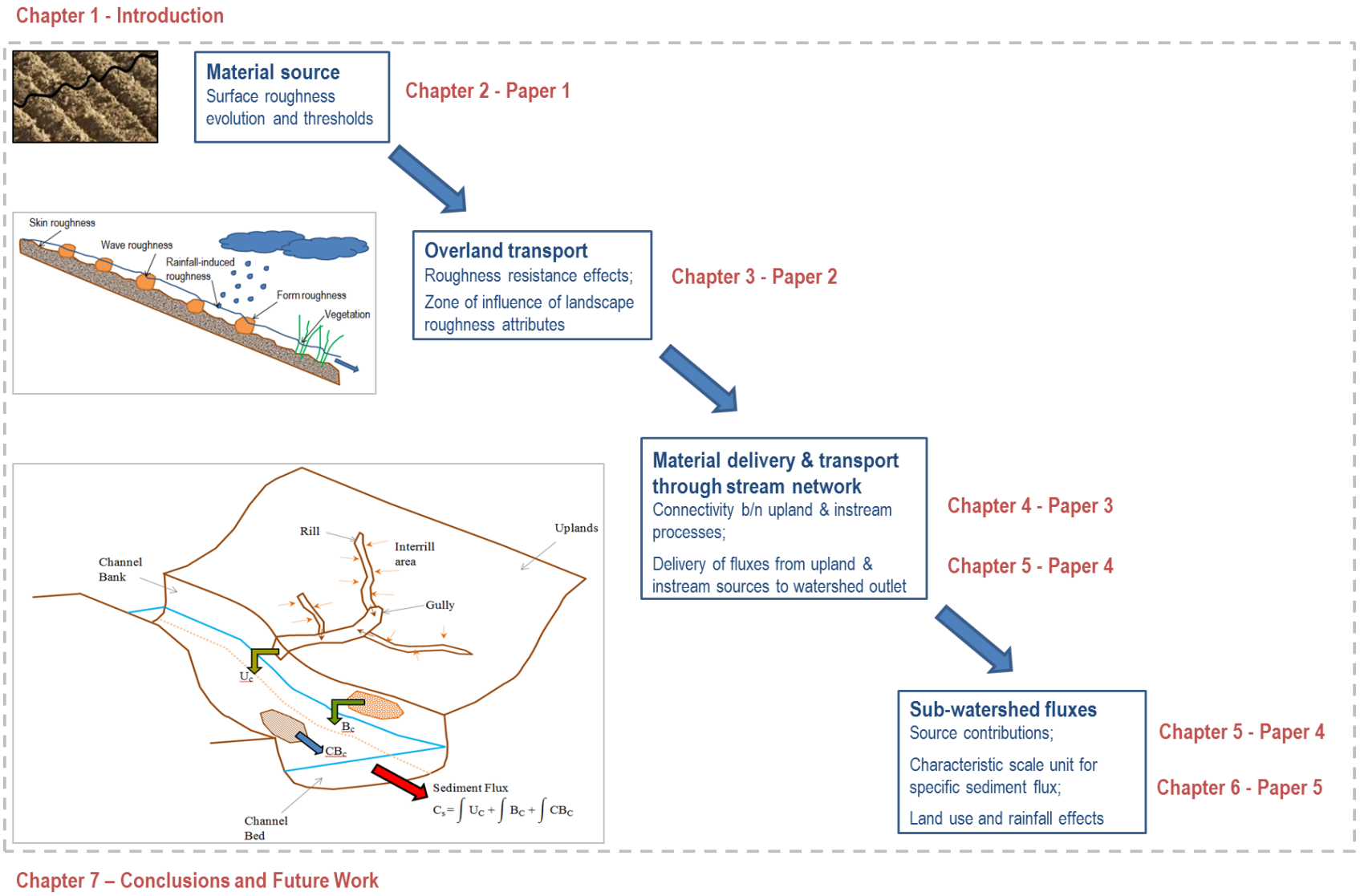

Figure 1.7: Dissertation Roadmap

Chapter 6 presents the complete modeling framework for IMLs, incorporating the outcomes from Chapters 2-5. A combination of terrestrial and instream experiments are used to measure travel times and fluxes of water and sediment from the plot to the sub-watershed scale for validating the framework. The validated framework is then used to investigate the existence of a characteristic scale unit at which local-scale variability in landscape and hydrologic properties does not significantly affect the specific sediment discharge, as well as any factors that may affect this scale.

Finally, *Chapter 7* synthesizes and summarizes the key findings from Chapters 2-6 and provides recommendations for future research. Except for Chapters 1 and 7, each chapter in the dissertation is presented in the form of a standalone paper.

References

Abban, B., A.N. Papanicolaou, M.K. Cowles, C.G. Wilson, O. Abaci, K. Wacha, K. Schilling, and D. Schnoebelen (2016), An Enhanced Bayesian Fingerprinting Framework for Studying Sediment Source Dynamics in Intensively Managed Landscapes, Water Resources Research, DOI: 10.1002/2015WR018030.

Brantley, S.L., and M. Lebedeva (2011), Learning to Read the Chemistry of Regolith to Understand the Critical Zone, Annual Review of Earth and Planetary Sciences, 39:387-416.

Belmont, P., Kumarasamy, K., Kelly, S.A., Schaffrath, K.R., Beach, T.J. (2014). The cascade of non-stationarity. American Geophysical Union Fall meeting. December 2014. San Francisco, CA.

Blöschl, G., Grayson, R. B., and Sivapalan, M. (1995), On the representative elementary area concept and its utility for distributed rainfall-runoff modeling, Hydrological Processes, 9: 313-330.

Blöschl, G., Ardoin-Bardin, S., Bonell, M., Dorninger, M., Goodrich, D., Gutknecht, D., Matamoros, D., Merz, B., Shand, P. and Szolgay, J. (2007), At what scales do climate variability and land cover change impact on flooding and low flows?. Hydrol. Process., 21: 1241–1247. doi:10.1002/hyp.6669.

Conroy W. J., R. H. Hotchkiss, and W. J. Elliot (2006), A coupled upland-erosion and instream hydrodynamic-sediment transport model for evaluating sediment transport in forested watersheds, Transactions of the ASABE, 49(6), 1713–1722.

Dermisis, D. (2012) Developing and improved, shock-capturing numerical model for predicting spatially variable runoff and soil erosion, PhD Thesis, University of Iowa.

Finkner, S.C., M.A. Nearing, G.R. Foster and J.E. Gilley (1989), A simplified equation for modeling sediment transport capacity. Trans. ASAE 32(5):1545-1550.

Govers G., R. Giménez, and K. Van Oost (2007), Rill erosion: Exploring the relationship between experiments, modelling and field observations, Earth-Science Reviews, 84 (2007), 87-102.

Kumar, P., A.N. Papanicolaou, A. Anders, E. A. Bettis, T. Filley, et al. (2016), Critical Zone Observatory for Intensively Managed Landscapes (IML-CZO) Annual Report, NSF Award #1331906.

Michaelides, K. and J. Wainwright (2008), Internal testing of a numerical model of hillslope-channel coupling using laboratory-flume experiments, Earth Surface Processes and Landforms, 27: 1441-1458.

Papanicolaou, A.N. and B. Abban (2016), Channel Erosion and Sediment Transport, in Handbook of Applied Hydrology, 2nd Edition, edited by V.P. Singh, Chapter 65, McGraw Hill. ISBN:9780071835107.

Papanicolaou, A.N., B.K.B. Abban, D.C. Dermisis, C.P. Giannopoulos, D.C. Flanagan, J.R. Frankenberger, and K.M. Wacha (2018), Flow Resistance Interactions on Hillslopes With Heterogeneous Attributes: Effects on Runoff Hydrograph Characteristics, Water Resources Research, 54. DOI: 10.1002/2017WR021109.

Papanicolaou, A.N., K.M. Wacha, B.K. Abban, C.G. Wilson, J. Hatfield, C. Stanier, and T. Filley (2015), From Soilscapes to Landscapes: A Landscape-oriented Approach to Simulate Soil Organic Carbon Dynamics in Intensively Managed Landscapes, Journal of Geophysical Research: Biogeosciences, 120, DOI: 10.1002/2015JG003078.

Sloan (2013), Hydrologic impacts of tile drainage in Iowa, MS Thesis, University of Iowa.

Sullivan, P., A. Wymore, W. McDowell et al. 2017. New Opportunities for Critical Zone Science. June 2017 Arlington Meeting for CZ Science White Booklet, Critical Zone Observatories, US NSF National Program.

Sutarto, T., A. N. Papanicolaou, C. G. Wilson, and E. J. Langendoen (2014), Stability Analysis of Semicohesive Streambanks with CONCEPTS: Coupling Field and Laboratory Investigations to Quantify the Onset of Fluvial Erosion and Mass Failure, J Hydraul Eng, 140(9).

Tayfur, G., and M.L. Kavvas (1998), Areally-averaged overland flow equations at hillslope scale, Hydrological Sciences, 43, 361-378.

USDA (2015), Natural Resources Conservation Service, Soil Science and Resource Assessment, United States Department of Agriculture, Resource Assessment Division, Beltsville, MD.

Van Meter, K.J., N.B. Basu, J.J. Veenstra, and C.L. Burras (2016), The nitrogen legacy: emerging evidence of nitrogen accumulation in anthropogenic landscapes, Environmental Research Letters, 11(3).

Wilson, C. G., A. N. T. Papanicolaou, and K. D. Denn (2012), Partitioning fine sediment loads in a headwater system with intensive agriculture, J Soil Sediment, 12(6), 966-981.

Woo, D., and P. Kumar (2017), Role of micro-topographic variability on the distribution of inorganic soil-nitrogen age in intensively managed landscape, Water Resources Research, 53: 8404–8422. https://doi.org/10.1002/2017WR021053.

Wood, E. F., Sivapalan, M., Beven, K., and Band, L. (1988), Effects of spatial variability and scale with implications to hydrologic modeling, J. Hydrol., 102, 29-47.

Wu W. M. (2008), Computational river dynamics. Taylor & Francis Group, London.

Yu, M. (2017), Analysis of sediment dynamics in intensively managed landscapes, PhD Dissertation, University of Illinois at Urbana-Champaign, Urbana, IL.

Chapter 2

Quantifying the changes of soil surface microroughness due to rainfall impact on a smooth surface

Abstract

This study examines the rainfall induced change in soil microroughness of a bare smooth soil surface in an agricultural field. The majority of soil microroughness studies have focused on surface roughness on the order of ~5-50 mm and have reported a decay of soil surface roughness with rainfall. However, there is quantitative evidence from few studies suggesting that surfaces with microroughness less than 5 mm may undergo an increase in roughness when subject to rainfall action. The focus herein is on initial microroughness length scales on the order of 2 mm, a low roughness condition observed seasonally in some landscapes under bare conditions, and chosen to systematically examine the increasing roughness phenomenon. Three rainfall intensities of 30 mm/h, 60 mm/h and 75 mm/h are applied to a smoothened bed surface in a field plot via a rainfall simulator. Soil surface microroughness is recorded via a surface-profile laser scanner. Several indices are utilized to quantify the soil surface microroughness, namely the Random Roughness (RR) index, the crossover length, the variance scale from the Markov-Gaussian model, and the limiting difference. Findings show a consistent increase in roughness under the action of rainfall, with an overall agreement between all indices in terms of trend and magnitude. Although this study is limited to a narrow range of rainfall and soil conditions, the results suggest that the outcome of the interaction between rainfall and a soil surface can be different for smooth and rough surfaces, and thus warrant the need for a better understanding of this interaction. Further, an important implication of the findings is that a surface undergoing roughness increase or decrease under rainfall action will approach a limiting threshold where the RR ceases to change significantly. This threshold needs to be accounted for in existing models.

2.1. Introduction

Soil surface roughness influences many hydrologic processes such as flow partitioning between runoff and infiltration, flow unsteadiness, as well as soil mobilization and re-deposition at scales ranging from a few millimeters to hillslope level [e.g. *Huang and Bradford*, 1990; *Magunda et al*., 1997; *Zhang et al*., 2014]. There are three distinct classes of microtopography surface roughness for agricultural landscapes, each one of them depicting a representative length scale [*Römkens and Wang*, 1986; *Potter*, 1990]. Following *Oades and Waters* [1991], the first class includes microrelief variations from individual soil grains to aggregates in the order of

0.053-2.0 mm. The second class consists of variations due to soil clods ranging between 2-100 mm. The third class of soil surface roughness is systematic elevation differences due to tillage, referred to as oriented roughness (OR), ranging between 100-300 mm.

From the outlined above, the first two classes are the so-called random roughness (RR), and constitute the main focus of the present research. RR is quantified on a surface after correction for both slope and tillage marks. Contrary to OR, which changes seasonally and during crop rotations, RR changes on an event base [*Abaci and Papanicolaou*, 2009]. RR reflects the effects of rainfall action on the soil surface and inherently varies in space and time. As a result, RR affects key hydrologic processes at the soil scape and ultimately at the hillslope scale e.g., infiltration, overland flow, etc. [*Gómez and Nearing*, 2005; *Chi et al*., 2012].

Several studies have been performed to characterize RR. Most have focused on initial microroughness length scales of 5-50 mm [e.g., *Zobeck and Onstad*, 1987; *Gilley and Finkner*, 1991]. In these studies, a decay of roughness due to precipitation action is predicted, since rainfall impact and runoff "smoothen" the rough edges of soil grains, aggregates and clods, especially in the absence of cover [*Potter*, 1990; *Bertuzzi et al*., 1990; *Vázquez et al*., 2008; *Vermang et al*., 2013]. There are few studies that have examined surfaces with initial microroughness less than 5 mm, a low roughness condition observed seasonally in some landscapes under bare conditions [e.g., *Kamphorst et al*., 2000; *Vázquez et al*., 2008; *Zheng et al.*, 2014]. Hereafter, for shortness, tests with initial RR less than 5 mm will be referred to as "smooth", whereas tests with initial RR greater than 5 mm will be referred to as "rough". There are some quantitative indications that under bare smooth surface conditions, soil surface roughness may actually increase under the action of rainfall. Specifically, the study by *Huang and Bradford* [1992] calculated the semi-variance with respect to length scale before and after rainfall, and an increase in roughness with rainfall was denoted using the Markov-Gaussian model for a surface with low initial roughness. *Rosa et al*. [2012] introduced an index (called Roughness Index) estimated from the semivariogram to describe roughness, and an increase of the index with rainfall was observed under some conditions, and attributed to the fragmentation of aggregates and clods to smaller aggregates. *Zheng et al*. [2014] also reported an increase in values of the RR after the application of rainfall on smooth soil surfaces. However, none of the above studies acknowledged and related the increasing trend in surface microroughness to rainfall impact on smooth surfaces.

The main goal of this study is to examine changes in RR under rainfall impact for initial microroughness less than 2 mm, since this appears to be the lower limit of roughness scales examined in the literature. It is postulated that an increase in microroughness may occur under the action of rainfall on pre-existing smooth surfaces due to the nature of the interaction between rainfall and the soil surface. An implication of this postulate is that a surface undergoing roughness increase or decrease under rainfall action will approach a limiting threshold where the RR ceases to change significantly. To meet the study goal, we employ four commonly used indices, the RR index, the crossover length, the variance scale from the Markov-Gaussian model, and the limiting difference. The last three indices are alternate methods and used here to supplement the RR index analysis for relative change in roughness.

2.2. Materials and Methods

2.2.1. Experimental Conditions

This study was conducted on an experimental plot of the U.S. National Science Foundation Intensively Managed Landscapes Critical Zone Observatory in the headwaters of Clear Creek, IA (41.74º N, -91.94º W and an elevation of 250 m above mean sea level; Figure 2.1 and Figure 2.2). The soil series at the plot where the experiments were conducted is Tama (fine-silty, mixed, superactive, mesic Cumulic Endoaquoll) (http://criticalzone.org/iml/infrastructure/field-areas-iml/). It consists of 5% sand, 26% clay, 68% silt, and an organic matter content of 4.4%. The aggregate size distribution of the soil consists of 19% of the soil size fraction less than 250 μm, 48% between 250 μm and 2 mm, and 33% greater than 2 mm. These soils contain both smectite and illite, with high cation exchange capacity between 15 and 30 Meq/100 g. The experimental plot was uniform in terms of downslope curvature, its gradient was 9% and the plot size was approximately 7 m long by 1.2 m wide.

The soil surface was prepared before each experiment by tamping using a plywood board to create a smoothened surface. This was done to ensure a consistency in surface roughness between the experiments, as well as to ensure that any potential bias introduced in the plot preparation would be also be consistent, if not minimal. This was confirmed by the observed roughness of the experiment replicates. Rainfall was applied to the plot using Norton Ladder Multiple Intensity Rainfall Simulators designed by the USDA-ARS National Soil Erosion Research Laboratory, IN.

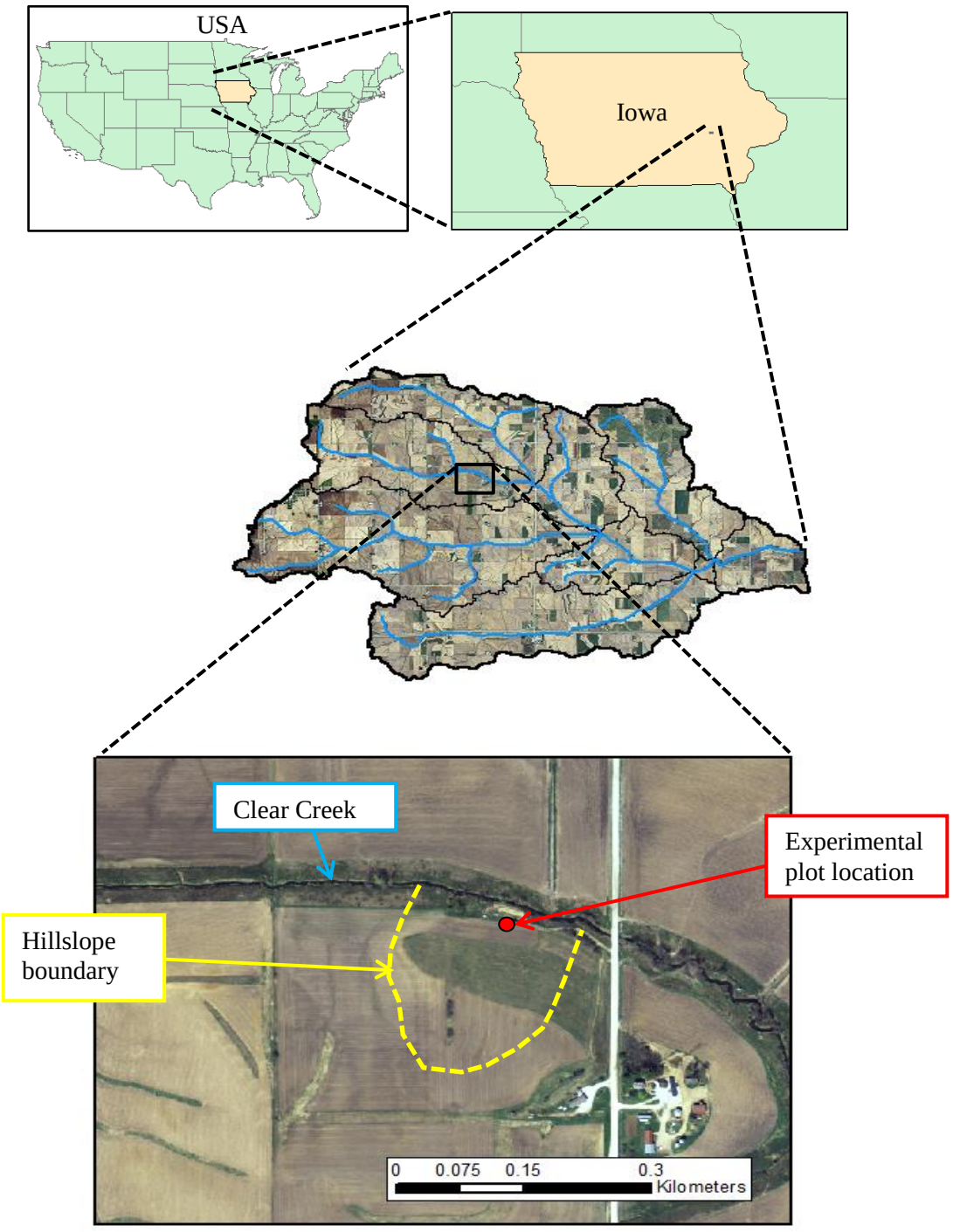

Figure 2.1: Location of experimental plot in the headwaters of Clear Creek, IA(41.74º N, -91.94º W)

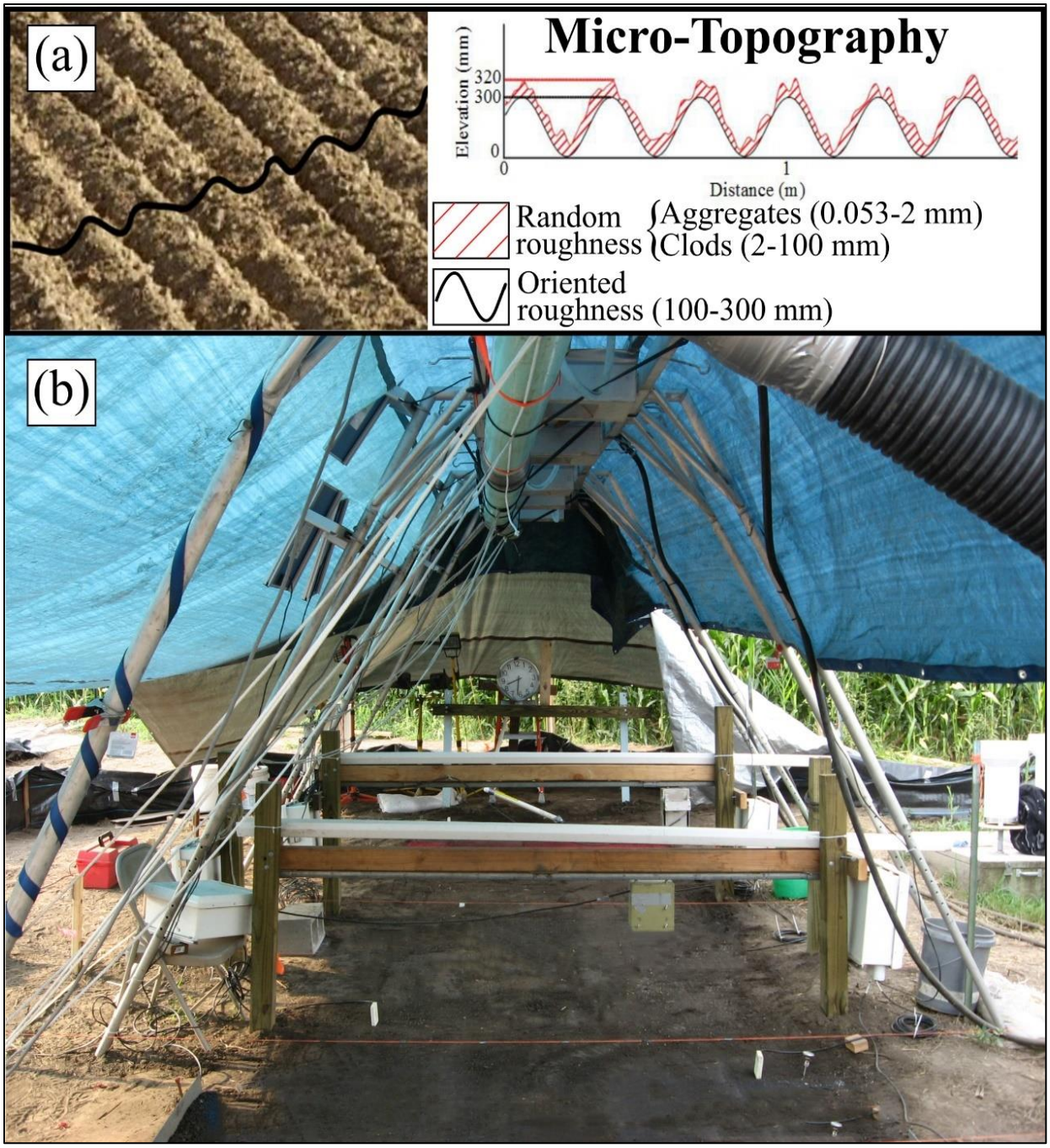

Figure 2.2: (a) Types of soil surface microroughness. (b) Experimental plot. The rainfall simulator is placed above the bare soil surface and a base made of wood is put into place to facilitate the movement of the surface-profile laser scanner.

Figure 2.3 shows the setup for all the experimental runs considered in the present study. For each test, three rainfall simulators were mounted in series over the experimental plot (Figure 2.3a) and approximately 2.5 m atop the plot surface (Figure 2.3b) in order to ensure that raindrop terminal velocity was reached. Water was continuously pumped from a water tank under controlled pressure, and uniform rainfall was applied through oscillating VeeJet nozzles which provided spherical drops with median diameters between 2.25-2.75 mm and a terminal velocity between 6.8-7.7 m/s depending on the rainfall intensity. The distribution of raindrop sizes generated by the rainfall simulators was calibrated using a disdrometer and followed a Marshall-Palmer distribution [*Elhakeem and Papanicolaou*, 2009], which is a widely accepted distribution for natural raindrop sizes in the U.S. Midwest where the study was performed [*Marshall and Palmer*, 1948]. The calibration of the raindrop sizes was achieved by adjusting the pressure and swing frequency of the VeeJet nozzles. This level of attention was taken to minimize any potential biases compared to natural rainfall with respect to raindrop size distribution, and, thus, render the rainfall simulation experiments scalable to other regions experiencing the same type of soil, bare surface, roughness conditions, and natural rainfall characteristics.

Surface elevations were obtained prior to and after the completion of the experiments via an instantaneous digital surface-profile laser scanner [*Darboux and Huang*, 2003], developed by the USDA-ARS National Soil Erosion Research Laboratory, IN (Figure 2.4a). Laser scanner measurements before the runs confirmed that the overall microrelief was less than 2 mm. Horizontal and vertical accuracies of the laser are 0.5 mm. Thus, microroughness features less than 0.5 mm may not have been captured in the analysis. Points were measured every 1 mm. The system consists of two laser diodes mounted 40 cm apart to project a laser plane over the targeted surface. The beam is captured by an 8-bit, high-resolution progressive scan charge-couple device camera with 1030 rows x 1300 columns and a 9 mm lens. The camera and lasers are mounted on a 5 m long carriage assembly and their movement on the carriage is controlled by software that regulates the travel distance based on a user-specified distance (Figure 2.4a). Information captured by the camera is recorded with an attached computer. The information from each scan is converted into a set of (x,y,z) coordinates using a calibration file and the software developed from the USDA-ARS National Soil Erosion Research Laboratory for data transformation as explained by *Darboux and Huang* [2003]. The set of (x,y,z) coordinates obtained for each experiment are imported into ArcGIS 10.3.1 in order to create the

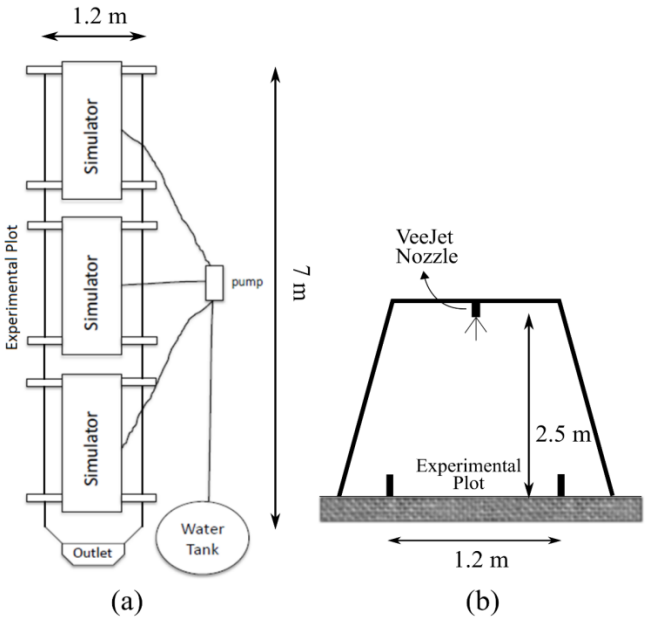

Figure 2.3: Setup of the experimental tests: (a) Rainfall simulators are mounted in series and a pump provides them with water from a tank. (b) Rainfall simulators are placed and adjusted at a height of 2.5 m above the experimental plot surface to ensure drop terminal velocity is reached.

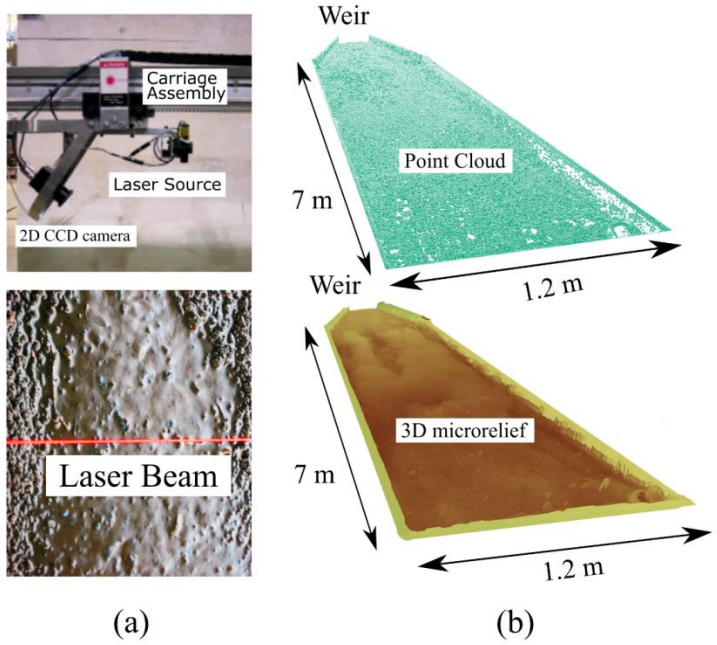

Figure 2.4: (a) Instantaneous digital surface-profile laser scanner used in the experimental runs and laser beam projected on the soil surface. (b) Cloud of (x,y,z) data acquired from the laser scanner for an experimental test along with the associated 3D representation of the soil surface microrelief through inverse distance weighted interpolation .

corresponding Digital Elevation Models (DEMs) through inverse distance weighting interpolation and thereby visualize or analyze the surfaces (Figure 2.4b). The resulting DEMs have a horizontal resolution of 1 mm and an accuracy of 0.5 mm in the vertical.

Three tests of varying rainfall intensity were conducted on the experimental plot. Rainfall intensities were respectively 30, 60 and 75 mm/h for experiments 1, 2 and 3. These simulated intensities represent typical storms observed in the region of South Amana where the plot is located [*Huff and Angel*, 1992]. Three replicates of each rainfall intensity case were performed until steady state conditions, and repeatability was confirmed by evaluation of changes in RR at specific cross-sections in the rainsplash dominated zone. It was found that on an average, the relative error of the RR ratios between replicates did not exceed 7%. The volumetric water content was recorded via six 5TE soil moisture sensors manufactured by Decagon Devices, Inc. and placed along the plot to a depth of 10 mm. The initial volumetric water content was found to be similar for each experiment and approximately equal to 35% at the whole plot, where the field capacity of the specific soil is 38%. Each experiment was run for nearly 5 hours, sufficiently long to reach steady state conditions, as confirmed by weir readings and discrete samples taken at the outlet of the plot. The infiltration rate was estimated during all rainfall simulation runs by subtracting the measured runoff rates from the constant rainfall rates. This approach has been commonly used in plot experiments and provides a good estimate of the spatially averaged infiltration rates [e.g., *Mohamoud et al*., 1990; *Wainwright et al*., 2000]. Averaged saturated hydraulic conductivity values ranged from 3.20 – 4.56 mm/h, which are in agreement with the averaged saturated hydraulic conductivity value of 4.3 mm/h measured by *Papanicolaou et al*. [2015a] using semi-automated double ring infiltrometers at the field where the study was performed. Although the average saturated hydraulic conductivity values were low with respect to the applied rainfall rates, minimal ponding was observed on the experimental plot, owing to the smooth bare conditions and the high plot gradient of 9%, which led to low depression storage.

The initial microroughness length scale in Experiment 1 (1.17 mm) was greater than that of Experiment 2 (0.42 mm) and Experiment 3 (0.32 mm) – see Table 1. This is attributed to the different timing of the experiment runs with respect to tillage. Experiment 1 was performed in early August, soon after harvest, so the soil surface had recently been disturbed. However, for Experiments 2 and 3 which were performed in late September, the soil presented less surface

disturbance due to the cumulative action of runoff from upslope areas on the plots arising from natural rainfall within that period [*Papanicolaou et al*., 2015b]. Therefore, despite tamping with plywood, remnants of tillage effects remained in Experiment 1 yielding different initial microroughness length scales than Experiments 2 and 3. This, however, is not an issue since all the results are presented herein in a dimensionless form (see Section 2.2.2 below on the index ratios). All cases, nonetheless, exhibited initial microroughness length less than 2 mm corresponding to smooth surface bed conditions as confirmed with the laser scanner. Dry soil bulk density was 1.25 g/cm^3 for Experiment 1, and about 6% higher for Experiments 2 and 3 due to self-weigh consolidation of soil.

Figure 2.5a provides an example of the experimental plot at pre-rainfall and post-rainfall conditions. Since the focus of this research is only on plot regions where raindrop detachment is dominant over runoff, we are using the scanned profiles that correspond only to these upslope locations, which are shown in Figure 2.5b. Rill formation was not observed in these regions throughout the experiments. Visual observations confirmed that raindrop detachment was dominant and the main driver of the change in soil surface roughness. For scanned profiles within the Region of Interest (ROI) (i.e., a selected 200 mm x 200 mm window size), we extracted the data for further statistical and geostatistical analyses by utilizing the public domain R software (https://www.r-project.org/). The geostatistics ('gstat') and spatial analysis ('sp') libraries were imported to create sample semivariograms.

2.2.2. Soil Surface Roughness Quantification

According to *Paz-Ferreiro et al*. [2008], the RR index, which was first proposed by *Allmaras et al*. [1966], is the most widely used statistical microrelief index for the evaluation of soil surface roughness. The RR index was initially calculated per *Allmaras et al*. [1966] as the standard deviation of the log-transformed residual point elevation data. In this study, it is calculated according to *Currence and Lovely* [1970] as the standard deviation of bed surface elevation data around the mean elevation, after correction for slope using the best fit plane and removal of tillage effects in the individual height readings:

$$RR = \sqrt{\frac{\sum_{i=1}^{n}(Z_i - \bar{Z})^2}{n}} \quad (1)$$

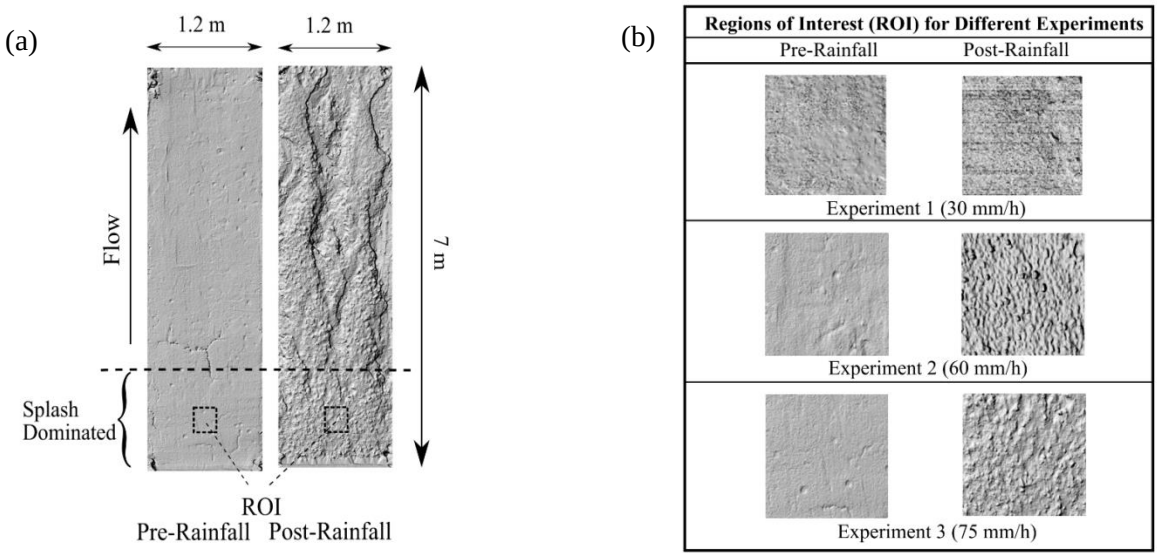

Figure 2.5: (a) Experimental plot under pre- and post-rainfall conditions for an experimental test. The dashed boxes indicate the extent of the Region of Interest (ROI), where raindrop detachment is dominant over runoff. (b) Scanned profiles extracted from the laser-scanned areas of the three experimental tests considered, under both pre- and post-rainfall conditions.

where Z_i and $\bar{Z}$ are individual elevation height readings and their mean, respectively, and n is the total number of readings.

The RR index calculated from Eq. (1) is the principal method to quantify soil surface roughness due to its frequent and widespread use in various studies and landscape models as a descriptor of microroughness. The RR index, however, requires that there is no spatial correlation between the surface elevations [*Huang and Bradford*, 1992]. Hence, special care must be taken in adopting the RR index. If correlation exists within a certain spatial scale, the RR index will likely change with the changing window size of observed data [*Paz-Ferreiro et al*., 2008] and may be dependent on the resolution of the measurement device [*Huang and Bradford*, 1992]. Thus, alternative scale-independent methods that consider spatial correlation have been developed by other researchers in order to address this issue. These methods include first-order variogram analysis [*Linden and van Doren*, 1986; *Paz-Ferreiro et al*., 2008], semivariogram analysis [*Vázquez et al*., 2005; *Oleschko et al*., 2008; *Rosa et al*. 2012; *Vermang et al*., 2013], fractal models based on Fractional Brownian Motion [*Burrough*, 1983a; *Vázquez et al*., 2005; *Papanicolaou et al*., 2012; *Vermang et al*., 2013], multifractal analysis [*Lovejoy and*

Schertzer, 2007; *Vázquez et al*., 2008], Markov-Gaussian model [*Huang and Bradford*, 1992; *Vermang et al*., 2013], and two-dimensional Fourier Transform [*Cheng et al*., 2012], among others. We herein employ additional indices derived from the first-order variogram and the semivariogram as alternatives to the RR index, which is also utilized accounting for its limitations. These include the crossover length, the Markov-Gaussian variance length scale, and the limiting difference.

The crossover length derived from semivariogram analysis is an index that is commonly used in most recent soil microrelief studies to describe surface microroughness. It has the advantage of its quantification being scale independent through the consideration of the spatial correlation between surface elevations [*Vázquez et al*., 2007; *Paz-Ferreiro et al*., 2008; *Tarquis et al*., 2008]. The semivariogram is calculated from the following equation:

$$\gamma(h) = \frac{1}{2n(h)} \sum_{i=1}^{n(h)} [Z(x_i + h) - Z(x_i)]^2 \quad (2)$$

where $\gamma(h)$ is the semivariance, h is the lag-distance between data points, $Z(x)$ is the elevation height value at location x after correction for both slope and tillage marks and $n(h)$ is the total number of pairs separated by lag-distance h considered in the calculation. The semivariogram is the plot of the semivariance with respect to the lag-distance.

Key indices for describing soil surface roughness can be derived from the semivariogram. Assuming a fractional Brownian motion model for describing soil surface roughness, as proposed in the pioneering work of *Mandelbrot and van Ness* [1968], the following expression for $\gamma(h)$ that incorporates the generalized Hurst exponent, H, is obtained [*Huang and Bradford*, 1992; *Vázquez et al*., 2007; *Paz-Ferreiro et al*., 2008; *Tarquis et al*., 2008]:

$$\gamma(h) = l^{2-2H} h^{2H} \quad (3)$$

where H is a measure of the degree of correlation between the surface elevations at lag distance h with $0 < H < 1$ and l is the crossover length. The crossover length is a measure of the vertical variability of soil surface roughness at the particular scale where the fractal dimension is estimated, hence greater roughness is associated with larger crossover length values and vice versa (Huang and Bradford, 1992). The generalized Hurst exponent is a less sensitive descriptor

of soil surface evolution as influenced by rainfall [*Vázquez et al*., 2005], hence attention is mostly centered on the crossover length. Given the semivariogram plot calculated using Eq. (2), *H* and *l* can be extracted by fitting a power law relationship in the form of $y = Ax^B$ to the semivariance-lag distance data, where $y = \gamma(h)$ and $x = h$. According to Eq. (3), the *B* regression variable gives the generalized Hurst exponent value and the *A* regression variable yields the crossover length.

The Markov-Gaussian model is a random process that has been adopted for the quantification of soil surface roughness [*Huang and Bradford*, 1992; *Vermang et al*., 2013]. In that case, the semivariogram is written as an exponential-type function with the following form:

$$\gamma(h) = \sigma^2\left(1 - e^{-h/L}\right) \quad (4)$$

where σ is the variance length scale, representing the roughness of a surface at the large scale, and L is the correlation length scale, which is a measure of the rate at which small scale roughness variations approach the constant value of σ. These indices are obtained by fitting the exponential-type function of Eq. (4) to the semivariogram obtained from Eq. (2).

Finally, the limiting difference (*LD*) index is another index adopted to quantify soil surface roughness. It is calculated from the first-order variogram with elevation data corrected for both slope and tillage marks [*Linden and van Doren*, 1986; *Paz-Ferreiro et al*., 2008], which is written in the form:

$$\Delta Z(h) = \frac{1}{n(h)}\sum_{i=1}^{n(h)}|Z(x_i + h) - Z(x_i)| \quad (5)$$

Then, a linear relationship is fitted between $1/\Delta Z(h)$ and $1/h$:

$$1/\Delta Z(h) = a + b/h \quad (6)$$

The limiting difference (*LD*) index is then calculated as $LD = 1/a$. *LD* has units of length, and represents the value of the first-order variance at large lag distances. It is considered as an indicator of soil surface roughness, thus adopted in the present study as an additional roughness index.

In order to negate the effects of the differences that existed in the initial microrelief amongst the three runs due to the different timing of the experiments (see Section 2.2.1), and compare rainfall-induced changes in relative terms, the results from the rainfall experiments are presented in the form of ratios of the roughness indices. More precisely, the RR ratio, defined as the ratio of the RR index post-rainfall over the RR index prior to the rainfall (RR_{post}/RR_{pre}), is calculated for each experiment. Semivariograms are plotted under pre- and post-rainfall conditions at the ROI to assess the spatial correlation of surface elevations. Along the same lines, ratios between pre- and post-rainfall conditions are calculated for the crossover length, the variance length scale of the Markov-Gaussian model, and the limiting difference to assess changes in microroughness along with the RR ratio.

2.3. Results

2.3.1. Changes in the RR index

Based on visual inspection of the DEMs in Figure 2.5b, it is evident that microroughness in the splash-dominated region increases with rainfall. Table 2.1 summarizes the results of this study along with results from other studies focused on smooth surfaces, documenting the RR index values before and after the rainfall events, the cumulative rainfall, as well as the associated RR ratio. The present study, along with *Vázquez et al*. [2008] and *Zheng et al*. [2014] generally report an increase in RR with rainfall under the conditions examined. The *Vázquez et al*. (2008) study, however, differs from the present study and *Zheng et al*. [2014] in that it examined roughness evolution under successive rainfall events per run. Only the RR data collected on completion of the last rainfall succession in each run conducted by *Vázquez et al*. [2008] are presented in Table 2.1. The final RR values after the last rainfall succession were selected for being the more closely comparable to the steady-state conditions examined herein. Although both *Vázquez et al*. [2008] and *Zheng et al*. [2014] recorded an increase in RR with rainfall, they had significantly lower values of RR ratio than the present study. This could be due to several factors including, but not limited to, lower applied rainfall intensity and amount, the initial surface microroughness, and different soil conditions.

Other studies not included in Table 2.1 have also shown increasing trends of roughness with rainfall, as quantified with the use of different indices. For instance, *Huang and Bradford* [1992] calculated the semivariograms for different surfaces and used fractal and Markov-

Table 2.1: Summary of the rainfall induced change in the RR index in the experimental tests of this study, as well as in experiments reported in the literature. Smooth conditions refer to initial microroughness less than 5 mm. Cumulative rainfall amounts are also provided.

Study	Rainfall Intensity (mm/h)	Cumulative Rainfall (mm)	Soil Type	Pre-rainfall RR (mm)	Post-rainfall RR (mm)	RR Ratio
Present study	30	150	silty clay loam	1.17	1.57	1.34
	60	300	silty clay loam	0.42	1.48	3.55
	75	375	silty clay loam	0.32	1.46	4.56
Vázquez et al., [2008]*	30	85	silt loam	3.39	3.70	1.09
	30	50	silt loam	3.00	2.13	0.71
	65	195	silt loam	4.72	5.10	1.08
Zheng et al., [2014]	40	~60	silty clay loam	2.01	2.35	1.17
	90	~135	silty clay loam	2.40	2.68	1.12

* The *Vázquez et al*. [2008] study looked at RR evolution under successive rainfall events, unlike the other two studies. Post-rainfall RR data presented for *Vázquez et al*. [2008] are those that were determined on completion of the last rainfall succession in each experiment.

Gaussian parameters to quantify the roughness. Markov-Gaussian analysis showed a relative increase in the roughness parameter for a surface of low initial roughness. Finally, *Rosa et al.* [2012] introduced the Roughness Index, which is estimated from the semivariogram sill (i.e., the upper value where the semi-variance levels out), in order to quantify roughness, and observed an increase with rainfall under low initial roughness conditions. That increase was attributed to the fragmentation of aggregates and clods to smaller aggregates but was not linked to smooth bare soil surface conditions. Overall, the experimental evidence suggests that the interaction between rainfall and smooth soil surfaces can lead to an increase in microroughness.

The results outlined above for the use of the RR index as a descriptor of change in microroughness have been based on the assumption that there is no statistically significant spatial correlation in elevation readings between neighboring locations at the ROI. This condition was indeed not violated due to the choice in ROI. The following subsection outlines and discusses the results of the semivariogram analysis and additional indices used to confirm the validity of the assumption and their comparison with the RR index method.

2.3.2. Changes in alternative roughness indices

Semivariograms and first-order variograms were obtained from geostatistical analysis and plotted at four different angles – 0°, 45°, 90°, and 135°– with respect to the downslope direction Since the action of rainfall is isotropic and adds no systematic trend along any direction, no significant differences were expected between semivariograms. A nonparametric test for spatial isotropy was performed per *Guan et al*. [2004] using the public domain R statistical package with the 'spTest' library. The spatial isotropy hypothesis was confirmed ($p < 0.05$). Thus, no bias was determined in taking any direction to calculate the semivariograms and the associated crossover lengths.

The semivariograms calculated at the ROI were chosen to be in the downslope direction at an angle of 0° and are presented for each experiment in Figure 2.6. The vertical dashed lines designate the lag distances above which the spatial autocorrelation of the elevations is not statistically significant. These lag distances are approximately 10 mm, so the selected 200 mm window size of the ROI is almost 20 times greater than the spatial autocorrelation range. This implies that the window size of the ROI falls at the scale of the semivariogram sill (which is defined as the near-constant value of semivariance at large lag distances where the semivariogram levels out – see horizontal dashed lines in Figure 2.6). RR is directly related to the semivariogram sill [e.g., *Vázquez et al*., 2005; *Vermang et al*., 2013], therefore it can be considered independent of the selected window size, given that the latter far exceeds the spatial autocorrelation range.

Figure 2.6 shows that the post-rainfall sills are greater than their corresponding pre-rainfall values. Also, the difference in sills between pre- and post-rainfall conditions for the 30 mm/h precipitation intensity is much lower than those of the 60 mm/h and 75 mm/h events. These observations are in accordance with visual inspection of the surfaces as well as with the results noted earlier for the RR ratio (see Table 2.1). Complete agreement between the trends of the RR index, the semivariogram sill, and visual inspection of the surfaces justify the use of the RR index as a representative and unbiased descriptor of microroughness.

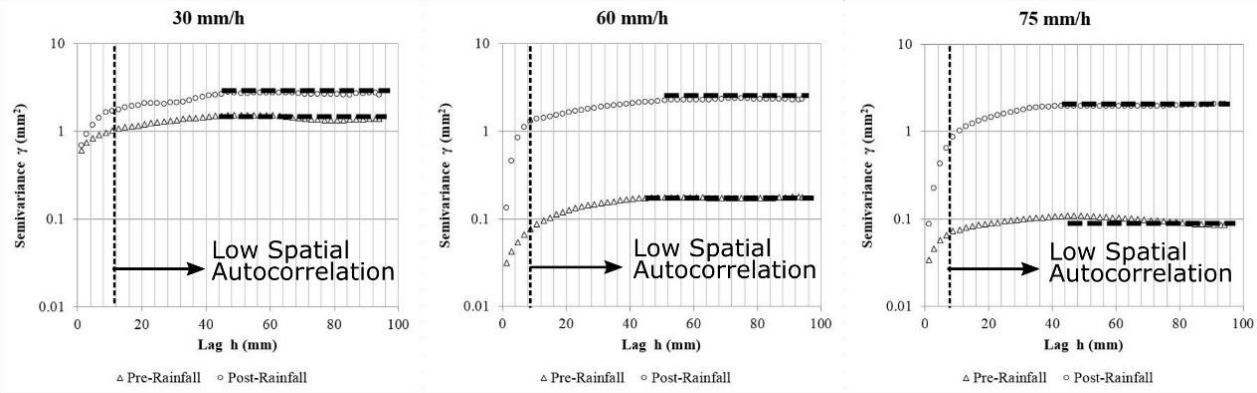

Figure 2.6: Semivariograms at the region of interest for the three experimental tests, under pre- and post-rainfall conditions. Horizontal dashed lines indicate the semivariogram sills and vertical dashed lines indicate the lag distance above which the spatial autocorrelation of the elevations is negligible.

Table 2.2 lists the crossover length, the Markov-Gaussian variance length scale and the limiting difference indices for the three experimental tests, and their relative change after the rainfall. These indices show an increase with rainfall that is of the same magnitude and trend as the RR index and crossover length, and provide a supplemental analysis about the role of rainfall intensities on the relative increase in roughness. Our findings were compared against those reported in the literature. *Huang and Bradford* [1992] studied the evolution of soil surface roughness with the Markov-Gaussian variance length scale, and saw an increase of 6% in roughness for a surface of low initial roughness. Moreover, *Paz-Ferreiro et al*. [2008], who used the *LD* index to quantify soil surface roughness, also recorded a 10% increase in the *LD* index for a low roughness conventional tillage soil surface. The higher relative increase in roughness seen in our study (Table 2.2) compared to other studies is attributed to the lower initial roughness conditions in addition to different soil types and management.

Overall, the results provided suggest that all the indices employed in this study may be used interchangeably to characterize rainfall induced changes in soil surface roughness, and can capture an increase in soil surface roughness, especially for smooth soil surfaces. For these microroughness scales, the relative increase in roughness is also shown to increase with rainfall intensity under the conditions examined herein.

Table 2.2: Summary of the rainfall induced change in the crossover length, the Markov-Gaussian variance length scale and limiting difference indices for the experimental tests of this study.

Index	Rainfall Intensity (mm/h)	Cumulative Rainfall (mm)	Pre-rainfall value	Post-rainfall value	Index Ratio
l (mm)	30	150	0.71	0.73	1.03
	60	300	0.09	0.20	2.13
	75	375	0.15	0.39	2.56
σ (mm)	30	150	1.19	1.63	1.37
	60	300	0.42	1.52	3.62
	75	375	0.31	1.43	4.56
LD (mm)	30	150	0.79	0.87	1.10
	60	300	0.26	0.87	3.39
	75	375	0.15	0.71	4.84

2.4. Discussion and Conclusions

Many studies have examined the response of rough surfaces to rainfall, and have reported a decay of roughness. Few studies have assessed microscale variation of smooth surfaces in response to rainfall under controlled conditions. The experiments presented herein were designed to help us decipher the role of rainsplash on RR for smooth surfaces with initial microroughness on the order of 2 mm by isolating the role of other factors such as runoff, variable water content, bare soil surface, and soil texture, among others. Our results show a consistent increase in roughness under the action of rainfall, with an overall agreement between all the roughness indices examined herein in terms of trend and magnitude. Our findings are consistent with findings of other studies that have examined length scales less than 5 mm and suggest the possible existence of a characteristic roughness threshold below which RR is expected to increase due to the action of rainfall. The value of this threshold may depend on the specific soil and rainfall conditions. A caveat of our study is that due to the limited range of conditions examined herein more experiments are needed to further solidify the conditions under which RR is expected to increase under rainfall action. An outcome of this study is the awareness that within landscape regions where smooth surfaces are present, an increase in RR may occur during the early part of the storm where rainsplash action is more important than runoff. Another

outcome is the fact that the mere action of rainfall cannot completely smoothen out a decaying soil surface roughness. Thus, localized microroughness residuals will always remain at locations where the action of runoff is low or absent. This limiting threshold needs to be accounted for in upland models.

This study suggests that the effects of the interaction between rainfall and a soil surface can be different for smooth and rough surfaces, and highlights the need for a better understanding of the interaction due to its potential impact on hydrologic response. This potential impact is demonstrated with the following established pedotransfer function for the effects of soil crusting, roughness, and rainfall kinetic energy on the bare hydraulic conductivity, K_{br}, [*Risse et al*., 1995]:

$$K_{br} = K_b\left[CF + (1 - CF)e^{-C.E_a(1-RR_t/RR_{t-max})}\right] \quad (7)$$

where K_b is the baseline hydraulic conductivity, *CF* is the crust factor, *C* is soil stability factor, E_a is the cumulative rainfall kinetic energy since the last tillage, RR_t is random roughness height, and $RR_{t\text{-}max}$ is the maximum random roughness height. Using the following typical values for the study site based on literature [*Flanagan et al*., 1995; *Chang*, 2010]: E_a = 10,000 J/m², C = 0.0002 m²/J, $RR_{t\text{-}max}$ = 40 mm, the percentage change in bare hydraulic conductivity for increasing roughness can be estimated for an initial RR_t value of 2 mm and minimal *CF* factor. Performing the analysis for the range of random roughness ratios observed in this study (~1.3 – 4.5), the percentage increase in hydraulic conductivity is found to range between 5% –42%, which will have a significant impact on rainfall-runoff partitioning.

It is recognized that the soil preparation method in our study could have introduced some bias to the soil properties such as aggregate size distribution, compaction, and aggregate stability. Nonetheless, for the purpose this study was designed for, this preparation method ensured consistency in the initial and final roughness states, as confirmed by replications of our experimental runs. It is also recognized that drier, silty type soils may not exhibit the increase in RR shown here. Further, the role of sealing may be important on roughness development under bare soil conditions and needs further examination. Soil water retention characteristics of the soils under sealing and its implication to RR must be considered [*Saxton and Rawls*, 2006].

Finally, the role of successive storm events on changing roughness for smooth surfaces is not covered in this study and needs to be examined.

The exact mechanisms leading to increase in roughness remain unknown and are not the focus of this study. However, changes in roughness during a storm event have been attributed to compression and drag forces from the raindrop impact on the soil, angular displacement due to rainsplash, aggregate fragmentation, and differential swelling [*Al-Durrah and Bradford*, 1982; *Warrington et al*., 2009; *Rosa et al*., 2012; *Fu et al*., 2016]. Regions exhibiting different median raindrop diameters may experience different soil surface roughness evolution due to different aggregate fragmentation and rain splash effects [*Warrington et al*., 2009; *Rosa et al*., 2012; *Fu et al*., 2016]. Future research should explore these mechanisms.

References

Abaci, O. and A. N. Papanicolaou (2009), Long-term effects of management practices on water-driven soil erosion in an intense agricultural sub-watershed: monitoring and modelling, *Hydrological Processes 23*, 2818–2837, doi:10.1002/hyp.7380.

Al-Durrah, M. M., and J.M. Bradford (1982), The mechanism of raindrop splash on soil surfaces, *Soil Science Society of America Journal*, 46, 1086, doi:10.2136/sssaj1982.03615995004600050040x.

Allmaras, R. R., R. E. Burwell, W. E. Larson, and R. F. Holt (1966), Total porosity and random roughness of the interrow zone as influenced by tillage, USDA Conservation Re. Rep., 7, 22.

Bertuzzi, P., G. Rauws, and D. Courault (1990), Testing roughness indices to estimate soil surface roughness changes due to simulated rainfall, *Soil and Tillage Research*, *17*, 87–99, doi:10.1016/0167-1987(90)90008-2.

Burrough, P. A. (1983a), Multiscale sources of spatial variation in soil. I. The application of fractal concepts to nested levels of soil variation. *Journal of Soil Science 34*, 577–597, doi:10.1111/j.1365-2389.1983.tb01057.x.

Burrough, P. A (1983b), Multiscale sources of spatial variation in soil. II. A non-Brownian fractal model and its application in soil survey, *Journal of Soil Science, 34*, 599–620, doi:10.1111/j.1365-2389.1983.tb01058.x.

Chang, Y. (2010), Predictions of saturated hydraulic conductivity dynamics in a midwestern agriculture watershed, Iowa, M. Sc. Thesis, The University of Iowa, Iowa City, IA, USA.

Cheng, Q., Y. Sun, J. Lin, L. Damerow, P. Schulze Lammers, and H. Hueging, (2012), Applying two-dimensional Fourier Transform to investigate soil surface porosity by laser-scanned data. *Soil and Tillage Research, 124*, 183–189, doi:10.1016/j.still.2012.06.016.

Chi, Y., Yang, J., D. Bogart, and X. Chu (2012), Fractal Analysis of Surface Microtopography and its Application in Understanding Hydrologic Processes, *Transactions of the ASABE, 55*, 1781–1792, doi:10.13031/2013.42370.

Currence, H. D. and W.G. Lovely (1970), The analysis of soil surface roughness, *Transactions of the ASAE, 13*, 710–0714.

Darboux, F. and C. Huang (2003), An instantaneous-profile laser scanner to measure soil surface microtopography, *Soil Science Society of America Journal, 67*, 92, doi:10.2136/sssaj2003.9200.

Elhakeem, M. and A. N. Papanicolaou (2009), Estimation of the runoff curve number via direct rainfall simulator measurements in the State of Iowa, USA, Water Resources Management, 23, 2455–2473, doi:10.1007/s11269-008-9390-1.

Flanagan, D. C., and M. A. Nearing (1995), USDA Water Erosion Prediction Project: Hillslope Profile and Watershed Model Documentation, NSERL Report No. 10, USDA-ARS National Soil Erosion Research Laboratory, West Lafayette, IN, USA.

Fu, Y., Li, G., T. Zheng, B. Li, and T. Zhang (2016), Impact of raindrop characteristics on the selective detachment and transport of aggregate fragments in the Loess Plateau of China, *Soil Science Society of America Journal, 80*, 1071, doi:10.2136/sssaj2016.03.0084.

Gilley, J. E., and S.C. Finkner (1991), Hydraulic roughness coefficients as affected by random roughness, *Transactions of the ASAE, 34*, 0897–0903, doi:10.13031/2013.31746.

Gómez, J. A., and M. A. Nearing (2005), Runoff and sediment losses from rough and smooth soil surfaces in a laboratory experiment, *Catena, 59*, 253–266, doi:10.1016/j.catena.2004.09.008.

Guan, Y., M. Sherman, and J. A. Calvin (2004), A nonparametric test for spatial isotropy using subsampling, *Journal of the American Statistical Association, 99*, 810–821, doi:10.1198/016214504000001150.

Huang, C. and J. M. Bradford (1990), Depressional storage for Markov-Gaussian surfaces, *Water Resources Research, 26*, 2235–2242, doi:10.1029/WR026i009p02235.

Huang, C. and J. M. Bradford (1992), Applications of a laser scanner to quantify soil microtopography, *Soil Science Society of America Journal, 56*, 14, doi:10.2136/sssaj1992.03615995005600010002x.

Huff, F. A. and J. R. Angel, J. R. (1992), Rainfall Frequency Atlas of the Midwest. Midwestern Climate Center Research Report, 92-03, Champaign, IL.

Hunt, A. G. and B. Ghanbarian, (2016), Percolation theory for solute transport in porous media: Geochemistry, geomorphology, and carbon cycling: Solute transport in porous media, *Water Resources Research, 52*, 7444–7459, doi:10.1002/2016WR019289.

Kamphorst, E. C., V. Jetten, J. Guérif, J. Pitkanen, B. V. Iversen, J. T. Douglas, and A. Paz (2000), Predicting depressional storage from soil surface roughness, *Soil Science Society of America Journal 64*, 1749, doi:10.2136/sssaj2000.6451749x.

Linden, D. R., and D. M. Van Doren (1986), Parameters for characterizing tillage-induced soil surface roughness, *Soil Science Society of America Journal, 50*, 1560, doi:10.2136/sssaj1986.03615995005000060035x.

Liu, Q. Q. and V. P. Singh (2004), Effect of microtopography, slope length and gradient, and vegetative cover on overland flow through simulation, *Journal of Hydrologic Engineering, 9*, 375–382, doi:10.1061/(ASCE)1084-0699(2004)9:5(375).

Lovejoy, S. and D. Schertzer, (2007), Scaling and multifractal fields in the solid earth and topography, *Nonlinear Processes in Geophysics 14*, 465–502, doi:10.5194/npg-14-465-2007.

Magunda, M. K., W. E. Larson, D. R. Linden, and E. A. Nater (1997), Changes in microrelief and their effects on infiltration and erosion during simulated rainfall, *Soil Technology, 10*, 57–67, doi:10.1016/0933-3630(95)00039-9.

Mandelbrot, B. B. and J. W.Van Ness (1968), Fractional Brownian motions, fractional noises and applications, SIAM Review, 10, 422–437.

Marshall, J. S., W. M. K. Palmer (1948), The distribution of raindrops with size, *Journal of Meteorology, 5*, 165–166, doi:10.1175/1520-0469(1948)005<0165:TDORWS>2.0.CO;2.

Oades, J. and A. Waters (1991), Aggregate hierarchy in soils, *Australian Journal of Soil Research, 29*, 815, doi:10.1071/SR9910815.

Oleschko, K., G. Korvin, A. Muñoz, J. Velazquez, M. E. Miranda, D. Carreon, L. Flores, M. Martínez, M. Velásquez-Valle, F. Brambila, J. F. Parrot, and G. Ronquillo (2008), Mapping soil fractal dimension in agricultural fields with GPR, *Nonlinear Processes in Geophysics, 15*, 711–725, doi:10.5194/npg-15-711-2008.

Onstad, C. A. (1984), Depressional storage on tilled soil surfaces, *Transactions of the ASAE, 27*, 729–732, doi:10.13031/2013.32861.

Papanicolaou, A. N., A.G. Tsakiris, and K. Strom (2012), The use of fractals to quantify the morphology of cluster microform, *Geomorphology, 139-140*, 91-108, doi:10.1016/j.geomorph.2011.10.007.

Papanicolaou, A. N., M. Elhakeem, C. G. Wilson, C. L. Burras, L. T. West, H. Lin, B. Clark, and B. E. Oneal (2015a), Spatial variability of saturated hydraulic conductivity at the hillslope scale: Understanding the role of land management and erosional effect, *Geoderma, 243–244*, 58–68, doi:10.1016/j.geoderma.2014.12.010.

Papanicolaou, A. N., K. M. Wacha, B. K. Abban, C. G. Wilson, J. L. Hatfield, C. O. Stanier, and T. R. Filley (2015b), From soilscapes to landscapes: A landscape-oriented approach to simulate soil organic carbon dynamics in intensively managed landscapes, *Journal of Geophysical Research: Biogeosciences, 120*, 2375–2401, doi:10.1002/2015JG003078, 2015b.

Paz-Ferreiro, J., I. Bertol, and E. V. Vázquez (2008), Quantification of tillage, plant cover, and cumulative rainfall effects on soil surface microrelief by statistical, geostatistical and fractal indices, Nonlinear Processes in Geophysics, 15, 575–590. doi:10.5194/npg-15-575-2008.

Potter, K. N. (1990), Soil properties effect on random roughness decay by rainfall, *Transactions of the ASAE, 33*, 1889–1892.

Risse, L.M., B. Y. Liu, and M. A. Nearing (1995), Using curve numbers to determine base-line values of Green-Ampt effective hydraulic conductivities, *Water Resources Bulletin, 31-1*,147-158.

Römkens, M. J. and J. Y. Wang (1986), Effect of tillage on surface roughness, *Transactions of the ASAE, 29*, 0429–0433, doi:10.13031/2013.30167, 1986.

Rosa, J. D., M. Cooper, F. Darboux, and J.C. Medeiros (2012), Soil roughness evolution in different tillage systems under simulated rainfall using a semivariogram-based index, *Soil and Tillage Research, 124*, 226–232, doi:10.1016/j.still.2012.06.001.

Saxton, K. E. and W. J. Rawls (2006), Soil water characteristic estimates by texture and organic matter for hydrologic solutions, *Soil Science Society of America Journal*, *70*, 1569, doi:10.2136/sssaj2005.0117.

Smith, M. W., N. J. Cox, and L. J. Bracken (2011), Terrestrial laser scanning soil surfaces: a field methodology to examine soil surface roughness and overland flow hydraulics, *Hydrological Processes*, *25*, 842–860, doi:10.1002/hyp.7871.

Tarquis, A. M., R. J. Heck, J. B. Grau, J. Fabregat, M. E. Sanchez, and J. M. Antón (2008), Influence of thresholding in mass and entropy dimension of 3-D soil images, *Nonlinear Processes in Geophysics, 15*, 881–891, doi:10.5194/npg-15-881-2008.

Unger, P. W. (1984), Tillage effects on surface soil physical conditions and sorghum emergence. *Soil Science Society of America Journal, 48*, 1423, doi:10.2136/sssaj1984.03615995004800060044x.

Vázquez, E. V., J. G. V. Miranda, and A. P. González (2005), Characterizing anisotropy and heterogeneity of soil surface microtopography using fractal models, *Ecological Modelling, 182*, 337–353, doi:10.1016/j.ecolmodel.2004.04.012.

Vázquez, E. V., J. G. V. Miranda, and A. P. González (2007), Describing soil surface microrelief by crossover length and fractal dimension, *Nonlinear Processes in Geophysics, 14*, 223–235.

Vázquez, E. V., R. G. Moreno, J. G. V. Miranda, M. C. Díaz, A. S. Requejo, J. Paz-Ferreiro, and A. M. Tarquis (2008), Assessing soil surface roughness decay during simulated rainfall by multifractal analysis, *Nonlinear Processes in Geophysics*, *15*, 457–468, doi:10.5194/npg-15-457-2008.

Vermang, J., L. D. Norton, J. M. Baetens, C. Huang, W. M. Cornelis, and D. Gabriels (2013), Quantification of soil surface roughness evolution under simulated rainfall, *Transactions of the ASABE, 56*, 505–514, doi:10.13031/2013.42670.

Warrington, D. N., A. I. Mamedov, A. K. Bhardwaj, and G. J. Levy (2009), Primary particle size distribution of eroded material affected by degree of aggregate slaking and seal development, *European Journal of Soil Science, 60*, 84–93, doi:10.1111/j.1365-2389.2008.01090.x.

Zhang, X., G. Q. Yu, Z. B. Li, and P. Li (2014), Experimental study on slope runoff, erosion and sediment under different vegetation types, *Water resources management, 28*(9), 2415-2433.

Zheng, Z. C., S. Q. He, and F. Wu (2014), Changes of soil surface roughness under water erosion process: Soil surface roughness under water erosion, *Hydrological Processes, 28*, 3919–3929, doi:10.1002/hyp.9939.

Zobeck, T. M. and C. A. Onstad, (1987), Tillage and rainfall effects on random roughness: A review, *Soil and Tillage Research, 9*, 1–20, doi:10.1016/0167-1987(87)90047-X.

Chapter 3

Flow Resistance Interactions on Hillslopes with Heterogeneous Attributes: Effects on Runoff Hydrograph Characteristics

Abstract

An improved modeling framework for capturing the effects of space and time-variant resistance to overland flow is developed for intensively managed landscapes. The framework builds on the WEPP model but it removes the limitations of the "equivalent" plane and time-invariant roughness assumption. The enhanced model therefore accounts for spatiotemporal changes in flow resistance along a hillslope due to changes in roughness, in profile curvature, and downslope variability. The model is used to quantify the degree of influence – from individual soil grains to aggregates, "isolated roughness elements", and vegetation – on overland flow characteristics under different storm magnitudes, downslope gradients, and profile curvatures. It was found that the net effects of land use change from vegetation to a bare surface resulted in hydrograph peaks that were up to 133% larger. Changes in hillslope profile curvature instead resulted in peak runoff rate changes that were only up to 16%. The stream power concept is utilized to develop a taxonomy that relates the influence of grains, isolated roughness elements, and vegetation, on overland flow under different storm magnitudes and hillslope gradients. Critical storm magnitudes and hillslope gradients were found beyond which the effects of these landscape attributes on the peak stream power were negligible. The results also highlight weaknesses of the space/time-invariant flow resistance assumption and demonstrate that assumptions on landscape terrain characteristics exert a strong control both on the shape and magnitude of hydrographs, with deviations reaching 65% in the peak runoff when space/time-variant resistance effects are ignored in some cases.

3.1. Introduction

Overland flow is the main agent for the transport and delivery of water and soil particles [e.g., *Kirkby*, 1988], dissolved chemicals as well as sediment-borne pollutants from hillslopes into the stream networks [e.g., *Lal and Stewart*, 1994; *Loperfido et al.*, 2010]. In landscapes, spatially heterogeneous hillslope attributes such as soil surface characteristics, surface cover/vegetation, and downslope profile curvature, contribute to landscape bed surface roughness. During a storm event, this roughness impacts resistance to flow and plays an important role in the generation and transport mechanisms of surface runoff, sediment delivery

pathways, and nutrient distribution [e.g., *Woolhiser et al.*, 1989; *Flanagan and Nearing*, 1995; *Wicks and Bathurst*, 1996; *Wang and Hjelmfelt*, 1998; *Katul et al.*, 2011].

Figure 3.1 presents representative types of landscape attributes that are ubiquitous in intensively managed landscapes. These include "microrelief variations" from individual soil grains to aggregates (less than 2 mm) and "isolated roughness elements" (stones and clods ~2-100 mm in size), as well as vegetation [*Römkens and Wang*, 1986]. In addition to these attributes, features such as oriented roughness (~100-300 mm) that are formed from tillage implements can significantly affect overland flow and pathways of water and sediment delivery. Other landscape features such as profile curvature (uniform, concave or convex), hereafter referred to as macro-scale features, can also further affect overland flow and its distribution [*Reike-Zapp and Nearing*, 2005].

Different landscape attributes can in turn create different types of overland flow resistance [*Shen and Li*, 1973; *Abrahams et al.*, 1992; *Abrahams*, 1998; *Lawrence*, 2000; *Gomez and Nearing, 2005; Hu and Abrahams*, 2006]. The types of flow resistance associated with the landscape attribute roughness are presented in Figure 3.2 and include skin, rainfall-induced, form, and wave resistance, which are briefly defined hereafter. Skin resistance refers to the resistance offered by bed surface grain and the submerged sides of isolated roughness elements (i.e., clods, stones). Form resistance is prevalent where the height of bed roughness elements is comparable to the runoff depth. That is, $h/D_r \leq 1$, where h/D_r is defined as the relative submergence, h is the approaching flow depth and D_r denotes the isolated element tip height [*Lawrence*, 1997; *Papanicolaou et al*., 2011]. The obstruction to the flow in the case of a roughness element or an array of roughness elements results in complex, highly varied overland flow patterns that yield energy dissipation through eddy separation, localized increases in shear stress, and secondary currents [*Abrahams et al.*, 1992; *Clifford et al.*, 1992; *Nikora et al*., 2001; *Lacey and Roy*, 2008; *Papanicolaou*, 2012]. In addition, partially submerged roughness elements can introduce significant wave resistance associated with the deformation of the water surface around these elements under certain ranges of flow [*Abrahams et al.*, 1992].

The aforementioned types of flow resistances vary in space and time since they arise from the interactions between the landscape attributes and overland flow depth/velocity, which change in space and time over the course of a storm event in response to storm patterns and changes in attribute resistance as the flow conditions change [*Abaci and Papanicolaou*, 2009;

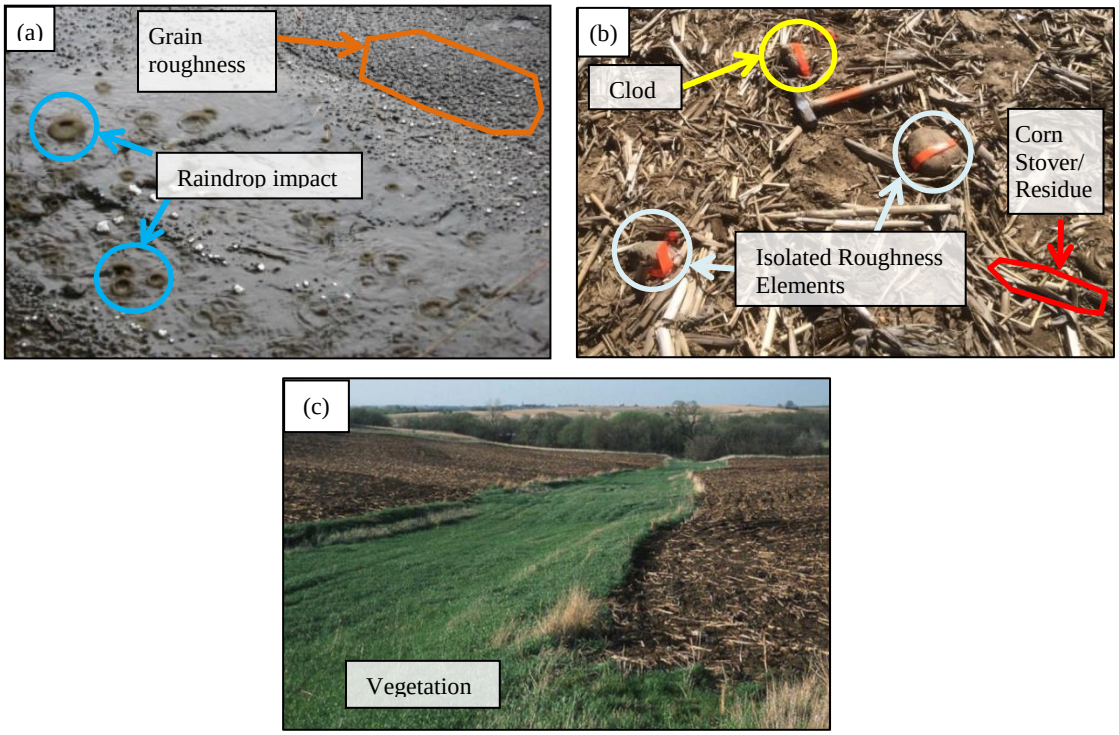

Figure 3.1: Images illustrating the various types of roughness encountered in Intensively Managed Landscapes that are examined in this study: (a) Grain roughness and raindrop impact; (b) Isolated roughness elements; and (c) Vegetation. All images are from the Clear Creek Watershed, IA, and the Upper Sangamon River Basin, IL.

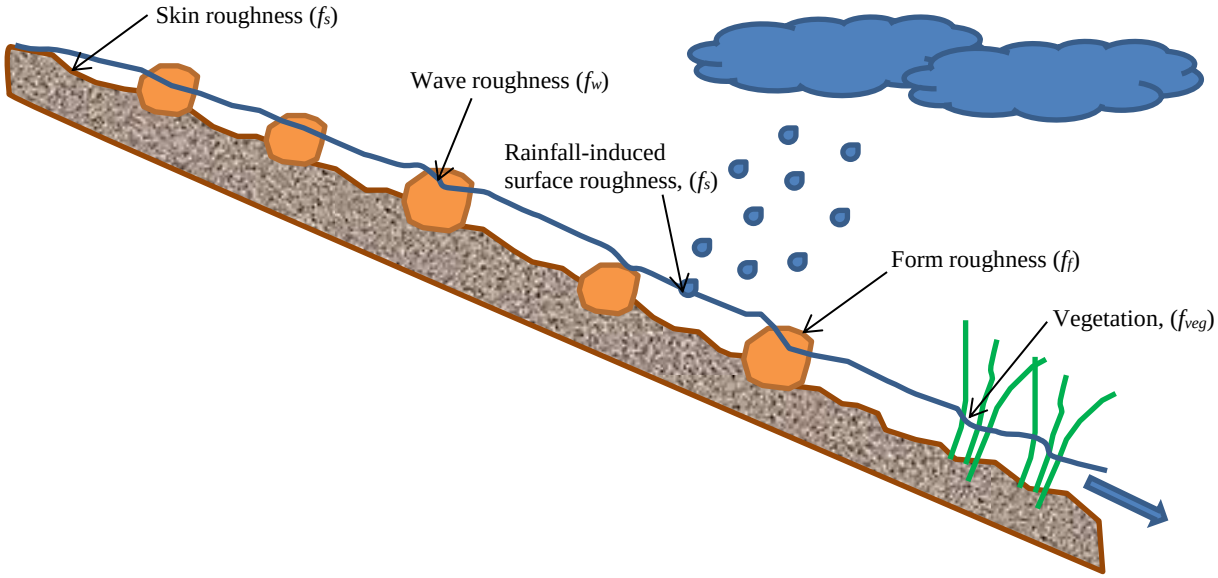

Figure 3.2: Definition sketch of the types of flow resistance associated with the various roughness types

Abban et al., 2017]. Although several studies have examined the need to account for the space/time-variant resistance offered by individual roughness [e.g., *Shen and Li*, 1973; *Lawrence*, 2000; *Katul et al.*, 2011], none have examined the need to account for their collective effects and interplay with profile curvature on hydrograph properties at the hillslope scale. Most studies still treat the resistances as space/time-invariant from the plot to the hillslope scale and further studies are therefore still needed to examine these effects. It is postulated here that the net effects of the space and time varying interactions between landscape attributes and overland flow are ensemble averaged (i.e., integrated over space and time) at the hillslope outlet, where the effects are depicted through changes in the shape, peak, and modality of the runoff hydrograph. In other words, local scale interactions between the flow and landscape attributes, such as grain, isolated roughness elements, and vegetation, further interact with macro-scale attributes, such as profile curvature, and through this interaction shape the overall characteristics of runoff hydrographs at the hillslope outlet [*Abrahams*, 1998; *Lawrence*, 2000; *Hu and Abrahams*, 2006; *Katul et al.*, 2011; *Thompson et al.*, 2011]. For example, *Young and Mutchler* [1969] found runoff velocities to be higher in the upper parts of concave plots compared to convex plots, due to steeper slopes. However, whereas runoff velocities on convex plots doubled in low-lying positions as the slope steepened, runoff velocities on concave plots decreased marginally. *Neibling and Alberts* [1979] and *Dermisis et al.* [2010] concluded that vegetated strip length inversely affected runoff velocity, promoting infiltration and reducing runoff volumes and sediment yields. It was also suggested by *Dermisis et al.* [2010] that there was a threshold scale unit beyond which no appreciable changes in runoff and sediment yields was observed. In summary, these studies highlighted the need for more research to identify the threshold scale unit where the net effects of the spatiotemporal interactions between different landscape attributes and overland flow seize to play a role on runoff characteristics.

The spatiotemporal interactions of flow with the landscape attributes can also lead to other effects such as the manifestation of kinematic shock waves [*Iwagaki*, 1955; *Kibler and Woolhiser*, 1972; *Borah et al.*, 1980; *Hairsine and Parlange*, 1986; *Schmid*, 1990; *Luo and Harlin*, 2003; *Huang and Lee*, 2009; *Costabile et al.*, 2012]. *Borah et al.* [1980] provide a few examples under which kinematic shock waves have been observed on agricultural catchments. They are generated when "fast" moving waves, propagating from an upstream surface, "catch-up" with "slower" moving waves propagating on a downstream surface with different roughness

features, resulting in the steepening of the wave front [*Miller*, 1984]. The explicit modulation of shock waves is currently lacking in most overland flow models [e.g. *Iwagaki*, 1955; *Kibler and Woolhiser*, 1972; *Borah et al*., 1980; *Croley and Hunt*, 1981*; Hairsine and Parlange*, 1986; *Schmid*, 1990; *Tseng*, 2010; *Papanicolaou et al*., 2010]. A space/time-invariant approximation of flow resistance is commonly adopted that inhibits shock wave resolution. In this approximation, a spatially averaged roughness resistance over the hillslope is considered and the resistance is treated as constant during a storm event. However, the explicit modulation of shock waves is needed because variations in the surface roughness in overland flows are usually of the same order of magnitude as the water depth and can lead to sharp flow gradients, thereby affecting hydrograph propagation, peakiness and modality [e.g., *Zhang and Cundy*, 1989; *Jirka and Uijttewaal*, 2004; *Nikora et al.*, 2007].

It is hypothesized here that the net effects of space/time-variant resistance to overland flow under different types of landscape attributes (i.e., grain roughness, isolated roughness elements, and vegetation) can lead to different shape and modality hydrographs at the hillslope outlet. It is also hypothesized that there exists a critical storm magnitude and hillslope gradient beyond which the net resistance effects of a surface roughness type on the runoff hydrograph at the hillslope outlet will be relatively insignificant for a given hillslope length.

Consequently, this study undertakes the following specific objectives: (1) evaluation of the implications of the space/time-invariant resistance assumption on flow routing; (2) examination of the degree of influence of the landscape attributes on runoff hydrograph characteristics, and; (3) identification of the critical storm magnitude and hillslope gradient where the net resistance effects of a surface roughness type on the hydrograph characteristics become negligible. The study advances our understanding of the net effects of flow resistance on hydrographs from hillslopes with heterogeneous landscape attributes, by removing the limitation of the space/time-invariant resistance assumption in overland flow routing and accounting for the role of kinematic shock waves due to roughness variations. Profile curvature effects are explicitly considered. For the first time, the stream power concept, based on the product of the runoff rate and gradient, is used to quantify the degree of influence of the attributes under different storm events.

3.2. Methodology

The well-established Water Erosion Prediction Project (WEPP) model [Version 2012.8; *Flanagan et al.*, 2007] is utilized for developing and testing our modeling framework. In the current version of WEPP, however, there is a limitation in the representation of spatial variability of landscape attributes for flow routing through the use of the equilibrium storage concept of *Wu et al.* [1978]. This concept handicaps WEPP's ability to simulate space/time-variant resistance effects on flow on landscapes with spatially variable attributes, including shock wave formation and propagation.

For the purpose of this study, WEPP has been enhanced to remove the aggregated roughness restriction. Routing of the flow hydrograph along a cascade of overland flow elements (OFEs) is now performed on an "OFE-by-OFE" basis by considering the specific physical and geometric properties of each OFE (see Figure 3.3), without aggregating the properties of all the OFEs into a single equivalent plane. In addition, new physically-based resistance formulations have been incorporated into WEPP to account for resistance due to grain roughness, isolated roughness elements, and vegetation, as well as raindrop impact which can be significant under shallow flows [*Shen and Li*, 1973]. These formulations allow spatiotemporal updates of flow resistance during a storm event. Last but not least, a shock capturing scheme has been incorporated for addressing shock formation and propagation.

Using the enhanced WEPP model, the degree of influence of grain roughness, isolated roughness elements, and vegetation on runoff hydrograph characteristics (see hypothesis) is examined for different storm events and hillslope gradients. To identify the critical storm magnitude and hillslope gradient where their influence diminishes, the dimensionless stream power, Ψ_*, defined as the product between the normalized flow rate and normalized hillslope gradient (i.e., $\Psi_* = q_* S_{o*}$, where q_* and S_{o*} are normalized unit flow rates and slopes, respectively, with q_* reflecting soil texture and roughness effects, and S_{o*} reflecting topographic and curvature effects) is related to the dimensionless storm intensity, I_*, in the form of a power law as follows:

$$\Psi_* = k I_*^{\,l} \tag{1}$$

where k and l are coefficients. The values of k and l are examined for a wide range of intensities

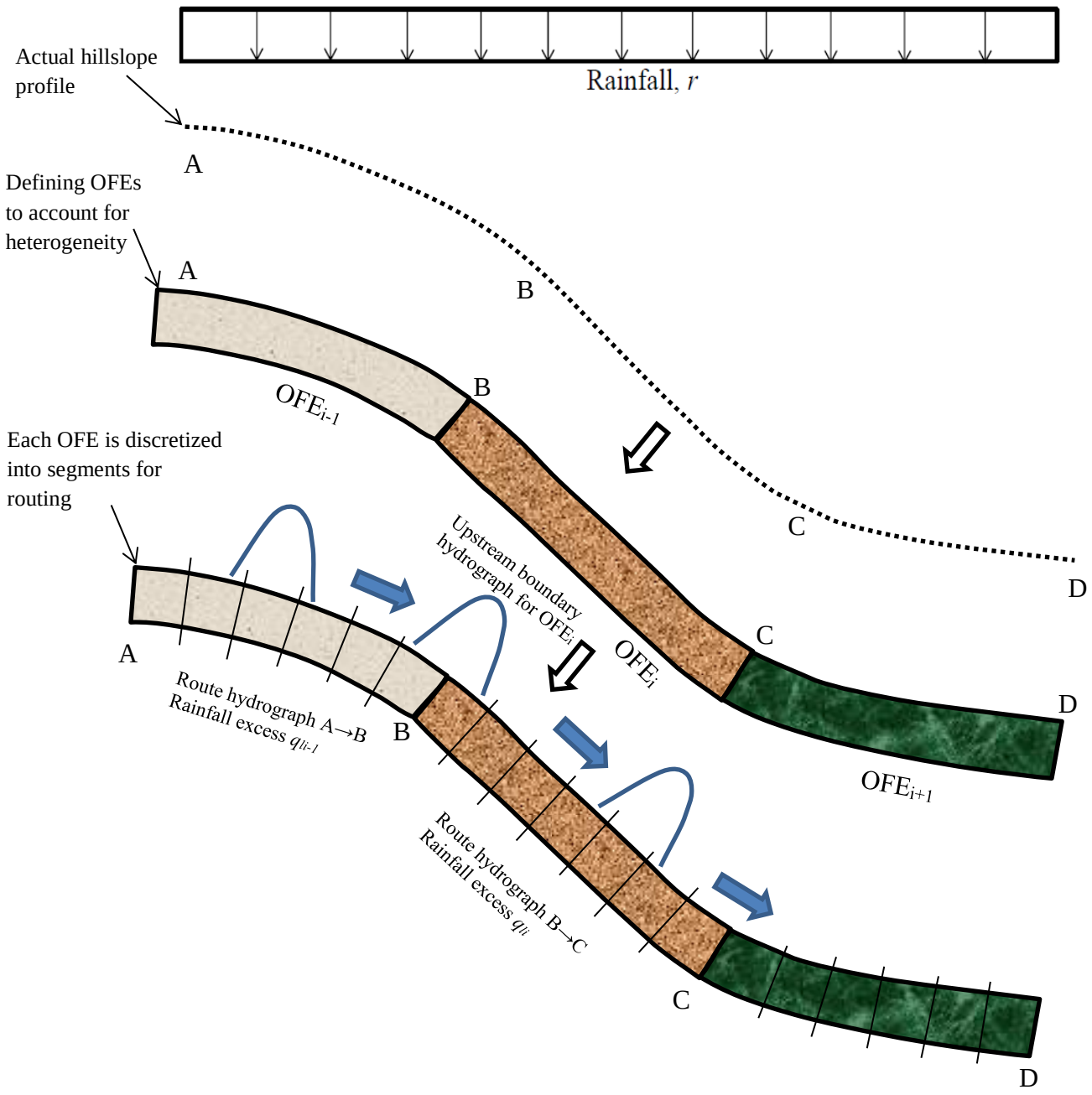

Figure 3.3: Illustration of enhanced WEPP model implementation steps for routing overland flow over a heterogeneous downslope.

and hillslope gradients for each of the attributes to establish its extent of influence in relation to the storm magnitude and gradient. The stream power concept is beneficial for this analysis because it combines storm and hillslope characteristics in a single metric that can be readily examined.

The approach described above is based on a set of assumptions, which are provided in detail below.

3.2.1. Modeling assumptions

The following assumptions are made for routing overland flow on an OFE-by-OFE basis and for examining the degree of influence of the landscape attributes:

1. A hillslope can be represented by a mosaic of discrete OFEs to adequately account for spatial heterogeneity in downslope profile curvature, surface roughness, and vegetation (see Figure 3.3). The number of OFEs is defined by the user to reflect the degree of spatial variability of the physical properties along the hillslope. It is assumed that rainfall excess can be routed sequentially from OFE to OFE from the hillslope summit to the outlet. For example, in Figure 3.3, the rainfall excess, v_{i-1}, is routed along OFE_{i-1} to produce a hydrograph at the downstream end of OFE_{i-1}. This calculated hydrograph is then used as an upstream boundary condition for the downstream overland flow element, OFE_i, and is then routed along with the rainfall excess v_i from OFE_i to OFE_{i+1}.
2. Infiltration rate, i_f, calculations performed *per* OFE using the Green-Ampt Mein-Larsen model (see Equation A1), rather than for a single equivalent plane as is originally done in the current WEPP version, can adequately resolve runoff generation on heterogeneous hillslopes [*Borah et al*., 1980]. Rainfall excess rate, *v*, is calculated for *each* OFE with adjustments being made for the effects of roughness on the depression storage. Before i_f and *v* are calculated, the rainfall rate, *r*, is also adjusted for losses due to canopy and surface residue cover interception.
3. The kinematic wave approximation (see Equations A1 and A2) is valid under the overland flow conditions examined (i.e., $S_oL_o/h_oF_o^2 \geq 20$ and $S_oL_o/h_o \geq 5$ for low Froude number flows [*Morris and Woolhiser*, 1980]; where S_o is the gradient, L_o is the length of the plane, h_o is the normal depth and F_o is the Froude number based on normal flow). This has been found to be a good assumption for most overland flows [e.g. *Ponce et al.*, 1978;

Govindaraju et al., 1988; *Singh*, 1994; *Singh*, 2017] and is widely adopted in existing hillslope models.

4. The depth-discharge coefficient, $\alpha = CS_o^{0.5}$ (see Equation A2), calculated for *each* OFE based on its gradient, S_o, and Chezy coefficient, C, is a time varying coefficient that can adequately represent time varying resistance effects through OFE-specific friction factor functions related to C. The friction factors, which represent the different types of roughness (see Section 3.2.2), are updated at the end of each computational time step to reflect current flow conditions.
5. The contributions of different types of flow resistances (friction factors) can be added to determine the overall resistance to overland flow (i.e. the equivalent friction factor, f_{eq}). While some studies have considered different forms of expressions for determining the overall resistance [e.g. *Hirsch*, 1996], other studies have found the additive assumption of roughness components to be a good approximation of the underlying physics [e.g. *Gilley and Weltz*, 1995; *Hu and Abrahams*, 2006].
6. The effects of the surface tension on the friction factors are minimal and can be ignored for the depth ranges considered here [*Papanicolaou et al*., 2011].

3.2.2. Friction factor relations for capturing the interdependency of roughness and flow

The semi-theoretical relations below have been incorporated into the enhanced WEPP model to describe skin, form, wave, and vegetation resistance. The effects of soil grains and raindrop impact on flow resistance are considered for two Reynolds number, *Re*, regimes ($Re=q/v$, where q is the unit flow discharge and v is the kinematic viscosity). For flows with $Re<1000$, *Shen and Li* [1973] provide the following formula based on laboratory rainfall experiments to calculate skin resistance, f_s, due to grains and raindrops, as function of the Reynolds number, the rainfall intensity (m/s), I,:

$$f_S(t) = \frac{3393 I(t)^{0.407} + k_o}{Re(h,t)} \tag{2}$$

where k_o is a friction coefficient. Values of k_o have been tabulated by *Woolhiser* [1975] for different roughness surfaces.

For flows with *Re*>1000, the skin resistance is represented with the formula by *Hirsch* [1996] (also adopted by *Liu and Sing*h [2004] and *Hu and Abrahams* [2006]):

$$f_S(t) = \frac{3.19}{Re(h,t)^{0.45}} \tag{3}$$

The form friction factor, f_f, is introduced based on the formula proposed by *Abrahams* [1998], which was derived from laboratory flume experiments performed by *Lawrence* [1997] on beds covered with protruding cylindrical elements with roughness concentrations, or packing densities, varying between 10 - 100%. The formula accounts for the role of relative submergence, and concentration of roughness elements in an array as follows [*Abrahams,* 1998]:

$$f_f(t) = \frac{16}{\pi} C_d \frac{h(t)}{D_r} \lambda \tag{4}$$

where C_d, D_r and λ are the drag coefficient (-), diameter (m) and concentration of the roughness elements (-), respectively.

When $h/D_r < 1$, waves are introduced into the flow by the roughness elements. In this case an additional friction factor is incorporated that depends on the Froude Number $Fr=q/(gh^3)^{0.5}$. For flows with $Fr > 0.5$, the wave friction factor, f_w, developed by *Hu and Abrahams* [2006] is incorporated in the model as follows:

$$f_w(t) = 3.32 \frac{\lambda}{Fr(h,t)^{0.5}} \tag{5}$$

When $Fr < 0.5$, the effects of wave roughness are assumed to increase proportionally from 0 to the maximum value of f_w at Fr=0.5 [*Abrahams and Parsons*, 1994].

A semi-empirical equation for the friction factor due to shallow vegetated flows, f_{veg}, is introduced based on the work by *Katul et al*. [2011] and *Thompson et al*. [2011] as follows:

$$\sqrt{\frac{8}{f_{veg}(t)}} = 2\beta \frac{L_c}{h(t)} \exp\left(-\frac{h_c}{2\beta^2 L_c}\right)\left(-1+\exp\left(\frac{1}{2\beta^2}\frac{h(t)}{L_c}\right)\right) \quad (6)$$

where β is the momentum absorption coefficient estimated as $\beta = \min(0.135\sqrt{LAI/h_c}, 0.33)$; h_{ci} (m) is the canopy height; and L_c (m) is the adjustment length scale equal to $(C_d\, LAI/h_c)^{-1}$, where LAI (m²/m²) is the leaf area index defined as the one-sided green leaf area per unit ground surface area.

Finally the overall friction factor, f_{eq}, which accounts for the collective effects of the different landscape attributes, is approximated as follows (see assumption 5 in Section 3.2.1):

$$f_{eq} \approx f_s + f_f + f_w + f_{veg} \quad (7)$$

where f_s, f_f, f_w, and f_{veg} are estimated from equations (1)-(5) above.

3.2.3. Shock-capturing scheme for overland flow routing

The Total Variation Diminishing (TVD) MacCormack scheme is adopted in WEPP because it is relatively simple to implement and has been documented to handle the formation and propagation of shocks without violating the continuity equation. The scheme is a finite difference scheme of second order accuracy capable of rendering solutions oscillation free [e.g., *Davis*, 1984; *Garcia-Navarro et al.*, 1992; *Mingham et al.*, 2001; *Papanicolaou et al*., 2010]. It is suitable for implementation in an explicit time-marching algorithm and involves a two-step procedure known as the "predictor-corrector" algorithm [*Garcia-Navarro et al.*, 1992]. To solve the 1-D KWE (see Appendix A), the computational domain, represented by each OFE (see Figure 3.3), is first discretized as $x_i = i\Delta x$ and $t_j = j\Delta t$, where i and Δx denote space and the size of the mesh, respectively, and j and Δt denote time and the time step, respectively. Then, the TVD-MacCormack scheme is applied as follows [*MacCormack*, 1969, 1985; *Tseng*, 2010]:

Predictor Step:

$$\tilde{h}_i = h_i^j - \frac{\Delta t}{\Delta x}\left[q_{i+1}^j - q_i^j\right] + v_i^j \Delta t \quad (8)$$

$$\tilde{q}_i = \alpha \tilde{h}_i^{1.5} \tag{9}$$

Corrector Step:

$$\approx{h}_i = h_i^j - \frac{\Delta t}{\Delta x}[\tilde{q}_i - \tilde{q}_{i-1}] + v_i^j \Delta t \tag{9}$$

where the symbols (~) and (≈) denote predictor and corrector steps, respectively, *h* denotes the flow depth, *q* is the unit flow discharge, and *v* is the rainfall excess rate.

A dissipative term, denoted as TVD_i and defined as follows, is used to provide an oscillation free solution in the presence of large gradients [*Mingham et al.*, 2001]:

$$TVD_i = Gr_i\left[h_{i+1} - h_i\right] - Gr_{i-1}\left[h_i - h_{i-1}\right] \tag{10}$$

where,

$$Gr_i = 0.5 \cdot Cf_i \cdot [1 - \varphi_i] \tag{10a}$$

where φ_i is the flux limiter function given as:

$$\varphi_i = \begin{cases} \min(2r_i, 1), & r_i < 0 \\ 0, & r_i \geq 0 \end{cases} \tag{10b}$$

and r_i is the ratio of successive gradients equal to

$$r_i = \frac{h_i - h_{i-1}}{h_{i+1} - h_i} \tag{10c}$$

In equation (10a), the function Cf_i is dependent on the local courant number, Cr_i, and is given as:

$$Cf_i = \begin{cases} 0.25, & Cr_i > 0.5 \\ Cr_i[1 - Cr_i], & Cr_i \leq 0.5 \end{cases} \tag{10d}$$

The courant number, Cr_i, is calculated as follows:

$$Cr_i = c_i \frac{\Delta t}{\Delta x} \tag{10e}$$

where c_i is the wave celerity equal to $1.5 C_i S_0^{0.5} h_i^{0.5}$. The TVD-MacCormack scheme must satisfy the Courant-Friedrichs-Lewy (CFL) criterion at each cell in order to be stable. The Δt is selected to satisfy the CFL criterion defined as:

$$Cr_i = \frac{\Delta t}{\Delta x} c_i \leq 1 \tag{11}$$

At the end of a time step, the final value for the cross-sectional flow depth is determined by averaging the predicted and corrected values (equations (7) and (9)) and adding the TVD_i term:

$$h_i^{j+1} = \frac{1}{2}(\tilde{h}_i + \tilde{\tilde{h}}_i) + TVD_i \tag{12}$$

The final flow discharge is then computed as follows:

$$q_i^{j+1} = \alpha h_i^{j+1^{1.5}} \tag{15}$$

where the α coefficient, which is a function of the f_{eq}, is updated at the end of each time step.

3.3. Experiments and Modeling Exercises

This section is organized as follows. First, model validation exercises are presented demonstrating the enhanced WEPP's ability to simulate the net effects of space/time-variant flow resistance on the runoff hydrograph using observed data from several field and laboratory experiments. These experiments have been performed by various investigators, including the

authors, for different surface roughness (grain, isolated roughness elements, and vegetation) under different sets of storm and hillslope gradient/curvature conditions.

Following the model validation, observations from a hillslope-scale field experiment performed by *Helmers et al*. [2012] are used to examine the effect of the space/time-invariant resistance assumption on runoff hydrograph prediction. This exercise compares the performance of the enhanced WEPP (space/time-variant resistance) and the original WEPP (space/time-invariant resistance) in simulating an observed runoff hydrograph from a hillslope with vegetated filter strips and an S-shaped profile curvature.

Last but not least, the *Helmers et al.* [2012] experiment is used as a basis to perform numerical experiments to examine the influence of grain roughness, isolated roughness elements, and vegetation on runoff hydrographs under different storm magnitudes and hillslope gradients. These experiments also compare of the effects of the individual roughness types. Emphasis is first placed on the net influence of the roughness types on runoff hydrograph characteristics at the hillslope outlet for three storm events of different rainfall amounts (i.e., small to large storms), as well as for hillslopes of three different gradients (i.e., mild to steep slopes). Then, building on the findings, the critical storm magnitudes and hillslope gradients beyond which the influence of the roughness types becomes negligible are identified.

3.3.1. Model Validation

Four validation cases were used to test the model's ability to capture the integrated effects of the space/time-variant flow resistance on the runoff hydrograph in the presence of the different landscape attributes; Case 1 examined the effects of grain roughness on a bare surface using measurements from field experiments by *Abban et al*. [2017]; Case 2 considered the effects of isolated roughness elements via laboratory flume experiments performed by *Jomaa et al*. [2012]; Case 3 evaluated the effects of vegetation and patchiness using field experiments by *Neibling and Alberts* [1979], and; Case 4 examined the effects of concave profile curvature and the ability of the model to capture shock formation and propagation using the flume experiments performed by *Iwagaki* [1955]. The details of each of the cases and relevant model inputs are summarized in Table 3.1.

Table 3.1: Model parameters for validation Cases

Model parameters	
Case 1: Bare hillslope	I = 60 mm/hr; S_o = 9% ; k_o = 500
Case 2: Isolated roughness elements	I = 74 mm/hr; S_o = 9%; k_o = 500; C_d = 1.0; D_r = 0.06 m; λ = 0.2
Case 3: Vegetation Patchiness	I = 74 mm/hr; LAI = 1; h_c = 0.1 m; C_d = 1.0
Case 4: Curvature	$q_{l,ofe1}$ = 0.108 cm/s; $q_{l,ofe2}$ = 0.064 cm/s; $q_{l,ofe3}$ = 0.08 cm/s; $S_{o,ofe1}$ = 2%; $S_{o,ofe2}$ = 1.5%; $S_{o,ofe3}$ = 1%;

In each validation case, the performance of the model was examined by comparing the numerically computed hydrographs at the hillslope outlet with the field or laboratory observations. The comparisons were made with the Nash-Sutcliffe model efficiency coefficient (E_f) proposed by *Nash and Sutcliffe* [1970] as follows:

$$E_f = 1 - \frac{\sum_{j=1}^{n} (O_j - M_j)^2}{\sum_{j=1}^{n} (O_j - \bar{O})^2} \tag{16}$$

where j is time counter, n is the number of data points, O is the observed (or measured) flow discharge, M is the modeled (or simulated) discharge, and $\bar{0}$ is the time-averaged observed discharge of the event. E_f provides a measure of a model's performance over the course of an event in comparison to the $\bar{0}$ of the event. An E_f value of 1.0 corresponds to a perfect agreement between the observed and simulated flow hydrographs whereas an E_f value of 0.0 shows no agreement.

3.3.1.1.Case 1: Effects of bare surface

Abban et al. [2017] performed field experiments to investigate space/time-variant resistance effects on overland flow and soil erosion under bare surface conditions. The experiments were performed on uniform-profile plots that had a gradient of 9% and were approximately 7.5 m long by 1.2 m wide. A uniform rainfall intensity of 60 mm/hr was applied over the plots for a period of 5 hrs using rainfall simulators. Flow rate measurements were taken

at the outlet at regular time intervals using a v-notch weir. The measurements were taken during the rising limb phase of the hydrograph and at steady state. No measurements were taken during the falling limb phase of the hydrograph. The soil type was silty loam.

Figure 3.4a provides a comparison of the measured and simulated flow hydrographs for one of the experimental runs. The figure illustrates very good agreement overall between the measured and enhanced WEPP simulated volumetric runoff rates, with $E_f \approx 0.91$. The simulated time to runoff initiation was ~5.0 min versus the ~7 min observed time. The figure also compares the performance of the enhanced and original WEPP models. The primary difference between the original WEPP and enhanced WEPP predicted hydrographs is seen in the rising limb. The rising limb in the original WEPP leads both observed and enhanced WEPP results by up to ~4 mins. This is because the original WEPP uses a fixed friction factor value, so at low flows it will tend to underestimate the flow resistance whereas at high flows it will overestimate the flow resistance.

3.3.1.2.Case 2: Effects of isolated roughness elements

Jomaa et al. [2012] performed laboratory experiments in a 2.2% slope, 6 m × 1m flume to investigate the effects of rock fragments coverage on overland flow and soil erosion. The experimental scenario simulated herein had a 20% coverage of isolated roughness elements (fluvial rock fragments) approximately 6 cm in diameter. Rainfall was applied at 74 mm/hr resulting in low submergence conditions. The measurements were only presented for the rising limb and steady state phases of the hydrograph.

Figure 3.4b provides a comparison of the flow hydrographs between the measured and simulated data. The enhanced WEPP and observed hydrographs illustrate good agreement, overall, with $E_f \approx 0.75$. The simulated time to runoff initiation was ~9.0 min versus the ~8.3 min observed during the flume experiments. For this case, the original WEPP and enhanced WEPP hydrographs are nearly identical. This is to be expected. At low flows, friction due to grain roughness is dominant. As the flow depth increases, friction due to grain roughness drops (see Eqn. 2). However, this drop in friction is counteracted by an increase in friction due to form roughness as the relative submergence of the isolated roughness elements increases (see Eqn. 4). The net effect of these balancing interactions is a fairly constant friction factor along the length of the plot considered herein.

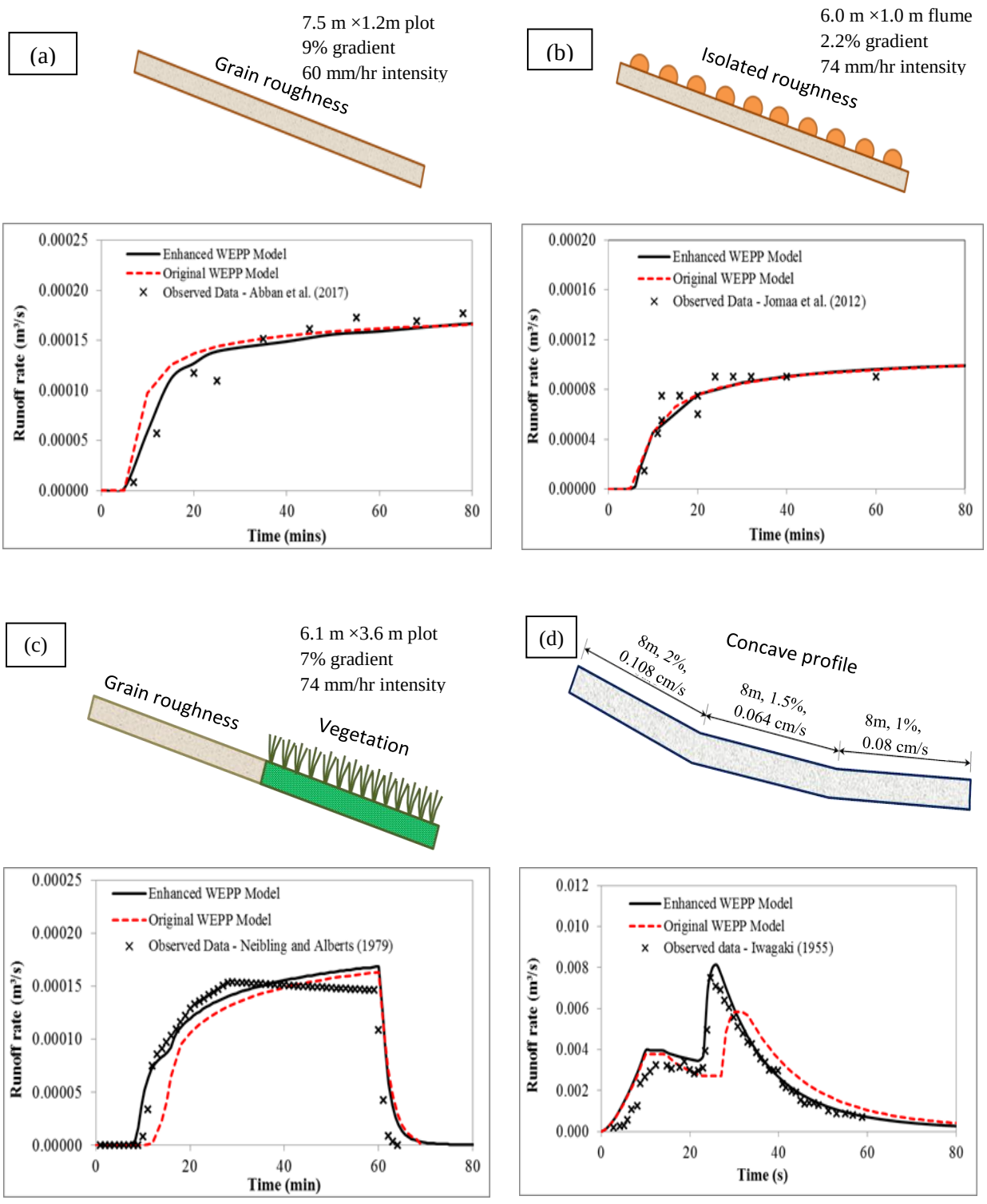

Figure 3.4: Validation of the enhanced WEPP model's ability to capture the effects of the interaction between the landscape attributes and overland flow on the runoff hydrograph for (a) a bare surface (b) a surface with isolated roughness elements (c) a surface with vegetation patchiness, and (d) a concave hillslope profile. The model simulations are compared to observed data from field or laboratory experiments.

3.3.1.3.Case 3: Effects of vegetation patchiness

Neibling and Alberts [1979] performed experiments on 6.1 m × 3.6 m field plots with gradient of 7% and a specified length of vegetation strip at the base of the plot. Their experiment with a vegetation strip length of 2.45 m is examined herein. Rainfall was supplied for about 1 hr at an intensity of 74 mm/hr. The calibrated flume captured runoff rates during the rising limb, at steady state, and during the falling limb of the hydrograph.

Figure 3.4c compares the measured and simulated flow hydrographs. As seen, there is very good agreement between the measured and enhanced WEPP simulated data which is in accordance with the $E_f \approx 0.87$. The simulated time to runoff was ~26 min whereas the observed time to runoff was ~30 min. The original WEPP overestimated the time to runoff initiation (~6 mins) and underestimated runoff rates. The spatial averaging of roughness effects impacts the ability to predict rainfall excess rates, as well as travel times that arise from the vegetation patchiness. On the other hand, the enhanced WEPP, which performs simulations on OFE-by-OFE basis, was better able to capture the different rainfall excess rates on the vegetated and bare surfaces, as well as the interaction between runoff from the two surfaces.

3.3.1.4.Case 4: Effects of curvature

The notable laboratory experiments of *Iwagaki* [1955] are employed herein to test the enhanced WEPP's ability to capture the effects of changes in the gradient along the downslope as well as shock formation and propagation on the runoff hydrograph at the outlet. The experiments were performed in a 24 m × 0.196 m flume. No rain was applied in these experiments. Water instead was supplied laterally for a duration of 10s in the flume at 0.108 cm/s, 0.0638 cm/s, and 0.08 cm/s, respectively, from top to bottom, at three sections 8 m in length each. The flume bed was impermeable, with respective gradients of 2%, 1.5%, and 1% for the three sections.

A comparison between the observed and simulated hydrographs is provided in Figure 3.4d. The E_f between the observed and enhanced WEPP simulated hydrographs is ~0.88, indicating very good agreement between them. A sharp increase in runoff rate is noted in the observed hydrograph around 23 s, depicted by the near vertical gradient in the rising limb. Iwagaki noted that this increase was due to a shock wave that had formed when faster upstream waves caught up with slower downstream waves generating steep wave fronts that propagated to

the outlet. As also shown in the figure, the original WEPP model is unable to capture both the peak runoff rate and the time to peak. The peak is ~25% less and the time to peak is ~5 s slower. This is because the original WEPP model uses an average hillslope gradient to route the flow downslope. Hence the influence of the concave curvature, where waves from upslope travel faster and catch up with downstream waves is not captured. The enhanced WEPP model, on the other hand, captures these dynamics and is able to better match the observed data.

3.3.2. Evaluation of the space/time-invariant resistance assumption for representing the interaction betweeen the landscape attributes and flow.

To examine the implications of the space/time-invariant resistance assumption, runoff on a hillslope in the Walnut Creek Watershed, IA, observed by *Helmers et al*. [2012] was simulated using both the enhanced and original WEPP models. A depiction of the examined hillslope (plan and cross-sectional views) is provided in Figure 3.5a and Figure 3.5b. The hillslope had an average gradient of 7.7% and a mean length of approximately 250 m. The management practice was a two-year no-till corn-soybean rotation, with three vegetated filter strips positioned at different locations along the downslope. The hillslope comprised silty loam soil. The simulated storm event occurred on 8/8/2010 and yielded ~46 mm of rainfall.

Figure 3.5c compares the observed runoff hydrograph (red solid line) to hydrographs simulated under the space/time-invariant resistance assumption (blue dotted line; original WEPP) and the space/time-variant resistance assumption (black dashed line; Enhanced WEPP). It is apparent that the assumption of a space/time-invariant resistance cannot adequately predict the peak runoff rate or hydrograph shape for hillslopes with the type of landscape attribute configuration examined herein. The space/time-invariant resistance under-predicts the peak runoff rate by as much as ~65% in this case. On the other hand, the space/time-variant resistance well predicts the peak runoff rate and hydrograph shape under these conditions. The excellent agreement between the space/time-variant-resistance-predicted hydrograph and the observed hydrograph also suggests that accounting for changes in resistance in space and time is indeed able to capture steep gradients in the hydrograph rising limb that arise from rainfall, topographic and roughness variability.

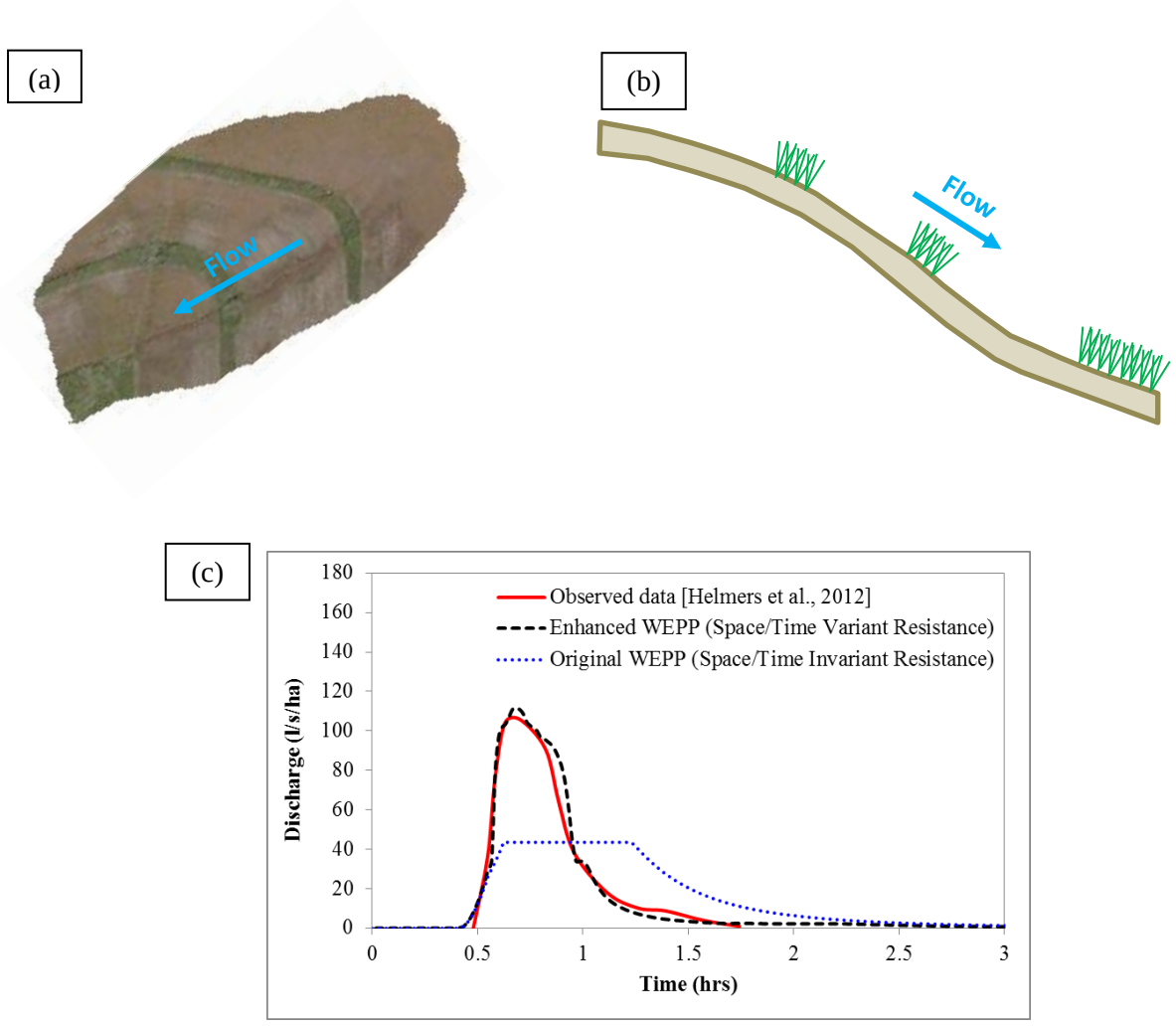

Figure 3.5: Implication of the space/time-invariant resistance assumption on flow hydrograph prediction. The figures show, respectively: (a) a plan view of the examined hillslope; (b) a depiction of the hillslope cross-section along the downslope, illustrating the profile curvature and vegetation patchiness; and (c) the observed vs simulated hydrographs. The solid red line represents the observed hydrograph [*Helmers et al.*, 2012], whereas the dashed black and dotted blue lines represent hydrographs that consider space/time-variant resistance (simulated with the enhanced version of WEPP) and space/time-invariant resistance (simulated with the original version of WEPP), respectively.

3.3.3. Evaluation of the degree of influence of landscape attributes on runoff hydrograph characteristics

To decipher the effects of the interplay of grain roughness, isolated roughness, and vegetation with runoff volume (Section 3.3.3.1) and hillslope gradient (Section 3.3.3.2), the validated enhanced WEPP model of the Walnut Creek hillslope presented in Section 3.3.2 above was used as a basis to perform "thought" experiments in which the storm magnitude and hillslope gradients were varied to evaluate the runoff hydrograph response. For each experiment, the surface was assumed to consist entirely of grain roughness, isolated roughness elements, or vegetation. Three storm magnitudes were examined that corresponded to rainfall amounts of 23 mm, 46 mm, and 92 mm (see Figure 3.6). The hillslope gradients examined were 3.5%, 7%, and 14% (see Figure 3.7). Thought experiments were also performed to examine profile curvature effects (i.e., concave, uniform, and convex slopes) on the hillslope hydrograph (see Figure 3.8).

The simulated runoff rates from the experiments are presented in Figure 3.6-Figure 3.8 in the form of normalized runoff hydrographs to enable comparison between the different roughness types, storm events, hillslope gradient, and curvature scenarios. In each case, the presented hydrographs are normalized using the highest peak runoff rate observed between the three roughness types. The results from these experiments are described below.

3.3.3.1. Effects of the interplay between surface roughness and event magnitude on runoff hydrographs

Figure 3.6a and Figure 3.6b examine the effects of grain roughness, isolated roughness elements, and vegetation for the three storm events with rainfall totals of 23mm, 46mm, and 92 mm, respectively. The storm distribution in each case is based on the storm from Section 3.3.2. The hillslope profile and the average hillslope gradient are the same as those in Section 3.3.2.

Effects on hydrograph peakiness, spread, and times to peak: Hydrographs on the bare surface with only grain roughness were peakier with narrower spreads compared to the other two surfaces. Vegetation tended to have a smoothening effect, resulting in less peaky, drawn out hydrographs with wider spreads. Peak runoff rates of 2.7×10^{-3} $m^3/s/m$ (Figure 3.6a), 8.3×10^{-3} $m^3/s/m$ (Figure 3.6b), and 19.9×10^{-3} $m^3/s/m$ (Figure 3.6c) were observed on the bare surface (grain roughness) for the 23, 46, and 92 mm events, respectively. For the isolated roughness elements and vegetated surfaces, peak runoff rates of 1.7×10^{-3} $m^3/s/m$, 4.8×10^{-3} $m^3/s/m$, and

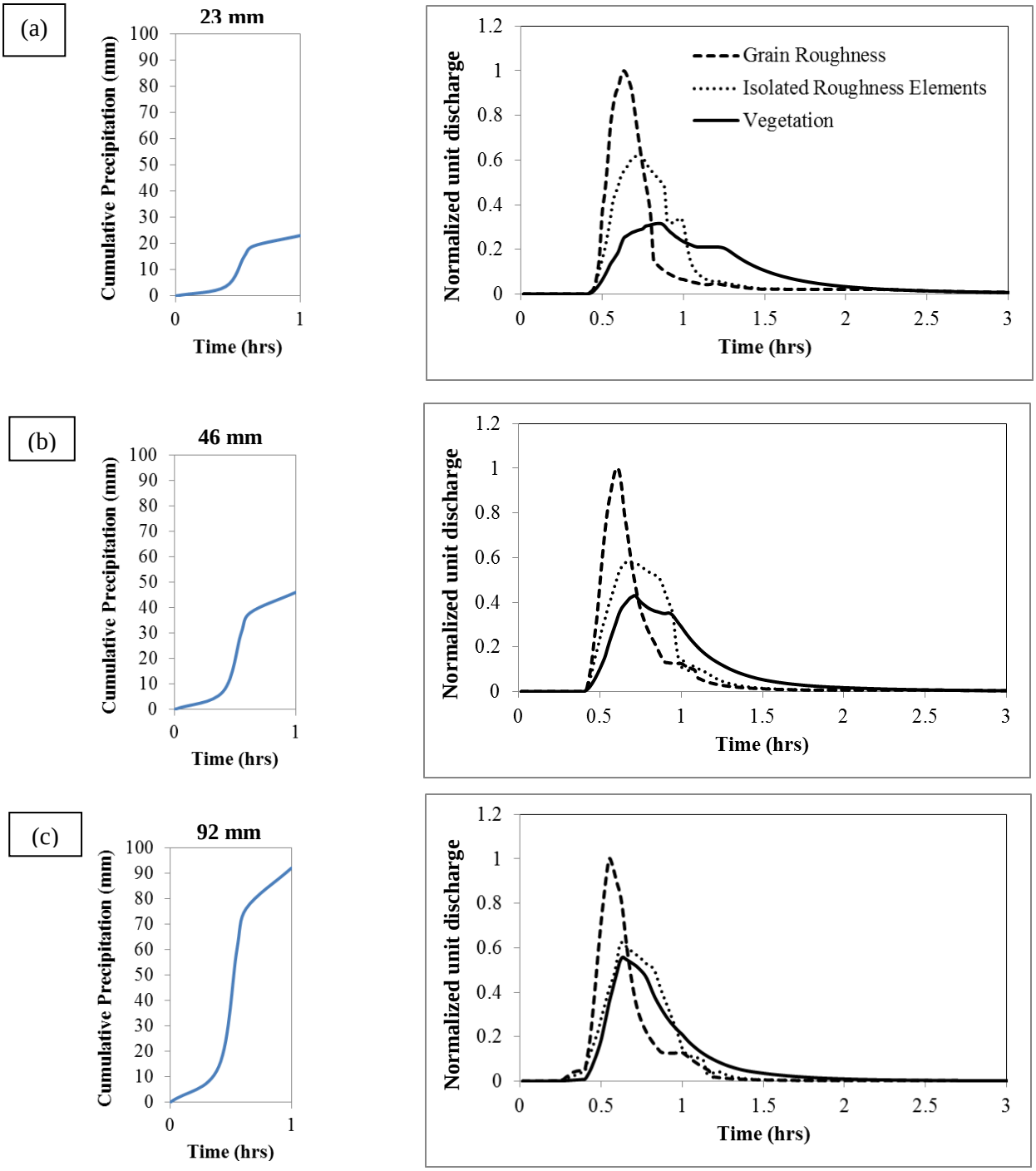

Figure 3.6: Normalized hydrographs simulated with the enhanced WEPP model demonstrating the net effects of the interplay between surface roughness and storm magnitude on hydrograph characteristics. The normalizing unit discharge in each case is the highest peak discharge between the three attribute hydrographs. They are 0.0027 $m^3/s/m$, 0.0083 $m^3/s/m$ and 0.019 $m^3/s/m$ for the (a) 23 mm, (b) 46 mm and (c) 92 mm storms, respectively.

12.4×10^{-3} m³/s/m, and 0.9×10^{-3} m³/s/m, 3.6×10^{-3} m³/s/m, and 11.1×10^{-3} m³/s/m, respectively, were observed.

The times corresponding to the hydrograph peaks for the three roughness types ranged between 38 – 51 mins for the 23 mm storm event, 36 – 43 mins for the 46 mm event, and 33 – 38 mins for the 92 mm event. In each case, the time to peak on the bare surface was shortest while the time to peak on the vegetated surfaces was longest. The decreasing range of times to peak from the lowest magnitude event (13 mins) to the highest magnitude event (5 mins) points towards an increasing similarity in the hydrographs as the storm magnitude increases. Further, as seen in Figure 3.6, the range of hydrograph start and end times were more similar for the highest event compared to the lowest event suggesting that the influence of the roughness types began to diminish as the storm magnitude increased.

Quantitative comparison of effects using the root-mean-square deviation (RMSD): The similarities in the hydrographs between the different landscape attributes were calculated using the RMSD. A low value of RMSD implied greater similarity whereas a high value implied less similarity. The vegetated surface hydrographs were used as the reference hydrographs for the RMSD calculations. The RMSD values between the bare and the vegetated surface hydrographs were 0.063, 0.051, and 0.049 for the 23, 46, and 92 mm events, respectively, confirming the greater similarity in hydrographs as the storm magnitude increased. The same trend was observed when comparing the hydrographs predicted on the isolated roughness elements surface with the vegetated surface, i.e., the RMSD reduced from 0.036 to 0.013 from the lowest to the highest magnitude event. Overall, the consistent reduction in RMSD from the lowest event to the highest event confirms that the influence of the examined surface roughness types on the runoff hydrograph diminishes with increasing runoff volume.

3.3.3.2. Effects of the interplay between surface roughness and hillslope gradient on runoff hydrographs

Figure 3.7a - Figure 3.7c examine the effects of grain roughness, isolated roughness elements, and vegetation on hillslopes with average gradients of 3.5%, 7%, and 14%, respectively. For this set of simulations, the simulated storm event in each case was the same as the storm in Section 3.3.2.

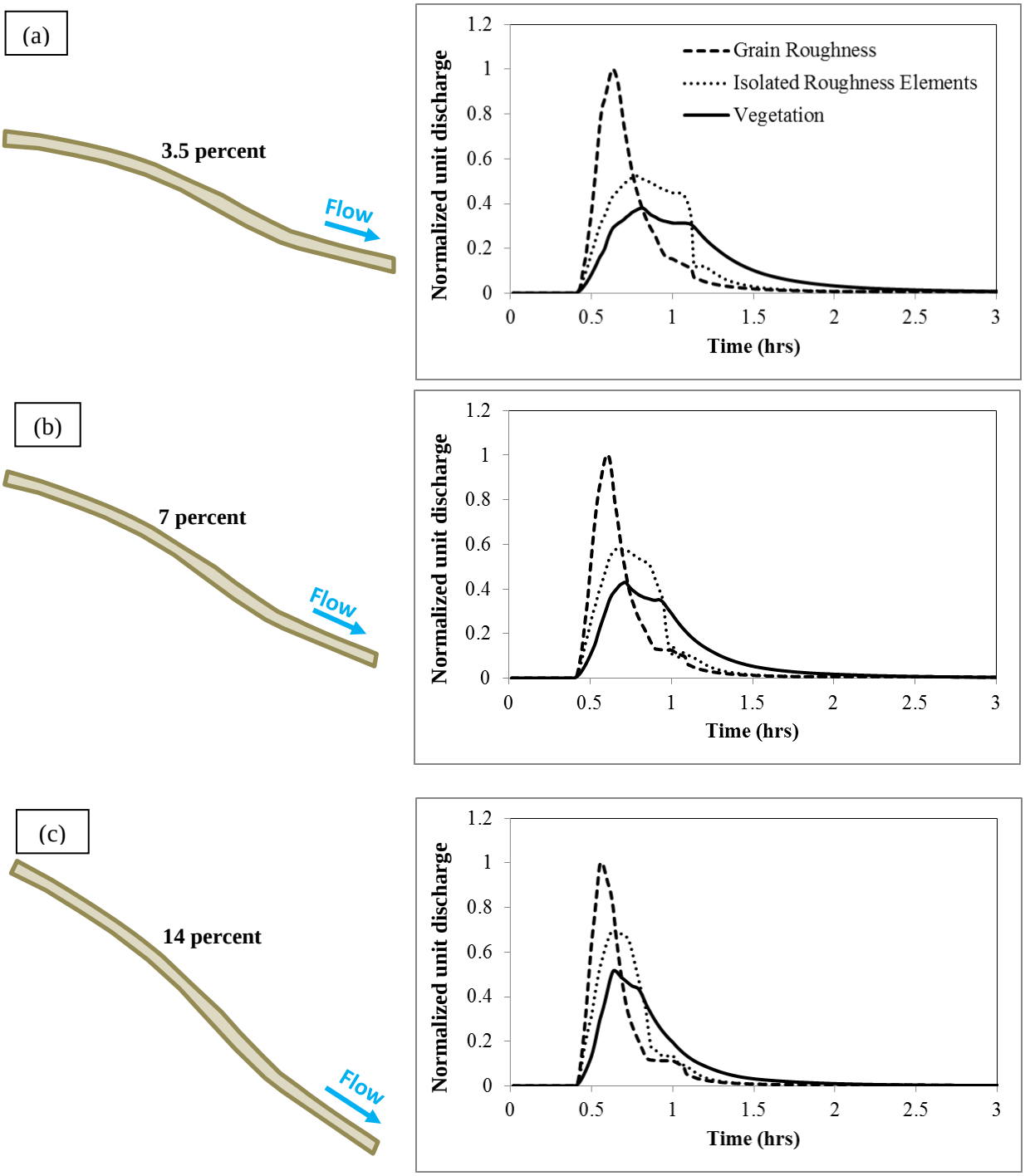

Figure 3.7: Normalized hydrographs simulated with the enhanced WEPP model demonstrating the net effects the interplay between surface roughness and hillslope gradient on hydrograph characteristics. The normalizing unit discharge in each case is the highest peak discharge between the three attribute hydrographs. They are 0.007 $m^3/s/m$, 0.0083 $m^3/s/m$, and 0.0092 $m^3/s/m$ for the (a) 3.5%, (b) 7% and (c) 14% gradients, respectively.

Effects on hydrograph peakiness, spread, and times to peak: The increase in hillslope gradient from 3.5% (Figure 3.7a) to 14% (Figure 3.7c) led to an increase in the peak runoff rate from 7.0×10^{-3} m³/s/m to 9.2×10^{-3} m³/s/m on the bare surface, and increases in the peak rates on the isolated roughness elements and vegetated surfaces from 3.7×10^{-3} m³/s/m to 6.4×10^{-3} m³/s/m, and 2.7×10^{-3} m³/s/m to 4.7×10^{-3} m³/s/m, respectively. The spread of the hydrographs reduced as the hillslope gradient increased. For example, on the vegetated surface, 95% of the runoff hydrograph volume fell between 0 – 142 mins on the 2% gradient whereas it only fell between 0 – 97 mins on the 14% gradient.

The range of the times to peak between the three roughness types reduced with increasing hillslope gradient. Whereas it fell between 38 – 49 mins for the 3.5% gradient, it fell between 34 – 38 mins for the 14% gradient. As expected, the range for the 7% gradient fell between those of the other two gradients, i.e. 36 – 43 mins.

Quantitative comparison of attribute effects using the RMSD: The RMSD comparing the normalized hydrographs between the bare and isolated roughness elements surfaces decreased from 0.049 to 0.037 from the 3.5% to the 14% gradient, suggesting that the differences in hydrographs reduced with increasing gradient. This was confirmed by comparing the RMSD between the bare and vegetated surfaces for the 3.5% and 14% gradients. In this case, the RMSD decreased from 0.058 to 0.051. This observed trend of growing similarity between the hydrographs with hillslope gradient is investigated in more detail in Section 3.3.4 where we examine if a continued growth in similarity with increasing gradient occurs, and if this increase in the gradient leads to a threshold stream power beyond which the differences in the hydrographs become negligible.

3.3.3.3. Effects of the interplay between surface roughness and downslope curvature on runoff hydrographs

This part of the study examines the effects of curvature on the runoff hydrograph at the outlet. It examines the same conditions on the *Helmer's et al*. [2012] hillslope, with only the profile curvature being modified. Concave, uniform, and convex profiles are examined. The results from these experiments are shown in Figure 3.8.

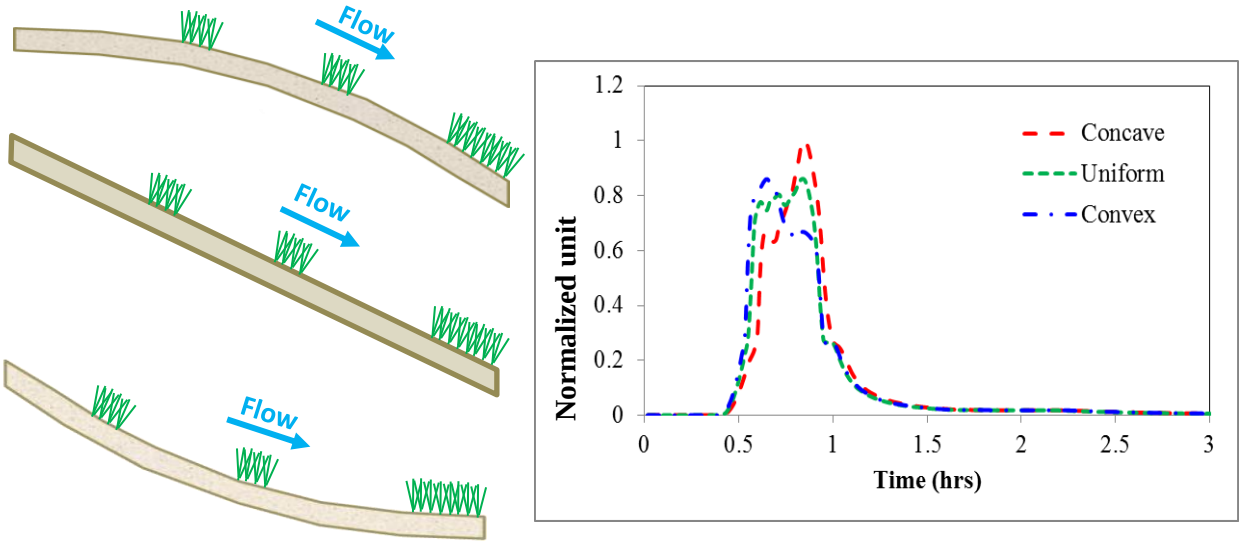

Figure 3.8: Normalized hydrographs simulated with the enhanced WEPP model demonstrating the net effects of curvature on hydrograph characteristics. The normalizing discharge, 0.0032 $m^3/s/m$, corresponds to the peak discharge on the concave hillslope. The red, green, and blue dashed lines represent, respectively, hydrographs on the concave, uniform, and convex hillslopes.

It is seen from the figure that curvature has an effect on the shape of the hydrograph. The times to peak on the convex hillslope was 39 mins, which was different than the times to peak on the uniform and concave hillslopes, which were 50 mins and 51 mins, respectively. Furthermore, an inspection of the hydrographs reveals that the hydrographs on the convex and concave hillslopes have two modes, whereas the hydrograph on the uniform hillslope has three modes. These differences are attributed to the differences in wave speeds on the three hillslopes that arise from curvature effects interacting with hillslope patchiness. The three modes on the uniform hillslope correspond to changes in the wave speed due to the three vegetation patches, whereas the two modes on the convex and concave hillslopes result from changes in the speed of one of the modes due to curvature effects.

Overall, the effects of curvature were smaller compared to the effects of surface roughness. For example, whereas the change from a vegetated surface to a surface with only grain roughness resulted in approximately a 133% increase in the peak runoff rate (3.6×10^{-3} $m^3/s/m$ to 8.3×10^{-3} $m^3/s/m$), the maximum change in peak runoff rate due to change in curvature was 16% (2.7×10^{-3} $m^3/s/m$ to 3.2×10^{-3} $m^3/s/m$) from the uniform to the concave profile.

3.3.4. Identification of the critical storm magnitude and hillslope gradient

The results presented in Sections 3.3.3.1 and 3.3.3.2 suggest the existence of a critical storm magnitude and hillslope gradient beyond which the effects of a surface roughness type on the runoff hydrograph will be relatively insignificant. To test this postulate, the peak unit stream power is examined for a range of 1-hr duration storms with intensities ranging between 25 mm/hr to 150 mm/hr on hillslopes with gradients ranging from 1% to 40%. The peak stream power is considered because it incorporates both runoff magnitude and hillslope gradient effects in a single metric. The range of intensities were selected to bracket the range of 1-hr intensities reported in the Iowa SUDAS (Statewide Urban Design and Specification) manual [2017] for storms of different return periods between 1-yr to 500-yr. The intensities are thus representative for a typical mid-western landscape. The range of gradients were also selected to bracket the range of hillslope gradients observed within the Clear Creek Watershed, IA, which is one of the watersheds constituting the Critical Zone Observatory for Intensively Managed Landscapes. The gradients were obtained from Lidar data provided by the Iowa Geographic Information Council (http://www.iowagic.org/projects/lidar-for-iowa/). This range of gradients is assumed to be representative of other similar watersheds in the region.

Figure 3.9 presents results from the analyses showing the normalized peak storm intensities, I_*, against the dimensionless peak stream power, $\Psi_* = q_* S_{o*}$ for each of the three surface roughness types (grain roughness, isolated roughness elements, and vegetation). The storm intensities are normalized using 150 mm/hr as the reference value, whilst the gradients are normalized with 40% as the reference gradient. For the unit flow discharge, the peak unit discharge on the 40% slope for the 150 mm/hr intensity storm is used as the reference. The curves are drawn for each hillslope gradient. For the curves presented, potential fits to the power law equation $\Psi_* = k I_*^{\,l}$, where k and l are coefficients that reflect the effects of surface roughness resistance and hillslope gradient on the stream power, are examined. Two distinct zones are apparent for each landscape attribute type (demarcated with the solid red lines): 1) Zone 1, where k is a function of the gradient, S_o, and l is a function of both resistance, f, and S_o, and; 2) Zone 2, where only k is a function of S_o and $l = 1$. The results confirm the existence of threshold values of Ψ_* and I_* beyond which the peak stream power is not affected by the presence of the roughness elements (i.e. Zone 2). Under these conditions, the peak stream power on a given hillslope is primarily governed by storm magnitude (runoff). Below the threshold value (i.e.,

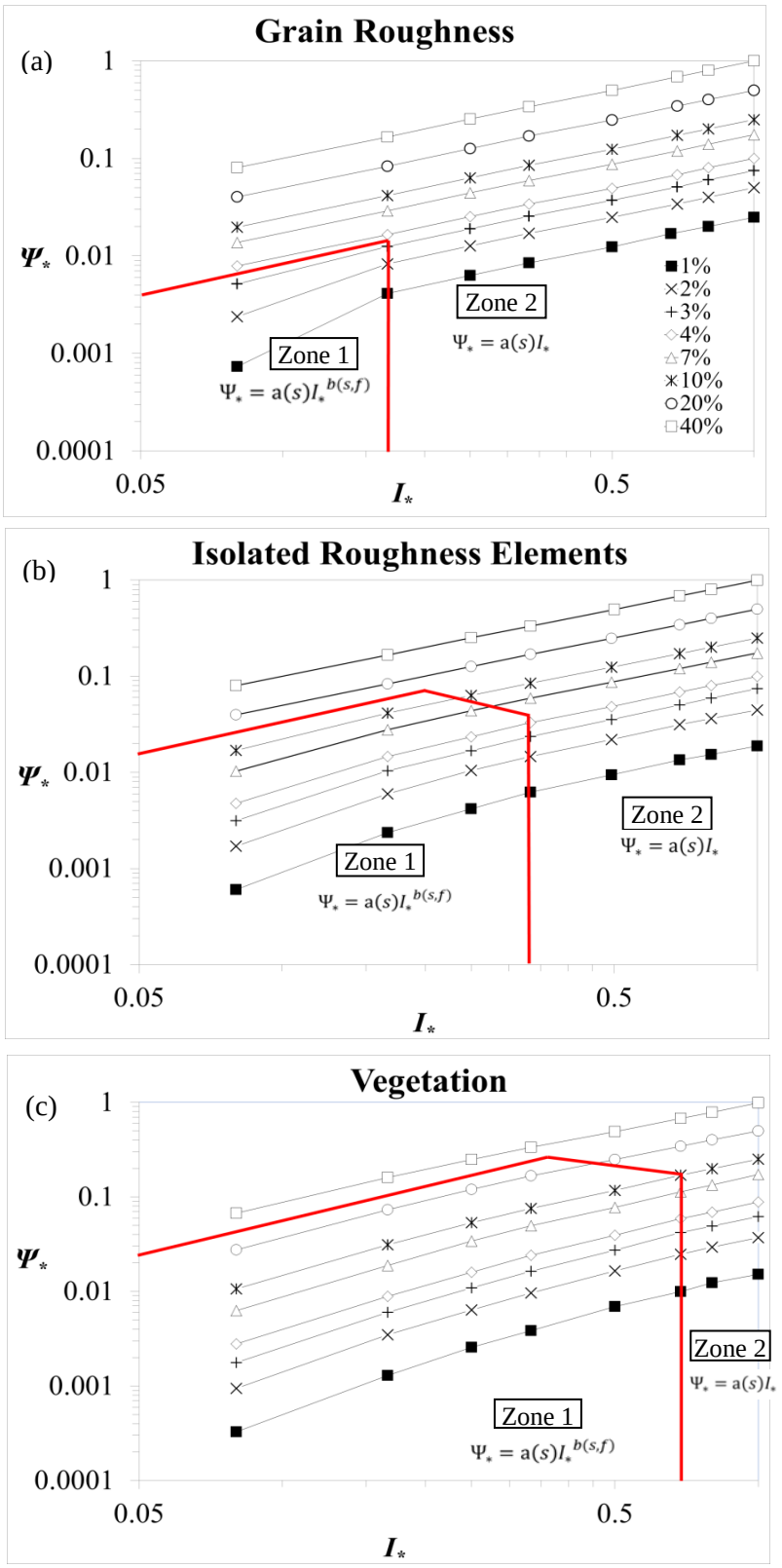

Figure 3.9: Variation of dimensionless peak stream power $\Psi_* = q_* S_*$ with dimensionless peak storm intensity I_* on uniform hillslope with: (a) grain roughness; (b) isolated roughness elements; and (c) vegetation.

Zone 1), the roughness elements have a clear effect on the peak stream power, exhibited in changing values of l (local slope) as the storm intensity changes for a given hillslope gradient (this is clearly seen in Figure 3.9b and Figure 3.9c). Both the effects of surface roughness resistance and storm intensity play an important role in this case. The effect of gradient is important in both zones as seen from the dependence of k and l on S_o in Zone 1 and the dependence of a on S_o in Zone 2.

Comparing the plots for the different surface roughness types (Figure 3.9a-Figure 3.9c), vegetation has the largest influence, affecting the peak stream power over the widest range of conditions, followed by the isolated roughness elements, and then the bare surface with grain roughness. The critical dimensionless intensity and stream power values for vegetation are 0.68 and 0.022, respectively, whereas they are 0.33 and 0.017, and 0.16 and 0.004 for the isolated roughness and grain roughness surfaces, respectively. This trend is in accordance with the predicted hydrograph characteristics presented in Figure 3.6 and Figure 3.7, where the vegetated surface has the largest influence on the runoff hydrograph due to the greater resistance to overland flow, followed by the isolated roughness elements and then the grain roughness surface. Thus, the degree of resistance offered by a surface roughness type to flow appears to dictate its influence on the critical stream power threshold between Zone 1 and Zone 2 for a given storm magnitude. A larger resistance leads to a larger threshold value and vice versa.

The above results are summarized in a generalized sketch in Figure 3.10, which presents a taxonomy on the degree of influence of surface roughness on the peak stream power for different storm intensities. The figure clearly shows the two zones separated by the threshold line. Below the threshold (Zone 1), the relationship between the stream power and the storm intensity is non-linear, whereas above the threshold (Zone 2), the relationship between the stream power and the storm intensity is linear. The linear relationship in Zone 2 depicts the finding that the main factors dominating this hillslope response are the storm intensity (runoff magnitude) and hillslope gradient. The non-linear relationship in Zone 1 highlights the added influence of the surface roughness types, and implies that the curve will intercept the horizontal axis at a point where the storm magnitude is just large enough to generate runoff under the given surface roughness.

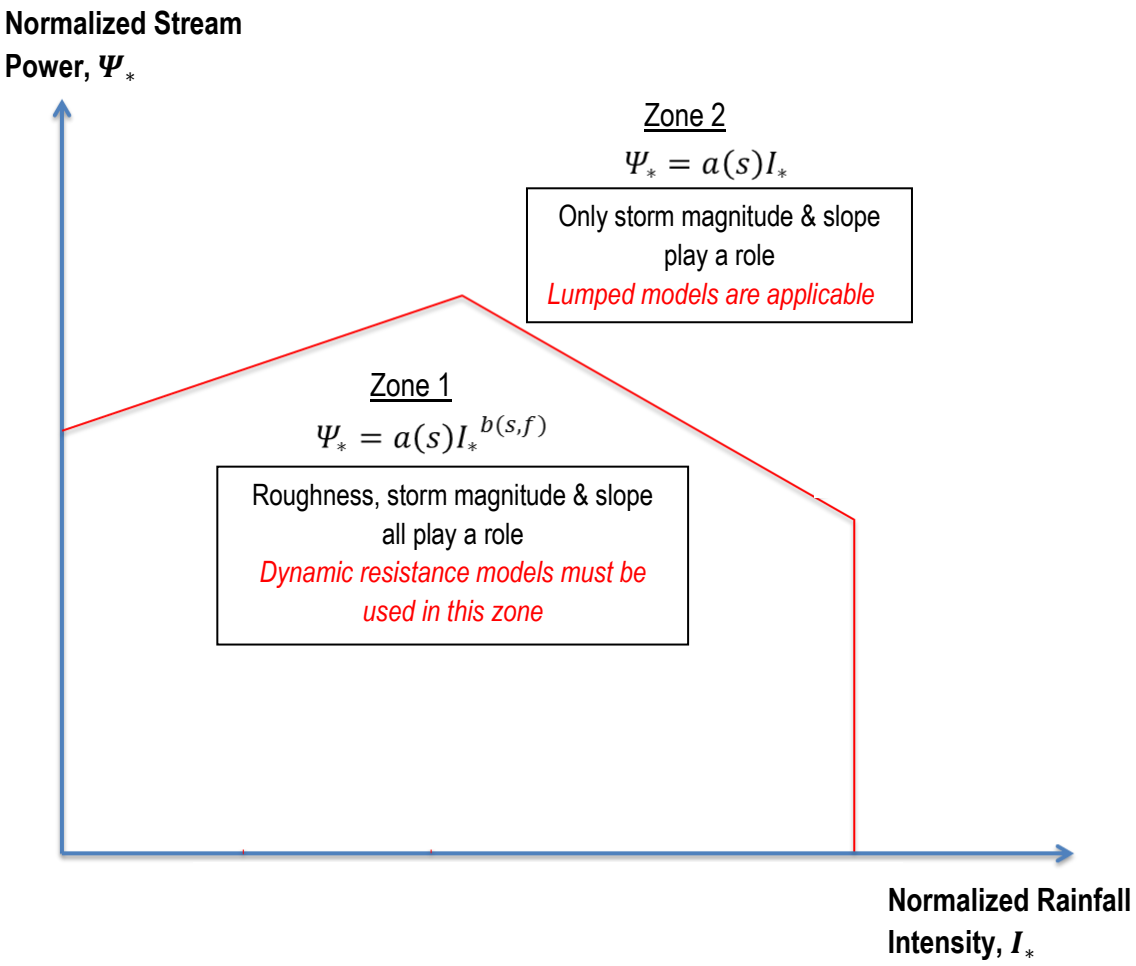

Figure 3.10: Conceptual representation of roughness effects - variation of dimensionless stream power $\Psi_*=q_*s_*$ with dimensionless storm intensity I_* on a uniform hillslope. The threshold line is derived from a logarithmic scale on both the vertical and horizontal axes, based on values of normalized stream power and storm magnitude in the physical ranges examined herein.

3.4. Discussions and Conclusion

A framework has been developed herein using an enhanced WEPP model that is capable of capturing the integrated effects of space/time-variant resistance on overland flow at the hillslope scale under different types of landscape attributes present in intensively managed landscapes. The framework was validated using observed data from field and laboratory experiments examining the effects of the different landscape attributes.

Using the framework, the implications of the assumption of invariant resistance over space and time on runoff hydrographs were examined for a hillslope in the Walnut Creek Watershed, IA, with isolated roughness elements and vegetation patches. It was found that this type of assumption can lead to discrepancies in the shape and magnitude of runoff hydrographs, with deviations in the peak runoff of up to 65% compared to hydrographs that consider the space/time-variant flow resistance.

The influence of surface roughness on runoff hydrograph characteristics and how these changed with storm magnitude and hillslope gradient was also investigated. Results from the analyses suggest that the conversion of a landscape from vegetation to a bare surface with only grain roughness or a surface with isolated roughness elements has a more profound effect on the runoff hydrograph than the effects of profile curvature. Whereas the change in cover from vegetation to a bare surface resulted in a 133% increase in the peak runoff rate, the maximum change in peak runoff rate due to change in profile curvature was 16%. In IMLs, crop rotations have resulted in landscapes where the soil surface is bare 30 – 75% of the time during the calendar year [*Abaci and Papanicolaou*, 2009]. Since naturally occurring storm events were simulated in this study, the above results provide a quantitative measure of the degree to which management practices can impact runoff, and consequently sediment fluxes, from different hillslopes within an IML watershed over the course of a season. Furthermore, the results also suggest that the use of Best Management Practices (BMPs) such as grassed waterways is likely to have a larger impact on fluxes than practices that modify the landscape through shaping of the hillslope.

The space/time-variant resistance offered by the different landscape attributes was also found to affect hydrograph characteristics such as the peak and modality. The results further suggested that the influence of surface roughness on runoff hydrograph characteristics reduced with increasing storm magnitude and hillslope gradient. This observed trend in hydrograph

characteristics with storm magnitude and hillslope gradient pointed towards the existence of a threshold beyond which the influence of surface roughness on hydrograph characteristics became relatively insignificant. This was examined using the concept of the overland stream power, a single metric that takes into account both runoff rates (storm magnitude) and gradient. Results from simulations covering a series of 1-hr duration storms, with different rainfall intensities on hillslopes with different gradients confirmed the existence of the threshold for the peak stream power (see Figure 3.9). Below the threshold, the peak stream power is dependent on the surface roughness flow resistance, the storm magnitude, and the hillslope gradient. Above the threshold, the peak stream power is governed primarily by storm magnitude and hillslope gradient. In this case, flow resistance from the surface roughness is negligible and so the peak stream power is at its highest possible value. These results for runoff have implications for sediment transport since the peak stream power has been shown to correlate with the sediment yield [e.g. *Dade*, 2012]. One must bear in mind, however, when translating these results to sediment transport, that the actual amount of energy available to mobilize and transport material from the bed surface will depend on how erodible the soil is, and how much of it is exposed and available for mobilization/ transportation. More in-depth studies that consider these factors are needed to determine how the findings in this study translate to sediment and nutrient transport.

Within the context of this study, since the threshold identifies the most dominant variables governing runoff fluxes from the hillslope, a practical benefit is that it can be used as a guide to determine the appropriate model complexity for examining event-based dynamics under different land cover and climatic forcing [e.g. *Woode et al*., 1995; *Blöschl et al*., 2007]. The study of processes and fluxes occurring at a scale below the threshold, i.e. in Zone 1 of Figure 3.10, will have to be based on the space/time-variant resistance representation of surface roughness in order to reveal the causal relationships and feedbacks occurring between the important processes concerned (i.e., a model such as the enhanced WEPP model introduced herein must be used). Beyond the threshold, i.e. Zone 2 of Figure 3.10, examination of flux dynamics may rely on spatially-averaged representation of the hillslope to adequately capture and understand causal relationships and feedbacks (i.e., the original WEPP model or other lumped models can be used in this case). Since the threshold is not static, but dependent on surface roughness, hillslope gradient, and storm event characteristics, it will have to be derived for storms of different return periods and under different roughness and gradients for a

watershed. From these, an envelope of thresholds can then be derived that landscape managers can use as a guide for determining the model complexity to consider when simulating fluxes and designing/evaluating BMPs under different conditions. A lack of consideration of this threshold envelope, especially in cases where lumped models are used, could lead to results that are error prone and have a large degree of uncertainty associated with them.

Another utility of this study pertains to the design of BMPs. *Dermisis et al*. [2010] examined grassed waterways (GWW) of different lengths in an IML in Iowa, and found a threshold length for a GWW to remain effective for a range of representative flows for the region (see Figures 7-10 in their study). This effective threshold length concept has subsequently been recommended in BMP design efforts e.g., in the *Agricultural BMP Handbook for Minnesota* [2012]. The threshold length determined in the *Dermisis et al*. [2010] study corresponds to the stream power threshold identified in this study, as it indicates the point at which the effects of flow magnitude overshadows the effects of vegetation. This is illustrated in Figure 3.11, where we utilize data from their study to plot the dimensionless stream power against dimensionless storm magnitude for a GWW length of 300 m on 2% gradient hillslope (the normalizing factors are based on the data from their study). For reference, we indicate on the figure the event numbers (used in their study) and peak flowrates, Q_{peak}, corresponding to each of the data points.

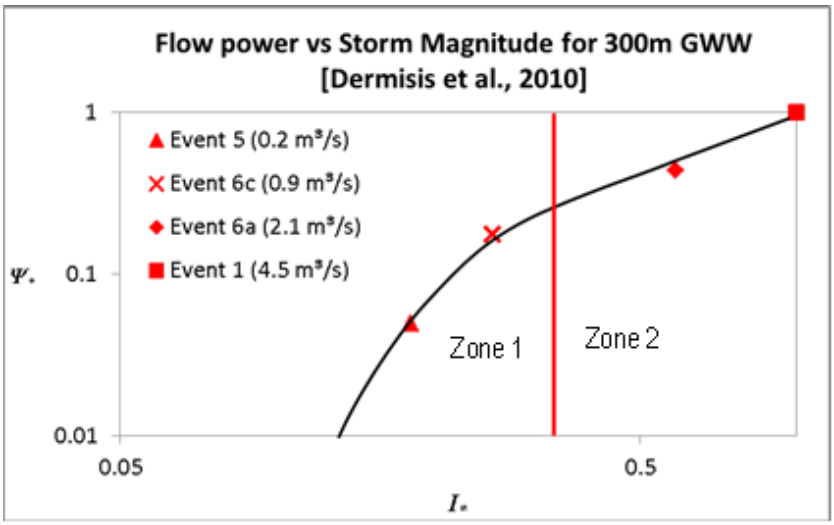

Figure 3.11: Stream power curve for a 300m GWW on a 2% gradient hillslope using data from *Dermisis et al*., [2010]. The event numbers used in the study and their corresponding peak runoff rates are shown in the legend.

The figure clearly shows two stream power zones and suggests that for storms with Q_{peak}'s larger than some value between 0.9-2.1 m^3/s, the storm magnitude plays a more dominant role than the GWW (Zone 2). This is in agreement with the findings shown in Figure 9 of the *Dermisis et al*. [2010] study, where it is seen that the 300 m GWW is only effective up to a peak flowrate of ~1.5 m^3/s. Thus, a practical benefit of this study is the provision of a direct approach with which effective BMP dimensions can be obtained for watershed management. This approach is illustrated in Figure 3.12. For a given watershed or region, a stream power threshold envelope can be developed for the range of storm magnitudes and hillslope gradients present, for different BMP dimensions (GWW length in this case). Then, for each location identified within the watershed where a BMP (GWW) can be deployed, the threshold envelope can be used to determine the appropriate effective BMP dimension (GWW length) using the gradient at the location and design storm magnitude – this step will involve interpolating the appropriate dimension from the threshold and stream power lines. For such an effort, the identification of potential BMP locations could be achieved by considering the spatial distribution of stream power as described in the following paragraph, or using a tool such as the Agricultural Conservation Planning Framework tool [2013].

The stream power concept can also be used to evaluate where on the landscape BMPs may be needed, or how alternative BMPs will perform. A spatial map of the landscape showing the distribution of stream power on the landscape could be examined to determine locations where the stream power exceeds the threshold and mitigation is needed. Corresponding stream power maps could then be created for alternative BMPs to determine how they perform and the economic costs associated with each option. An example of an alternative to GWW is contour farming, which although not examined directly in this study, is also expected to have a larger region of influence than a surface with isolated roughness elements due to the added oriented roughness perpendicular to the flow.

Finally, the numerical approach presented in this study, being a physically-based approach that is validated with measured baseline data for different roughness attributes, can be used for dynamic flow resistance casting (DFRC), where it serves as a "baseline model" for casting the flow resistance in real hillslopes (where all or a combination of roughness attributes are present but measured data are difficult to obtain) in order to isolate and examine the effects of each roughness type on the flow resistance. The main assumption behind this approach is that

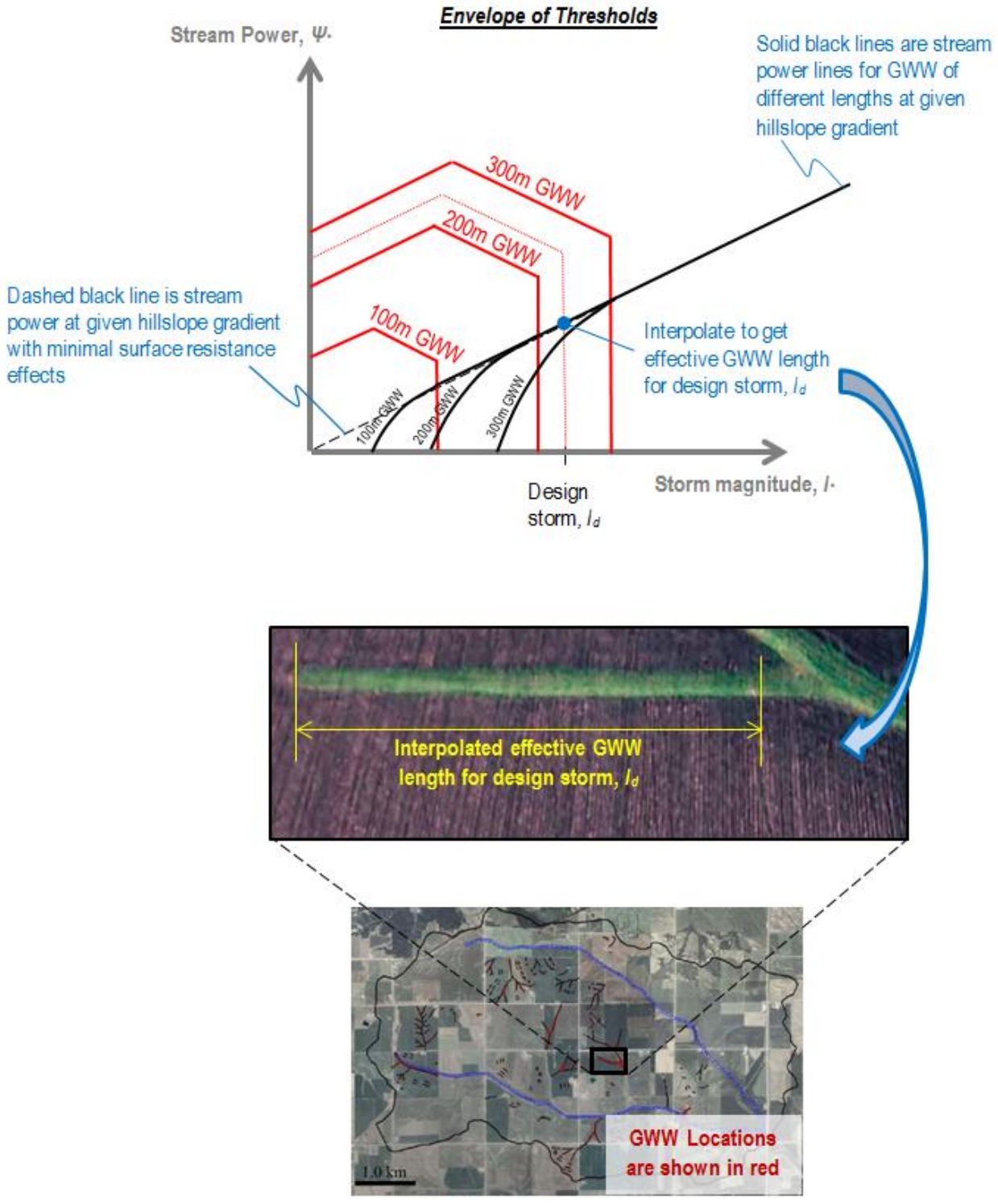

Figure 3.12: Illustration of methodology for determining effective GWW dimensions from stream power threshold envelope.

the space/time-variant friction relationships for grain, form, wave, and vegetation can be extended to the hillslope scale since they have been calibrated and validated with field data albeit at a smaller scale.

It is acknowledged that the assumption that the addition of the space/time-variant friction relationships to the WEPP model assumes that the other underlying WEPP model assumptions are not affected and that the relationships add processes that are currently missing in the original WEPP model, leading to a better resolution of hillslope scale fluxes. It is believed that validating the collective effects herein, using datasets other than what were originally used to develop the relationships (see Section 3.3.1), provides some validation to the approach used in this study.

References

Abaci, O., and A. N. Papanicolaou (2009), Long-term effects of management practices on water-driven soil erosion in an intense agricultural sub-watershed: monitoring and modelling, *Hydrol. Process.*, *23*(19), 2818-2837.

Abban, B., A.N. Papanicolaou, C.P. Giannopoulos, D. Dermisis, K.M. Wacha, C.G. Wilson, and M. Elhakeem (2017), Quantification of change in soil surface roughness at the raindrop detachment zone as a function of rainfall intensity under flatbed preconditions, *Nonlinear Proc. Geoph. Discussions*, DOI: 10.5194/npg-2016-76.

Abrahams A. D. (1998), Discussion: 'Macroscale surface roughness and frictional resistance in overland flow' by DSL Lawrence, *Earth Surf. Processes Landforms, 23*, 857–859.

Abrahams, A. D., and A. J. Parsons (1994), Hydraulics of interrill overland flow on stone-covered desert surfaces, *Catena*, *23*(1), 111-140.

Abrahams A. D., A. J Parsons, and P. J. Hirsch (1992), Field and laboratory studies of resistance to interrill overland flow on semiarid hillslopes, southern Arizona. In *Overland Flow: Hydraulics and Erosion Mechanics*, Parsons AJ, Abrahams AD (eds), UCL Press: London, 1–24.

Borah, D. K., S. N. Prasad, and C. V. Alonso (1980), Kinematic wave routing incorporating shock fitting, *Water Resour. Res.*, *16*(3), 529-541.

Clifford N. J., A. Robert, and K. S. Richards (1992), Estimation of flow resistance in gravel-bed rivers: a physical explanation of the multiplier of roughness length, *Earth Surf. Processes Landforms*, *17*, 111–126.

Costabile, P., C. Costanzo, and F. Macchione (2012), A storm event watershed model for surface runoff based on 2D fully dynamic wave equations, *Hydrol. Process.*, *27*(4), 554-569.

Croley II, T. E. and B. Hunt (1981), Multiple-valued and non-convergent solutions in kinematic cascademodels, J. Hydrol., 49, 121-138.

Dade, W. B. (2012), Transport-limitations on fluvial sediment supply to the sea, *Water Resour. Res.*, *48*, W11601.

Davis, S. F. (1984), TVD finite difference schemes and artificial viscosity (No. 84), National Aeronautics and Space Administration, Langley Research Center.

De Roo, A. P. J., C. G. Wesseling, and C. J. Ritsema (1996), LISEM: A single-event physically based hydrological and soil erosion model for drainage basins. I: Theory, input and output, *Hydrol. Process.*, *10*(8), 1107-1117.

Dermisis, D., O. Abaci, A. N. Papanicolaou, and C. G. Wilson (2010), Evaluating grassed waterway efficiency in southeastern Iowa using WEPP, *Soil Use Manage.*, *26*(2), 183-192.

Escoffier, F.F. and M.B. Boyd (1962), Stability aspects of flow in open channels, *J. Hydr. Div., ASCE*, *88*(6), 145-166.

Flanagan, D. C., and M. A. Nearing (eds.) (1995), USDA Water Erosion Prediction Project: Hillslope Profile and Watershed Model Documentation, NSERL Report No. 10, USDA-ARS National Soil Erosion Research Laboratory, West Lafayette, IN, USA.

Flanagan D. C., J. E. Gilley, and T. G. Franti (2007), Water Erosion Prediction Project (WEPP): development history, model capabilities and future enhancements, *Trans. ASABE*, *50*(5), 1603–1612.

Garcia-Navarro, P., F. Alcrudo, and J. M. Saviron (1992), 1-D open channel flow simulation using TVD-MacCormack scheme, *J. Hydraul. Eng.*, *118*(10), 1359–1372, doi:10.1061/(ASCE)0733-9429(1992)118:10 (1359).

Gilley, J. E., and M. A. Weltz (1995), Hydraulics of overland flow, *USDA-Water Erosion Prediction Project: Hillslope profile and watershed model documentation, Rep*, *10*, 10-1.

Gómez, J. A., and M. A. Nearing (2005), Runoff and sediment losses from rough and smooth soil surfaces in a laboratory experiment, *Catena*, *59*(3), 253-266.

Govindaraju, R. S., S. E. Jones, and M. L. Kavvas (1988), On the diffusion wave model for overland flow: 1. Solution for steep slopes, *Water Resour. Res.*, *24*(5), 734–744, doi:10.1029/WR024i005p00734.

Hairsine, S. Y., and J. Y. Parlange (1986), Kinematic shock waves on curved surfaces and application to the cascade approximation, *J. Hydrol.*, *87*(1), 187-200.

Hirsch P. J. (1996), Hydraulic Resistance to Overland Flow on Semiarid Hillslopes: A Physical Simulation, PhD dissertation, State University of New York at Buffalo.

Hu, S., and A. D. Abrahams (2006). Partitioning resistance to overland flow on rough mobile beds. *Earth Surf. Processes Landforms*, *31*(10), 1280-1291.

Huang, J. K., and K. T. Lee (2009), Influences of spatially heterogeneous roughness on flow hydrographs, *Adv. Water Resour.*, *32*(11), 1580-1587.

Iwagaki, Y. (1955), Fundamental studies on runoff analysis by characteristics, Bull. 10, 25 pp., Disaster Prev. Res. Inst., Kyoto Univ., Kyoto, Japan.

Jirka, G. H., and W. S. Uijttewaal (2004), Shallow flows: a definition, Shallow flows, 3-11.

Jomaa, S., D. A. Barry, B. C. P. Heng, A. Brovelli, G. C. Sander, and J.-Y. Parlange (2012), Influence of rock fragment coverage on soil erosion and hydrological response: Laboratory flume experiments and modeling, *Water Resour. Res.*, *48*(5), W05535, doi:10.1029/2011WR011255.

Julien, P. Y., and G. E. Moglen (1990), Similarity and length scale for spatially varied overland flow, *Water Resour. Res.*, *26*(8), 1819-1832.

Katul, G. G., D. Poggi, and L. Ridolfi (2011), A flow resistance model for assessing the impact of vegetation on flood routing mechanics, *Water Resour. Res.*, *47*(8), W08533, doi:10.1029/2010WR010278. .

Kibler, D. F., and D. A. Woolhiser(1972), Mathematical properties of the kinematic cascade, *J. Hydrol.*, *15*, 131-147.

Kirkby, M. (1988), Hillslope runoff processes and models, *J. Hydrol.*, *100*(1), 315-339.

Lacey, R. W. J., and A. G. Roy (2008), Fine-scale characterization of the turbulent shear layer of an instream pebble cluster, *J. Hydraul. Eng.*, *134*(7), 925-936.

Lal, R., and B. A. Stewart (1994), *Soil processes and water quality*, CRC/ Lewis Publishers, Boca Raton, FL, 398 pp.

Lawrence, D. S. L. (1997), Macroscale surface roughness and frictional resistance in overland flow, *Earth Surf. Processes Landforms*, *22*(4), 365-382.

Lawrence, D. S. L. (2000), Hydraulic resistance in overland flow during partial and marginal surface inundation: Experimental observations and modeling, *Water Resour. Res.*, *36*(8), 2381-2393.

Ligget, J. A. (1975), Unsteady flow in open channels, *Water Resour. Publ.*, Fort Collins, Colorado.

Liu, Q., and V. Singh (2004), Effect of microtopography, slope length and gradient, and vegetative cover on overland flow through simulation, *J. Hydrol. Eng.*, 10.1061/(ASCE)1084-0699(2004)9:5(375), 375-382.

Liu, Q., L. Chen, J. C. Li, and V. Singh (2005), Roll waves in overland flow, *J. Hydrol. Eng.*, 10(2), 110-117.

Loperfido, J. V., C. L. Just, A. N. Papanicolaou, and J. L. Schnoor (2010), In situ sensing to understand diel turbidity cycles, suspended solids, and nutrient transport in Clear Creek, Iowa, *Water Resour. Res.*, *46*(6), W06525.

Luo, W., and J. M. Harlin (2003), A theoretical travel time based on watershed hypsometry, *J. Am. Water Resour. Assoc. 39*(4), 785-792.

MacCormack, R. W. (1969), The effect of viscosity in hypervelocity impact cratering, in Frontiers of Computational Fluid Dynamics, edited by D. A. Caughey and M. M. Hafez, pp. 27–44, Am. Inst. of Aeronaut. and Astronaut., Cincinnati, Ohio.

MacCormack, R. W. (1985), Current status of numerical solutions of the Navier-Stokes equations, *AIAA Paper*, 85–32.

Morris, E. M., and D. A. Woolhiser (1980), Unsteady One-Dimensional Flow Over a Plane: Partial Equilibrium and Recession Hydrographs, *Water Resour. Res., 16*(2), 355-360.

Miller, J.E. (1984), Basic concepts of kinematic-wave models, US Geol. Surv. Prof. Pap., 1302

Mingham, C. G., D. M. Causon, and D. M. Ingram (2001), A TVD-MacCormack scheme for transcritical flow, *Proceedings of the ICE-Water and Maritime Engineering*, *148*(3), 167-175.

Nash, J., and J. V. Sutcliffe (1970), River flow forecasting through conceptual models part I—A discussion of principles, *J. Hydrol., 10*(3), 282-290.

Neibling, W. H., and E. E. Alberts(1979), Composition and yield of soil particles transported through sod strips, *American Society of Agricultural Engineers Paper*, 79-2065.

Nikora, V., I. McEwan, S. McLean, S. Coleman, D. Pokrajac, and R. Walters (2007), Double-averaging concept for rough-bed open-channel and overland flows: Theoretical background, *J. Hydraul. Eng.*, 10.1061/(ASCE)0733-9429(2007)133:8(873),873-883.

Papanicolaou, A. N., J. T. Sanford, D. C. Dermisis, and G. A. Mancilla (2010), A 1-D morphodynamic model for rill erosion, *Water Resour. Res., 46*(9), W09541, doi:10.1029/2009WR008486.

Papanicolaou, A. N., D. C. Dermisis, and M. Elhakeem (2011), Investigating the role of clasts on the movement of sand in gravel bed rivers, *J. Hydraul. Eng. 137*(9), 871-883.

Papanicolaou, A.N. (2012), Aspects of Secondary Flow in Open Channels: A Critical Literature Review. In: Church, M., P.M. Biron, A.G. Roy (eds). Gravel-Bed Rivers: Processes, Tools, Environments. John Wiley & Sons, Ltd, Chichester, UK. doi: 10.1002/9781119952497.ch3

Ponce, V. M., R. M. Li, and D. B. Simons (1978), Applicability of kinematic and diffusion models, *J. Hydr. Div., ASCE, 104*(3), 353–360.

Rieke-Zapp, D. H., and M. A. Nearing (2005), Slope shape effects on erosion, *Soil Sci. Soc. Am. J., 69*(5), 1463-1471.

Romkens, M. J. M., and J. Y. Wang (1986), Effect of tillage on surface roughness, *Trans. ASAE (Am Soc Agric Eng), 29*.

Schmid, B. H. (1990), On kinematic cascades: derivation of a generalized shock formation criterion. *J. Hydraul. Res., 28*(3), 331-340.

Shen, H. W., and R. M. Li (1973), Rainfall effect on sheet flow over smooth surface, *J. Hydraul. Div.*, *99*(5), 771-792.

Singh, V. P. (1994), Accuracy of kinematic wave and diffusion wave approximations for space independent flows, *Hydrol. Process*., *8*, 45–62, doi: 10.1002/hyp.336008010.

Singh, V. P. (1997), *Kinematic wave modeling in water resources: Environmental hydrology*, New York, Wiley.

Singh, V. P. (2001), Kinematic wave modelling in water resources: a historical perspective, *Hydrol. Process.*, *15*(4), 671-706.

Singh, V. P. (2017), Kinematic wave theory of overland flow, *Water Resour Manage*, (2017) 31:3147–3160.

Thompson, S., G. Katul, A. Konings, and L. Ridolfi (2011), Unsteady overland flow on flat surfaces induced by spatial permeability contrasts, *Adv. Water Res., 34*(8), 1049-1058.

Tseng, M. (2010), Kinematic wave computation using an efficient implicit method, *J. Hydroinform., 12*(3), 329-338.

Wang, M., and A. T. Hjelmfelt (1998), DEM based overland flow routing model, *J. Hydrol. Eng.*, *3*(1), 1-8.

Wicks, J. M., and J. C. Bathurst (1996), SHESED: a physically based, distributed erosion and sediment yield component for the SHE hydrological modelling system, *J. Hydrol.*, *175*(1), 213-238.

Woolhiser, D. A. (1975), Simulation of unsteady overland flow, *Unsteady flow in open channels*, *2*, 485-508.

Woolhiser, D. A., R. E. Smith, and D. C. Goodrich (1989), *KINEROS: a kinematic runoff and erosion model: documentation and user manual*, US Department of Agriculture, Agricultural Research Service.

Wu, Y. H., V. Yevjevich, and D. A. Woolhiser (1978), *Effects of surface roughness and its spatial distribution on runoff hydrographs*, Colorado State University.

Young, R. A., and C. K. Mutchler (1969), Effect of slope shape on erosion and runoff, *Trans. ASAE (Am Soc Agric Eng)*, *12*, 231-239.

Zhang, W., and T. W. Cundy (1989), Modeling of two-dimensional overland flow, *Water Resour. Res.*, *25*(9), 2019-2035.

Appendix A. Kinematic Wave Equations

For simulating overland flow, WEPP utilizes the 1-D kinematic wave approximation (KWA), which is considered adequate when the gravity forces predominate over pressure and inertia forces [e.g., *Woolhiser et al.*, 1989; *Julien and Moglen*, 1990; *Flanagan and Nearing*, 1995; *De Roo et al.*, 1996; *Singh*, 1997; *Singh*, 2001]. The 1-D KWA includes the continuity equation for flow over a planar surface (equation (1)) and a simplified version of the momentum equation (equation (2)), expressed as follows:

$$\frac{\partial h}{\partial t} + \frac{\partial q}{\partial x} = v = r - i_f \tag{A1}$$

$$q = \alpha h^m \tag{A2}$$

where, q is the flow discharge per unit width ($m^3/s/m$); h is the flow depth (m); x and t denote longitudinal distance (m) and time (s), respectively; r is the rainfall rate (m/s); i_f is the infiltration rate (m/s); v is the rainfall excess rate (m/s); m is a depth-discharge exponent equal to 1.5; and $\alpha = CS_o^{0.5}$ is the kinematic depth-discharge coefficient ($m^{1/2}/s$), where C denotes the Chezy roughness coefficient ($m^{1/2}/s$), and S_o denotes the slope of the planar surface (m/m). The Chezy coefficient is determined as $C = (8g/f_{eq})^{0.5}$, where g is the acceleration due to gravity (m/s^2), and f_{eq} is an equivalent Darcy-Weisbach friction factor (-) for the equivalent plane that accounts for both skin and form resistance, but in static (space/time-invariant) manner. The static f_{eq} assumption was mainly been made for computational expediency in the early development stages when computational power was limited [*J. E. Gilley*, personal communication, 2011].

Chapter 4

Coupling WEPP and 3ST1D models for improved prediction of flow and sediment transport at watershed scales

Abstract

Watershed modeling is a key component of watershed management that involves the simulation of hydrological and fluvial processes for predicting flow and sediment transport within a watershed. For practical purposes, most numerical models have been developed to simulate either runoff and soil erosion processes on uplands alone, or flow and sediment transport processes within channels that are isolated from the surrounding land. This lack of connectivity between the upland and in-stream processes introduces significant error in water volume and sediment yield estimates at watershed scales. The objective of this study is to develop a coupled model that bridges upland and in-stream processes, allowing more accurate estimates of water volume and sediment yield to be made at the watershed scale. The proposed coupled model utilizes the well-established physically based, distributed parameter Water Erosion Prediction Project (WEPP) model for simulating upland processes and the 3ST1D hydrodynamic and sediment transport model for simulating in-stream processes. The coupled model is applied to an agricultural watershed located in east-central Iowa in the United States. Model verification exercises indicate that the proposed coupled model can adequately simulate flow and sediment transport from the uplands to the outlet of a watershed.

4.1. Introduction

Soil erosion is a major environmental threat to the sustainability and productive capacity of agriculture. It is estimated that 90% of U.S. cropland is losing soil above the sustainable rate (i.e., the maximum rate of erosion that will not cause a reduction in long-term productivity). Moreover, the annual cost of erosion related problems in the United States is estimated to be ~ $44 billion [*Pimentel et al*., 1995]. In addition to the loss of arable lands, soil erosion drastically lowers water quality as surface runoff and erosion enhance transport of dissolved chemicals and sediment borne pollutants from the upland areas into natural streams [*Lal and Stewart*, 1994].

In response to soil degradation and decreasing water quality, various numerical models have been developed over the past decades to simulate hydrological and soil erosion processes for soil and water conservation planning, design, development, operation, and management [*Singh and Woolhiser*, 2002]. A considerable amount of work has been performed by researchers to understand and simulate these processes at the hillslope scale (i.e., “small” scale

processes in the upland areas). Yet, the challenge remains to accurately simulate these processes at the watershed scale (i.e., "large" scale processes within the watershed), where water and sediment are being transported from their original location in the upland areas towards the drainage network (i.e., streams, rivers) and through the network to the watershed outlet [*Jetten et al*., 2003]. Traditionally, most of the numerical models have been developed to simulate either: (a) rainfall-runoff and soil erosion processes in upland areas without providing an estimation of the flow and sediment transport from the drainage network to the watershed outlet; or (b) flow routing and sediment transport processes within the drainage network assuming that the drainage network is isolated from its surrounding land.

The separation/decomposition of the watershed scale processes into upland and in-stream processes may have some practical merits for the purposes of simulation [*Wu,* 2008]. However, since these two domains (upland and in-stream) are highly interrelated, the lack of connectivity between the upland erosion and the in-stream channel processes introduces significant error in the water volume and sediment yield estimates along the channel network [*Conroy et al*., 2006; *Wu*, 2008]. For example, accelerated upland erosion caused by anthropogenic activities (e.g., deforestation, mining) may increase the sediment yield to the channels, resulting in excess sedimentation and reduction of the transport capacity of the channels. The failure to account for this interaction will undoubtedly result in miscalculation of the simulated flow and sediment transport rates within the channels and the watershed as a whole.

Recent efforts to integrate upland and channel models include work by *Conroy et al*. [2006] who described a prototype modeling system using the Water Erosion Prediction Project (WEPP) [*Flanagan and Nearing*, 1995] and the National Center for Computational Hydrodynamics and Engineering One-Dimensional hydrodynamic and sediment transport model (CCHE1D) [*Wu and Vieira*, 2002] for assessing forest management-related erosion by predicting sediment transport within a watershed. A key limitation of the *Conroy et al*. [2006] study was that CCHE1D could only handle localized supercritical and transcritical flows without hydraulic jumps [*Wu and Vieira*, 2002]. *Wang et al*. [2010] also implemented hydrologic and hydraulic channel flow-routing routines in WEPP, utilizing the Muskingum-Cunge and the kinematic-wave methods, respectively. Both routing methods exhibit some important limitations. The Muskingum-Cunge method cannot account for backwater effects and may not provide accurate results when rapidly rising hydrographs are routed through flat channel sections [*USACE*, 1994].

The kinematic-wave method includes only the gravitational and frictional forces and neglects the inertial and pressure forces. Consequently, the kinematic-wave method is limited to flow conditions that do not demonstrate significant hydrograph attenuation and cannot be used where backwater condition and flow reversal occur [*USACE*, 1994].

This study develops a coupled upland-instream model for simulating fluxes at the watershed scale, taking into consideration all the relevant flow and sediment transport processes in both the upland and instream domains. The coupled model evaluates the transport of water and sediment from: (i) the hills to the main channels using a process-based hydrology and upland erosion prediction model; and (ii) the main channels to the watershed outlet using an advanced in-stream hydrodynamic and sediment transport model that overcomes limitations of previously developed models. The advanced in-stream model is be able to (a) account for the role of turbulence on sediment movement (b) handle the transport of both cohesive and non-cohesive sediments, and (c) accurately simulate backwater effects, transcritical flows along channel reaches, and the formation and location of hydraulic jumps. The coupled model is verified by: (i) testing its ability to route hydrographs through a benchmark hypothetical channel network; and (ii) applying it to route water and sediment fluxes from a small agricultural sub-watershed in the US Midwest and comparing the results against two observed sediment rating curves, one based on data at the sub-watershed outlet and the other based on global data [Dade, 2012].

4.2. Methodology

4.2.1. Upland erosion model -WEPP

WEPP is a well-established physically based, distributed parameter model developed by the US Department of Agriculture-Agricultural Research Service (USDA-ARS) to simulate rainfall-runoff and soil erosion processes for virtually any type of landscape management including rural, urban, cropland, rangeland, construction sites, and roads [*Flanagan and Nearing*, 1995]. WEPP uses fundamental physical equations governing overland flow hydraulics, infiltration, evapotranspiration, plant growth, erosion and deposition processes. Consequently, WEPP allows a more accurate representation of the processes and their interactions than empirically based models. Further, being a distributed parameter model, WEPP can account for the spatial variability of erosion by allowing the heterogeneity of soil, land use and topography to be adequately represented (i.e., a hillslope profile can be divided up to 10 sub-units) [*Flanagan*

and Livingston, 1995]. WEPP is applicable to hillslopes and small watersheds. However, its application at the watershed scale has the following limitations: (i) it does not explicitly include hydrodynamic channel network flood flow routing; and (ii) the sediment transport capacity equation the model uses for determining erosion and deposition within channels is mainly applicable for rill and interrill areas [*Conroy et al*., 2006]. As a result, WEPP does not provide an accurate estimation of the water volume and sediment rates in the main channels.

Recently, *Papanicolaou et al*. [2018] and *Papanicolaou et al*. [2015] have implemented updates to the overland flow and sediment transport components to the original WEPP (Version 2012.8; *Flanagan et al*., 2007) to account for space/time variant resistance effects, and preferential mobilization and transport of material of different size fractions from and to the soil active layer. The current terrestrial component of the enhanced WEPP model considers either concentrated flow downslope with lateral supply from interrill areas or unidirectional flow downslope representative of either a planar flow or flow along a contoured surface. These are depicted in Figure 4.1 below for some representative land cover types in intensively managed landscapes. For the first scenario of concentrated flow with lateral interrill supply, the flow within the concentrated pathway is simulated with the 1D St. Venant's equations [*Papanicolaou et al*., 2010], whereas the lateral supply is simulated with the 2D Diffusive wave model [*Lopez-Barrera et al*., 2012]. The second scenario of unidirectional flow downslope is also simulated with the 1D St. Venant's equations. In all cases, infiltration and rainfall excess calculations are performed using WEPP's modified Green-Ampt Mein-Larson infiltration model. The governing equations for flow are summarized as follows:

1D St. Venants:

$$\frac{\partial A}{\partial t} + \frac{\partial Q}{\partial x} = r_e + q_{li} \tag{1a}$$

$$\frac{\partial Q}{\partial t} + \frac{\partial}{\partial x}\left(\frac{Q^2}{A}\right) = -g\frac{\partial I_1}{\partial x} + gI_2 + gA(S_o - S_f) \tag{1b}$$

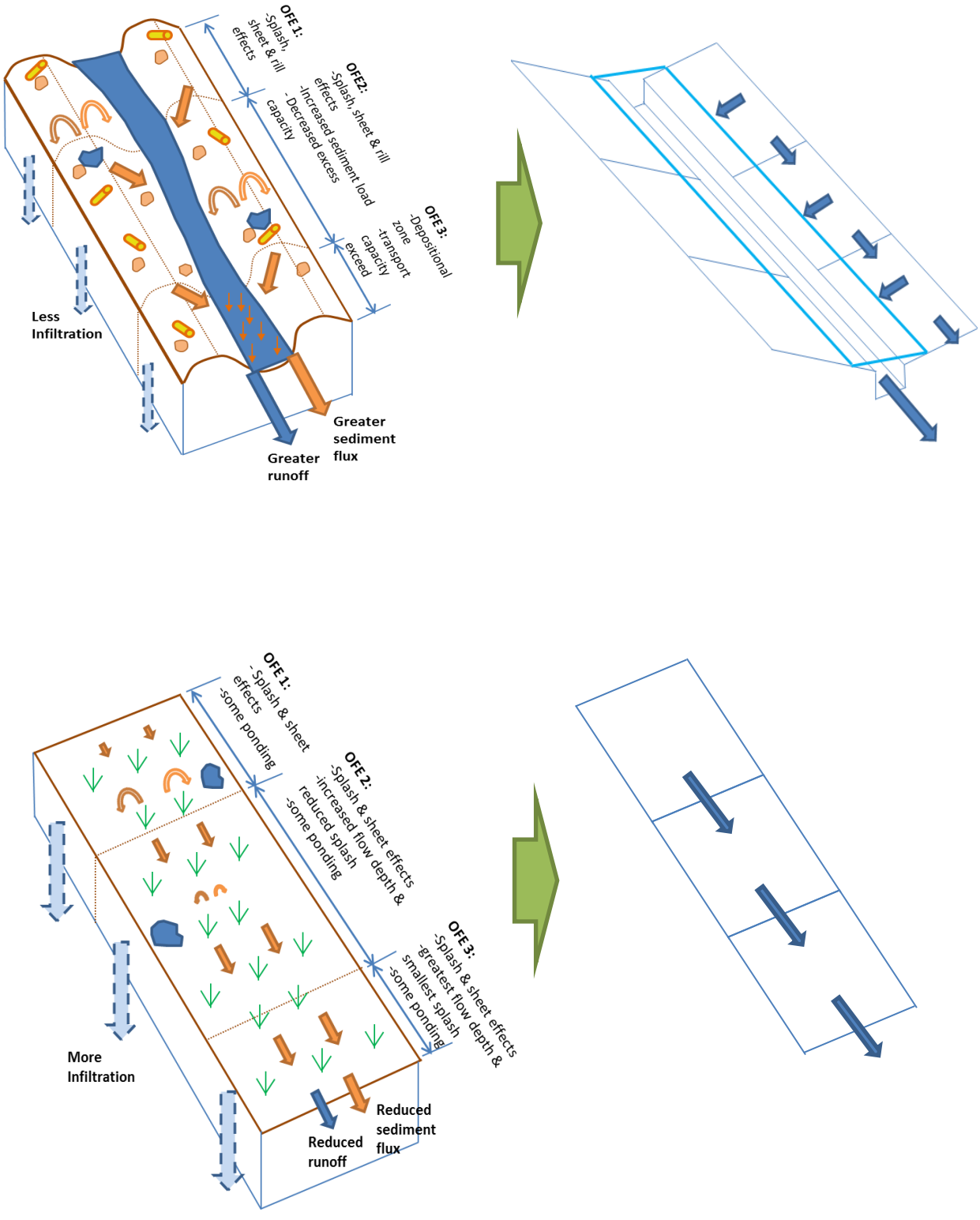

Figure 4.1: Representation of flow pathway conceptualization in coupled modeling framework

2D Diffusive Wave:

$$\frac{\partial h}{\partial t} + \frac{\partial hu}{\partial x} + \frac{\partial hv}{\partial y} = r_e \tag{2a}$$

$$\frac{\partial}{\partial x}\left(g\frac{h^2}{2}\right) = gh(S_{ox} - S_{fx}) \tag{2b}$$

$$\frac{\partial}{\partial y}\left(g\frac{h^2}{2}\right) = gh(S_{oy} - S_{fy}) \tag{2c}$$

where A is the flow cross-sectional area, Q is the cross-sectional flow discharge, r_e is the rainfall excess rate, q_{li} is the lateral flow supply from interrill areas, I_1 is a term that accounts for the hydrostatic forcing, I_2 accounts for changes in the cross-sectional width, S_o is the bed slope, S_f is the friction slope, *x, y* and *t* are the spatial and temporal coordinates, *h* is the flow depth, *u* and *v* are the depth averaged flow velocities direction in the *x* and *y* directions, respectively, and *g* is the acceleration due to gravity.

In both scenarios, the sediment continuity equation is used to simulate sediment fluxes on the landscape [*Tayfur et al*., 2002; *Wu*, 2002]. Following observations by various investigators, a transport capacity formula is not used for overland flow, since the transport capacity has been found to be non-unique for a given soil type, slope and flow rate [*Polyakov et al*., 2003; *Wainwright et al*., 2015]. The study follows the approach of *Sanders et al*. [2007] and *Cao et al*., [2016], and computes erosion and deposition separately, assuming that they are independent concurrent processes, allowing the "transport capacity" to evolve naturally as an outcome of the balance between the two processes. The sediment continuity relationships solved can be summarized as follows:

1D Sediment Continuity

$$\frac{\partial hC}{\partial t} + \frac{\partial uhC}{\partial x} = q_{lc} + E - D \tag{3}$$

2D Sediment Continuity

$$\frac{\partial hC}{\partial t} + \frac{\partial uhC}{\partial x} + \frac{\partial vhC}{\partial y} = E - D \tag{4}$$

where C is the depth-averaged sediment concentration, q_{lc} is the lateral sediment flux from interrill areas, E is the erosion from the soil active layer, and D is the deposition to the soil active layer. E is computed as the sum of rain splash erosion and shear-driven erosion using the concepts presented in *Foster et al*. [1995], *Papanicolaou et al*. [2015]. Likewise *D* is estimated as a function of the sediment concentration and particle fall velocity [*Flanagan and Nearing*, 2000; *Papanicolaou et al*., 2015].

4.2.2. In-stream hydrodynamic and sediment transport model – 3ST1D

Within the stream network, the 3ST1D model is used to route flow along each channel, which receives contributions from terrestrial sources. 3ST1D is a one-dimensional (1-D) numerical model developed by *Papanicolaou et al*. [2004] for simulating unsteady flow and sediment transport in both steep and mild streams. The input files of 3ST1D, including the boundary and initial conditions, grain size distribution and cross-sectional data, were modified to read basic output data from the WEPP hillslope simulations, such as runoff, storm duration and soil loss. The coupling of the two models is illustrated in Figure 4.2.

The hydrodynamic component of 3ST1D is based on the unsteady form of the 1-D full St. Venant continuity and momentum equations (dynamic wave model), respectively:

1D St. Venants

$$\frac{\partial A}{\partial t} + \frac{\partial Q}{\partial x} = q_{lt} \tag{5a}$$

$$\frac{\partial Q}{\partial t} + \frac{\partial}{\partial x}\left(\frac{Q^2}{A}\right) = -g\frac{\partial I_1}{\partial x} + gI_2 + gA(S_o - S_f) \tag{5b}$$

where A is the flow cross-sectional area, Q is the cross-sectional flow discharge, q_{lt} is the lateral flow supply from terrestrial sources, I_1 is a term that accounts for the hydrostatic forcing, I_2 accounts for changes in the cross-sectional width, S_o is the bed slope, S_f is the friction slope, *x*, and *t* are the spatial and temporal coordinates, *h* is the flow depth, *u* is the depth averaged flow velocity, and g is the acceleration due to gravity.

A 1D advective-dispersive equation is used route sediment fluxes, where the source contributions are from terrestrial, bank and bed sources. This is expressed as follows:

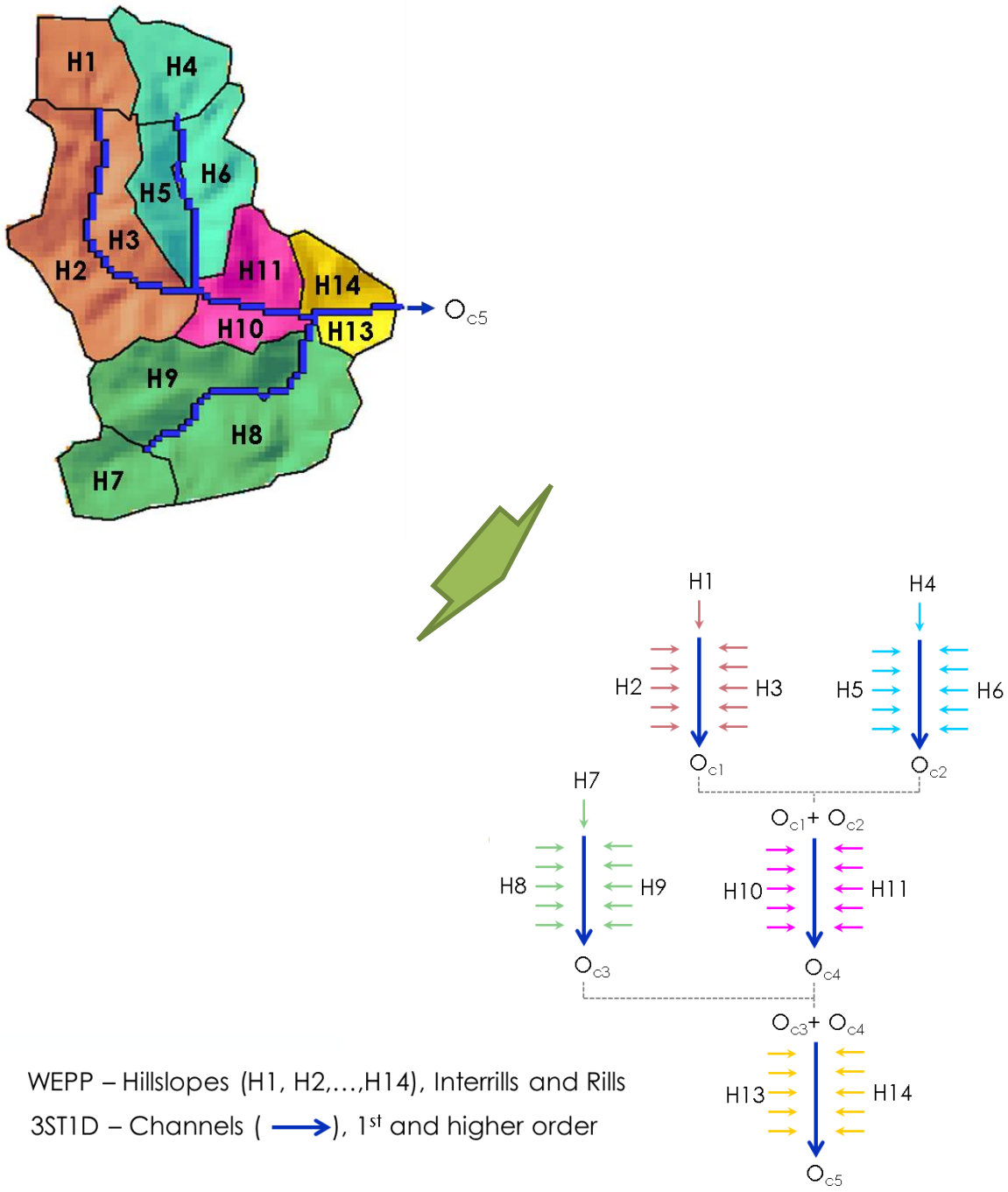

Figure 4.2: Depiction of WEPP-3ST1D. Each hillslope is first simulated with WEPP, then terrestrial fluxes are passed on to the 3ST1D network model where they are routed along with instream contributions to the watershed outlet.

1D Sediment Continuity

$$\frac{\partial hC}{\partial t} + \frac{\partial uhC}{\partial x} = \frac{\partial}{\partial x}\left(K\frac{\partial hC}{\partial x}\right) + q_{ltc} + E - D \quad (6)$$

where C is the depth-averaged sediment concentration, K is the dispersion coefficient, q_{ltc} is the lateral sediment flux from terrestrial sources, E is the eroded material from the soil active layer and banks, and D is the deposition to the soil active layer [*Papanicolaou et al*., 2004; *Papanicolaou et al*., 2015; *Sutarto et al*., 2014].

Junctions in 3ST1D are treated using mass continuity and energy or momentum conservation. Prevailing flow conditions dictate which equations are solved to obtain the key variables at a new time step. Sub-critical flows through a junction are simulated by either approximating the energy equation with stage equality across the branches [*Akan and Yen*, 1981], or by utilizing a model which applies momentum conservation principles [*Shabayek et al*., 2002]. *Kesserwani et al*. [2008a] found that the stage equality approximation was adequate for resolving flows with low Froude numbers whilst those with high Froude numbers were best simulated using momentum conservation principles. A user-specified threshold Froude number is thus used to determine which model to apply during simulations. Supercritical flows are treated using the *Kesserwani et al*. [2008b] approach based on mass and momentum conservation. In all cases, the method of characteristics is used to provide the extra equations needed to close the system.

4.2.3. Active Layer Updates

The sediment transport equations described above are solved for different size fractions as described in *Papanicolaou et al*. [2011] and *Papanicolaou et al*. [2015]. The active layer concept employed in those studies is utilized herein to simulate updates to the active layer due to preferential mobilization, transport, and deposition of sediment of different size fractions within both the terrestrial and instream domains.

4.2.4. Numerical Schemes

Total variation diminishing (TVD) and Gudnov numerical schemes have been employed to solve the governing equations presented above. The reader is referred to *Papanicolaou et al*.

[2011], [*Lopez-Barrera et al*., 2012], and *Papanicolaou et al*. [2018] for a more detailed description of the discretization and solution methods of these schemes.

4.3. Model Verification

The performance of the enhanced WEPP model in simulating terrestrial fluxes of water and sediment of different size fractions has been verified by *Papanicolaou* [2018] and *Papanicolaou et al*. [2015], respectively. Emphasis in this section is, thus, placed on verification of the model coupling and the simulation of fluxes through the network. This section first verifies the model's ability to simulate boundary water fluxes and backwater effects through the channel network. Next, it verifies the WEPP-3ST1D coupling and the model's ability to simulate lateral and upstream terrestrial water fluxes through the network. Finally, the model's ability to simulate sediment fluxes from the various watershed sources to the outlet is examined

4.3.1. Verification of flow discharge routing through channel network

To verify the channel network model, it is applied to route hypothetical hydrographs through an artificial channel network. The example used is adopted from work by *Akan and Yen* [1981] and includes a network of six channels and two junctions (Figure 4.3). This example has also been used by *Venkata Reddy et al*. [2011] for verification purposes. Figure 4.3 provides a sketch of the channel network and Table 4.1 summarizes the properties of the individual channels.

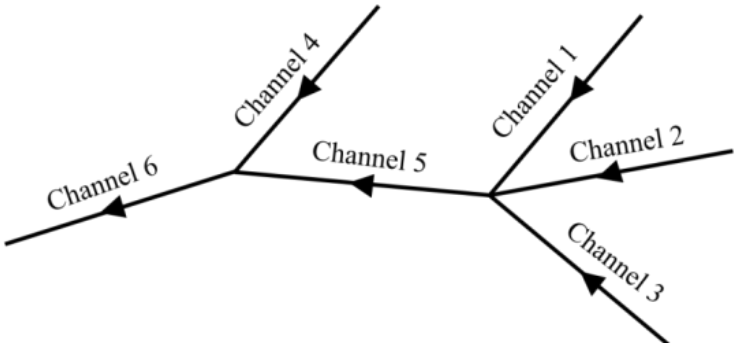

Figure 4.3: The hypothetical channel network used to verify the network model proposed by *Akan and Yen* [1981]

Table 4.1: Properties of the channel network

Channel number	Length (m)	Slope	Width (m)	Manning's n
1	600	0.005	5	0.0138
2	600	0.005	5	0.0207
3	600	0.005	5	0.0207
4	600	0.005	5	0.0138
5	600	0.001	8	0.0141
6	600	0.001	10	0.0125

All channels are assumed to have rectangular cross-sections. The simulation is performed for the two sets of upstream inflow hydrographs shown in Figure 4.4a and Figure 4.5a. The initial condition for both cases is a steady flow condition corresponding to a discharge of 3 m^3/s in channels 1 and 4, 2 m^3/s in channels 2 and 3, 7 m^3/s in channel 5, and 10 m^3/s in channel 6. The downstream boundary condition at the exit of channel 6 is established assuming uniform flow conditions.

Figure 4.4b provides a comparison of the simulated hydrographs at the outlet of channel 6 using the TVD MacCormack scheme (used in 3ST1D) and the four-point implicit finite difference scheme (adopted by *Akan and Yen* [1981]) for solving the full St. Venant equations. The comparison shows that there is a good agreement between the two schemes. The peak discharge and runoff volume using the TVD MacCormack scheme are ~ 4 % and ~ 1 % higher, respectively, than the ones determined from the four-point implicit scheme, whereas the time to peak is ~ 10 % lower.

Along the same lines, Figure 4.4c illustrates a comparison of the simulated hydrographs at the outlet of channels 2 and 3 using the aforementioned methods. Figure 4.4c illustrates the backwater effects occurring at the outlet of channels 2 and 3. According to *Akan and Yen* [1981], although a steady state condition was applied in channels 2 and 3 throughout the duration of the simulation (see the inflow hydrograph in Figure 4.3a), the flood wave traveling through channel 1 raises the water elevation in the junction where the channels 1, 2, and 3 join. Consequently, the flood wave propagates upstream the channels 2 and 3, reducing the flow discharge (see Figure 4.4c between 0 – 11 min). As the backwater effects reduce with time, the discharge will start increasing until it gets back to the steady state condition (see Figure 4.4c between 11 – 35 min). It is evident that both numerical schemes can capture the backwater effects.

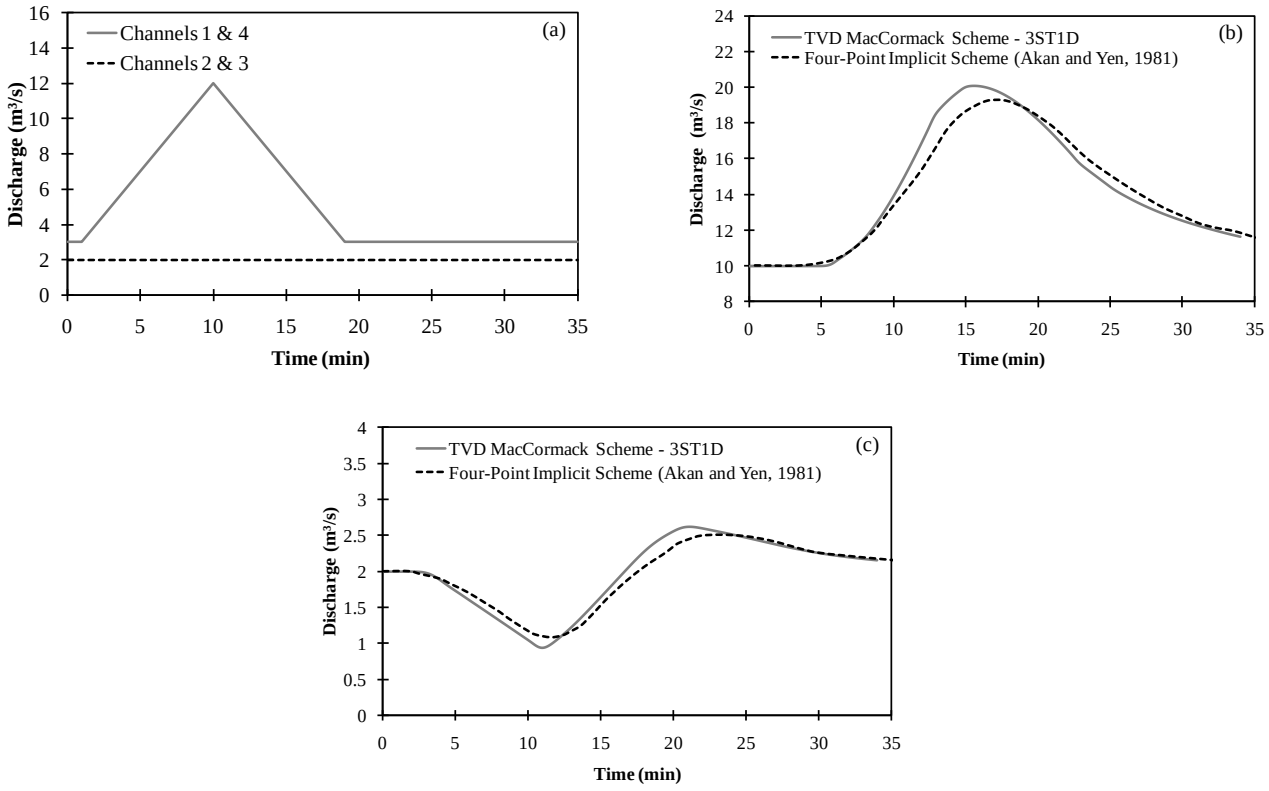

Figure 4.4: (a) The hypothetical inflow hydrograph for the four channels (case I); Comparison of the simulated outflow hydrograph between the TVD MacCormack (3ST1D) and four-point implicit (Akan and Yen 1981) numerical schemes from (b) channel 6 and (c) channels 2 and 3

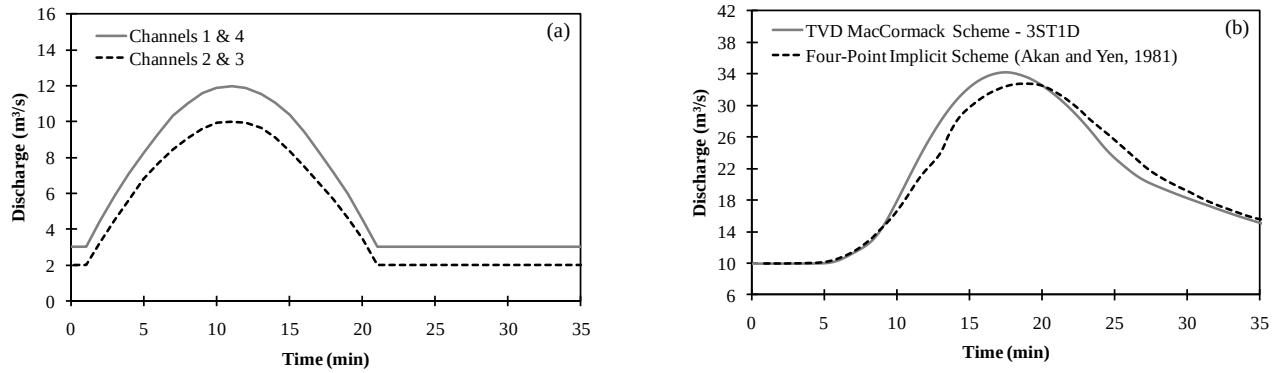

Figure 4.5: (a) The hypothetical inflow hydrograph for the four channels (case II); (b) Comparison of the simulated outflow hydrograph from channel 6 between the TVD MacCormack (3ST1D) and four-point implicit (Akan and Yen, 1981) numerical schemes

Figure 4.5b compares the hydrographs simulated with the two numerical schemes at the outlet of channel 6 for the bell-shaped inflow hydrographs presented in Figure 4.5a. In this case the peak discharge and runoff volume using the TVD MacCormack scheme are ~ 5 % and ~ 2 % higher, respectively, than the ones determined with the four-point implicit scheme, whereas the time to peak is ~ 7 % shorter.

4.3.2. Verification of terrestrial-instream coupling of water fluxes

The proposed coupled model is applied to a 4.6 km² portion of the South Amana Sub-watershed (SASW) located in east-central Iowa in the United States. The SASW, located at the headwaters of the Clear Creek Watershed system, has been reported to have high erosion rates due to the presence of highly erodible soils, steep gradients and intensive agriculture [*Abaci and Papanicolaou*, 2009]. The study site has elevations ranging from 802 to 900 ft above mean sea level (Figure 4.6a), and slopes varying between 0.2 – 40 % (Figure 4.6b). Three soil types are present, namely Tama, Colo, and Muscatine (Figure 4.6c). Of these, Tama is the most prominent, covering over 91 % of the site whilst Colo and Muscatine cover only 2.5 and 6.5 % respectively. The current land uses at the site are pasture and row-crop agriculture which involve Corn-Soybean rotations and a growing season that lasts approximately six months, from April to October (Figure 4.6d). The SASW has a mean annual rainfall of about 889 mm/year with most of the contributions occurring between April and September, and the peak occurring in June.

The key factors that affect runoff generation and soil erosion are rainfall, soil type, soil biogeochemical properties, management practices, land use, and terrain characteristics. These factors vary both spatially and temporally, and typically result in a high variation of runoff and soil erosion across a watershed. A good representation of the study site and rainfall distribution is therefore needed to adequately simulate the natural processes that occur within the site.

For this study, a simulation was performed for a single storm event that took place on 12 September 2008 yielding 36.4 mm of rainfall (Figure 4.7). The storm lasted approximately 24 hrs and had a peak intensity of 10.3 mm/hr. The study site was divided into a total of 28 hillslopes and 11 channels as shown in the maps in Figure 4.6. These maps were used to generate the necessary input files for the simulation. Summaries of the hillslope and channel properties are given in Table 4.2 and Table 4.3, respectively.

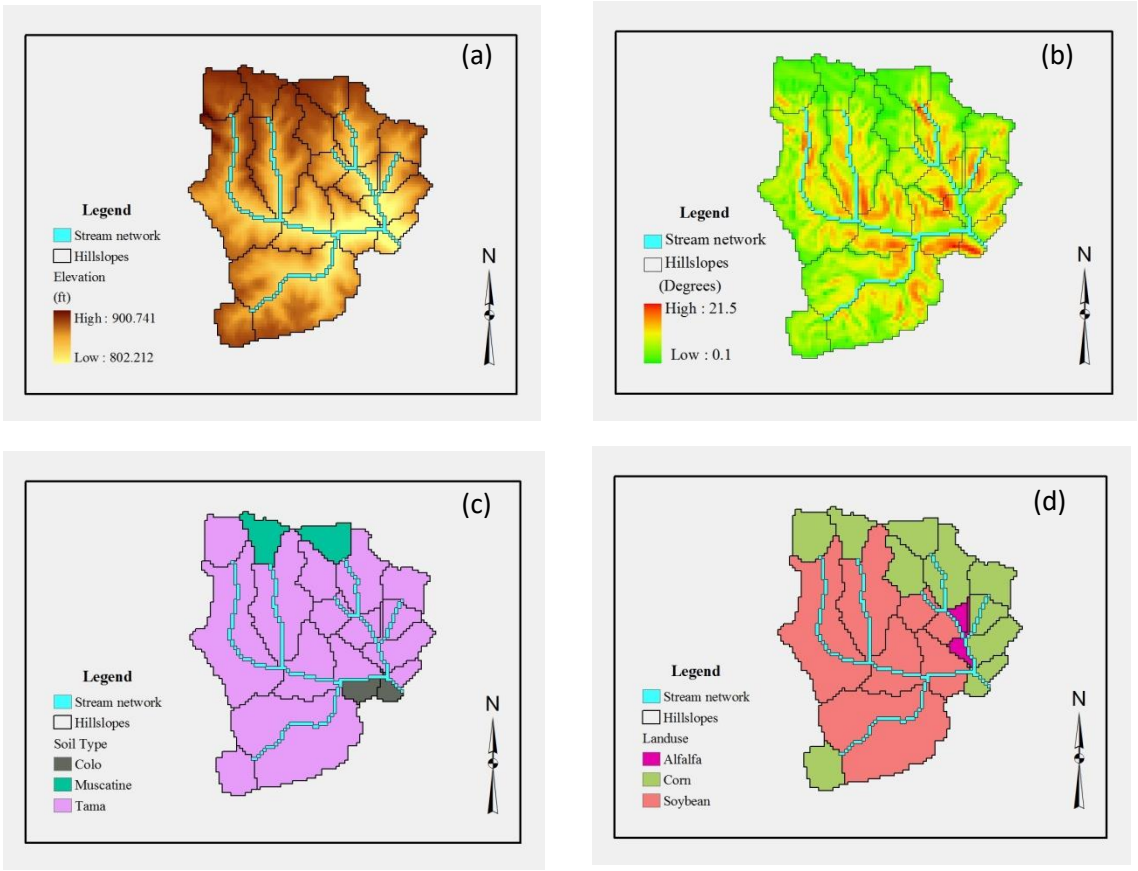

Figure 4.6: (a) DEM of study area; (b) Slope map; (c) Soil type map and (d) Land use map

Table 4.2: Hillslope properties

Number of hillslopes	Area (km^2)	Slope (%)
28	0.015 – 0.539	0.2 - 40

Table 4.3: Properties of the channel network

Number of channels	Length (m)	Slope	Width (m)	Manning's n
11	260 - 1575	0.008 - 0.063	0.2 – 1.4	0.025

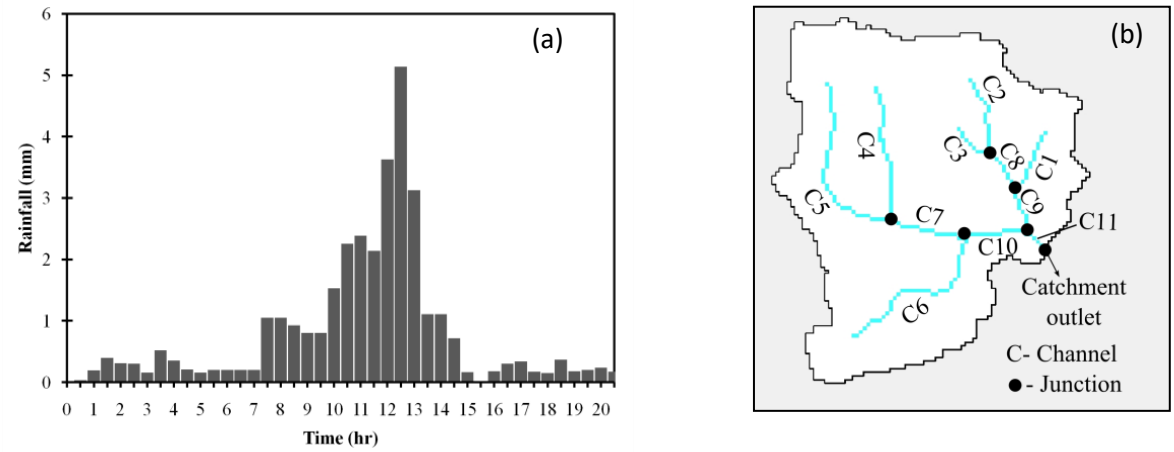

Figure 4.7: (a) Rainfall hyetograph; (b) Channel network

The storm event was first simulated in WEPP to generate hillslope runoff hydrographs, which were then exported to 3ST1D through pass files. The runoff hydrographs were introduced into the channel network as boundary conditions and the network routing was performed until the end of the storm event. Figure 4.8 shows the predicted runoffs entering Channel 5 (defined in Figure 4.7b) as well as its outflow hydrograph. The hydrographs from the left and right hillslopes were introduced as uniform lateral inflows whilst the hydrograph from the top hillslope was introduced as the upstream boundary condition. The uplands are generally characterized by steep slopes, which typically result in runoff hydrographs with steep rising and falling limbs. This is seen in Figure 4.8 where the hydrographs from the left and right hillslopes have relatively steep rising and falling limbs, highlighting the need for a model capable of handling shocks and transcritical flows. The TVD MacCormack scheme used in 3ST1D was able to handle the rapid changes in slope associated with the predicted hillslope hydrographs.

Figure 4.9 shows the predicted hydrograph at the watershed outlet. The time to peak and the predicted peak discharge were 12.75 hrs and 8.5 m^3/s respectively. The current study was performed on a small watershed to allow comparison between its results and results from WEPP's standalone watershed model, which is known to perform well for small watersheds. The predicted peak runoff with the WEPP watershed model was 10 m^3/s, about 17.6 % higher than the peak discharge predicted with the coupled model. Whilst the results from the two models are comparable, the WEPP watershed model is constrained by the size of the watershed that can be simulated and significant differences in the results are expected for larger watersheds.

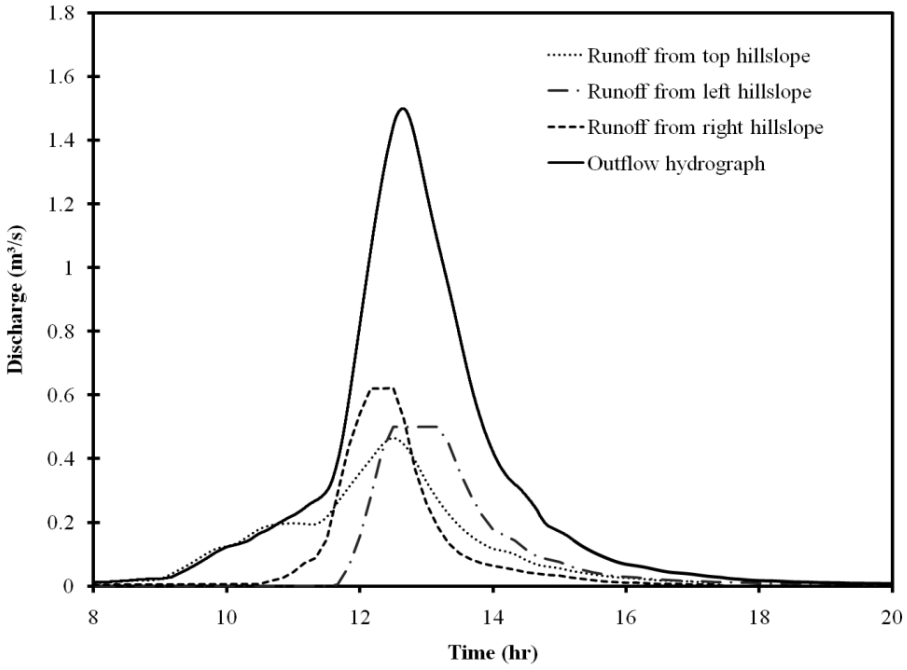

Figure 4.8: Inflow and outflow hydrographs - Channel 5

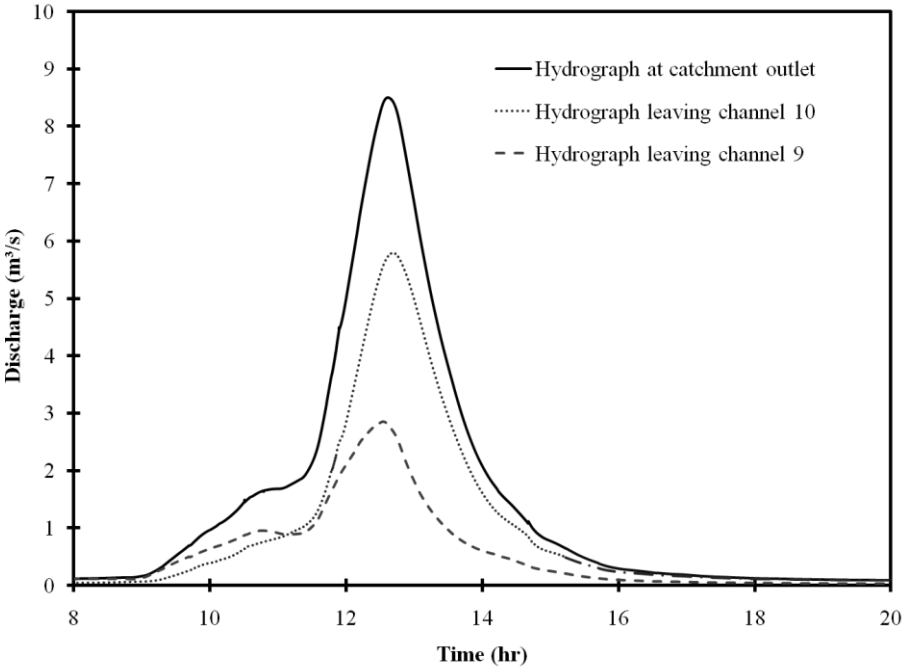

Figure 4.9: Hydrograph at the outlet of the sub-watershed

The hydrographs entering the last channel downstream (Channel ll) are also presented in the Figure 4.9 to show the relative contributions of the two main network branches. The sub-watershed that drains to Channel 10 is about two times the size of the one that drains to Channel 9, explaining the higher runoff volume passing through Channel 10. The hydrograph exiting Channel 9 peaks about 8 min earlier than the one exiting Channel 10, also illustrating the shorter time of concentration associated with the sub-watershed draining to Channel 9. Overall, the coupled model appears to perform well in simulating the flow of runoff from the hillslopes through the channel network to the watershed outlet. However, it should be noted that subsurface flows are not currently accounted for once runoff enters the channel network.

4.3.3. Verification of the coupled model's ability to simulate watershed sediment fluxes

The models ability to simulate sediment fluxes at the watershed outlet was examined for the 26 km² South Amana Sub-watershed described in Section 4.3.2. The coupled model was used to simulate fluxes from storm events that took place in 2007 and 2014. These events are summarized in Table 4.4 below. The predicted fluxes were compared against a sediment rating curve developed for the site based on flow discharge and sediment flux measurements at the outlet of the watershed [*Ellis*, 2009]. The comparison is shown in Figure 4.10.

As seen in the figure, the observed and predicted fluxes were compared for a flow range between 0.5 m³/s and 10 m³/s. This is because the predicted flow rates for the storm events were generally greater than 0.5 m³/s while the observed flows were only up to 10 m³/s. Nonetheless, it is clearly seen that the coupled model is able to predict well the trend in the relationship between the flow discharge and the sediment flux. Moreover, the variability in its predicted fluxes also matches the variability in the observed fluxes, further confirming its ability to simulate flow and sediment fluxes at the watershed outlet.

Table 4.4: Summary of storm events considered in characteristic scale unit analyses

Month	Event	Year	Peak Intensity (mm/hr)	Total Duration	Effective Peak Duration
June	1	2014	51.88	6.67	0.88
	2	2007	60.56	7.25	0.97
July	1	2014	62.84	2.75	0.70
	2	2007	22.08	7.25	1.41

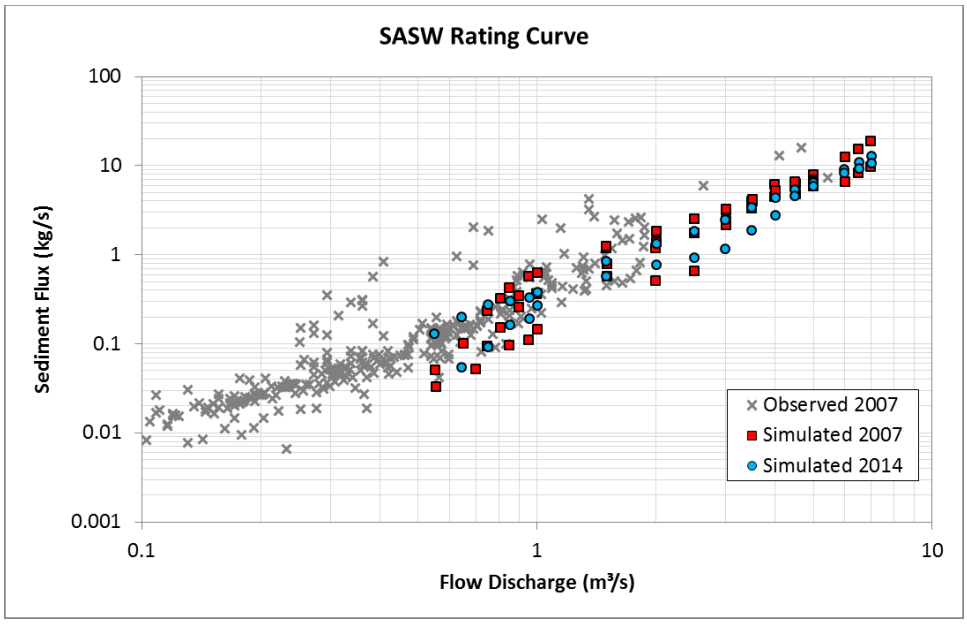

Figure 4.10: Sediment Rating Curve at outlet of sub-watershed

The model's performance was further examined against observed water and sediment fluxes (normalized) at the outlets of 402 rivers around the globe. This comparison is shown in Figure 4.11, which is adapted from *Dade* [2012]. According to *Dade* [2012], the rivers collectively drain about one-third of the Earth's land area that overall sheds on average just under two km^3, or equivalently, about 5 billion metric tons, of sediment each year. The figure presents normalized sediment fluxes as a function of the normalized stream power. As seen, the model predictions are in good agreement with the global data. It is able to predict the mean trends and the variability in the predicted fluxes fall within the range of variability in the observed fluxes. Overall, the plotted data for SASW fall on the mid-part of the graph, suggesting that the stream power and sediment fluxes in SASW are moderate compared to other systems across the globe. It must be noted, however, that the data plotted in Figure 4.11 are restricted to the events and conditions examined in this manuscript, which mostly cover low flows and moderate storm events. Higher water and sediment fluxes have been noted in some years in SASW, particularly in June months, by *Abaci and Papanicolaou* [2009], *Wilson et al.* [2012], and *Abban et al*. [2016].

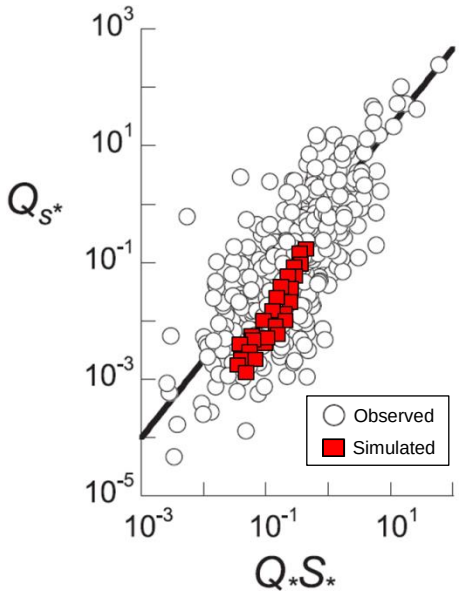

Figure 4.11: Volumetric river-mouth sediment flux Q_s shown as a function of the product of volumetric water discharge Q and average steepness S of river basins. All quantities normalized by relevant global averages. Hollow circles are data from 402 streams around the globe. [*Dade*, 2012].

4.4. Conclusions

The current lack of connectivity between upland and in-stream processes in existing numerical models is known to produce significant errors in water and sediment yield estimates at large spatial scales. A coupled upland-instream model has, thus, been developed to bridge the gap between the processes, thereby paving the way for the evaluation of water and sediment transport at varying spatial scales. This has entailed the coupling of the process-based hydrologic and upland erosion prediction model, WEPP, with the in-stream hydraulic and sediment transport model, 3ST1D.

The coupled model has been verified and applied successfully to the agricultural South Amana sub-watershed in east-central Iowa in the United States to predict flow and sediment fluxes for typical storm events at the site. The findings indicate that the coupled model performs well in simulating flow and sediment transport from the uplands through the channel network to the watershed outlet, capturing important features such as backwater effects. The general steepness of the uplands and the steep slopes associated with headwater channels necessitated the use of a model capable of handling shocks along the channel network. The TVD MacCormack scheme employed in 3ST1D was well suited for this purpose [*Papanicolaou et al.*, 2010] and

performed well in the model verification exercise. Despite the coupled model's good performance, there are still a number of limitations associated with it. For one, subsurface flows are not accounted for within the channel network. Also, 3ST1D assumes a time invariant channel width and does not account for freeze-thaw effects.

References

Abaci, O., and A. N. T. Papanicolaou (2009), Long-term effects of management practices on water-driven soil erosion in an intense agricultural sub-watershed: monitoring and modelling, *Hydrological Processes*, *23*(19), 2818-2837.

Abban, B., A.N. Papanicolaou, M.K. Cowles, C.G. Wilson, O. Abaci, K. Wacha, K. Schilling, and D. Schnoebelen (2016), An Enhanced Bayesian Fingerprinting Framework for Studying Sediment Source Dynamics in Intensively Managed Landscapes, Water Resources Research, DOI: 10.1002/2015WR018030.

Akan, A. O., and B. C. Yen (1981), Diffusion-wave flood routing in channel networks, *Journal of the Hydraulics Division*, *107*(6), 719–732.

Conroy, W. J., R. H. Hotchkiss, and W. J. Elliot (2006), A coupled upland-erosion and instream hydrodynamic-sediment transport model for evaluating sediment transport in forested watersheds, *Transactions of the ASABE*, *49*(6), 1713–1722.

Dade, W. B., "Transport-limitations on fluvial sediment supply to the sea," Water Resources Research, 48: W11601, 2012.

Ellis, P.A. (2009), Non-point source pollution in an agricultural watershed: uplands soil erosion and in-stream sediment transport. M.Sc. Thesis, The University of Iowa, Iowa City, USA.

Flanagan, D. C., and S. J. Livingston (1995), Water Erosion Prediction Project (WEPP) User Summary-NSERL Report No.11, USDA-ARS National Soil Erosion Research Laboratory, West Lafayette, IN.

Flanagan, D. C., and M. A. Nearing (1995), Water erosion prediction project hillslope profile and watershed model documentation. NSERL Rep. No. 10, National Soil Erosion Research Laboratory West Lafayette, IN.

Foster, G. R., D. C. Flanagan, M. A. Nearing, L. J. Lane, L. M. Risse, and S. C. Finkner (1995), Hillslope erosion component, In: USDA-Water Erosion Prediction Project: Hillslope profile and watershed model documentation, Rep. 10, 11.1–11.12, Natl. Soil Erosion Res. Lab., West Lafayette, IN.

Garcia-Navarro, P., F. Alcrudo, and J. M. Saviron (1992), 1-D open channel flow simulation using TVD-MacCormack scheme, *Journal of Hydraulic Engineering*, 118 (10), 1359–1372.

Jetten, V., G. Govers, and R. Hessel (2003), Erosion models: quality of spatial predictions, *Hydrological Processes*, *17*(5), 887–900.

Kesserwani, G., R. Ghostine, J. Vazquez, R. Mosé, M. Abdallah, and A. Ghenaim (2008a), Simulation of subcritical flow at open-channel junction, *Advances in Water Resources*, *31*(2), 287–297.

Kesserwani, G., R. Ghostine, J. Vazquez, A. Ghenaim, and R. Mosé (2008b), One-dimensional simulation of supercritical flow at a confluence by means of a nonlinear junction model applied with the RKDG2 method. *Int. J. Numer. Meth. Fluids*, *57*, 1695–1708.

Lal, R., and B. A. (1994), Soil Processes and Water Quality. Adv. Soil Sci., CRC/ Lewis Publishers, Boca Raton, FL, 398 pp.

MacCormack, R. W. (1969), The effect of viscosity in hypervelocity impact cratering. Frontiers of Computational Fluid Dynamics, edited by D. A. Caughey and M. M. Hafez, American Institute of Aeronaut and Astronaut, Cincinnati, Ohio, pp. 27–44.

Papanicolaou, A. N., A. Bdour, and E. Wicklein (2004), One-dimensional hydrodynamic/sediment transport model applicable to steep mountain streams. *J. Hydraul. Res.*, *42*(4), 357–375.

Papanicolaou, A. N., J. T. Sanford, D. Dermisis, and G. A. Mancilla (2010), A 1-D morphodynamic model for rill erosion. *Water Resources Research*, *46*, 1–26.

Pimentel, D., C. Harvey, P. Resosudarmo, K. Sinclair, D. Kurz, M. McNair, S. Crist, L. Shpritz, L. Fitton, R. Saffouri, and R. Blair (1995), Environmental and economic costs of soil erosion and conservation benefits, *Science*, *267*, 1117–1123.

Shabayek, S., P. Steffler, and F. Hicks (2002), Dynamic Model for Subcritical Combining Flows in Channel Junctions, *J. Hydraul. Eng*., *128*(9), 821–828.

Singh, V. P., and D. A. Woolhiser (2002), Mathematical modeling of watershed hydrology, *J. Hydrol. Eng.*, 7(4), 270–292.

Tseng, M. (2003), The improved surface gradient method for flows simulation in variable bed topography channel using TVD-MacCormack scheme. *Int. J. Numer. Meth. Fluids*, 43(1), 71–91.

USACE (1994), Flood-Runoff Analysis. Technical Engineering and Design Guides, ASCE Press, New York, NY.

Venkata Reddy, K., T. I. Eldho, E. P. Rao, and A. T. Kulkarni (2011), FEM-GIS based channel network model for runoff simulation in agricultural watersheds using remotely sensed data, *Intl. J. River Basin Management*, *9*(1), 17–30.

Wang, L., J.Q. Wu, W.J. Elliott, S. Dun, S. Lapin, F. R. Fiedler, D. C. Flanagan (2010), Implementation of Channel-Routing Routines in the Water Erosion Prediction Project (WEPP) Model. In: Proceedings of the Society for Industrial and Applied Mathematics Conference on Mathematics for Industry, October 9-10, 2009, San Francisco, CA., pp. 8.

Wilson, C. G., A. N. T. Papanicolaou, and K. D. Denn (2012), Partitioning fine sediment loads in a headwater system with intensive agriculture, J Soil Sediment, 12(6), 966-981.

Wu, W., and D. A. Vieira (2002), One-Dimensional Channel Network Model CCHE1D Version 3.0: Technical Manual. Technical Report No. NCCHE-TR-2002-1. University, MS: National Center for Computational Hydroscience and Engineering.

Wu, W. M. (2008), Computational river dynamics. Taylor & Francis Group, London.

Chapter 5

An Enhanced Bayesian Fingerprinting Framework for Studying Sediment Source Dynamics in Intensively Managed Landscapes

Abstract

An enhanced revision of the *Fox and Papanicolaou* [2008a] Bayesian, Markov Chain Monte Carlo fingerprinting framework (hereafter referred to as F-P framework) for estimating sediment source contributions and their associated uncertainties is presented. The F-P framework included two key deterministic parameters, α and β, that respectively reflected the spatial origin attributes of sources and the time history of eroded material delivered to and collected at the watershed outlet. However, the deterministic treatment of α and β is limited to cases with well-defined spatial partitioning of sources, high sediment delivery and relatively short travel times with little variability in transport within the watershed. For event-based studies in intensively managed landscapes, this may be inadequate since landscape heterogeneity results in variabilities in source contributions, their pathways, delivery times and storage within the watershed. Thus, probabilistic treatments of α and β are implemented in the enhanced framework to account for these variabilities. To evaluate the effects of the treatments of α and β on source partitioning, both frameworks are applied to the South Amana Sub-Watershed (SASW) in the US Midwest. The enhanced framework is found to estimate mean source contributions that are in good agreement with estimates from other studies in SASW. The enhanced framework is also able to produce expected trends in uncertainty during the study period, unlike the F-P framework, which does not perform as expected. Overall, the enhanced framework is found to be less sensitive to changes in α and β than the F-P framework, and, therefore, is more robust and desirable from a management standpoint.

5.1. Introduction

Understanding sediment source dynamics is important for managing the impacts of natural processes and anthropogenic activities on water resources and soil quality. This importance cannot be overstated for intensively cultivated agricultural watersheds, where non-conservation management practices can leave the landscape vulnerable to accelerated soil erosion with implications for the land productivity, soil biogeochemistry, and water quality [*Lal,* 2001].

Terrestrial sources of eroded soil, such as those derived from interrill areas, rills, gullies, ditches, etc., as well as instream sources, such as bank soils and channel bed sediment, can

collectively contribute to the total amount of transported material [*Matisoff and Whiting*, 2011; *Gellis and Mukundan*, 2013; *Walling*, 2013; *Sutarto et al.*, 2014]. The proportions of terrestrial and instream contributions to the total transported material in streams can vary depending on a number of factors including: hydrologic characteristics, landscape characteristics, seasonality, land use/land cover (LULC) and associated management practices to name a few. It is, therefore, important to identify the provenance of the transported material in order to better identify "hot spots" (i.e., areas with disproportionately high erosion rates relative to their surroundings) and "hot moments" (i.e., time periods with disproportionately high erosion rates relative to longer intervening time periods) for effectively designing best management practices (BMPs) [*U.S. EPA*, 1999; *Walling and Collins*, 2008; *Gellis and Walling*, 2011; *Mukundan et al.*, 2012].

Different studies have determined the relative contributions of terrestrial and instream sources to the total load [e.g., *Yu and Oldfield*, 1989; *Wallbrink et al.*, 1998; *Papanicolaou et al.*, 2003; *Collins and Walling*, 2004; *Matisoff et al.*, 2005; *Walling*, 2005; *Fox and Papanicolaou*, 2007; 2008a; 2008b; *Bonn and Rounds*, 2010; *Wilson et al.*, 2012; *Cooper et al.*, 2015]. These studies, which are generally referred to as "fingerprinting" studies, have relied on the unique physical and biogeochemical characteristics of natural and artificial tracers (e.g., $\delta^{15}N$, $\delta^{13}C$, C/N, ^{210}Pb, ^{137}Cs, Al, Fe, Mg, soil texture, soil color, etc.) as a means of distinguishing between soil (terrestrial) and sediment (instream) sources [*Davis and Fox*, 2009; *Guzman et al.*, 2013]. Hereafter, the term tracer "signature" is used to refer to the physical and biogeochemical characteristics of natural and artificial tracers [e.g., *Mukundan et al.*, 2012; *Dutton et al.*, 2013]. The schematic in Figure 5.1 shows different source areas contributing to the total load and the erosion mechanisms triggering terrestrial and instream contributions within a watershed. The signature of transported eroded material collected at the watershed outlet (Figure 5.1), which is comprised of contributions from terrestrial and instream sources, is related to the unique signatures of these sources through mass balance to determine the relative source contributions.

Fingerprinting studies combine the aforementioned tracers with statistical tools, known as un-mixing models, to relate the signatures of the transported material to the signatures of the source soils. A key assertion in the approach is that the transported soils/sediments retain the unique signatures of their sources of origin [*Yu and Oldfield*, 1989; *Guzman et al.*, 2013; *Walling*, 2013]. Different types of un-mixing models have been proposed including a least

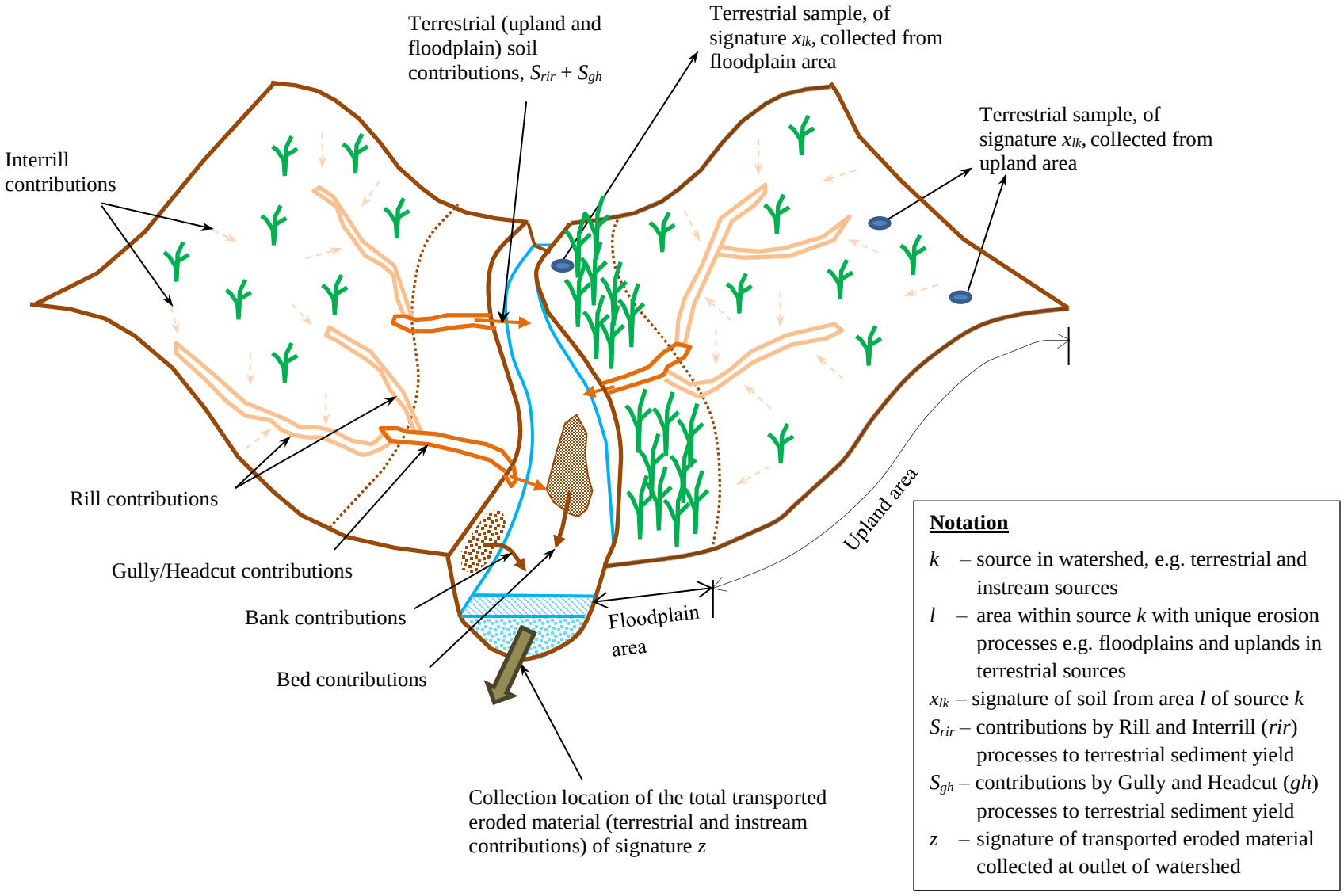

Figure 5.1: Conceptual sketch of watershed showing typical terrestrial and instream soil/sediment sources in a watershed.

squares approach [e.g., *Collins et al.*, 1998; *Owens et al.*, 1999; *Walling and Amos*, 1999], an end-member mixing approach [e.g., *Christophersen and Hooper*, 1992; *Burns et al.*, 2001; *Wilson et al.*, 2008; *Wilson et al.*, 2012], and more recently a Bayesian approach [e.g., *Small et al.*, 2002; *Douglas et al.*, 2003; *Small et al.*, 2004; *Douglas et al.*, 2007; *Fox and Papanicolaou*, 2007; 2008a; *Palmer and Douglas*, 2008; *D'Haen et al.*, 2013; *Dutton et al.*, 2013; *Massoudieh et al.*, 2013; *Cooper et al.*, 2015].

Unlike the two former approaches, the Bayesian approach combines past data in the form of a "prior" probability distribution with new data in the form of a "likelihood" to obtain updated information on the origin of soil/sediment fluxes derived from different sources in the form of a "posterior" probability distribution [e.g., *Small et al.*, 2002]. Using prior knowledge for model parameters relaxes the assumption that tracers are fully characterized throughout the source areas and at the watershed outlet [*Billheimer*, 2001]. It is therefore considered here as the preferred un-mixing method for representing uncertainty in source contributions.

Fox and Papanicolaou [2008a] utilized a Bayesian un-mixing framework that incorporated two new parameters, namely α and β, to represent watershed erosion processes and to perform source fingerprinting. Their study built on work from *Fox and Papanicolaou* [2007] that used natural biogeochemical tracers, namely $\delta^{15}N$ and $\delta^{13}C$, to differentiate soils derived from upland-floodplain areas of forested and agricultural sources. In their un-mixing framework, α was used to define the spatial origin attributes of the contributing sources, while β accounted for the time history (delivery, and residence time/integration) of source soils/sediments delivered to and at the collection point. The framework was applied to a first-order, high gradient tributary of the Palouse River, ID, where instream contributions were negligible due to relatively low bank heights and coarse gravel stream beds. Both α and β were treated as deterministic parameters due in part to the well-defined spatial partitioning of the source areas and the high relief of the small watershed which led to short pathways and travel times with little variability.

However, the deterministic treatment of α and β may not be justifiable in other landscapes where agricultural activities are intense and erosion processes are highly episodic [*Gellis and Walling*, 2011; *Mukundan et al.*, 2012]. In these landscapes, erosion and sediment transport processes can be highly variable due to the complex interactions of water, soil/sediment, and crop rotations, leading to a highly variable α and β [*Tayfur and Kavvas*, 1998; *Govers et al.*, 2007; *Liu et al.*, 2007; *Giménez et al.*, 2004; *Papanicolaou et al*., 2015].

Also, instream sources in these landscapes cannot be neglected as they have been found to contribute significantly to material at the outlet with implications to the roles of α and β and their variability in an un-mixing analysis [Wilson et al., 2012]. The importance of accounting for the variabilities in α and β in un-mixing frameworks is discussed by *Walling* [2013], who explains the need for explicitly accounting for these inherent variabilities to adequately represent the uncertainty associated with source characterization, and to propagate this uncertainty to the final source ascription results. This is readily achieved in the Bayesian framework through probabilistic treatments of α and β.

Thus, the current study builds on the *Fox and Papanicolaou* [2008a] Bayesian un-mixing framework to develop and test an enhanced version of the framework that offers a probabilistic treatment of α and β. Specifically, it: (1) develops stochastic representations of α and β capable of accommodating information on the variability in source contributions, their delivery times and storage within the watershed, and, thus, better reflecting uncertainty in source contributions; and (2) demonstrates the application of the enhanced framework for a representative intensively managed watershed, Clear Creek, IA, where instream contributions are significant. In doing so, this study combines the use of the Bayesian un-mixing model with natural $\delta^{13}C$ and $\delta^{15}N$ tracers. These tracers provide a strong dependence of soil tracer signature with LULC and associated management practices [e.g., *Fox and Papanicolaou*, 2007].

5.2. Existing Bayesian Un-mixing Framework

5.2.1. Description of Key Framework Principles

A synoptic description of the key principles of the Bayesian un-mixing framework is presented here to better familiarize the reader with the associated concepts and notations. The reader is directed to *Fox and Papanicolaou* [2008a] for a more in-depth study of the details and principles.

Figure 5.2 depicts the un-mixing framework in the form of a directed acyclic graph. Following a general Bayesian framework, the tracer signature, *z*, of the total (terrestrial and instream) eroded material collected at the outlet of a study area can be considered as a random draw from the following probability distribution:

$$z \sim \mathrm{MVN_T}(\varphi, \Gamma) \quad (1)$$

where MVN_T is a multivariate normal distribution of dimension T; φ is the expected value of the signature of the collected eroded material; and Γ is a $T \times T$ covariance matrix representing the uncertainty in z. This uncertainty is collectively attributed to the above-mentioned variability in source material mobilization and storage, as well as measurement errors. φ is determined using mass balance as follows [*Walling*, 2013]:

$$\varphi = \sum_{k=1}^{N}(x_k \times P_k), \text{ with } \sum_{k=1}^{N} P_k = 1 \text{ and } 0 \leq P_k \leq 1 \quad (2)$$

where k represents a sediment source; x_k is the tracer signature of the eroded material corresponding to the k^{th} source; P_k is the proportion of the collected eroded material originating from the k^{th} source; and N is the total number of sources considered (see Figure 5.1).

In Eq. (2), the vector of proportions, P_k, is the unknown parameter to be determined and is given a non-informative Dirichlet prior probability distribution in the model [*Massoudieh et al.*, 2013]. x_k, which reflects the signature of eroded material from source k integrated over a period of time, can be considered as a draw from the following probability distribution:

$$x_k \sim \mathrm{MVN_T}(\mu_k, \Sigma_k) \quad (3)$$

where μ_k is the expected value of the tracer signature of eroded material from source k and Σ_k is the covariance matrix representing the variability in the signatures of time-integrated eroded soil/sediment contributions.

Several studies have found a strong dependence of soil tracer signature with dominant erosion processes for biogeochemical tracers such as $\delta^{15}N$ and $\delta^{13}C$ [e.g. *Fox and Papanicolaou*, 2007; *Mukundan et al.*, 2010; *Blake et al.*, 2012]. *Fox and Papanicolaou* [2007] found that upland soils had different signatures than floodplain soils and so contributions from the predominant rill and interrill erosion processes in the uplands had a different signature than contributions from gully and headcut erosion processes on the floodplain. To accommodate these differences, *Fox and Papanicolaou* [2008a] assumed that each $x_k$was a weighted sum of the tracer signatures of soil/sediment from the areas contributing to source k. Thus, they expressed μ_k in Eq. (3) as follows:

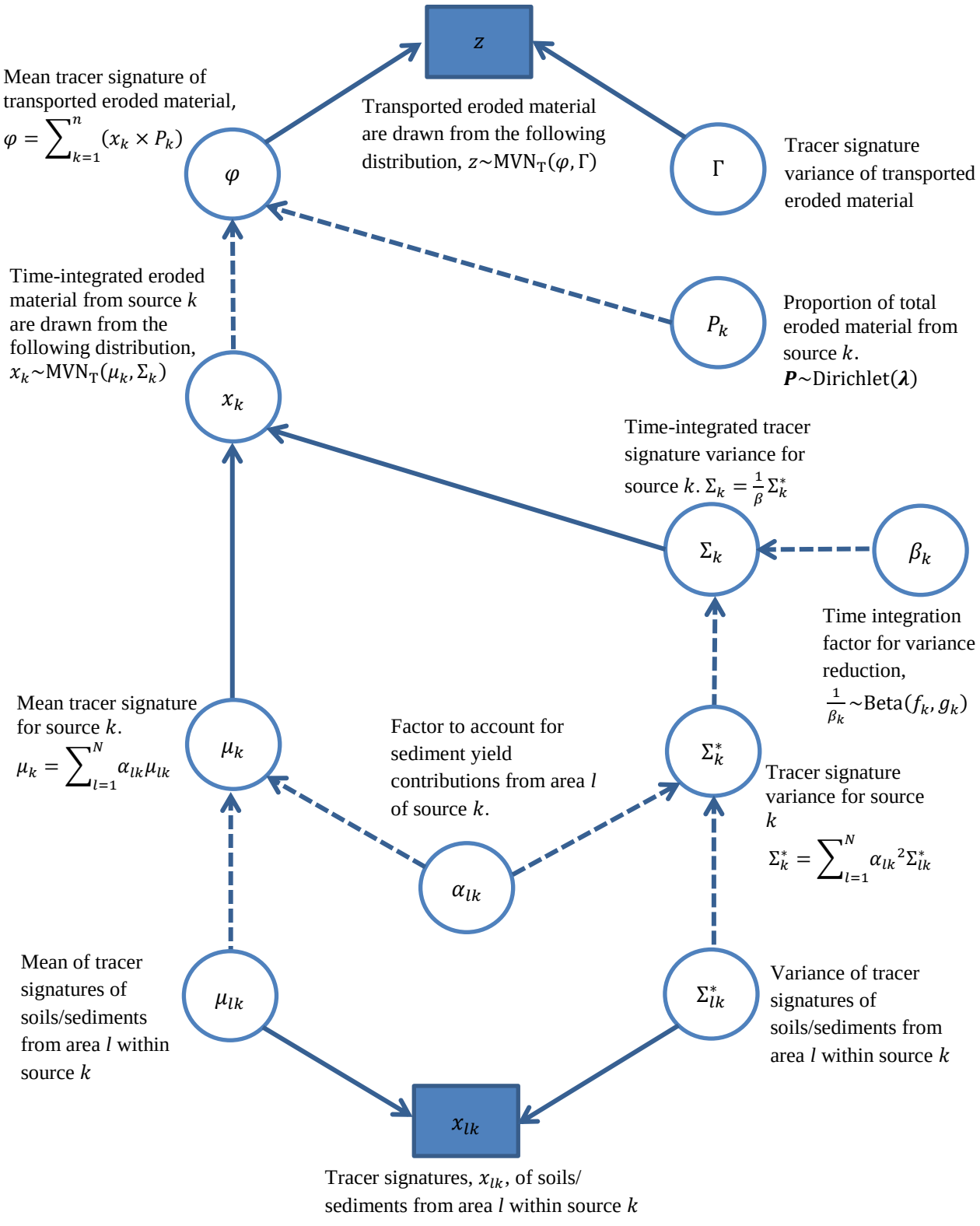

Figure 5.2: Directed Acyclic Graph showing the relationships between the model parameters; plates representing multiple instances of objects are omitted for simplicity. The observed data are presented in the shaded boxes. The solid arrows represent stochastic dependence while the dashed arrows represent deterministic dependence.

$$\mu_k = \sum_{l=1}^{N}(\alpha_{lk} \times \mu_{lk}) \quad (4)$$

where μ_{lk} is the expected value of the tracer signature of soil/sediment from area *l* of source *k*; and α_{lk} is the respective weight expressed as the proportion of the sediment yield from source *k* contributed by the erosion processes (e.g., interrill erosion, rill erosion, gully erosion etc.) in area *l*. In their study, α_l, was calculated deterministically as:

$$\alpha_{rir} = \frac{S_{rir}}{S_{rir}+S_{gh}}, \alpha_{gh} = \frac{S_{gh}}{S_{rir}+S_{gh}} \quad (5)$$

where *rir* and *gh* denote areas dominated by rill/interrill and gully/headcut erosion processes, respectively (see Figure 5.1). S_{rir} is the sediment yield contribution (in kg) by rill and interrill processes and S_{gh} is the sediment yield contribution (in kg) by gully and headcut processes. S_{rir} and S_{gh}were estimated as proportions in *Fox and Papanicolaou* [2008a] using calibrated process-based numerical models for rill/interrill and gully/headcut erosion, respectively. Further information on S_{rir} and S_{gh} can be found in *Fox and Papanicolaou* [2008a]. *Fox and Papanicolaou* [2008a] also suggested that $\alpha_l$in Eq. (5) could be estimated using historical trends from the watershed or scientific judgment.

Similarly, Σ_k in Eq. (3) was determined as follows:

$$\Sigma_k = \frac{1}{\beta_k}\sum_{l=1}^{N}({\alpha_{lk}}^2 \times \Sigma_{lk}^*) \quad (6)$$

where Σ_{lk}^* represents the variability in the tracer signatures of soils/sediments from area *l* of source *k*; and β_k is a factor that accounts for the change in variability of the signatures of eroded material from source *k* due to integration of the material over discrete time periods at the collection point. β_k was also treated as deterministic and determined through optimization by modifying the variance of a source tracer distribution to match the variance of observed time-integrated signatures of the total eroded material from the source. α_{lk} in Eq. (6) is squared because of the assumption that the normal distribution in Eq. (3) representing the source

signature x_k is a weighted sum of the normal distributions of the signatures of the upland and floodplain soils (with α_{lk} being the weights; *Albright et al.* [2010]).

μ_{lk} and Σ_{lk}^* in Eqs. (4) and (6), respectively, were estimated from the tracer signatures, x_{kl}, of soil/sediment collected from contributing terrestrial and instream source areas as follows:

$$x_{kl} \sim \mathrm{MVN_T}(\mu_{lk}, \Sigma_{lk}^*) \tag{7}$$

Following Bayes theorem, the joint posterior distribution of all the models parameters was expressed as:

$$\overbrace{p(\varphi, \Gamma, x_k, P_k, \mu_k, \Sigma_k, \mu_{lk}, \Sigma_{lk}^* | x_{kl}, \alpha_{lk}, \beta_k, z)}^{\text{Posterior Distribution}} \propto \overbrace{p(\varphi, \Gamma, x_k, P_k, \mu_k, \Sigma_k, \mu_{lk}, \Sigma_{lk}^*)}^{\text{Prior Distribution}} \times \underbrace{p(x_{kl}, \alpha_{lk}, \beta_k, z | \varphi, \Gamma, x_k, P_k, \mu_k, \Sigma_k, \mu_{lk}, \Sigma_{lk}^*)}_{\text{Likelihood}} \tag{8}$$

where the first term on the right hand side is the joint prior probability distribution and the last term is the likelihood. The marginal posterior distribution of each of the parameters on the left hand side of Eq. (8) was determined using conventional MCMC methods [*Cowles*, 2013]. Hereafter, the *Fox and Papanicolaou* [2008a] model will be referred to as the "F-P" framework.

5.2.2. Limitations of the F-P Framework

In the *Fox and Papanicolaou* [2008a] study, the well-defined spatial partitioning of the source areas and high relief (with short pathways and travel times) ensured extensive integration of source contributions for most storms, thus, lowering uncertainty and permitting the use of the deterministic α and β parameters with little impact on source contribution estimates.

However, as previously mentioned, the deterministic treatment of α and β may not be justifiable in landscapes where erosion processes are highly variable. This is especially true in intensively managed landscapes. The complex interactions of water, soil/sediment, and crop rotations, can lead to a highly variable α. Also, instream sediments in these landscapes (including those from bank erosion) can exhibit different biogeochemical properties and transport characteristics than terrestrial soils [*Rinaldi and Darby*, 2008; *Sloan*, 2013] with

implications for the role of α and its variability in estimating relative contributions. Further, differences in travel times of the terrestrial soils and instream sediments in this case could significantly affect the fractions and amounts of eroded material delivered to the outlet over time with implications for β estimation and variability. The length of time over which transported eroded material from different origins is collected and integrated, in relation to the transport times of the source contributions, dictates the extent of variability in the signatures of time-integrated source material at the outlet [*Fox and Papanicolaou*, 2008a]. Clearly, an appropriate time-integration during collection at the outlet must be determined in an un-mixing framework to adequately capture variability in source contributions, terrestrial and instream, as well as variability in their delivery time at the watershed outlet [*Fox and Papanicolaou*, 2008a].

Thus, probabilistic treatments of α and β are proposed below to account for the variabilities. These probabilistic treatments of α and β are evidently more pressing in intensively managed landscapes where straightening of the stream channels and farming (often to the bank line) have affected the connectivity of these landscapes with direct implications on the relative contributions of sources and travel times to the outlet [*Bellanger et al.*, 2004].

5.3. Proposed Enhanced Bayesian Un-mixing Framework

5.3.1. Modification of the Representation for α

To remove the limitation of using a fixed value for α, we adopt herein a stochastic treatment for α that can accommodate varying degrees of information regarding the spatially distributed erosion processes in a watershed. In our approach, a Dirichlet distribution is used to represent α to account for the relative contributions from different spatially distributed source areas [*Bandeen-Roche and Ruppert*, 1991; *Gelman et al.*, 2004; *Lingwall et al.*, 2008; *Parnell et al.*, 2013]:

$$(\alpha_1, \dots, \alpha_l) \sim \text{Dirichlet}(e_1, \dots, e_l) \tag{9}$$

where e_l represents the relative sediment yield from each source area l adjusted for uncertainty. An informative prior is developed for α based on prior erosion data, when such information is available. In this case, e_l can be determined through optimization to obtain a sediment yield

proportion distribution that is similar to what is observed for source *l* [e.g., *Yang et al.*, 2006]. When no direct observations of erosion are available for the watershed, non-informative priors can be used instead, or priors for α can be based on data from watersheds with similar characteristics as the study site.

5.3.2. Modification of the Representation for β

Likewise, a stochastic representation of β is proposed to incorporate sediment delivery variability and time-integration effects into the analysis [*Moore and Semmens*, 2008; *Solomon et al.*, 2011]:

$$1/\beta \sim \text{Beta}(f_k, g_k) \tag{10}$$

where f_k and g_k are parameters that describe the shape of the distribution. The Beta distribution has previously been shown by de *Rooij and Stagnitti* [2004] to be applicable to soil solute fluxes by adequately representing the temporal variation of solute transport combined with the proportion of the study area contributing the solute. The authors suggest that the shape factors of the Beta distribution for their case represent the effects of space and time, respectively.

Consequently, the proposed Beta distribution represents the temporal variation of soil transport, combined with the proportion of the study area from which eroded soil is delivered to the watershed outlet. Thus, the Beta distribution herein reflects the effects of both travel times and sediment delivery, which collectively determine the extent of integration for the mobilized material collected at the outlet. This could imply that the shape of the Beta distribution reflects all these factors affecting soil/sediment transport intermittency, namely, landscape properties heterogeneity, storm magnitude and duration, number and sequence of storm events, and soil/sediment mobilization and storage.

We posit herein that under conditions that promote significant sediment mobilization and delivery to the watershed outlet with short travel times, such as steep, bare landscapes experiencing intense high magnitude storm events, the Beta distribution will be narrow with a large mean value of β representing significant integration of material at the outlet. On the contrary, under conditions with little sediment mobilization, delivery and long travel times, such

as low-gradient, vegetated-covered surfaces experiencing low magnitude storm events, the distribution will be wider with a smaller mean value of β representing less integration of material at the outlet. A wider distribution suggests a wide range of travel, or equivalently, resting times.

For un-mixing at the outlet, Eq. 10 allows the framework to sample over all plausible time-integrated signatures representative of the soil/sediment delivery rates and integration intervals during the collection period. Where prior information on time-integrated signatures is available [e.g., *Fox and Papanicolaou*, 2008a], the values for f_k and g_k can be determined through optimization to get a distribution of $1/\beta$ that produces a modified source tracer distribution that better matches the observed time-integrated tracer signatures of material from the source. Otherwise, a non-informative prior can be used, or a prior can be used that is based on data from a watershed with similar characteristics as the study site.

5.3.3. Updated Posterior Distribution

The stochastic expressions for α and β in Eqs. (9) and (10) above incorporate prior information on α and β into the Bayesian framework. Hence, for the "enhanced framework", the joint posterior distribution includes α and β as follows:

$$\overbrace{p(\varphi,\Gamma,x_k,P_k,\mu_k,\Sigma_k,\mu_{lk},\Sigma_{lk}^*,\alpha_{lk},\beta_k|x_{kl},z)}^{\text{Posterior Distribution}} \propto \overbrace{p(\varphi,\Gamma,x_k,P_k,\mu_k,\Sigma_k,\mu_{lk},\Sigma_{lk}^*,\alpha_{lk},\beta_k)}^{\text{Prior Distribution}} \times \underbrace{p(x_{kl},z|\varphi,\Gamma,x_k,P_k,\mu_k,\Sigma_k,\mu_{lk},\Sigma_{lk}^*,\alpha_{lk},\beta_k)}_{\text{Likelihood}} \quad (11)$$

where marginal posterior distributions for α and β are obtained as part of the solution. The freely available Bayesian, MCMC software, OpenBUGS v3.2.2 [*Lunn et al.*, 2009], is employed in this study to estimate the marginal distributions of interest. It utilizes the Gibbs sampling MCMC algorithm to obtain the target distributions from which inferences can be made.

5.4. Description of Study Area, Tracer Techniques and Measurements

We selected the study area and simulation periods for facilitating comparisons between the "F-P" and "enhanced" un-mixing frameworks. The selected datasets capture major changes

in the spatial and temporal variability of source contributions for different event magnitude and LULC, and yet at a resolution that produced enough material for performing the un-mixing analyses in each time interval.

5.4.1. Study Area

The study area, known as the South Amana Sub-watershed (SASW), is located in the headwaters of the Clear Creek Watershed in southeastern Iowa, USA. Clear Creek has recently become a U.S. National Science Foundation Intensively Managed Landscapes-Critical Zone Observatory (IML-CZO) [http://criticalzone.org/iml/]. SASW is a 26 km² sub-watershed that contains 1st and 2nd order channels with source areas similar to the ones depicted in Figure 5.1. In SASW the terrestrial and instream contributions have been observed to vary over the course of a season in response to changing hydrologic forcing and LULC [*Abaci and Papanicolaou*, 2009; *Wilson et al., 2012*]. The elevations, topography, land uses and soil types in SASW are shown in Figure 5.3. The hillslope gradients range between 0.5% and 8% with an average of 4%. The land use is predominantly row-crop agriculture with two-year corn-soybean rotations, and the dominant soil texture is silty clay loam [*Abaci and Papanicolaou*, 2009]. The average annual precipitation is ~890±220 mm/yr [*Dermisis et al.*, 2010], with convective thunderstorms occurring between May and September with the peak month being June [*Cruse et al.*, 2006].

5.4.2. Description of Tracers

A key component of this study is the use of naturally occurring $\delta^{13}C$ and $\delta^{15}N$ tracers capable of distinguishing sources of eroded material with different pedologic and anthropogenic histories [*Fox and Papanicolaou*, 2007; 2008a; 2008b; *Laceby et al.*, 2014]. $\delta^{13}C$ and $\delta^{15}N$ are the relative amounts of ^{13}C and ^{12}C, and ^{15}N and ^{14}N stable isotopes present in the soil, respectively, in relation to a standard. Specifically, the delta notation (δ) in $\delta^{13}C$ and $\delta^{15}N$ is defined as follows:

$$\delta X = \left(\frac{R_{sample}}{R_{std}} - 1\right) \times 10^3 \quad (12)$$

where X for this study is ^{13}C or ^{15}N; R_{sample} is the isotopic ratio of the sample ($^{13}C/^{12}C$ or

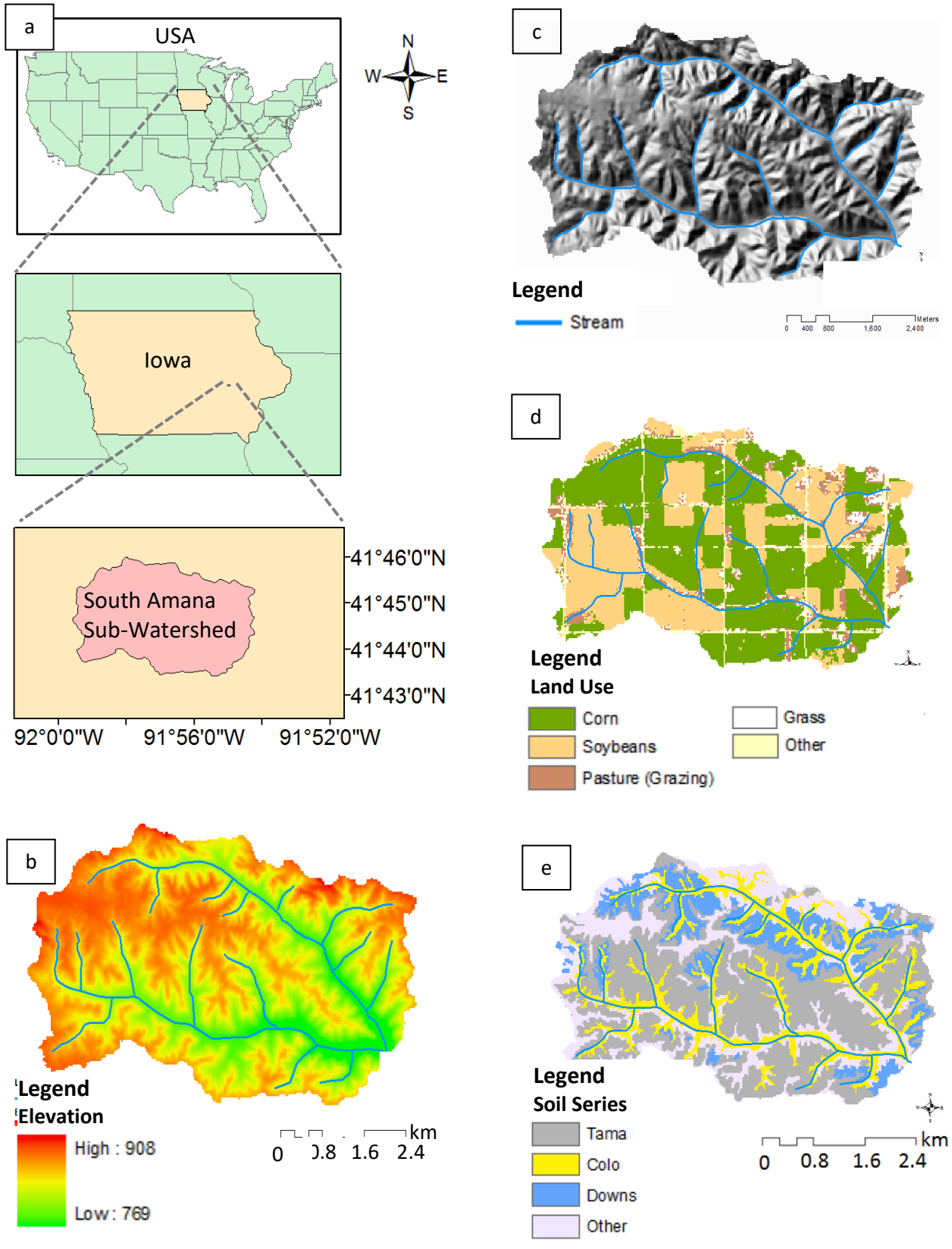

Figure 5.3: South Amana Sub-Watershed a) Elevation b) Topography (Hillshade) c) Land-uses d) Soil series.

$^{15}N/^{14}N$); and R_{std} is the isotopic ratio of a standard (Vienna Pee Dee Belemnite and atmospheric nitrogen, respectively). δ, expressed in ‰, indicates a depletion (-) or enrichment (+) of the heavier stable isotopes (^{13}C, ^{15}N) compared to the lighter stable isotopes (^{12}C, ^{14}N) in the soil.

The carbon and nitrogen isotopic ratios in a soil volume are mainly dependent on the soil organic matter (SOM) derived from vegetation and plant roots undergoing decay in the soil [*Ussiri and Lal*, 2009]. The ratios are indicative of vegetation type and management, as well as the local biogeochemical processes [*Mann*, 1986; *Behre et al., 2012*]. An in-depth review of how these factors affect the ratios are provided in *Fox and Papanicolaou* [2007; 2008b].

5.4.3. Dataset Acquisition

The selected dataset was obtained as part of a previous field study undertaken in 2007 (unpublished). The watershed sources and processes are summarized in Figure 5.4 and were identified based on the following considerations: 1) The total organic material collected at the outlet of SASW is a mixture of material from terrestrial, instream, and algal and detrital sources [*Wilson et al.*, 2012; *Delong and Thorp*, 2006]; and 2) Source areas in the watershed that promote terrestrial soil/instream sediment deposition and re-suspension affect travel times of eroded material with potential impacts on time-integrated source tracer signatures [*Olley*, 2002].

Sampling of source soils/sediments and transported eroded material was done during three consecutive time periods, each approximately one month long, from May to July of 2007. Table 5.1 provides the dates of these time periods as well as a summary of the rainfall and runoff characteristics for each period. Rainfall data for the study period were obtained from a digital rain gauge situated within the sub-watershed. The soil surface was initially bare at the beginning of the study period, but transformed to complete coverage as the crops grew during the study. This is seen in Figure 5.5 which shows Enhanced Thematic Mapper satellite imagery [Landsat 7, http://earthexplorer.usgs.gov/] for SASW for the study period.

Terrestrial soil samples were collected from five fields distributed within the watershed (Figure 5.6a) that were considered to be representative of the land uses, soil types, and topography in SASW. In each field, surface soil samples (0-5 cm and 5-10 cm) were collected along 75- to 100-m long planar transects located along the downslope to capture planar and downslope heterogeneity from the summit to the backslope, toeslope, and floodplain.

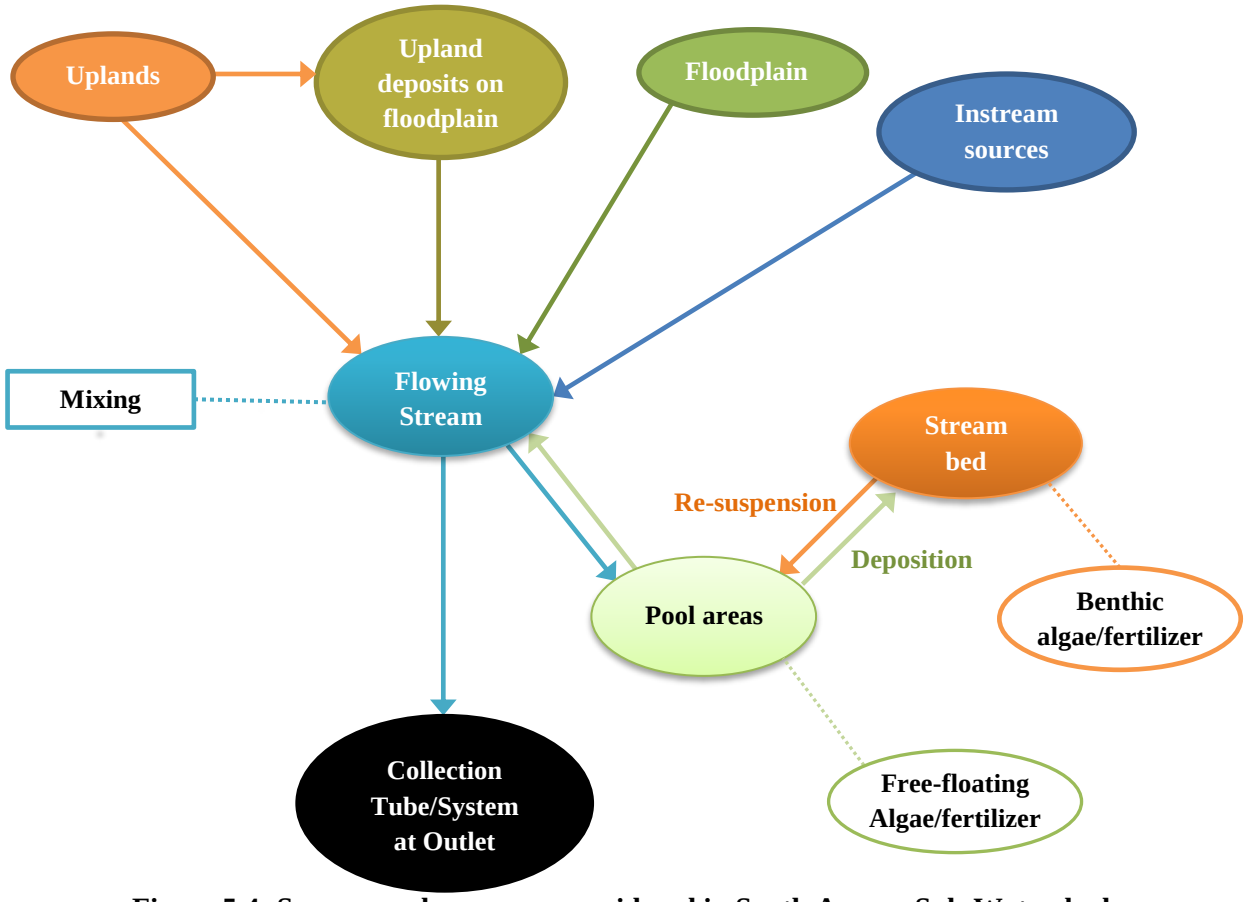

Figure 5.4: Sources and processes considered in South Amana Sub-Watershed

Table 5.1: Rainfall and runoff characteristics over study period

Period	Dates	Rainfall Amount (mm)	Runoff Amount (mm)	Average Intensity (mm/hr)	Runoff Coefficient*	Extent of Land Use/Land Cover
1	05/10/07 - 06/08/07	113	14	1.9	0.12	Low to Medium
2	06/08/07 - 06/29/07	86	25	3.6	0.29	Low to Medium
3	06/29/07 - 07/24/07	74	10	2.8	0.14	Medium to High

*Runoff Coefficient = (Runoff Amount)/(Rainfall Amount)

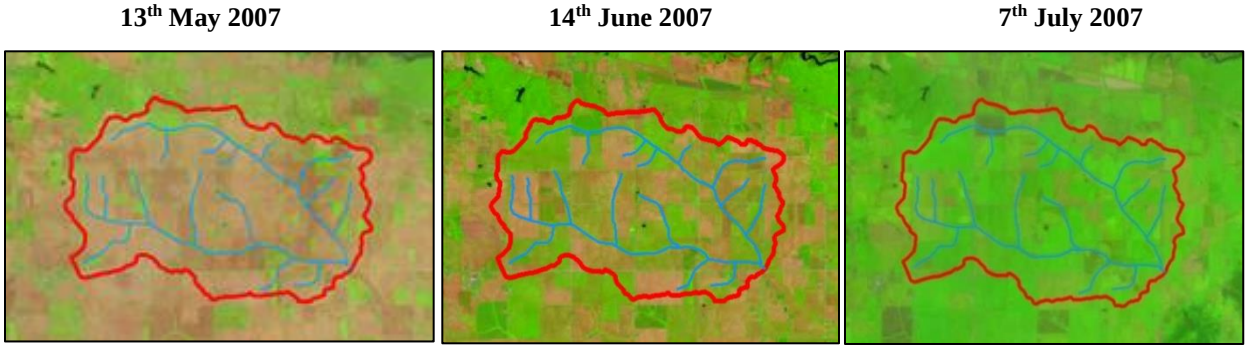

Figure 5.5: Natural color satellite imagery showing establishment of vegetative cover over the study period (Source: http://earthexplorer.usgs.gov/)

Figure 5.6b shows the transect locations for two of the fields with No Till Bean – Spring Till Corn (NTB-STC) and Fall Till Bean – Spring Till Corn (FTB-STC) rotations and their underlying soil series. In the first field, Transects 1, 2, and 3 were located on the summit, backslope and toeslope, respectively, whilst Transects 4 and 5 were located on the floodplain. Similarly, for the second field, Transects 10, 9, and 8 were located on the summit, backslope and toeslope, respectively, whilst Transects 6 and 7 were on the floodplain. The upslope soil series are predominantly Tama, while the floodplain soil series type are Colo. As shown in Figure 5.6b with dots, there were approximately eight sampling locations per transect to best capture planar heterogeneity in the transect. At each dot location, samples were taken at two depths, since previous studies had shown that tracer signatures of the active layer (usually the top 10-20 cm depending on plowing depth) could vary with depth [*Fox*, 2005; *Fox and Papanicolaou*, 2008b]. To characterize instream sediment sources, discrete samples were collected during non-flood flows using Sigma suspended sediment samplers following the *Olley* [2002] approach.

Sampling of the total transported eroded material at the SASW outlet was done using stream tubes (Figure 5.6c), which are described in detail by *Phillips et al.* [2000] and *Fox and Papanicolaou* [2007]. For each of the three sampling periods (Table 5.1), two to four stream tubes were placed close to the bed of the stream outlet to continuously capture suspended eroded material over the period. Stream conditions were such that the tubes primarily captured contributions from the storms that occurred during the period.

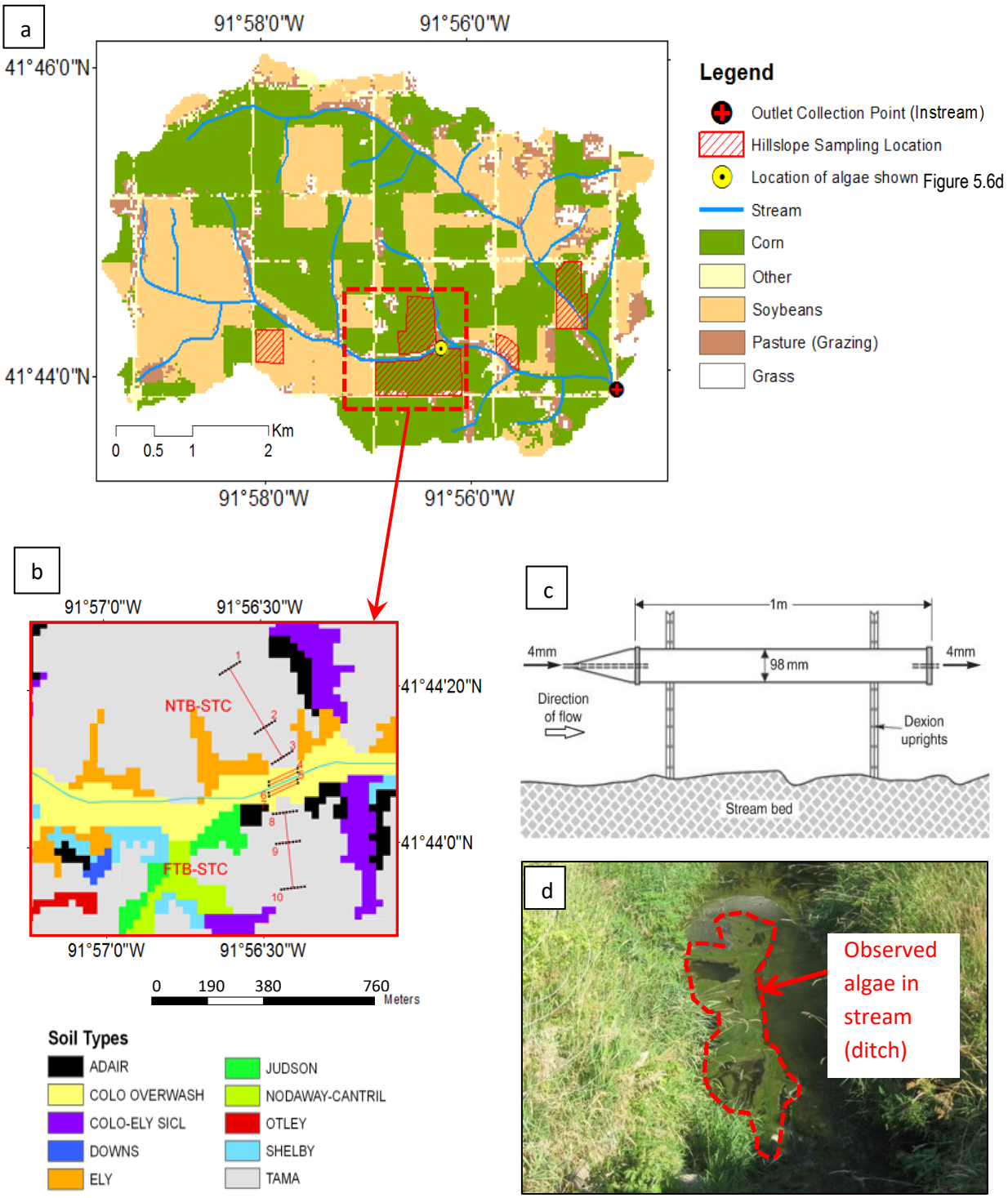

Figure 5.6 : a) Sampling locations; b) Typical sampling transects showing different soil series (NTB-STC and FTB-STC represent No Till Bean, Spring Till Corn and Fall Till Bean, Spring Till Corn crop rotations respectively); c) Stream tube used for in-stream sampling [after *Fox and Papanicolaou*, 2007]; d) Instream photographs taken in the headwaters of SASW showing evidence of the presence of algae 2.4 river kilometers upstream from the outlet collection point.

5.4.4. Tracer Signature Determination

After the samples were collected, the $\delta^{13}C$ and $\delta^{15}N$ signatures of the fine grained portion (<53 μm) of each sample were quantified using mass spectrometry. In previous studies [*Bellanger et al.*, 2004; *Fox and Papanicolaou*, 2008b], the associated $\delta^{13}C$ and $\delta^{15}N$ of the fine grained portion were found to be conservative due to the recalcitrant nature of the fine organic matter and the small fractionation of the size class during transport. The samples were initially dried at 60°C. Then the coarse particulate organic matter (diameter >250 μm) was removed. Sub-samples between 15-30 g were disaggregated in 50 mL of 0.5 mol/L Na-hexametaphosphate and gently washed through a 53 μm sieve [*Cambardella and Elliott*, 1992]. Material passing through the 53 μm sieve was allowed to settle at 4°C, the overlying water was decanted, and then dried again at 60°C. The material was then ground on an orbital ball-mill for the mass spectrometry analysis to determine the $\delta^{13}C$ and $\delta^{15}N$ signatures.

The stable isotope values were measured at the commercial Idaho Stable Isotopes Laboratory of the University of Idaho and represent bulk signatures of the soils. The samples were initially combusted in a NC 2500 Elemental Analyzer (CE instruments) and the gases were passed in a helium flow to a continuous flow isotope ratioing mass spectrometer (Delta plusXL, Finnigan MAT GmbH, 28197 Bremen, Germany). Precision of this method is typically better than 0.2‰ for nitrogen and 0.1‰ for carbon. The measured values of each sample were compared against a standard. The standard for the nitrogen is atmospheric nitrogen, while for carbon, the standard is from the Peedee Belemnite (PDB) marine fossil formation. Additionally, each batch run of 40 samples contained a quality control sample with a known isotopic ratio. The percent differences between the reported and measured QC samples averaged 4% for the $\delta^{15}N$ and 0.5% for the $\delta^{13}C$.

Studies by *Delong et al.* [2001] and *Delong and Thorp* [2006] performed in the Upper Mississippi River, whose watershed characteristics are similar to SASW, suggested the presence of detritus and algae in organic matter ranging 1-100 μm in size. Algal and detrital material although not ubiquitous in Clear Creek has been observed in the headwaters of SASW (2.4 river kilometers upstream from the outlet where the creek is mostly a ditch) at certain times of the growing season where stagnant waters were present (Figure 5.6d). Despite careful placement of stream tubes in flowing sections of the stream to minimize any algal and detrital influence, the potential settling of detrital matter and dead algae in the stream tube must be considered.

Although rather unlikely, it is also possible that incorporation of some suspended detritus and algae during sample retrieval could have contributed to the signatures of the eroded mixture samples at the outlet if indeed this was the case. However, algal and detrital samples were not collected during the SASW study period. Thus, literature ranges of $\delta^{13}C$ and $\delta^{15}N$ algae signatures based on the *Delong et al.* [2001] and *Delong and Thorp* [2006] studies, verified with the signature of a suspended benthic algal sample in Clear Creek from October 2015 (courtesy of Neal Blair and Adam Ward), were considered for further examination of possible contributions to the signature of the collected material in the tubes. These are shown in Figure 5.7.

5.5. Methodology for Applying Framework to the SASW dataset

5.5.1. Simulation Periods

Considering the hydrologic parameters and the degree of land use/land cover (LULC) for the three study periods presented in Table 5.1 and section 4, we evaluated the performance of the "F-P" and "enhanced" frameworks. First, time periods 1 and 2 were compared as they had similar land cover extents (i.e., low to medium cover, although period 2 was slightly more), but dissimilar hydrologic conditions. Period 2 experienced a much higher average storm intensity than period 1 (3.6 mm/hr vs. 1.9 mm/hr) and had a larger runoff coefficient (0.29 vs. 0.12). This allowed us to isolate the role of hydrologic effects on relative source contributions via the estimated posterior probability density functions (PDFs).

Time periods 2 and 3 were then compared as these had dissimilar land cover extents but similar hydrologic conditions. Period 2 had low to medium cover, whereas period 3 had high cover. The rainfall amounts were similar (85 mm in period 2 vs. 74 mm in period 3) with fairly high mean average rainfall intensities (3.6 mm/hr in period 2 vs. 2.8 mm/hr in period 3), although the values were slightly smaller for period 3. Nonetheless, this scenario allowed the examination of the effects of LULC for nearly identical hydrologic conditions.

5.5.2. Specification of Priors on α and β

Since landscape heterogeneity and storm characteristics (magnitude and duration) affect the mean values and PDFs of both α and β, similar considerations must be made in specifying both prior probability distributions (Eqs. 9 and 10). Before constructing the priors for SASW, a

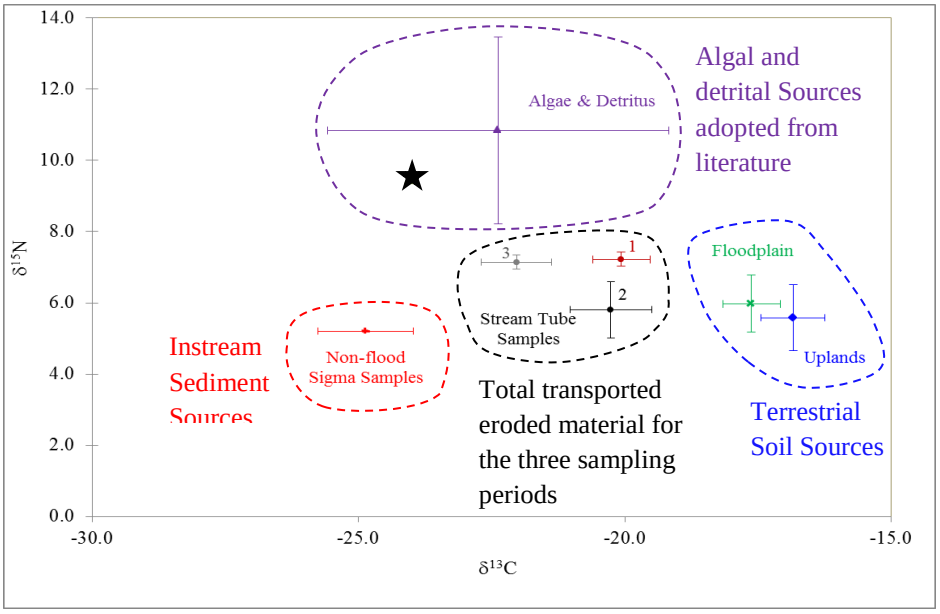

Figure 5.7: Isotopic distributions for terrestrial, instream, and algae and detritus sources for study period. The algae and detritus signatures are adopted from Delong et al. [2001] and Delong and Thorp [2006]. The black star represents the signatures of a suspended algal sample from the Clear Creek watershed (courtesy of Neal Blair and Adam Ward).

conceptual matrix was established in Table 5.2 to provide a qualitative assessment of how several combinations of hydrologic and LULC factors were likely to affect α and β. For large storm events on relatively bare soil, significant mobilization with short transport times and high delivery of both terrestrial and instream contributions to the watershed outlet was expected. For events with little runoff, lower mobilization of soil with longer transport times and low delivery to the watershed outlet was expected.

Comparing the observed hydrologic and LULC conditions presented in Table 5.1 to the matrix developed in Table 5.2 [*Fox and Papanicolaou*, 2008a; *Abaci and Papanicolaou*, 2009; *Wilson et al.*, 2012], we informed our initial selection of the expected mean values for α and β during each of the three periods to reflect the expected trends in hydrological forcing and land cover at the site. We then selected appropriate values for the parameters in Eqs. 9 and 10 to adequately represent α and β by matching the means and variances of the probability distribution with their expected values (the physical ranges are provided in the paragraph below). The selected values are summarized in **Error! Reference source not found.**.

Table 5.2: Effects of hydrologic conditions and land use/land cover on α and β

Rainfall Intensity	Runoff Amount	Surface Cover	Sediment Delivery & Time Integration	Impact on α	Impact on β	Comment
high	small	low	moderate	Interrill erosion is important everywhere. Smaller transport capacity in downslope (toe slope and floodplain regions) compared to the upslope (summit and backslope regions)	moderate reduction in variance of source tracer is expected	moderate uncertainty in α and β
high	large	low	high	Interrill and concentrated flow erosion in most areas. Lower downslope gradients and transport capacity result in less mobilization by concentrated flows in the downslope	large reduction in variance of source tracer is expected.	small uncertainty in α and β
high	small	high	low	Surface cover regulates rainsplash effects. Lower downslope gradients and transport capacity result in less mobilization by concentrated flows in the downslope	small reduction in variance of source tracer is expected	large uncertainty in α and β
low	small	low/high	low	Little contributions from most areas. Upslope areas will contribute more but excess transport capacity in downslope may be greater compared to other scenarios due to limited supply from upslope	small reduction in variance of source tracer is expected	large uncertainty in α and β
low	large	low	moderate	Contributions primarily due to concentrated flow from both upslope and downslope zones. Lower downslope gradients and transport capacity result in less mobilization by concentrated flows in the downslope	moderate reduction in variance of source tracer is expected	moderate uncertainty in α and β

Table 5.3: Summary of α and β parameters

Period	F-P Framework			Enhanced Framework		
	α (uplands, floodplains)	$1/\beta$ (terrestrial)	$1/\beta$ (instream)	α (uplands, floodplains)	$1/\beta$ (terrestrial)	$1/\beta$ (instream)
1 (05/10/07 – 06/08/07)	0.55, 0.45	0.6	0.5	Dirichlet(5.5, 4.5)	Beta(6, 4)	Beta(5, 5)
2 (06/08/07 – 06/29/07)	0.65, 0.35	0.1	0.1	Dirichlet(6.5, 3.5)	Beta(1,9)	Beta(1,9)
3 (06/29/07 – 07/24/07)	0.60, 0.40	0.8	0.7	Dirichlet(6, 4)	Beta(8,2)	Beta(7,3)

Previous studies in SASW and other studies in the region with similar watershed characteristics suggest that the proportions of eroded terrestrial material from gullies and other erosion processes in the floodplain normally range between 0.19 to 0.45 [*Laflen*,1985; *Spomer and Hjelmfelt*,1986; *Poesen et al.*, 2003; *Abaci and Papanicolaou*, 2009]. This was used as a guide to select the expected mean values of α. We based our α variability on estimates from the calibrated SASW model of *Abaci and Papanicolaou* [2009] which suggested a standard deviation of the order of 0.15. Similarly for $1/\beta$, we considered expected mean values in relation to ranges derived from time-integration data in the literature [*Bellenger et al.*, 2004; *Fox and Papanicolaou*, 2008a], which fell between 0.01 to 0.8. The data also suggested standard deviations of the order of 0.12.

5.5.3. Bayesian Analyses in OpenBUGS

Three MCMC chains with overdispersed initial values were used in each model run. In all, a total of 100,000 iterations were performed per run. Model convergence was examined in a variety of ways including the Brooks, Gelman, and Rubin diagnostic [*Brooks and Gelman*, 1998], also known as the "BGR" diagnostic, history and autocorrelation plots, and Monte Carlo (MC) error. The BGR diagnostic was used to quantitatively determine the burn-in period. Burn-in lengths were generally less than 5,000 iterations. Examination of the history plots following burn-in confirmed that the three chains were drawing from the same range of values and the plots resembled white-noise. The autocorrelation plots suggested autocorrelation of iterates up to a maximum lag of about 100. Hence we used long unthinned chains, i.e. ~95,000 iterates per chain, for Bayesian inference (as a more efficient alternative to thinning as concluded in *Link and*

Eaton [2012]). Finally, in all cases we ensured that the MC error for each parameter was less than 1/20th of the estimated posterior standard deviation [*Cowles*, 2013].

5.6. Results

Figure 5.7 shows bivariate plots of $\delta^{13}C$ and $\delta^{15}N$ signatures obtained for the sources and transported eroded material. Hotelling's T^2 tests performed on the tracer distributions confirmed that they were significantly different from each other ($p < 0.05$) and, thus, could be used to distinguish the sources. The differences in isotopic signatures between the 0-5 and 5-10 cm samples were found to be insignificant ($p > 0.05$) and so differentiation of contributions between source depths could be ignored.

The estimated mean source contributions for the three periods are summarized in Table 5.4. We also present the posterior marginal PDFs produced for terrestrial and instream source contributions in Figure 5.8 to evaluate the performance of the two frameworks in capturing the uncertainty in relative soil/sediment source contributions via α and β. Uncertainty in a source contribution is reflected in the spread and peak of its PDF; a wider spread and lower peak reflects greater uncertainty than a narrower spread and higher peak. In Figure 5.8, the red dashed lines represent the PDFs produced with the F-P framework whilst the blue solid lines represent the PDFs produced with the enhanced framework. The left hand side of the figure has the terrestrial contributions, while the right hand side contains the instream contributions. The contributions for the three periods appear from top to bottom for periods 1, 2 and 3, respectively. Table 5.5 summarizes the performance of the enhanced and F-P frameworks in estimating mean source contributions and their associated "credible intervals" conceptually defined as the Bayesian form of confidence intervals. A credible interval is an interval in the domain of the posterior PDF used to determine uncertainty i.e. the probability that the true source contribution lies within the interval. Table 5.5 also summarizes the sensitivities of both frameworks to the choice of α and β. These are discussed in greater detail below.

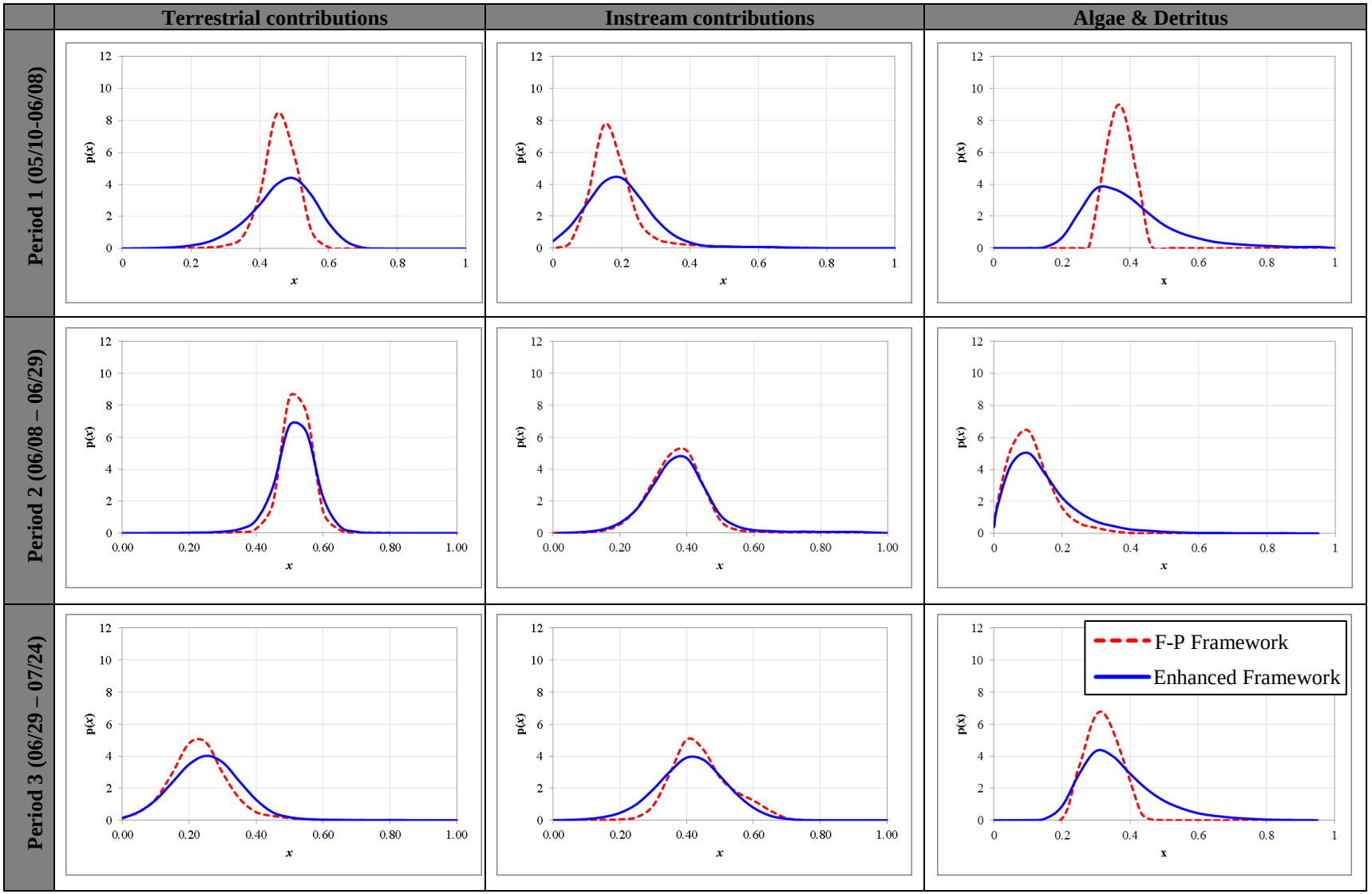

Figure 5.8: Predicted posterior probability density functions of terrestrial and instream source contributions for the F-P (dashed red) and enhanced (solid blue) frameworks.

Table 5.4: Predicted means source contributions

Period	F-P Framework			Enhanced Framework		
	Terrestrial	Instream	Algae & Detritus	Terrestrial	Instream	Algae & Detritus
1 (05/10/07 – 06/08/07)	0.46	0.16	0.38	0.47	0.19	0.34
2 (06/08/07 – 06/29/07)	0.53	0.37	0.10	0.54	0.37	0.09
3 (06/29/07 – 07/24/07)	0.23	0.41	0.36	0.21	0.45	0.34

Table 5.5: Summary of framework performance and sensitivity to α and β

Framework	**Performance in estimating source contributions and uncertainty**		**Sensitivity to the choice of α and β**		**Applicability to Best Management Practice (BMP) design and management**
	Mean source contribution	**Uncertainty (credible interval)**	**Mean source contribution estimates**	**Uncertainty in source contribution estimates**	
F-P	Can adequately predict mean contributions for all storm types given sufficient data.	Only adequate for large magnitude, long duration reoccurring storms.	Only sensitive to the choice of α. Not affected by β since β is assumed to only affect the variance in source signatures.	More sensitive to the choice of α and β due to their deterministic treatment.	Less suitable for management purposes when BMP design depends on single storm events with relatively short durations. It is also less robust (more sensitive).
Enhanced	Can adequately predict mean contributions for all storm types given sufficient data.	Adequate for all storm types, including single storm events as well as a collection of events.	Only sensitive to the choice of α. Not affected by β since β is assumed to only affect the variance in source signatures. A similar performance as the F-P framework was noted due to the high degree of differentiation between the terrestrial and instream source signatures.	Less sensitive to the choice of α and β due to their probabilistic treatment. The probabilistic treatment accounts for variabilities in source contributions, travel times and storage of material in the watershed.	More suitable for management purposes since it is more robust (less sensitive) and better at predicting uncertainty (it can also be applied to single storm events) for BMP design and management.

5.6.1. Mean Relative Source Contributions

Based on the results presented in Table 5.4, both the F-P and enhanced frameworks estimated mean terrestrial soil contributions to be larger than mean instream sediment contributions during both periods 1 and 2, with terrestrial contributions ranging between 46-54% and instream contributions between 16-37%. This trend is consistent with observations from previous studies in the same watershed by *Abaci and Papanicolaou* [2009] who found terrestrial sources to yield the most eroded material in May and June, which correspond to periods 1 and 2. This is attributed, for the most part, to less land cover and more bare soil. In addition, both frameworks estimated the mean instream sediment contributions during period 2 to be greater than the mean instream sediment contributions during period 1 (0.37 vs 0.18, respectively, on average). This is consistent with the greater amount of runoff generated in period 2 resulting in more instream erosion [*Sutarto et al.*, 2014] and the slightly greater cover in the period resulting in relatively less terrestrial erosion. The results in Table 5.4 also suggest that mean algal and detrital contributions were relatively more in period 1 than in period 2 (0.36 vs 0.10, respectively, on average). This is conceivably due to the much larger fluxes of eroded material leading to relatively more sediment contributions comparatively to algal and detrital contributions in period 2. Also, data from SASW [*IML-CZO*, unpublished data - see supplementary material] suggest an inverse relationship between the runoff discharge and the flux of algal concentrations following an event at the outlet, which is consistent with observations from other studies [e.g. *Dorris et al.*, 1963; *Baker and Baker*, 1979; *Reynolds and Descy*, 1996; *Ford and Fox*, 2012]. The prolonged runoff discharge during period 1 would have led to smaller algal concentrations in period 2 and thus a smaller algal influence.

The agreement in estimated mean contributions between the two frameworks for all the sources was also noted in the period 2 vs. period 3 comparison, where both frameworks estimated mean terrestrial soil contributions to be less than mean instream sediment contributions in period 3, contrary to period 2. Here, mean algal and detrital contributions were estimated to be more in period 3 comparatively to period 2. The smaller mean terrestrial contributions for period 3 is attributed to the establishment of extensive surface cover, which has been shown to minimize rain drop impact and reduce erosion by both sheet and concentrated flow [*Papanicolaou and Abaci*, 2008; *Dermisis et al.*, 2010; *Gumiere et al.*, 2011]. Similar to the trends in periods 1 and 2, the smaller mean relative algal and detrital contributions in period 2

comparatively to period 3 is attributed to the larger fluxes of eroded material in period 2. Further the reduced runoff discharge in period 3 due to land cover establishment would have led to increased algal concentrations, which would likely have increased algal influence in period 3 as observed [*IML-CZO*, unpublished data - see supplementary document].

A comparison of the estimated mean soil/sediment source contributions from Table 5.4 with numerical and field observations from previous studies in SASW confirms the ability of both frameworks to accurately estimate mean source contributions. Upland erosion estimates for period 2 (June 2007) obtained from the calibrated Water Erosion Prediction Project (WEPP) model by *Abaci and Papanicolaou* [2009], along with bank erosion estimates based on field observed rates by *Sutarto et al.* [2014] and stream bed erosion estimates from the 3ST1D model by *Papanicolaou et al*. [2004] were combined and validated against field observed data of eroded material fluxes presented in *Ellis* [2009]. The SASW estimates from the aforementioned studies suggested relative terrestrial and instream source contributions of eroded material (expressed as proportions) of 0.59 and 0.41, respectively. This is in good agreement with the F-P and enhanced framework estimates in this study of approximately 0.6 and 0.4 for terrestrial and instream sediment source contributions, respectively. Further, a separate fingerprinting study performed by *Wilson et al.* [2012] for 2009 using radionuclide tracers found relative instream sediment contributions between 0.66-0.74 for certain events in SASW where the supply of material from terrestrial sources was limited. This range agrees well with the F-P and enhanced framework relative sediment source estimates of approximately 0.7 and 0.3 for instream and terrestrial sources, respectively, in period 3 of this study where land cover is expected to limit the supply of material from terrestrial sources.

The consistent, nearly identical relative source contribution estimates by both the F-P and enhanced frameworks for all periods suggests that for the same expected mean α and β values in both frameworks, the estimated mean source contributions are not affected by the variability in soil/sediment fluxes and delivery to the collection point at the watershed outlet. This conclusion is consistent with the findings of *Phillips and Gregg* [2001], who, using analytically-derived equations for uncertainty (verified with experimental data), showed that the mean relative source contributions were fairly independent of their standard error, and, thus, independent of the variability in the source signatures when their mean values were fixed (see Figure 2d of their

study). This was also verified herein through un-mixing analyses on synthetic datasets (see Appendix A).

5.6.2. Uncertainty in Relative Source Contributions

For the period 1 vs. period 2 comparison in Figure 5.8, the enhanced framework produced terrestrial and instream PDFs in period 2 that were narrower with higher peaks (i.e. had less uncertainty) than their corresponding PDFs in period 1. This, however, was not the case for the F-P framework, which produced an instream PDF in period 2 that was wider with a lower peak (i.e. had greater uncertainty) than the instream PDF in period 1. For the period 2 vs. period 3 comparison (also in Figure 5.8), the trends in the PDFs were more consistent, with both frameworks yielding terrestrial and instream PDFs that were narrower with higher peaks in period 2 than their corresponding PDFs in period 3.

Phillips and Gregg [2001] showed that the uncertainty in estimated source contributions, were mostly dependent on the signature difference between the sources, the standard deviation in source and mixture signatures, and number of collected samples. Since for this study, the standard deviation of the mixture (collected eroded material) signatures and the number of samples that were collected are fixed, we pay attention here to the signature difference between the sources and the standard deviation of source signatures as they pertain to α and β, and use that to examine the expected and estimated trends in uncertainty in the three periods.

The analytically-derived uncertainty equations in the *Phillips and Gregg* [2001] study revealed that the standard deviation of source tracer signatures had a substantial linear effect on the uncertainty of estimated source contributions. This trend was also confirmed by *Small et al.* [2002] using a Bayesian framework. Thus, since the β parameter, which reflects delivery of eroded material and time-integration, reduces the variance of source tracer signatures, it is also expected to reduce uncertainty in estimated source contributions, and hence, the spread of their PDFs. Comparing periods 1 and 2, given the greater average rainfall intensity and the greater amount of runoff during period 2, more erosion and a greater delivery of material to the watershed outlet is expected for period 2, resulting in more integration of collected eroded material. Hence, both terrestrial and instream PDFs for period 2 are expected to be narrower with higher peaks than their corresponding PDFs for period 1, reflecting less uncertainty in period 2. As seen in Figure 5.8, only the enhanced framework was able to fully replicate this

when compared to the F-P framework, suggesting that the F-P framework may not fully convey the uncertainty related to source contribution estimates. It is worth noting, however, that there was a good correspondence between the two frameworks for period 2.

Comparing periods 2 and 3, the greater protection offered by the surface cover during period 3 would have led to less mobilization of material in addition to the reduced runoff rates. In addition to that, the greater resistance offered to the flow by the vegetation would promote more deposition and reduce soil/sediment transport times and delivery rates to the watershed outlet [*Neibling and Alberts*, 1979; *Thompson et al.*, 2011; *Jones and Schilling*, 2011]. Further, the high hydrologic forcing in period 2 would "create" a piston effect where action (flow) creates reaction (transported fluxes) with minimal delay and less intermittency in transported material. Hence one would expect less integration of material collected at the outlet during period 3 and corresponding PDFs with wider spreads and smaller peaks, comparatively to period 2. Both frameworks performed as expected in this case (see Figure 5.8).

The *Phillips and Gregg* [2001] analytical uncertainty equations also revealed that the uncertainty in estimated source contributions varied inversely with signature difference between the sources. The α parameter, which reflects spatial contributions from upland and floodplain areas of terrestrial sources, affects the signature difference between terrestrial and instream source signatures. For a given isotope, an increase in signature difference between the two sources is expected to result in a decrease in the uncertainty and vice versa.

The expected difference in the variance of terrestrial source signatures across the three periods due to the effects of α alone (for the chosen α priors) is estimated (with Eq. 6) to be less than 11%. Hence its effects on the uncertainty of estimated source contributions, compared to that of β (which varied by as much as 87.5 % between the periods) is relatively less, and the trends in β are expected to dominate (see Eq. 6) the trends in the uncertainty of the source contribution PDFs above.

Generally, the PDFs for the enhanced framework show wider spreads than the PDFs for the F-P framework. This is expected since the deterministic specifications of α and β do not convey the variability in source contributions, their delivery times and storage within the watershed. On the contrary, the spreads of the probability distributions for α and β in the enhanced framework are reflected in the spreads of the source contribution PDFs as the wider spreads.

5.6.3. Sensitivity of the SASW Source Contribution Estimates to the α and β priors

We evaluated the SASW relative source contribution estimates for their sensitivity to the application of α and β priors falling outside the observed range of physical values. In the first set of simulations, we applied "extreme" values of α priors whilst keeping all other model parameters fixed. These extreme values corresponded to two scenarios: one with contributions primarily from the uplands, and; one with contributions primarily from the floodplain. In the second set of simulations, we applied "extreme" values of β priors whilst maintaining the same values for all other model parameters. The two extreme values in this case represented: a scenario with considerable time-integration of material, and; a scenario with no time-integration of material. The chosen priors for each scenario are summarized in Table 5.6.

5.6.3.1. Effect of high α priors

For our evaluations, we consider the results from Section 6.1 as the "true" values as they have been shown to be in good agreement with field observations and other studies. A summary of results from the first set of simulations examining the effect of α on mean source contributions is provided in Figure 5.9 as deviations from the true values. The performances of the two frameworks were similar for this set of tests. The deviation of the estimated mean source contributions from the true mean values ranged between 0 and 0.04. The similar performance of the two frameworks is expected since the mean values of α are the same for both frameworks. This implies that the mean terrestrial source signature will be the same in each case. Thus, since the mean relative source contributions are dependent on only the mean signatures of the sources [*Phillips and Gregg*, 2001; see Section 6.1], the two frameworks should predict the same mean values.

The percentage changes in the widths of the 95% credible intervals vary from the results in Section 6.2. by up to 20%. Here as well, the impact of the choice of α on the spreads of the source contribution PDFs is similar for both two frameworks. A likely reason for this is the distance or differentiation between the source signatures. Synthetic analyses performed in this study (Section 6.4), as well as the results from the *Phillips and Gregg* [2001] study suggests that the distance between source signatures affects both uncertainty in source contributions estimates as well as their sensitivity to the source signature variances (see Table A.1 and Figure A.2).

Table 5.6: Parameter values used to examine uncertainty in the choice of α and β priors

Scenario	Period	α (uplands, floodplains)		$1/\beta$ (terrestrial/instream)	
		F-P Framework*	Enhanced Framework*	F-P Framework+	Enhanced Framework+
1	All periods	0.99, 0.01	Dirichlet(9.9,0.1)	0.01	Beta(0.1, 9.9)
2	All periods	0.01, 0.99	Dirichlet(0.1,9.9)	1	Beta(9.9, 0.1)

∗ $1/\beta$ parameters remain the same as in **Error! Reference source not found.**
+ α parameters remain the same as in **Error! Reference source not found.**

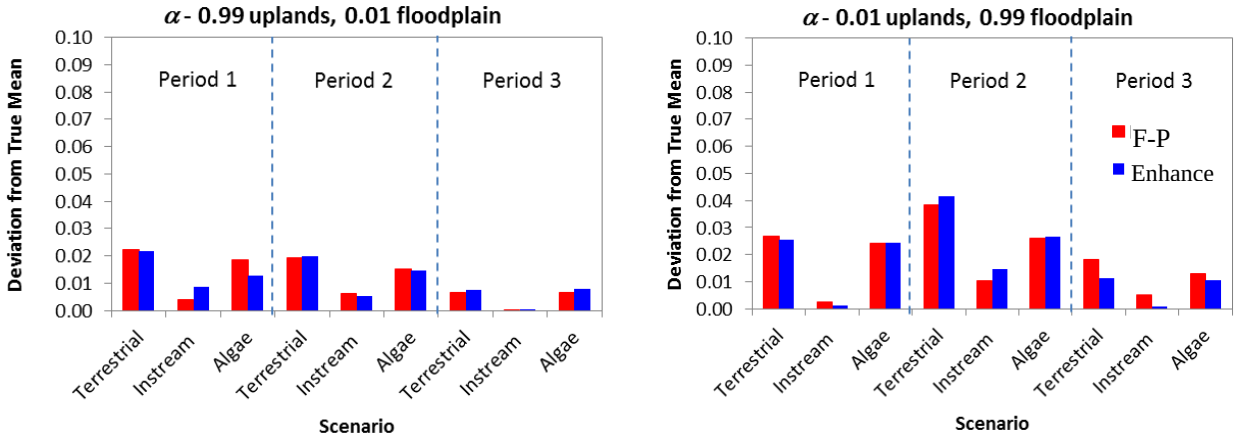

Figure 5.9: Deviation of source contributions from the true mean for α priors outside the observed range of physical ranges.

The larger the distance between the source signatures, the less uncertainty there is in source contribution estimates and the less sensitive the source contribution estimates are to the source signature variances. Thus, although the α parameter affects the distance between all the three source signatures and the variance of the terrestrial source signatures, its effects can be minimal if the source signatures are sufficiently far apart. Under this condition, both frameworks are expected to perform similarly.

5.6.3.2. Effect of high β priors

The choice of β did not affect the mean source contribution estimates, but did affect the spreads of the estimated source contribution PDFs since it was assumed in both frameworks to only account for the reduction in the variance of the source signatures due to time-integration (See Eqs. 4 and 6). A summary of the percentage change in the 95% credible intervals of the source contribution PDFs due to β choices beyond the range of observed physical values is provided in Figure 5.10. The response of the source contribution PDFs to the choice of β was marked for each framework. This was expected since the choice of different β values reflected different degrees of time-integration and, hence, different variances in time-integrated source signatures, which would affect the spread of the source contribution PDFs [*Small et al.*, 2002]. Although both frameworks showed marked response to the choice of β, the spreads produced by the F-P framework appeared to be more sensitive to the choice of β than the spreads produced by the enhanced framework. For example, in Period 2 of the $1/\beta$ =1 scenario, the percentage change in 95% credible interval varied by as much as ~120% for terrestrial sources in the F-P framework, whereas the corresponding percentage change in the enhanced framework was ~50%. A similar consistent trend is noted across all the three periods for the different sources.

The greater sensitivity of the F-P framework is attributed to the deterministic treatment of α and β as opposed to their probabilistic treatment in the enhanced framework. As explained in the section above, unlike the F-P framework, the spreads of the probability distributions for α and β in the enhanced framework are reflected in the spreads of the estimated source contribution PDFs (as wider credible intervals) since the estimated source contribution PDFs represent the range of possible α and β values. Thus, in changing the mean value of β, the spreads of the probability distributions of α and β act as a "cushion" to reduce the relative

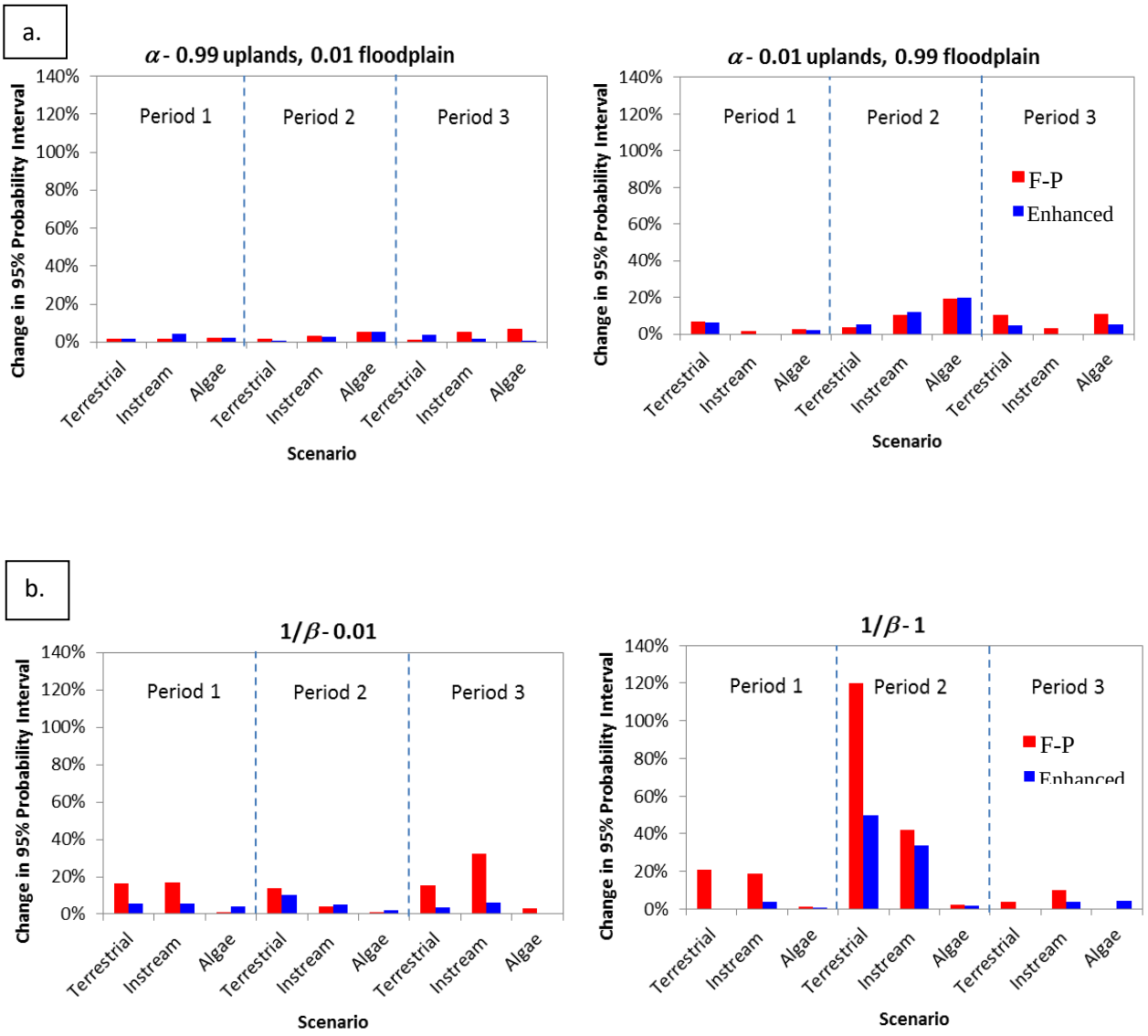

Figure 5.10: Percentage change in 95% credible interval for the a) α values outside observed physical ranges, and b) $1/\beta$ values outside observed physical ranges.

sensitivity of the estimated source contribution PDFs to the change, comparatively to the F-P framework in which only single fixed values are used for α and β and source contribution PDFs are narrower.

5.6.4. Further Evaluation of Framework Sensitivity to α and β priors using Synthetic Data

To provide further insight into the sensitivities of the two frameworks to α and β, as well as some guidance to modelers on conditions under which the frameworks could be applied to other un-mixing studies in intensively managed landscapes, we performed extra sets of analyses using synthetic datasets for which the true source contributions were known. The details of these extra sets of analyses and the observations are discussed in depth in Appendix A. The synthetic datasets were generated to allow us to evaluate the effects of the degree of landscape heterogeneity, source signature variability, differentiation between sources, and the number of sources on the framework sensitivity to α and β priors. Overall, the results from the synthetic analyses were in agreement with our observations and conclusions in Sections 6.1, 6.2, and 6.3 above. For the examined scenarios, the enhanced framework was found to be consistently more robust than the F-P framework due to the probabilistic treatments of α and β. Also, the performance of the two frameworks tended to converge when extensive integration of eroded material was assumed, and to diverge when little integration was assumed. This confirmed the limitation of the F-P framework to scenarios with large magnitude storm events and long integration periods (yielding extensive integration of eroded material), unlike the enhanced framework, which was not limited and thus more generally applicable.

5.7. Discussion and Conclusions

Several studies have highlighted the need to adopt un-mixing frameworks that are capable of adequately capturing uncertainty in relative source contributions for improved management of soil and sediment fluxes [e.g. *Walling*, 2013, *Cooper et al.*, 2014]. This study presents an enhanced revision of the Bayesian, fingerprinting un-mixing framework of *Fox and Papanicolaou* [2008a], capable of adequately estimating source contributions and their associated uncertainties in a watershed. The enhanced framework, contrary to the F-P framework, offers a probabilistic treatment of the α and β parameters that can better account for

the variability in source contributions, delivery times and storage within the watershed (see Table 5.5).

Results from the study indicate that, whereas both the F-P and enhanced frameworks may adequately estimate mean source contributions, the performance of the F-P framework in estimating associated uncertainty is limited to large magnitude and long duration reoccurring storm events. The two frameworks estimated similar results during period 2 of the study in which there was substantial amount of material transported from the terrestrial and instream sources to the outlet. However, based on the other periods, the enhanced framework was better able to represent source contributions and associated uncertainties without requiring the occurrence of large magnitude storm events and longer integration periods like the F-P framework did. The absence of this precondition makes the enhanced framework applicable to both single storm events and a collection of events, and thus makes it more versatile for management decisions since the design and implementation of BMPs are also based on single storm events.

The importance of the probabilistic treatments of α and β are further highlighted in Figure 5.11. In the figure, we show the probability density functions (PDFs) of α and β derived from observed data in relation to values of α and β that would be used in the F-P framework. We argue that the range of values for α and β in the PDFs are very much reflective of the degree of connectivity within the watershed and the associated variabilities in contributions, travel times and storage of material in the watershed. Moreover, the estimated 95% credible intervals for source contributions were found to be less sensitive to changes in α and β in the enhanced framework comparatively to the F-P framework due to the probabilistic treatments of α and β with several consequences in LULC management. From a management standpoint, a less-sensitive framework is more desirable since it reduces uncertainty in decision making. Thus, by accounting for the variability in source contributions, their delivery times and storage within the watershed, we have provided a more robust framework that better quantifies uncertainty in un-mixing analyses.

However, as with any framework, there are some caveats associated with the enhanced framework and the analyses presented herein. Since we used two tracers, we assumed that the signatures of both the source soils and eroded material mixtures followed multivariate normal distributions (no skewness). In reality, however, each of them could follow either log-normal or

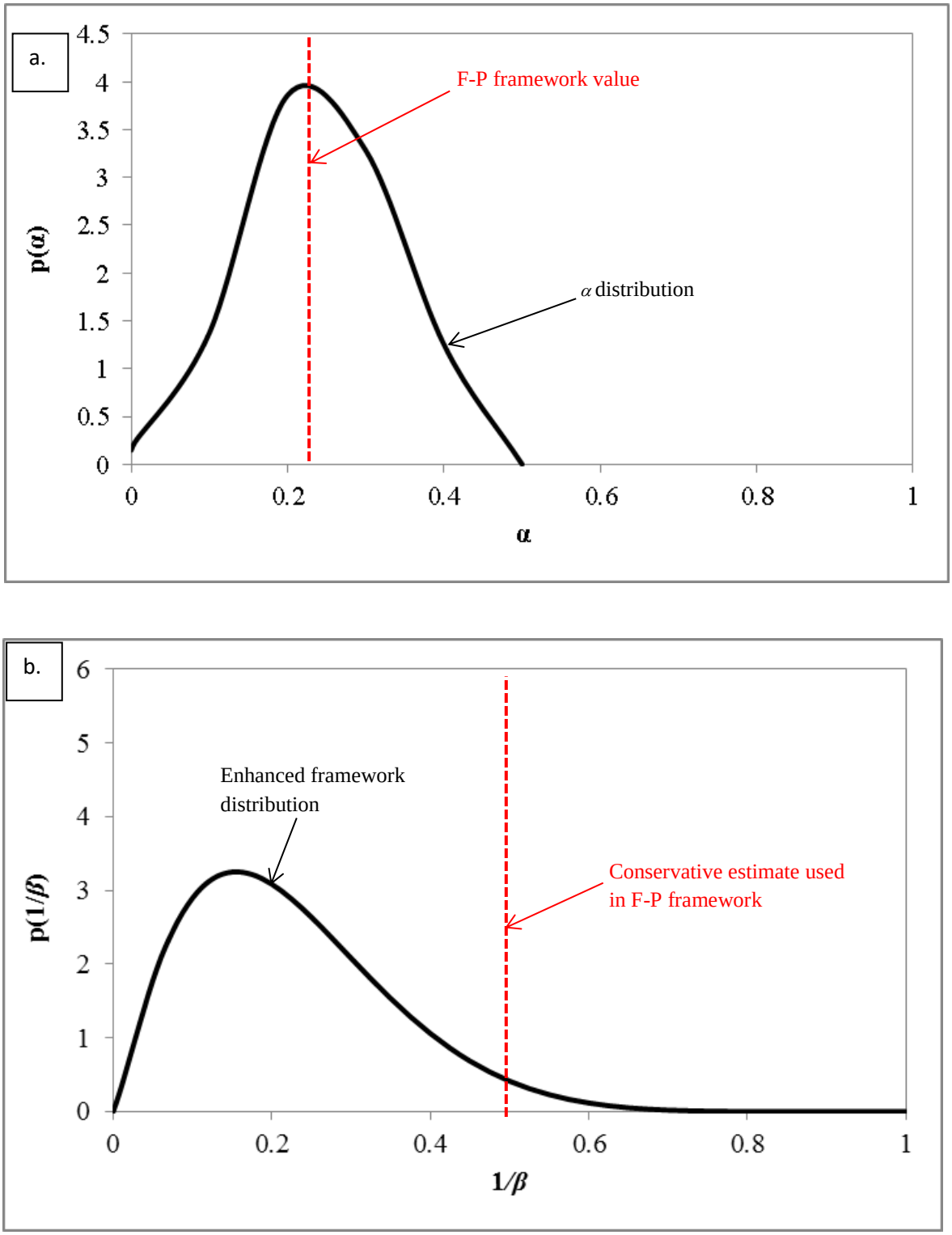

Figure 5.11: a) Sample probability distribution of α for a section of a hillslope derived from data in *Abaci and Papanicolaou* [2009]; b) Sample probability distribution of $1/\beta$ from time-integrated data from *Fox and Papanicolaou*[2008a].

gamma distributions depending on the types of sources and erosion processes [e.g. *Hilton et al.*, 2013]. However, the more general multivariate treatment of these other types of distributions can be quite challenging [*Krishnaiah and Rao*, 1961; *Tsionas*, 2004; *Das and Dey*, 2010]. Thus, for simplicity and computational expediency, the multivariate normal is the most feasible choice of distribution. In instances where the true distributions are roughly symmetric and not terribly heavy-tailed, as is the case for SASW (see Figure 5.12), the use of multivariate normal distributions should not have a substantial effect on inference based on the model. This however may not be the case if the distributions are actually extremely skewed.

Another potential shortcoming of this study is the use of algal and detrital signatures from other studies with similar watershed characteristics. Whilst this is common practice [e.g., *Olley*, 2002], the broad range of algal and detrital signature values reported in the literature introduces some uncertainty into estimated contributions and so a more detailed representation of algal and detrital signatures from field campaigns could be beneficial for further constraining the credible intervals of estimated contributions of eroded material. Nonetheless, the known flashiness of the SASW system [*Sloan*, 2013] and the careful placement of the stream tubes 2.4 km downstream the ditch location where algae usually grow ensured that the influence of the algal and detrital sources on the uncertainty of collected eroded material was kept to a minimum. Further, our approach was justified by the close agreement of estimated eroded material contributions with observations from other studies [*Abaci and Papanicolaou*, 2009; *Sutarto et al.*, 2014; *Ellis*, 2009; *Wilson et al.* 2012], as well as in parts by the qualitative agreement of the estimated trends in mean algal and detrital contributions with the unpublished data of *Papanicolaou et al.* [2014] showing an inverse relationship between runoff discharge and algal concentrations following an event.

Last but not least, the analyses using both frameworks suggested that source contribution estimates could be affected by the choice of α and β priors. Applying an α value outside the range of observed physical values led to a change in source contributions of 0.04 in some cases. This is 4% of the range of likely values of source contributions. This change did not affect inferences regarding the relative importance of terrestrial and instream sources in SASW. The prudent choice of tracers in SASW ensured that mean source signatures were separated far enough to minimize uncertainty in the mean contribution estimates due to α. The effect of β was however more pronounced, with changes in the widths of the 95% credible intervals of up to

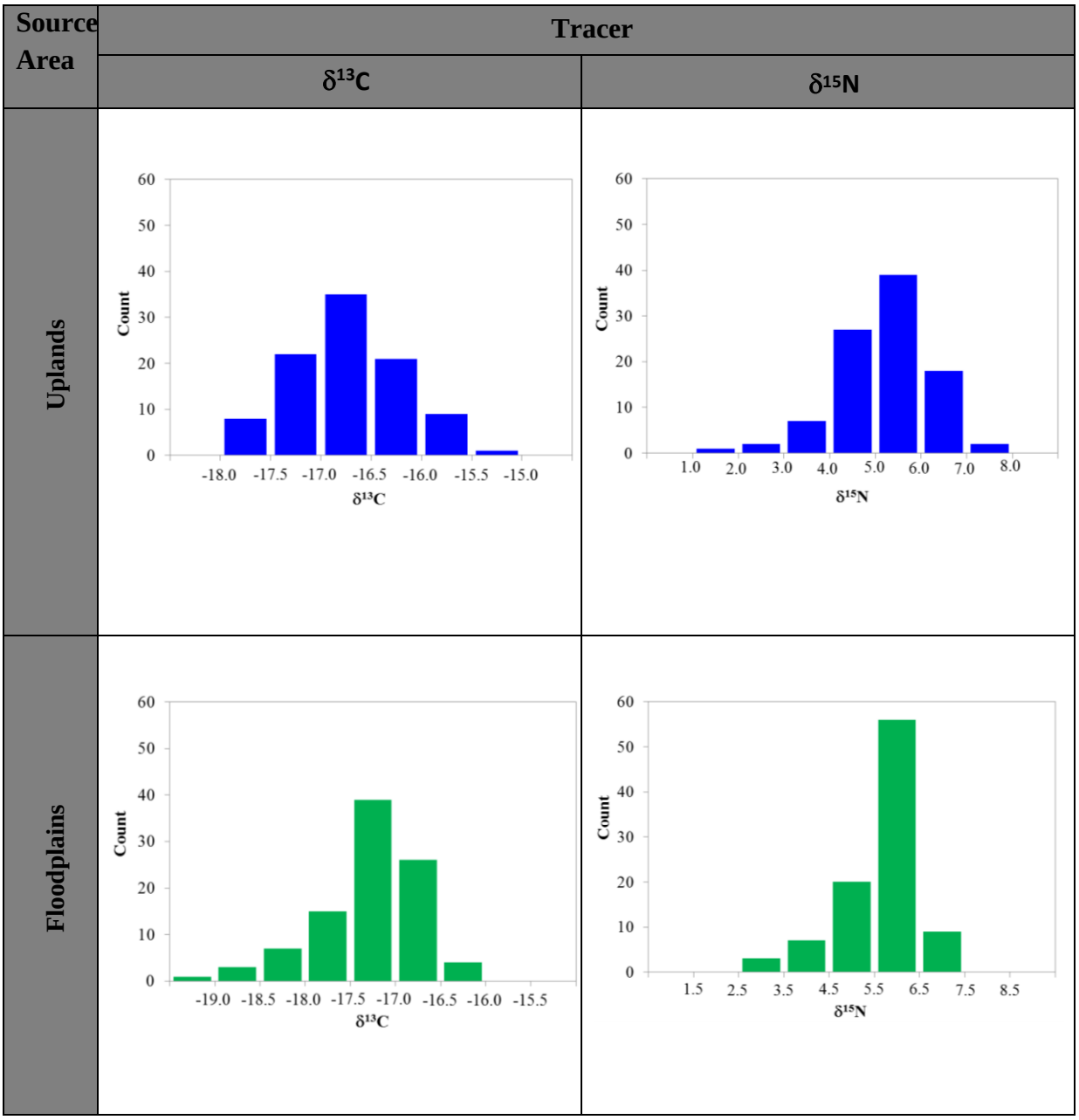

Figure 5.12: Sample histograms for SASW showing tracer distributions of upland and floodplain soils that are roughly symmetric and not terribly skewed

120% compared to that of 20% for α. The response of the two frameworks to the choice of both α and β suggests that careful attention must be paid in un-mixing studies to select priors that are reflective of conditions observed in the field. For datasets such as the SASW dataset, where mean source signatures are considerably far apart, inferences from the un-mixing results may not be significantly affected by the choice of priors [*Phillips and Gregg*, 2001].

Several studies have recommended the adoption of watershed management approaches that combine sediment source fingerprinting with sediment budgeting investigations (determination of flux magnitudes and links between sources, sinks, and yields) to provide a good understanding of sediment source dynamics for developing management strategies [*Gellis and Walling*, 2011; *Munkundan et al.*, 2012]. A key aspect of such an approach will be the synthesis of mechanistic numerical modeling with field-based investigations to obtain sediment budgets. Source fingerprinting techniques can be used in addition to conventional approaches of utilizing point field observations, such as sediment fluxes with time at the outlet, to calibrate and validate the numerical models, resulting in a more comprehensive synthesis of the two approaches and allowing the dynamics between the sources to be better replicated and understood. Knowledge of source dynamics is important for understanding how implemented BMPs will perform and how effective they will be in attaining targeted load reductions. Many cases have been reported in the literature where extensive BMPs were applied in agricultural areas to mitigate high magnitude events, and yet downstream water and sediment volumes increased for more than 10 years after the BMP installation [e.g., *Garrison and Asplund*, 1993]. In such cases, the following question arises: "are the BMPs ineffective or does it just take several years to see the downstream benefits of the BMPs?". The accommodation of natural variability in sediment fluxes in model predictions with the probabilistic treatment of α and β is important if uncertainty in erosion estimates and BMP performance are to be considered in the management efforts. α and β in the PDFs reflect variabilities in contributions, travel times and storage of material in the watershed which collectively affect BMP performance. In this regard, the probabilistic fingerprinting technique presented herein is invaluable and will allow uncertainty estimates to be quantified naturally based on the accommodation of the spatiotemporal variability in erosion processes discussed earlier.

References

Abaci, O., and A. N. T. Papanicolaou (2009), Long-term effects of management practices on water-driven soil erosion in an intense agricultural sub-watershed: monitoring and modelling, *Hydrol Process*, *23*(19), 2818-2837.

Albright, S.C., Winston, W.L., and Zappe, C.J. (2010), Data Analysis and Decision Making, South-Western CENGAGE Learning.

Balesdent, J., and A. Mariotti (1996), Measurement of soil organic matter turnover using ^{13}C natural abundance, in *Mass spectrometry of soils*, edited by T. Boutton and S. Yamasaki, pp. 83-111, Marcel Dekker, New York.

Baker, A. L., and K. B. Baker (1979), Effect of temperature and current discharge on the concentration and photosynthetic activity of the phytoplankton in the upper Mississippi River, *Freshwater Biology 9*: 191-198.

Baker D.B., R.P. Richards, T.T. Loftus, and J.W. Kramer (2004), A new flashiness index: characteristics and applications to midwestern rivers and streams, *J Am Water Resour As*, *40*, 503-522.

Bandeen-Roche, K., and D. Ruppert (1991), Source Apportionment with One Source Unknown, *Chemometr Intell Lab*, *10*(1-2), 169-184.

Bellanger, B., S. Huon, F. Velasquez, V. Valles, C. Girardin, and A. Mariotti (2004), Monitoring soil organic carbon erosion with delta(13)C and delta(15)N on experimental field plots in the Venezuelan Andes, *Catena*, *58*(2), 125-150.

Berhe, A., J. W. Harden, M. S. Torn, M. Kleber, S. D. Burton, and J. Harte (2012), Persistence of soil organic matter in eroding versus depositional landform positions. *J. Geophys. Res.*, 117(2), G02019.

Billheimer D. (2001), Compositional receptor modeling. *Environmetrics 12*, 451–467.

Blake W. H., K. J. Ficken, P. Taylor, M. A. Russell, D. E. Walling (2012), Tracing crop–specific sediment sources in agricultural catchments, Geomorphology 139–140, 322–329.

Bonn, B. A., and S. A. Rounds (2010), Use of stable isotopes of carbon and nitrogen to identify sources of organic matter to bed sediments of the Tualatin River, Oregon, U. S. Geological Survey, Report 2010-5154, 58 pp.

Bracken, L. J., and M. J. Kirkby (2005), Differences in hillslope runoff and sediment transport rates within two semi-arid catchments in southeast Spain, *Geomorphology*, *68*(3-4), 183-200.

Brooks, S. P., and A. Gelman (1998), General methods for monitoring convergence of iterative simulations, *Journal of Computational and Graphical Statistics*, *7*(4): 434-455.

Burns, D. A., J. J. McDonnell, R. P. Hooper, N. E. Peters, J. E. Freer, C. Kendall, and K. Beven (2001), Quantifying contributions to storm runoff through end-member mixing analysis and hydrologic measurements at the Panola Mountain Research Watershed (Georgia, USA), *Hydrol Process*, *15*(10), 1903-1924.

Cambardella, C. A., and E. T. Elliott (1992), Particulate Soil Organic-Matter Changes across a Grassland Cultivation Sequence, *Soil Sci Soc Am J*, *56*(3), 777-783.

Christophersen, N., and R. P. Hooper (1992), Multivariate-Analysis of Stream Water Chemical-Data - the Use of Principal Components-Analysis for the End-Member Mixing Problem, *Water Resour Res*, *28*(1), 99-107.

Collins, A. L., and D. E. Walling (2004), Documenting catchment suspended sediment sources: problems, approaches and prospects, *Prog Phys Geog*, *28*(2), 159-196.

Collins, A. L., and D. E. Walling (2007), The storage and provenance of fine sediment on the channel bed of two contrasting lowland permeable catchments, UK, *River Res Appl*, *23*(4), 429-450.

Collins, A. L., D. Walling, and G. Leeks (1998), Use of composite fingerprints to determine the provenance of the contemporary suspended sediment load transported by rivers, *Earth Surf Proc Land*, *23*(1), 31-52.

Cooper, R.J., T. Krueger, K.M. Hiscock, and B.G. Rawlins (2014), Sensitivity of fluvial sediment source apportionment to mixing model assumptions: A Bayesian model comparison, *Water Resour Res*, *50*, 9031-9047, doi 10.1002/2014WR016194.

Cooper, R.J., T. Krueger, K.M. Hiscock, and B.G. Rawlins (2015), High-temporal resolution fluvial sediment source fingerprinting with uncertainty: a Bayesian approach, *Earth Surf Proc Land*, 40, 78-92.

Cowles, M. K. (2013), *Applied Bayesian statistics: with R and OpenBUGS examples*, Springer.

Cruse, R., D. Flanagan, J. Frankenberger, B. Gelger, D. Herzmann, D. James, W. Krajewski, M. Kraszewski, J. Laflen, J. Opsomer, and D. Todey (2006), Daily estimates of rainfall, water runoff, and soil erosion in Iowa, *J Soil Water Conserv*, *61*(4), 191-199.

D'Haen, K., G. Verstraeten, B. Dusar, P. Degryse, J. Haex, and M. Waelkens (2013), Unravelling changing sediment sources in a Mediterranean mountain catchment: a Bayesian fingerprinting approach, *Hydrol Process*, *27*(6), 896-910.

Das, S., and Dey, D. K. (2010), On Bayesian Inference for Generalized Multivariate Gamma Distribution, Statistics and Probability Letters, 80(19-20), 1492-1499.

Davis, C. M., and J. F. Fox (2009), Sediment Fingerprinting: Review of the Method and Future Improvements for Allocating Nonpoint Source Pollution, *J Environ Eng-Asce*, *135*(7), 490-504.

de Rooij, G.H., and F. Stagnitti, (2004), Applications of the Beta Distribution in Soil Science, Chapter 20, In: *Handbook of Beta Distribution and Its Applications*, Eds: A.K Gupta and S. Nadarajah, CRC Press.

de Santisteban, L., J. Casalí, and J. López (2005), Evaluation of rill and ephemeral gully erosion in cultivated areas of Navarre (Spain), *International Journal of Sediment Research*, *20*(3), 270.

Delong, M. D., and J. H. Thorp (2006), Significance of instream autotrophs in trophic dynamics of the Upper Mississippi River, *Oecologia*, *147*(1), 76-85.

Delong, M. D., J. H. Thorp, K. S. Greenwood, and M. C. Miller (2001), Responses of consumers and food resources to a high magnitude, unpredicted flood in the upper Mississippi River basin, *Regul River*, *17*(3), 217-234.

Dermisis, D., O. Abaci, A. N. Papanicolaou, and C. G. Wilson (2010), Evaluating grassed waterway efficiency in southeastern Iowa using WEPP, *Soil Use Manage*, *26*(2), 183-192.

Dorris T. C., B. J. Copeland, and G. J. Lauer (1963), Limnology of the middle Mississippi River IV. Physical and chemical limnology of river and chute. *Limnol. Oceanogr*. 8, 79-89.

Douglas, G., M. Palmer, and G. Caitcheon (2003), The provenance of sediments in Moreton Bay, Australia: a synthesis of major, trace element and Sr-Nd-Pb isotopic geochemistry, modelling and landscape analysis, *Hydrobiologia*, *494*(1-3), 145-152.

Douglas, G., M. Palmer, G. Caitcheon, and P. Orr (2007), Identification of sediment sources to lake wivenhoe, south-east Queensland, Australia, *Mar Freshwater Res*, *58*(9), 793-810.

Dutton, C., S. C. Anisfeld, and H. Ernstberger (2013), A novel sediment fingerprinting method using filtration: application to the Mara River, East Africa, *J Soil Sediment*, *13*(10), 1708-1723.

Ellis, P.A. (2009), Non-point source pollution in an agricutultural watershed: upland soil erosion and instream sediment transport, MS Thesis, University of Iowa.

Evans, R. D. (2007), Soil nitrogen isotope composition, in *Stable isotopes in ecology and environmental science*, edited by R. Michener and K. Lajtha, pp. 83-98, Blackwell Publishing.

Ford, W. I., and J. F. Fox (2014), Model of particulate organic carbon transport in an agriculturally impacted stream, *Hydrol Process*, *28*(3), 662-675.

Fox, J. F. (2005), Fingerprinting using biogeochemical tracers to investigate watershed processes, PhD Thesis, University of Iowa.

Fox, J. F., and A. N. Papanicolaou (2007), The Use of Carbon and Nitrogen Isotopes to Study Watershed Erosion Processes, *J Am Water Resour As*, 43(4), 1047-1064.

Fox, J. F., and A. N. Papanicolaou (2008a), An un-mixing model to study watershed erosion processes, *Advances in water resources*, *31*(1), 96-108.

Fox, J. F., and A. N. Papanicolaou (2008b), Application of the spatial distribution of nitrogen stable isotopes for sediment tracing at the watershed scale, *J Hydrol*, *358*(1-2), 46-55.

Garrison, P.J., and T.R. Asplund. 1993. Long-term (15 years) results of NPS controls in an agricultural watershed upon a receiving lake's water quality. Water Science and Technology. 28(3-5):441-449.

Gellis, A. C., and D. E. Walling (2011), Sediment Source Fingerprinting (Tracing) and Sediment Budgets as Tools in Targeting River and Watershed Restoration Programs, *Geophys Monogr Ser*, *194*, 263-291.

Gellis, A. C., and R. Mukundan (2013), Watershed sediment source identification: tools, approaches, and case studies, *J Soil Sediment*, *13*(10), 1655-1657.

Gelman, A., J. B. Carlin, H. S. Stern, and D. B. Rubin (2004), *Bayesian data analysis*, CRC press, Chapman and Hall, London.

Giménez, R., O. Planchon, N. Silvera, and G. Govers (2004), Longitudinal velocity patterns and bed morphology interaction in a rill, *Earth Surf. Proc. Land. 29*, 105-114.

Govers, G., and J. Poesen (1988), Assessment of the interrill and rill contributions to total soil loss from an upland field plot, *Geomorphology*, *1*(4), 343-354.

Govers G., R. Giménez, and K. Van Oost (2007), Rill erosion: Exploring the relationship between experiments, modelling and field observations, *Earth-Science Reviews, 84 (2007)*, 87-102

Gumiere, S. J., Le Bissonnais, Y., Raclot, D., & Cheviron, B. (2011), Vegetated filter effects on sedimentological connectivity of agricultural catchments in erosion modelling: a review, *Earth Surf. Proc. Land.*, 36(1), 3-19.

Guzman, G., J. N. Quinton, M. A. Nearing, L. Mabit, and J. A. Gomez (2013), Sediment tracers in water erosion studies: current approaches and challenges, *J Soil Sediment*, *13*(4), 816-833.

Heaton, T. H. E. (1986), Isotopic Studies of Nitrogen Pollution in the Hydrosphere and Atmosphere - a Review, *Chem Geol*, *59*(1), 87-102.

Hilton, R. G., A. Galy, A. J. West, N. Hovius, and G.G. Roberts, Geomorphic control on the δ15N of mountain forests. Biogeosciences. 2013;10:1693-1705.

Jain, S. C. (1992), Note on Lag in Bedload Discharge, *J Hydraul Eng-Asce*, *118*(6), 904-917.

Jones, C. S., and Schilling, K. E. (2011), From agricultural intensification to conservation: sediment transport in the Racoon River, Iowa, 1916-2009, *J. Environ Qual*, *40*, 1911-1923.

Kendall, C., and J. J. McDonnell (1998), *Isotope Tracers in Catchment Hydrology*, Elsevier.

Krishnaiah, P.R. and M.M. Rao (1961), Remarks on Multivariate Gamma Distribution, *American Mathematical Monthly*, *68*, 342-346.

Lal, R. (2001), Soil degradation by erosion, *Land Degrad Develop*, *12*, 519-539.

Laceby, J. P., J. Olley, T. J. Pietsch, F. Sheldon, and S. E. Bunn (2014), Identifying subsoil sediment sources with carbon and nitrogen stable isotope ratios, *Hydrol Process*, DOI: 10.1002/hyp.10311.

Lingwall, J. W., W. F. Christensen, and C. S. Reese (2008), Dirichlet based Bayesian multivariate receptor modeling, *Environmetrics*, *19*(6), 618-629.

Link and Eaton (2012), On thinning of chains in MCMC, *Methods in Ecology and Evolution*, 3, 112-115.

Liu, Q.Q., L. Chen, J.C. Li, and V.P. Singh (2007), A non-equilibrium sediment transport model for rill erosion. *Hydrol Process*, *21*, 1074-1084.

Liu, G., M. Y. Yang, D. N. Warrington, P. L. Liu, and J. L. Tian (2011), Using beryllium-7 to monitor the relative proportions of interrill and rill erosion from loessal soil slopes in a single rainfall event, *Earth Surf Proc Land*, *36*(4), 439-448.

Lunn, D., D. Spiegelhalter, A. Thomas, and N. Best (2009), The BUGS project: Evolution, critique and future directions, *Stat Med*, *28*(25), 3049-3067.

Mann L. K. (1986), Changes in soil carbon after cultivation, Soil Sci., 142, 279-288.

Marshall, J. D., J. R. Brooks, and K. Lajtha (2007), Sources of variation in the stable isotopic composition of plants, in *Stable isotopes in ecology and environmental science*, edited by R. Michener and K. Lajtha, pp. 22-60, Blackwell Publishing

Massoudieh, A., A. Gellis, W. S. Banks, and M. E. Wieczorek (2013), Suspended sediment source apportionment in Chesapeake Bay watershed using Bayesian chemical mass balance receptor modeling, *Hydrol Process*, *27*(24), 3363-3374.

Matisoff, G., and P. J. Whiting (2011), Measuring Soil Erosion Rates Using Natural (Be-7, Pb-210) and Anthropogenic (Cs-137, Pu-239,Pu-240) Radionuclides, in *Handbook of Environmental Isotope Geochemistry, Vols 1 and 2*, edited by M. Baskaran, pp. 487-519, Springer, New York.

Matisoff, G., C. G. Wilson, and P. J. Whiting (2005), The Be-7/Pb-210(xs) ratio as an indicator of suspended sediment age or fraction new sediment in suspension, *Earth Surf Proc Land*, *30*(9), 1191-1201.

Michener, R. and K. Lajtha (2007), *Stable isotopes in ecology and environmental science*, Blackwell Publishing.

Moore, J. W., and B. X. Semmens (2008), Incorporating uncertainty and prior information into stable isotope mixing models, *Ecol Lett*, *11*(5), 470-480.

Mukundan, R., D. E. Walling, A. C. Gellis, M. C. Slattery, and D. E. Radcliffe (2012), Sediment Source Fingerprinting: Transforming From a Research Tool to a Management Tool, *J Am Water Resour As*, *48*(6), 1241-1257.

Neibling, W. H., and E.E. Alberts (1979), Composition and yield of soil particles transported through sod strips, *American Society of Agricultural Engineers Paper*, 79-2065.

Olley, J. M. (2002), Organic carbon supply to a large lowland river and implications for aquatic ecosystems, *International Association of Hydrological Sciences Publication* (276), 27-33.

Owens, P. N., D. E. Walling, and G. J. Leeks (1999), Use of floodplain sediment cores to investigate recent historical changes in overbank sedimentation rates and sediment sources in the catchment of the River Ouse, Yorkshire, UK, *Catena*, *36*(1), 21-47.

Palmer, M. J., and G. B. Douglas (2008), A Bayesian statistical model for end member analysis of sediment geochemistry, incorporating spatial dependences, *J R Stat Soc C-Appl*, *57*, 313-327.

Papanicolaou, A. N., J. F. Fox, and J. Marshall (2003), Soil fingerprinting in the Palouse Basin, USA, using stable carbon and nitrogen isotopes, *International Journal of Sediment Research*, *18*(2), 278-284.

Papanicolaou, A.N., M. Elhakeem, C.G. Wilson, C.L.Burras, L.T. West, H. Lin, B. Clark, and B.E. Oneal (2015), Spatial Variability of Saturated Hydraulic Conductivity at the Hillslope Scale: Understanding the Role of Land Management and Erosional Effect, *Geoderma, 243-244 (2015)*, 58-68.

Parnell, A. C., D. L. Phillips, S. Bearhop, B. X. Semmens, E. J. Ward, J. W. Moore, A. L. Jackson, J. Grey, D. J. Kelly, and R. Inger (2013), Bayesian stable isotope mixing models, *Environmetrics*, *24*(6), 387-399.

Phillips, J. M., M. A. Russell, and D. E. Walling (2000), Time-integrated sampling of fluvial suspended sediment: a simple methodology for small catchments, *Hydrol Process*, *14*(14), 2589-2602.

Phillips, D. L., and J. W. Gregg (2001), Uncertainty in source partitioning using stable isotopes, *Oecologia*, (2001) 127: 171-179.

Poesen, J., J. Nachtergaele, G. Verstraeten, and C. Valentin (2003), Gully erosion and environmental change: importance and research needs, *Catena*, *50*(2), 91-133.

Reynolds, C. S., and J.-P. Descy (1996), The production, biomass and structure of phytoplankton in large rivers, *Large Rivers 10(1-4)*: 161-187

Rinaldi, M., and S. E. Darby (2008), Modelling river-bank-erosion processes and mass failure mechanisms: Progress towards fully coupled simulations, in Gravel Bed Rivers 6—From Process Understanding to River Restoration Dev, Earth Surf. Processes,11, edited by H. Habersack et al., pp. 213–239, Elsevier, New York.

Sloan (2013), Hydrologic impacts of tile drainage in Iowa, MS Thesis, University of Iowa

Small, I. F., J. S. Rowan, and S. W. Franks (2002), Quantitative sediment fingerprinting using a Bayesian uncertainty estimation framework, in *Structure, Function and Management Implications of Fluvial Sedimentary Systems*, edited by F. J. Dyer, M. C. Thomas and J. M. Olley, IAHS Publication 276, pp. 443-450.

Small, I. F., J. S. Rowan, S. W. Franks, A. Wyatt, and R. W. Duck (2004), Sediment fingerprinting using a Bayesian approach yields a robust tool for environmental forensic applications, in *Forensic geosciences: principles, techniques and applications*, edited by K. Pye and D. A. Croft, Geological Society Special Publication 232, pp. 207-213.

Solomon, C. T., S. R. Carpenter, M. K. Clayton, J. J. Cole, J. J. Coloso, M. L. Pace, M. J. Vander Zanden, and B. C. Weidel (2011), Terrestrial, benthic, and pelagic resource use in lakes: results from a three-isotope Bayesian mixing model, *Ecology*, *92*(5), 1115-1125.

Sutarto, T., A. N. Papanicolaou, C. G. Wilson, and E. J. Langendoen (2014), Stability Analysis of Semicohesive Streambanks with CONCEPTS: Coupling Field and Laboratory Investigations to Quantify the Onset of Fluvial Erosion and Mass Failure, *J Hydraul Eng*, *140*(9).

Tayfur, G., and M.L. Kavvas (1998), Areally-averaged overland flow equations at hillslope scale, *Hydrological Sciences, 43*, 361-378.

Thompson, S., G. Katul, A. Konings, and L. Ridolfi (2011), Unsteady overland flow on flat surfaces induced by spatial permeability contrasts, *Adv. Water Res.*, *34*(8), 1049-1058.

Tsionas, E. (2004), Bayesian Inference for multivariate gamma distribution, *Statistics and Computing*, *14*, 223-233.

U.S. EPA (1999), Protocol for Developing Sediment TMDLs*Rep. EPA 841-B-99-004*, 132 pp, United States Environmental Protection Agency, Washington D.C.

Ussiri, D. A. N., and R. Lal (2009), Long-term tillage effects on soil carbon storage and carbon dioxide emissions in continuous corn cropping system from an alfisol in Ohio, *Soil Till Res*, *104*(1), 39-47.

Wallbrink, P. J., A. S. Murray, J. M. Olley, and L. J. Olive (1998), Determining sources and transit times of suspended sediment in the Murrumbidgee River, New South Wales, Australia, using fallout Cs-137 and Pb-210, *Water Resour Res*, *34*(4), 879-887.

Walling, D. E. (2005), Tracing suspended sediment sources in catchments and river systems, *Sci Total Environ*, *344*(1-3), 159-184.

Walling, D. E. (2013), The evolution of sediment source fingerprinting investigations in fluvial systems, *J Soil Sediment*, *13*(10), 1658-1675.

Walling, D. E., and C. M. Amos (1999), Source, storage and mobilisation of fine sediment in a chalk stream system, *Hydrol Process*, *13*(3), 323-340.

Walling, D. E., and A. L. Collins (2008), The catchment sediment budget as a management tool, *Environ Sci Policy*, *11*(2), 136-143.

Wilson, C. G., A. N. T. Papanicolaou, and K. D. Denn (2012), Partitioning fine sediment loads in a headwater system with intensive agriculture, *J Soil Sediment*, *12*(6), 966-981.

Wilson, C. G., R. A. Kuhnle, D. D. Bosch, J. L. Steiner, P. J. Starks, M. D. Tomer, and G. V. Wilson (2008), Quantifying relative contributions from sediment sources in Conservation Effects Assessment Project watersheds, *J Soil Water Conserv*, *63*(6), 523-532.

Yang, M. Y., D. E. Walling, J. L. Tian, and P. L. Liu (2006), Partitioning the contributions of sheet and rill erosion using beryllium-7 and cesium-137, *Soil Sci Soc Am J*, *70*(5), 1579-1590.

Yeshaneh, E., A. Eder, and G. Blöschl (2013), Temporal variation of Suspended Sediment transport in the Koga Catchment, North Western Ethiopia and environmental implications, *Hydrol Process*.

Yoneyama, T. (1996), Characterization of ^{15}N abundance in soils, in *Mass spectrometry of soils*, edited by T. Boutton and S. Yamasaki, pp. 205-224, Marcel Dekker, New York.

Yu, L., and F. Oldfield (1989), A multivariate mixing model for identifying sediment source from magnetic measurements, *Quaternary Research*, *32*(2), 168-181.

Appendix A: Sensitivity of the F-P and Enhanced Frameworks to the choice of α and β priors

We evaluate herein the sensitivity of the two frameworks to the choice of α and β priors using synthetic datasets for which the true source contributions are known. The synthetic datasets have been generated to allow us to evaluate the effects that the degree of heterogeneity on the landscape, source signature variability, the degree of differentiation between sources and number of sources considered have on the sensitivity of the model to the α and β priors. For each scenario examined, we first generate artificial signatures for the various sources (based roughly on the observed data for SASW), and then perform artificial mixing with known proportions as well as known α and β priors. Un-mixing analyses are then performed on the resultant mixtures with each framework assuming high α and β priors. The model predictions are then examined to evaluate the sensitivity of each framework to the selection of α and β and how these sensitivities are affected by the aforementioned properties. Table A.1 summarizes the examined scenarios. The results from the un-mixing analyses with the synthetic datasets are presented below.

A.1. Sensitivity of un-mixing analysis to the choice of high α priors.

Table A.1, Table A.2 and Figure A.1 summarize the un-mixing analyses performed to evaluate the effects of α. Since only terrestrial and instream sources are considered, results are only presented for terrestrial sources (the results for instream sources mirror those of the terrestrial sources). Overall, both frameworks predict similar mean source contributions regardless of the choice of α. This outcome is consistent with the findings of Phillips and Gregg [2001], who, using analytically-derived equations for uncertainty (verified with experimental data), showed that the mean relative source contributions were fairly independent of their uncertainty, and, thus, independent of the variability in the source signatures. Since the mean values of the source and mixture signatures as well as those of α are the same in both frameworks, the predicted mean source contributions should be the same, as observed. This is also consistent with the findings in Section 6.1.

Table A.1: Examined Scenarios and Parameters for the Synthetic Analyses

	Sensitivity priors examined	Source Area	Distribution parameter	Examined Scenarios* ($\delta^{13}C$, $\delta^{15}N$)			
				Baseline	Heterogeneity	Signature Variability	Signature Differentiation
α (uplands, floodplains)	F-P: α = (0.99,0.01) Enhanced: α ~ Dirichlet(9.9,0.1)	Upland	Mean	(-15.00, 3.20)	(-15.50, 4.00)	(-15.00, 3.20)	(-13.00, 3.20)
			Variance	(2.25, 2.25)	(2.25, 2.25)	(1.00, 1.00)	(2.25, 2.25)
		Floodplain	Mean	(-17.50, 7.00)	(-16.80, 6.00)	(-17.50, 7.00)	(-15.00, 7.00)
			Variance	(2.25, 2.25)	(2.25, 2.25)	(1.00, 1.00)	(2.25, 2.25)
		Instream	Mean	(-24.86,5.21)	(-24.86,5.21)	(-24.86,5.21)	(-27.36, 5.21)
			Variance	(2.25, 2.25)	(2.25, 2.25)	(1.00, 1.00)	(2.25, 2.25)
β (terrestrial / instream)	F-P: $1/\beta$ = 0.01; $1/\beta$ = 1 Enhanced: $1/\beta$ ~ Beta(0.1,9.9); $1/\beta$ ~ Beta(9.9,0.1)	Upland	Mean	(-15.00,4.50)	-	(-15.00,4.50)	(16.2, 4.5)
			Variance	(2.25, 2.25)	-	(9.00, 9.00)	(2.25, 2.25)
		Floodplain	Mean	(-17.28, 8.00)	-	(-17.28, 8.00)	(-17.60, 8.00)
			Variance	(2.25, 2.25)	-	(9.00, 9.00)	(2.25, 2.25)
		Instream	Mean	(-24.86,5.21)	-	(-24.86,5.21)	(-22.00, 5.20)
			Variance	(2.25, 2.25)	-	(9.00, 9.00)	(2.25, 2.25)

* α(0.5, 0.5) and β(0.5) were used in the synthetic mixing. 50 samples were generated for each source area.

Table A.2: Predicted Mean Terrestrial Source Contributions and 95% Credible Intervals (CI) for Synthetic Analyses examining the effects of Heterogeneity, Signature Variability and Signature Differentiation on model sensitivity to α

Scenario	Baseline		Less Heterogeneity		Less Signature Variability		More Signature Differentiation	
	Mean SC	95% CI	Mean SC	95% CI	Mean SC	95% CI	Mean SC	95% CI
True Value	**0.49**	-	0.495		**0.498**	-	**0.498**	-
Enhanced Framework	0.435	(0.23,0.64)	0.458	(0.28,0.62)	0.409	(0.30,0.51)	0.459	(0.35,0.56)
F-P Framework*	0.432	**(0.39,0.47)**	0.460	(0.42,0.50)	0.405	**(0.38,0.43)**	0.465	**(0.44,0.49)**

*Confidence intervals highlighted in red are those that do not bracket the true value of the source contribution

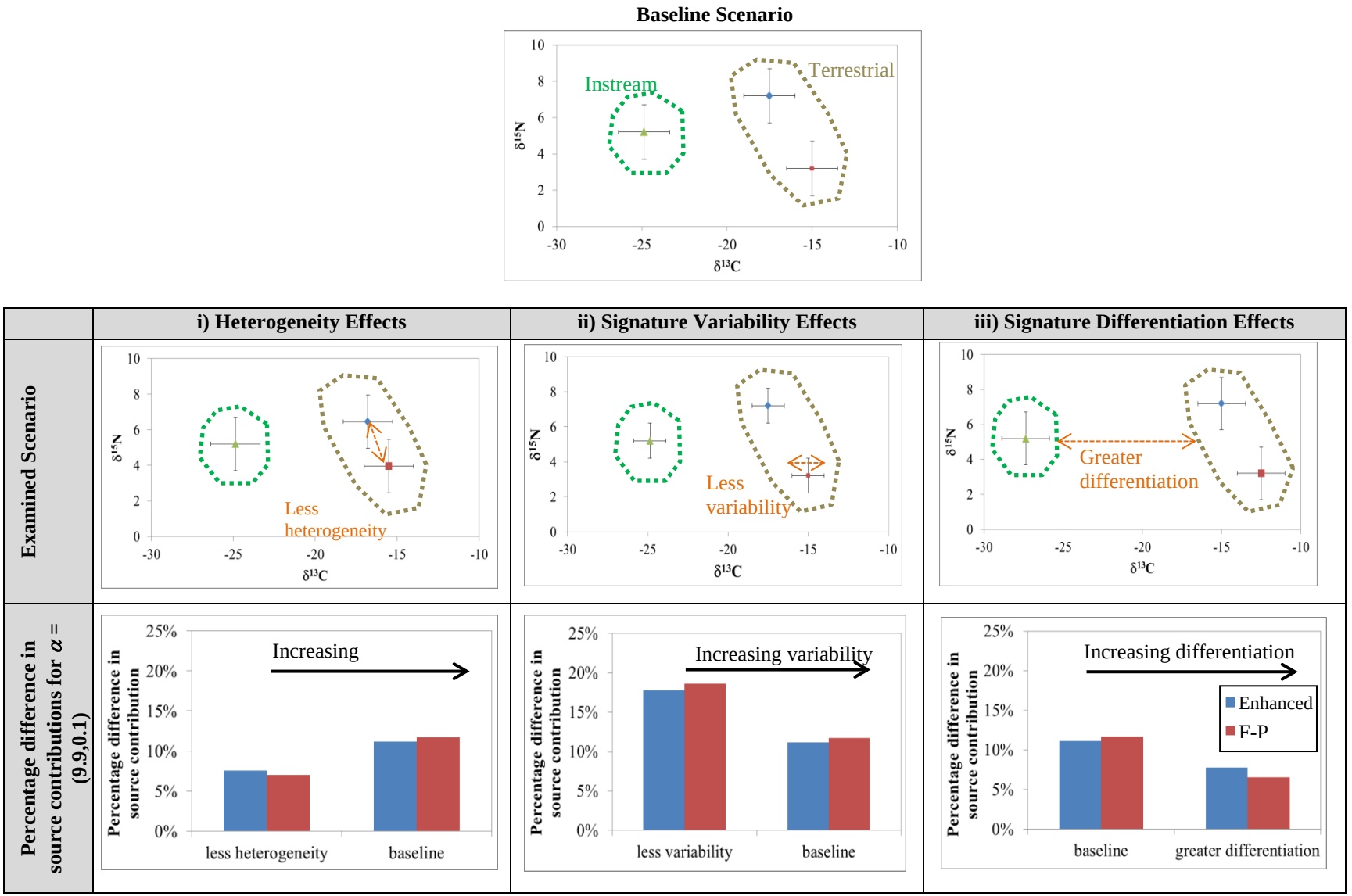

Figure A.1: Sensitivity of un-mixing analyses to the choice of α: a) influence of heterogeneity (less heterogeneity results in upland and floodplain signatures converging); b) signature variability effects; c) signature differentiation effects.

The primary difference between the two frameworks pertaining to the sensitivity to α, lay in their prediction of the 95% credible intervals. The enhanced framework consistently predicted wider 95% credible intervals than the F-P framework for the synthetic datasets. This was attributed to the used of probabilistic representation for α. As discussed in greater detail below, these differences have important implications to the robustness of the models in terms of model predictions and uncertainty quantification.

Effects of the degree of heterogeneity - Increasing heterogeneity within a source may result in increasing distinction between the signatures at different locations within the source experiencing different processes. The net effect of this is illustrated in Figure A.1, which shows that the sensitivity of mean source contribution predictions increases with increasing heterogeneity. The percentage difference between the true and predicted mean source contributions for the least heterogeneous scenario was ~8 % whereas it was ~11% for the most heterogeneous scenario. In each case, the enhanced framework was less sensitive to the choice of α than the F-P framework due to its larger 95% credible intervals. This is seen in Table A.2, where the 95% credible intervals predicted by the enhanced framework always bracketed the true source contribution. This was not the case for the F-P framework, whose 95% credible interval for the most heterogeneous (baseline) scenario, (0.39, 0.47), did not include the true contribution, 0.49, suggesting that the F-P framework is less robust than the enhanced framework. The increasing sensitivity with heterogeneity highlights the importance of adequately selecting and accounting for the effects of α in heterogeneous landscapes.

Effects of signature variability - Contrary to the effect of heterogeneity, increasing signature variability results in decreasing sensitivity of both frameworks to the choice of α. This is seen in Figure A.1 where the percentage difference between the true and predicted mean source contributions for the case with the least variability is ~18%, whereas it is ~11% for the case with the most variability. The decreasing sensitivity of the two frameworks with increasing signature variability is attributed to the greater role that uncertainty in the signatures plays in the un-mixing analysis, which overshadows the influence of spatial heterogeneity for which α is applied. The larger uncertainty in the data provides a greater degree of freedom in the models by providing larger sample spaces, thus reducing the influence of α and the model sensitivity to it. It is also noted for this set of analyses that the 95% credible intervals predicted by the enhanced framework are less sensitive than those predicted by the F-P framework (see Table A.2).

Similarly, unlike the enhanced framework, the F-P framework's 95% credible interval did not contain the true mean value in either of the scenarios examined, again confirming the better robustness of the enhanced framework.

Effects of differentiation between sources - Increasing differentiation between source signatures is generally known to result in better estimates of mean source contributions [*Phillips and Gregg*, 2001] by improving the ability of un-mixing models to distinguish between sources due to a reduction in the influence of signature variability and heterogeneity. This was the case for this set of analyses. Since the role of α is directly dependent on the roles of signature variability and heterogeneity (See Equations 4 and 6), the reduction in the influence of signature variability and heterogeneity is expected to minimize the role of α in determining the mean source contributions in the un-mixing analyses. This is noted in Figure A.1 where the sensitivity of mean source contributions to the choice of α is seen to diminish with increasing source signature differentiation. The reduction in the role of variability with increasing differentiation is further noted in Figure A.2, which shows a greater influence of variability when the source differentiation is lower (i.e. approximately 8% difference between the high variability and low variability scenarios) than when the source differentiation is greater (i.e. approximately 3% difference between the high variability and low variability scenarios). Likewise for this set of analyses, as noted from the 95% credible intervals, the enhanced framework is more robust than the F-P framework.

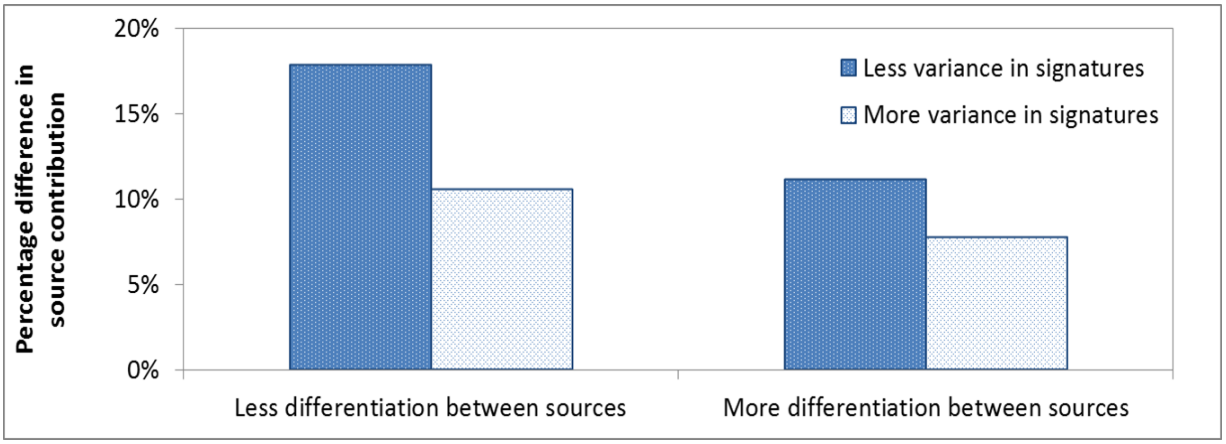

Figure A.2: Relative effects of source signature variability and differentiation on the choice of α. Increasing differentiation reduces model sensitivity to signature variability

A.2. Sensitivity of un-mixing analysis to the choice of high β priors.

Table A.1 and Figure A.3 summarize the un-mixing analyses performed to evaluate the effects of β. For each scenario we performed two sets of analyses assuming either considerable time integration ($1/\beta \sim 0.01$) or very little time integration ($1/\beta \sim 1$). Since the role of β in the mixing process only affects uncertainty in the signatures (see Equation 6), we do not present mean sources contributions from the analyses as these are unaffected. The performances of the two frameworks are evaluated based on the response of the widths of the 95% credible intervals.

As in the case of α, the enhanced framework consistently predicted wider 95% credible intervals than the F-P framework in these set of analyses because of the stochastic representation of β. The predicted trends and implications are presented in the following paragraphs.

Effects of signature variability - As seen in Figure A.3, the trend in the effects of signature variability on model sensitivity to the choice of β is similar to that of α i.e. there is a decrease in sensitivity with increasing signature variability for each framework. This is also attributed to the greater role that uncertainty in the signatures plays in the un-mixing analysis, which minimizes the influence of time integration effects for which β is applied. A further observation is that although the 95% credible intervals predicted by the enhanced framework are wider than the intervals for the F-P framework, the differences in the predictions of the two frameworks are smaller when considerable time integration is assumed (~15% - 16%) and greater when very little time integration is assumed (~28% - 45%). This agrees with the notion that the deterministic representation of β is justified when there is considerable time integration and so the two frameworks should converge under such a scenario. Conversely, the two frameworks should diverge when there is less integration, which is what is noted. Overall, the wider 95% credible intervals predicted with the enhanced framework makes it generally less sensitive comparatively to the F-P framework, which is more desirable from a management standpoint.

Effects of differentiation between sources - It has been alluded to above that increasing differentiation between the source signatures results in less uncertainty in source contribution estimates in un-mixing studies due to the diminishing role of source signature variability. The smaller uncertainty implies narrower 95% credible intervals of source contribution estimates, which will be relatively more sensitive to changes in the choice of β. On the contrary, a wider 95% credible interval will be less sensitive to choices of β. This is noted in Figure A.3, where

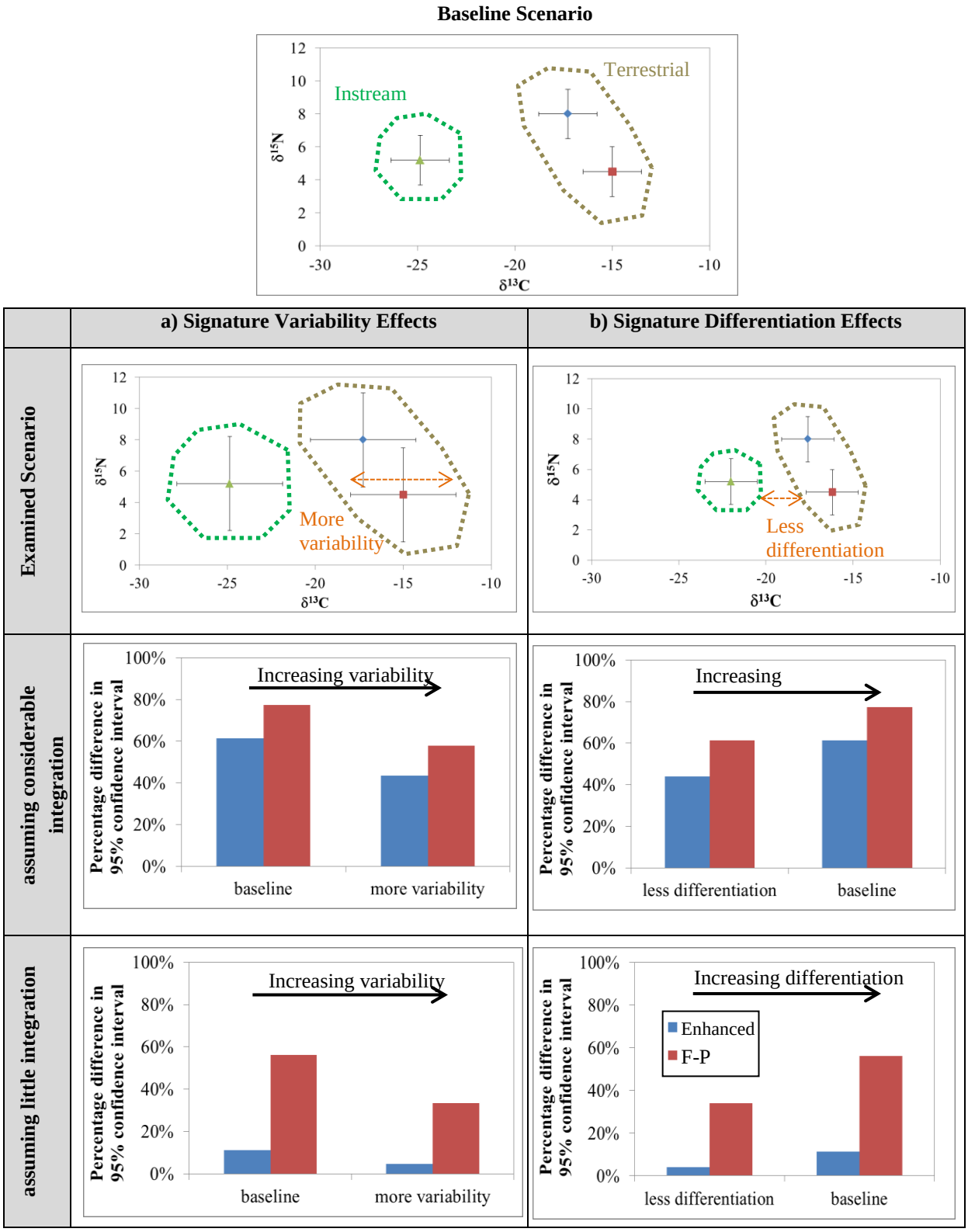

Figure A.3: Sensitivity of un-mixing analyses to the choice of β assuming little and considerable integration, respectively, under: a) signature variability effects; and b) signature differentiation effects

the sensitivity of both frameworks to the choice of β is seen to increase with increasing differentiation between the source signatures. The percentage difference in the width of the 95% credible increased from ~44%-60% to ~61%-77% when the spread between the source signatures was increased. It is also noted that the two frameworks tend to converge under the assumption of considerable time integration and diverge when little integration is assumed. Further, similar to all the other scenarios examined herein, the enhanced framework is generally less sensitive comparatively to the F-P framework.

A.3. Sensitivity of un-mixing analysis to the number of sources

We further examined the effect of one additional source on the choice of α and β based on the relative positions of the source signatures in SASW. The sensitivity of both frameworks increased with the additional source due to the relatively smaller contributions and confidence intervals per source. These are shown in Figure A.4. Since in general the inclusion of additional sources introduces a new complexity regarding the relative position of the sources, further analyses were not performed herein and will be the focus of future research on the roles of α and β.

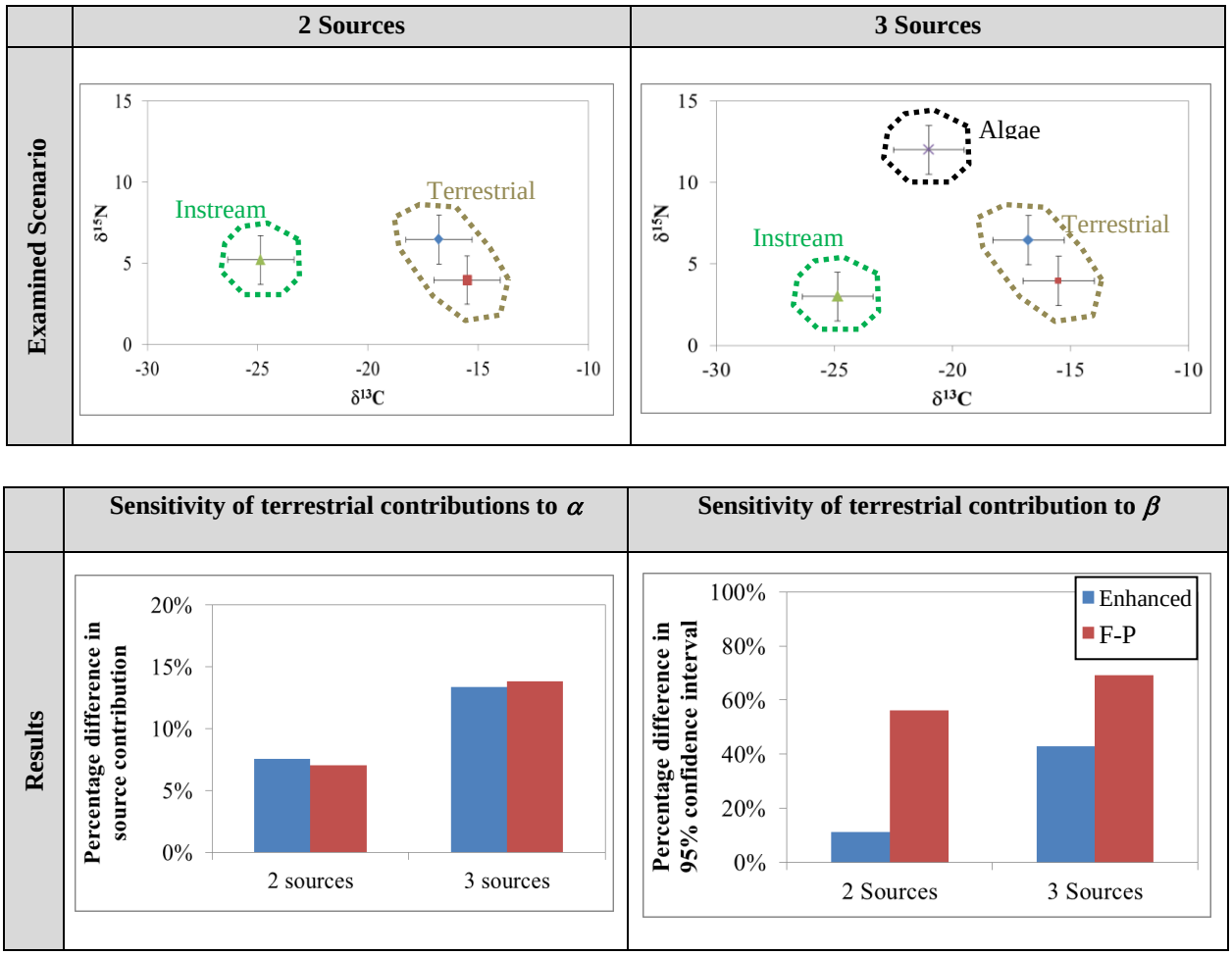

Figure A.4: Sensitivity of un-mixing analyses to the choice of α and β for scenarios with 2 and 3 sources

Chapter 6

Examination of characteristic scale units for flow and sediment at the Subwatershed scale

Abstract

A modeling framework to simulate water and sediment flux dynamics in intensively managed landscapes (IMLs) is presented in this study. The framework takes advantage of modeling advances from other IML studies to predict event-based water and sediment flux dynamics under different rainfall and land cover conditions in IMLs. An extensive field campaign covering terrestrial and instream fluxes at scales ranging from the plot to the watershed scale has been performed in the South Amana Sub-watershed, IA, and used to validate the framework model. The model has been found to adequately predict flow and sediment fluxes, as well as, the relative contributions of different source areas to the total sediment flux at the watershed outlet. The validated model was used to confirm the existence of a characteristic scale unit for sediment fluxes, and then, to compare it with the characteristic scale unit for water under different rainfall and land cover conditions. There were notable differences in the characteristic scale units for flow and sediment, with the flowrate and sediment concentration appearing to be correlated with the size of the characteristic scale unit for sediment. For the South Amana Sub-watershed, sediment source had a notable influence on the size of the sediment characteristic scale unit. It was smaller whenever instream source contributions for sediment fluxes were dominant, and larger whenever terrestrial source contributions were dominant. This was found to be due differences in sediment size characteristics between terrestrial and instream source contributions, which were finer and coarser, respectively. The identified sediment characteristic scale unit can be used as a parameterization unit for modeling larger watersheds. It is also an appropriate scale for monitoring watersheds and evaluating the performance of best management practices.

6.1. Introduction

Anthropogenic activities for food production and other life-sustaining services in regions such as the U.S. Midwest have significantly modified the landscapes on which they rely, transforming previous grasslands to lands that now display a considerable amount spatial heterogeneity and temporal variability in surface cover and material fluxes. The various practices have led to changes in the percentage of bare soil, soil surface roughness, flow pathways, soil fertilization, and erosion/depositional patterns, all of which change over the

course of a season, and from season to season [*Papanicolaou et al*., 2015; *Van Meter et al*., 2016]. Tile drain installation and channel straightening have modified material travel times and significantly altered the hydrologic regime of the systems, with more pronounced event-based dynamics compared to pre-Anthropocene conditions, which were mostly seasonal-driven [*Sloan*, 2013]. Consequently, the modifications and continued human intervention are believed to maintaining the systems in a non-stationary state in which material transport and transformation times are now much shorter, with implications to stream water quality and the continued productivity of the landscape [*Papanicolaou et al*., 2015; *Abban et al*., 2016; *Sullivan et al*., 2017].

Mitigating anthropogenic impacts will require an understanding of how the various land management practices are affecting critical zone processes. This calls for a two-pronged approach in which physical observations are combined with numerical modeling exercises to establish the causal relationships between key variables governing critical zone processes at different spatiotemporal scales. Although physical observations can enhance our understanding of critical zone process and reveal some cause-and-effect relationships, there is a limitation on how much inference can be drawn due to limited data in time and/or space. Physically-based numerical models have the potential to "fill in the blanks" and tease out direct cause-and-effect relationships between land surface modifications and fluxes across different spatiotemporal scales [*Michaelides and Wainwright*, 2008; *Brantley and Lebedeva*, 2011]. As such, they can be used to provide further insight on human impacts over a broad range of scales and how these can be mitigated appropriately.

Even though several models have been developed for simulating critical zone processes in intensively managed landscapes, most of the models have either focused on specific aspects or domains within the landscape or, in the case of watershed-scale models, have used lumped representations of terrestrial processes that are inadequate for capturing the event-based dynamics induced by human activity. For example, some models have been developed to simulate rainfall-runoff and soil erosion processes in terrestrial areas without considering flow and sediment transport within the stream network (e.g., WEPP, Dhara 3D, RUSLE, PALMs, etc), while others have been developed to simulate flow routing and sediment transport processes within the stream network without considering inputs from terrestrial areas (e.g. 3ST1D, CCHE1D, etc).

The separation or decomposition of watershed scale processes into terrestrial and instream processes may have some practical merits for the purposes of simulation [*Wu*, 2008]. However, since the two domains are highly interrelated, the lack of connectivity between the terrestrial and the instream processes introduces significant error in the water volume and sediment yield estimates along the stream network [*Conroy et al*., 2006; *Wu*, 2008; *Jensco et al*., 2009]. For example, accelerated upland erosion caused by anthropogenic activities may increase sediment yields to the channels, resulting in excess sedimentation and reduction in the transport capacity of the channels. Failure to account for this interaction will undoubtedly lead to the miscalculation of sediment transport rates within the channels and the watershed as a whole.

The use of lumped representation of terrestrial processes in some watershed models (e.g. SWAT, THREW, etc.) may be warranted at some scales and under certain conditions. *Woods et al*. [1995] identified a characteristic scale unit (i.e., a representative elementary area) above which local scale variabilities in landscape properties and rainfall characteristics played a minimal role on the average watershed hydrologic response. This scale unit was proposed as the fundamental building block for watershed modeling and considered appropriate for simulating water fluxes at larger scales [*Wood et al*., 1988]. Although a characteristic scale unit has been identified for water fluxes, no such scale unit has been explored for sediment fluxes. It is unknown whether or not such a scale unit exists, and if it does, what factors affect it and whether or not it differs from the scale unit for water fluxes. The existence of a characteristic scale unit for sediment fluxes would provide two key benefits: (a) a parameterization unit for simulating sediment fluxes at the watershed scale, and; (b) a landscape unit at which field observations could be used to monitor the impacts of human activities on mean trends in watershed sediment fluxes.

Besides hampering our ability to understand and mitigate the impact of anthropogenic activities in intensively managed landscapes, the lack of a reliable method for predicting fluxes of water and sediment from the plot scale to the watershed scale is also a key reason why a characteristic scale unit for sediment fluxes has not yet been explored. Identification of a characteristic scale unit must necessarily involve the examination of fluxes from the plot scale to the watershed scale, taking into consideration all flux pathways as well as connectivities between terrestrial and instream sources; only a systematic examination of the behavior of the mean sediment flux response with scale can reveal the threshold at which it becomes stationary (or

"pseudo-stationary") and is not significantly influenced by local-scale variations in landscape and rainfall properties.

There is a need, therefore, for the development a modeling framework that is capable of capturing all the relevant pathways and connectivities between terrestrial and instream sources, as impacted by humans, and the event-based dynamics that control fluxes from the plot scale to the watershed scale in intensively managed landscapes. Not only will such a framework help us understand how the various land management practices are affecting critical zone processes, it will also allow us to investigate the existence of a characteristic scale unit for sediment fluxes. It is hypothesized herein that a characteristic scale unit for sediment fluxes does indeed exist, but it differs from the characteristic scale unit for water fluxes due to differences in the travel times and processes involved.

The goals of this study are twofold: (a) to develop and validate a modeling framework that captures the pathways, connectivities, and event-based dynamics prevalent in intensively managed landscapes, for use in simulating fluxes of water and sediment from the plot scale to watershed scale, and; (b) to use the framework to investigate the existence of a characteristic scale unit for sediment fluxes, and factors that affect the scale unit. The framework is developed and tested in the South Amana Sub-watershed (SASW) located in the headwaters of the Clear Creek Watershed, IA, which is part of the NSF's Critical Zone Observatory for Intensively Managed Landscapes. The study couples state-of-the-art terrestrial, instream, and sediment sourcing models, which collectively encompass the key processes that occur in intensively managed landscapes. Observations from the plot scale to the sub-watershed scale are used to validate the coupled model, which is then used to examine fluxes under different land cover and rainfall conditions in SASW. Variations in the specific sediment discharge with scale are finally used to examine the characteristic scale unit.

6.2. Modeling Framework for Intensively Managed Landscapes

6.2.1. Overview

The modeling framework presented herein employs a coupled model for intensively managed landscapes [*Abban et al*., 2011] that utilizes the well-established watershed erosion prediction project (WEPP) model for representing terrestrial processes [*Flanagan et al*., 2007] and the widely validated Steep Stream Sediment Transport 1D (3ST1D) model for representing

instream processes [*Papanicolaou et al*., 2004]. For ensuring that the connectivities and interactions between terrestrial and instream sources are adequately represented, the framework also employs a Bayesian sediment sourcing model for intensively managed landscapes [*Abban et al*., 2016] to make sure that the model representation of the watershed predicts relative source contributions that fall within ranges they are most probable to occur in, under different land cover and rainfall conditions.

An overview of the modeling framework is illustrated in Figure 6.1. The modeling framework employs both terrestrial and instream field observations at different spatial scales for calibrating and validating the coupled models. It calibrates and validates fluxes at the plot scale, at the hillslope scale, at the interface between terrestrial and instream sources (i.e., at the banks), and at selected points within the channel network and the watershed outlet. By doing so, it deviates from most frameworks that typically calibrate watershed models only at selected points within the channel network. A further improvement is the use of observed tracer signatures of terrestrial sources, instream sources, and eroded material in an un-mixing model for calibrating and validating the predicted proportions of terrestrial and instream material (see the dashed, red box in Figure 6.1). Although the issue of equifinality in model predictions of sediment fluxes pertaining to source contributions has been raised in the past [e.g., *Belmont et al*., 2014], this is the first time that an approach has been developed to directly address the issue.

In addition to the comprehensive observational methodology used in the framework, the models employed also address critical watershed processes pertinent to intensively managed landscapes that are ignored or only partially addressed in other existing models. At the plot scale, *Abban et al*. [2017] recently identified a threshold scale below which surface roughness would increase with raindrop impact. A practical implication of the finding was that a rough surface manifesting decay in roughness with rainfall would approach a threshold roughness and not decay to smooth conditions. In the study, the threshold was identified to be of an order around 5 mm. Although roughness decay with cumulative rainfall is represented in a number of models, no official threshold has ever been established or formally specified based on experiments designed specifically for that purpose. The enhanced WEPP model utilized in this study enforces the threshold over the course of a season as roughness decays.

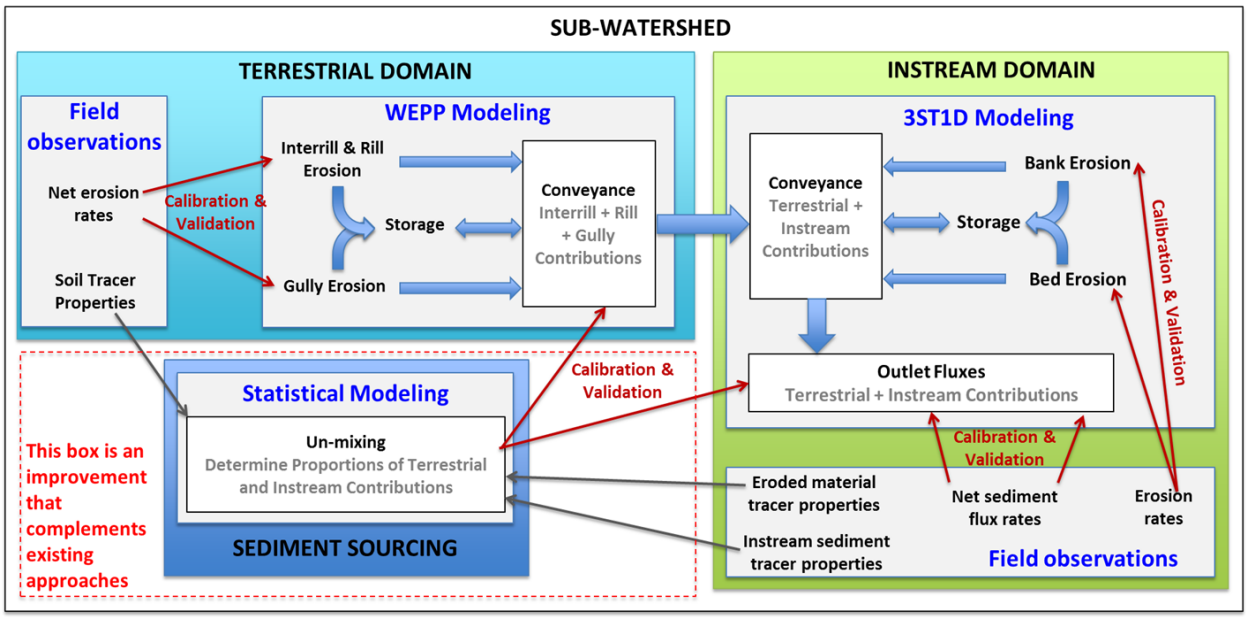

Figure 6.1: Conceptual Modeling Framework

The recent study by *Papanicolaou et al*. [2018] investigated the implications of the space and/or time invariant resistance assumption, commonly adopted in many terrestrial models, on runoff hydrographs at the hillslope scale. Modeling runoff from a storm event on an intensively managed hillslope in Jasper County, IA, it was found that the assumption could lead to errors in runoff rate predictions, with the peak rate departing from the observed rate by as much as 60%. The investigated hillslope was spatially heterogeneous in terms of cover, with portions covered by isolated roughness and vegetated filter strips. Although the assumption was found to be valid under some conditions for high magnitude events, only a space/time variant resistance representation was able to correctly replicate overland flow rates and runoff hydrographs at the hillslope outlet under all conditions. Thus, the space/time variant resistance representation of surface roughness effects, presented by *Papanicolaou et al*. [2018] for intensively managed landscapes, is adopted herein for the enhanced WEPP model used in the framework.

At the watershed scale, *Abban et al*. [2016] introduced an enhanced Bayesian sediment fingerprinting model for identifying sources of eroded material in intensively managed landscapes. The approach incorporated two key parameters important for intensively managed landscapes, but ignored in other sediment sourcing models. The two parameters, α and β,

collectively accounted for the spatial origin attributes of sources and the travel history of eroded material delivered to the watershed collection point. A crucial aspect of the representations of these two parameters was their ability to capture the effects of landscape heterogeneity on variabilities in source contributions, their pathways, delivery times and storage within the watershed. Thus, by accounting for the two parameters, *Abban et al*. [2016] were able to capture the connectivities between the sediment sources and the watershed outlet at different times of the season and for different events. The performance of the model was extensively tested in an intensively managed landscape in Clear Creek, IA. The *Abban et al*. [2016] model is incorporated into the framework presented herein for ensuring that the connectivities between terrestrial and instream sources are adequately captured and that their relative contributions to the net fluxes from the watershed are correctly predicted.

The description of the aforementioned models presented herein is brief to provide the reader with a general understanding of the important model components of the framework. The reader is referred to the works by *Papanicolaou et al*. [2010], *Abban et al*. [2011], *Papanicolaou et al*. [2015], *Abban et al*. [2016], and *Papanicolaou et al*. [2018] for a more in-depth description of the models.

6.3. Methodology

6.3.1. Study Site

The framework is developed and tested in the South Amana Sub-watershed (SASW), located in the headwaters of the Clear Creek Watershed in Southeastern Iowa, USA. Clear Creek has recently become a U.S. National Science Foundation Intensively Managed Landscapes-Critical Zone Observatory (IML-CZO) [http://criticalzone.org/iml/]. SASW is a 26 km² sub-watershed that contains 1st- and 2nd-order channels. The terrestrial and instream contributions in SASW have been observed to vary over the course of a season in response to changing hydrologic forcing and land use/land cover [*Abaci and Papanicolaou*, 2009; *Wilson et al*., 2012]. The hillslope gradients range between 0.5% and 8% with an average of 4%. The land use is predominantly row-crop agriculture with two-year corn-soybean rotations, and the dominant soil texture is silty clay loam [*Abaci and Papanicolaou*, 2009]. The average annual precipitation is ~890±220 mm/yr [*Dermisis et al*., 2010], with convective thunderstorms occurring between May and September with the peak month being June [*Cruse et al*., 2006].

6.3.2. Model Validation

Data for the model validation was collected in 2014 and 2017 from a series of terrestrial and instream field campaigns. This dataset was complemented with data from field studies undertaken in 2007 by *Abaci and Papanicolaou* [2009] and presented in *Abban et al.* [2016]. Rainfall data corresponding to storm events that occurred during the monitoring periods were obtained from a digital rain gauge situated within the sub-watershed. The datasets and the sampling methods are described below.

6.3.2.1. Terrestrial Sampling & Experiments

Plot scale experiments were performed in the summer of 2014 at selected sites located within established IML-CZO activity centers in the Clear Creek watershed. The sites were selected to be representative of the land use in the region. They were also selected to take advantage of other monitoring instruments in the watershed that were collecting continuous data on surface and subsurface flows. Two of the activity centers are shown in Figure 6.2. Table 6.1 summarizes the locations and characteristics of the plots where the experiments were performed.

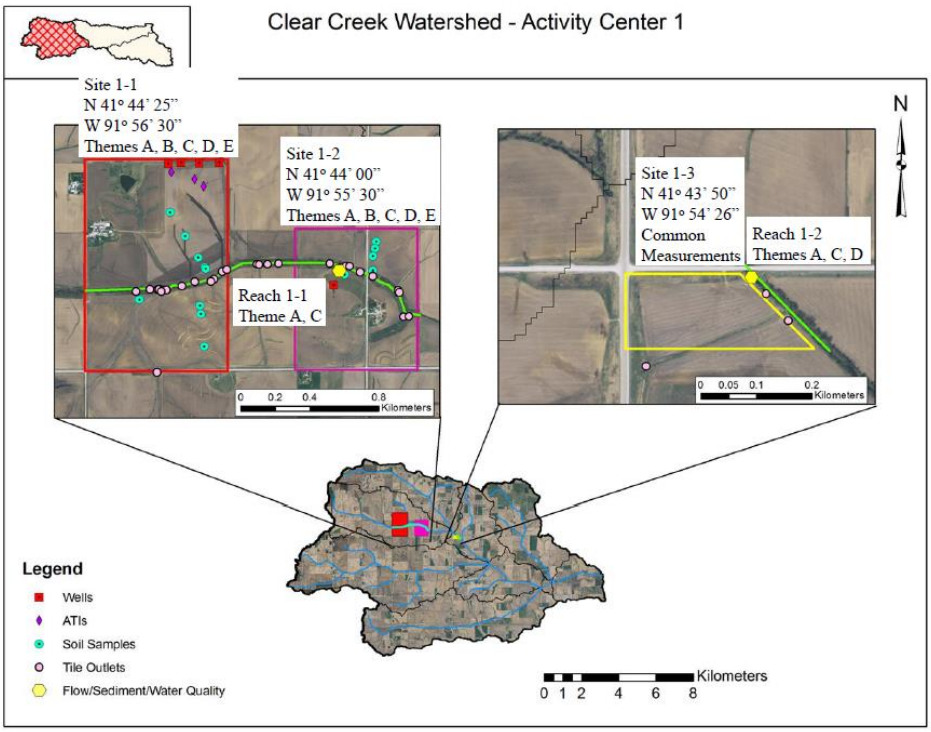

Figure 6.2: Activity Center where terrestrial experiments were performed

Table 6.1: Characteristics of plots where terrestrial experiments were performed

Plot	Coordinates	Management	Gradient	Flow type	Soil Series
1	41.7374, -91.9439	Corn-Soybean Rotation	8.5%	Rill-Interrill	Tama
2	41.7357, -91.9402	Corn-Soybean Rotation	2.5%	Rill-Interrill	Colo
3	41.7296, -91.7373	Vegetation	15.4%	Planar	Fayette
4	41.7359,- 91.9309	Bare	10%	Planar	Colo

The experiment at each site was performed on a plot approximately 7 m long by 1.8 m wide. Rainfall was applied to the plot using Norton Ladder Multiple Intensity Rainfall Simulators designed by the USDA-ARS National Soil Erosion Research Laboratory, IN. The setup is shown in Figure 6.3. For each experiment, three rainfall simulators were mounted in series over the plot and approximately 2.5 m atop the plot surface in order to ensure that raindrop terminal velocity was reached. Water was continuously pumped from a water tank under controlled pressure, and uniform rainfall was applied through oscillating VeeJet nozzles which provided spherical drops with median diameters between 2.25-2.75 mm and an average rainfall intensity of 60 mm/hr. The distribution of raindrop sizes generated by the rainfall simulators was calibrated using a disdrometer and followed a Marshall-Palmer distribution [*Elhakeem and Papanicolaou*, 2009].

Flow rate measurements were obtained at the plot outlet at regular time intervals using a 20° v-notch weir. Concurrently, samples for sediment concentration were taken via discrete sampling of runoff. The measurements were taken during the rising limb phase of the hydrograph and at steady state. Flow conditions at the weir were monitored continually until steady state conditions developed. Then rhodamine dye was used to estimate the flow velocity from the top of the plot to the outlet following the approach of *Abrahams et al*. [1986]. The sediment concentration samples obtained in the field were processed in the lab after each experiment. The mass of sediment within each sample was obtained via filtration and drying, and then used to estimate the sediment concentration corresponding to each flow rate measurement. Pictures from the plot experiments are also shown in Figure 6.3.

Figure 6.3: Pictures from terrestrial field experiments performed in 2014 showing the experimental setup, various land covers examined, and sampling methods

Samples were also extracted from several terrestrial locations in 2007 for the sediment sourcing analyses. Terrestrial soil samples were collected from five fields distributed within the watershed that were representative of the land uses, soil types, and topography [*Abban et al*., 2016]. In each field, surface soil samples (0-5 cm) were collected along 75 to 100 m long planar transects located along the downslope to capture planar and downslope heterogeneity from the summit to the floodplain. In all fields, three transects were located on the summit, backslope and toeslope, respectively, whilst two transects were located on the floodplain. The upslope soil series are predominantly Tama, while the floodplain soil series are Colo. The tracer signatures of the collected samples, i.e., the $\delta^{13}C$ and $\delta^{15}N$ signatures of the fine grained portion (<53 μm) of each sample, were quantified using mass spectrometry [*Fox and Papanicolaou*, 2008].

6.3.2.2. Instream sampling & experiments

Several instream flow rate and sediment concentration measurements were collected in the summers of 2014 and 2007 for model calibration and validation purposes. Dye tracer experiments were also performed in summer of 2017 to determine the flow travel times and dispersive properties under different conditions. The sampling locations, along with some of the instruments used for the various experiments, are shown in Figure 6.4 (see Figure 6.2 for the site coordinates).

The flow rate measurements were obtained via two different approaches. The first approach was based on USGS methods, and involved the use of a pressure transducer and an established stage-discharge relationship to provide continual measurements (~5 min intervals) of flow stage and discharge at the watershed outlet. The pressure transducer was installed within a stilling basin to minimize the effects of waves on the measurements. The second approach involved the use of the Flo-Mate2000^{TM} electromagnetic flow velocity meter and area-velocity method for flow discharge estimation. The six-tenths method was used to obtain mean velocity measurements within each section with a wading rod. This second approach was used at low flows and after storm events when conditions were deemed safe for wading.

Suspended sediment concentrations were obtained using automated suspended sediment samplers and discrete sampling techniques. The automated samplers were installed at three locations, one at the watershed outlet, and the other two at locations approximate 2 and 3 miles upstream of the outlet. These samplers were triggered at the start or during an event, and were

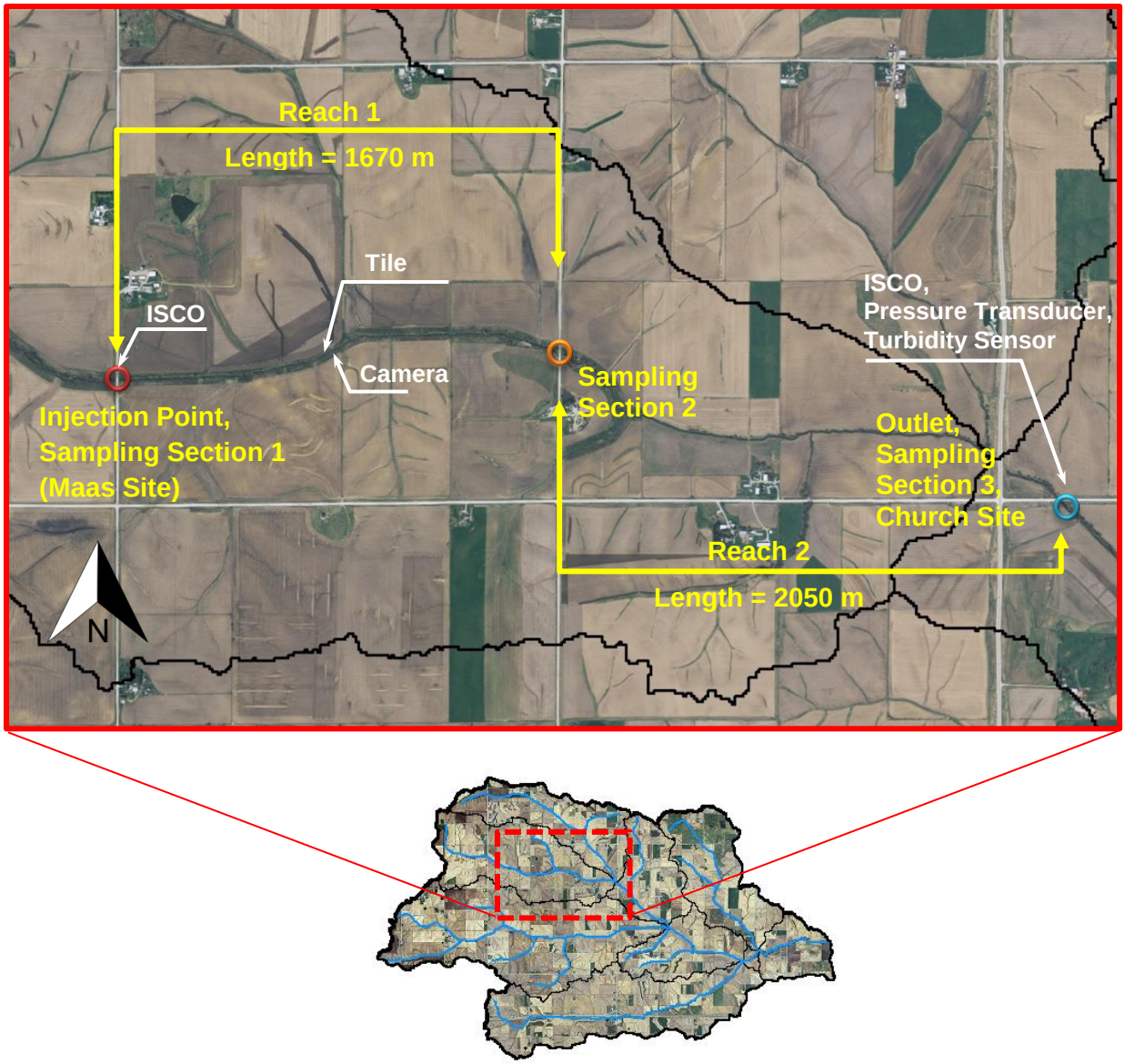

Figure 6.4: Instream sampling locations and instrumentation

set to collect samples at intervals ranging from 5 to 15 mins. Sampling tubes extended from the auto-samplers to inlet nozzles located in the flow at 10 and 70 cm above the bed [*Edwards and Glysson*, 1999]. In addition to the automated samplers, discrete samples were collected by lowering buckets into the center of the flow from bridges near the samplers.

Dye tracer experiments were performed to measure travel time and dispersion in streams following the USGS established method [*Hubbard et al*., 1982]. For each experiment, pre-determined, safe levels of dye were introduced at a bridge approximately 2 miles upstream of the sub-watershed outlet. Then, at two separate locations downstream of the injection point (i.e., ~1.7 and 3.8 km downstream), discrete samples were collected continually at intervals ranging from 5-10 mins by lowering buckets into the center of the flow from bridges. The stream was monitored visually for passage of the dye, and sampling was continued for 30-45 mins after the dye could no longer be detected by the eye. The dye concentration in the each sample was determined within 24 hours of the experiments using a Trilogy Laboratory Fluorometer.

The tracer signatures of instream sediment sources (the $\delta^{13}C$ and $\delta^{15}N$ signatures of the fine grained portion) were characterized using discrete sediment samples collected during non-flood flows following the *Olley* [2002] approach. Concurrently, sampling of the total transported eroded material at the sub-watershed outlet was done using stream tubes, which are described in detail by *Fox and Papanicolaou* [2007]. Two to four stream tubes were placed close to the bed of the stream outlet to continuously capture suspended eroded material over periods of approximately one month each. Stream conditions were such that the tubes primarily captured contributions from the storms that occurred during the period.

Other measurements within the sub-watershed that were considered for the model validation were the bank erosion measurements by *Sutarto et al*. [2014], and tile flow measurements made during the summer of 2016. The bank erosion measurements were used to provide bank erodibility values for the instream model. The tile flow measurements were performed using a calibrated time-lapse camera, which produced the flow stage within the tile that was then used to estimate the discharge. These data were used to assess the relative importance of tile flows to stream flow rates during storm events.

Figure 6.5 presents pictures taken during various instream monitoring exercises and device installations.

Figure 6.5: Pictures taken during various instream monitoring exercises and device installations

6.3.3. Determination of Characteristic Scale Unit

On validation of the modeling framework, a consistent methodology was used to examine the characteristic scale unit in the South Amana Sub-watershed for both flow and sediment for an ensemble of storm events, following the approach by *Woods et al.* [1995]. The approach defines the characteristic scale unit as the scale at which the average watershed response is invariant or varies only slowly with increasing watershed area. In the approach, sub-catchment specific outputs are arranged in order of increasing sub-catchment area. Then, a moving window that captures the sub-catchment specific outputs with area is considered. The variance and the standard deviation of the outputs within each window are computed. As the area of the sub-catchments increases, the variance and standard deviation of the specific output decrease to a point where they do not change or change slowly – this point is the characteristic scale unit.

This study considered a moving window whose size corresponded to the total area of five consecutive sub-catchments in the ordered list. A step size of one was used. Since all the predicted flow and sediment concentration values were the same order of magnitude, a threshold variance of 0.0005 (which was less than 1/1000 of the typical peak variance) was used to identify the characteristic scale unit for all cases. Areas where the variance within the window fell below the threshold were considered to be larger than the characteristic scale unit.

The characteristic scale unit was examined for an ensemble of storm events that occurred in South Amana over a period of 8 years, from 2007 to 2015, in the months of June and July. A summary of the characteristics of these storms are presented in Table **6.2** – the data were obtained from the digital rain gauge located within the sub-watershed. The months of June and July were selected to allow for the examination of the effects of both rainfall and land cover on the characteristic scale unit; differences in rainfall and land cover have been found to be statistically significant between the two months [*Abban et al.*, 2016].

The land cover data corresponding to the months of June and July for the characteristic scale unit simulations were obtained from Enhanced Thematic Mapper satellite imagery (Landsat 8; http://earthexplorer.usgs.gov/). False color images from 2014 showing the extent and degree of vegetation cover around mid-June and mid-July in SASW, are presented in Figure 6.6.

Table 6.2: Summary of storm events considered in characteristic scale unit analyses

Month	Event	Year	Peak Intensity (mm/hr)	Total Duration	Effective Peak Duration
June	1	2014	51.88	6.67	0.88
	2	2007	60.28	5.75	0.46
	3	2007	60.56	7.25	0.97
	4	2015	29.44	2.33	1.06
	5	2015	69.08	4.50	0.92
	6	2018	53.76	2.75	1.13
July	1	2014	62.84	2.75	0.70
	2	2014	56.56	2.82	0.40
	3	2007	22.08	7.25	1.41
	4	2013	46.24	6.25	0.86
	5	2008	26.20	8.75	1.66
	6	2015	51.80	2.67	0.55

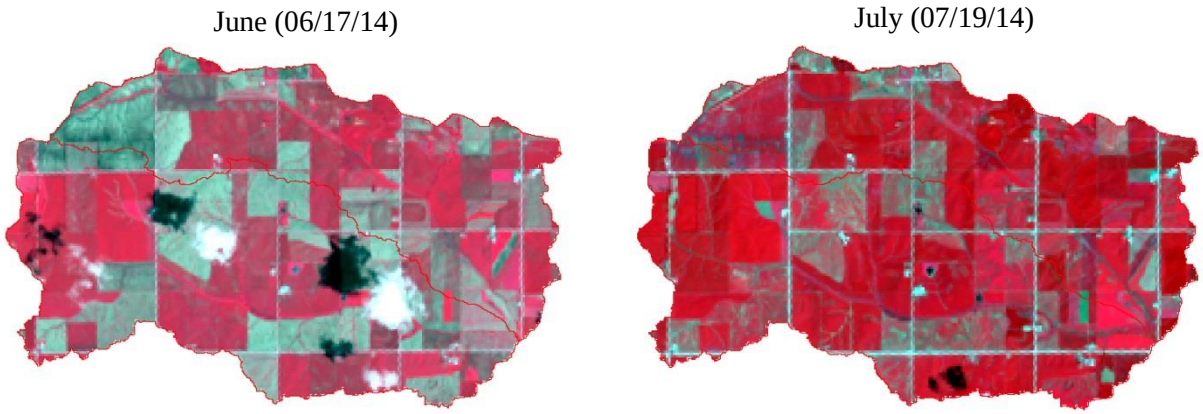

Figure 6.6: False color images of SASW using near infrared, red and green spectral bands mapped to RGB – this image shows the extent and degree of vegetation in a red tone, as vegetation reflects most light in the near infrared.

6.4. Results

This section presents outcomes of the model validation exercises and the simulations used to examine the characteristic scale unit. It is organized as follows. It starts with the validation of the model's ability to predict terrestrial fluxes and velocities of water and sediment for the different types of surfaces present in SASW. It then presents outcomes from instream advection-dispersion validation exercises. Thereafter, the model is used to simulate water and sediment fluxes at the watershed scale from past storm events in SASW. For some of these events, the model's ability to predict the correct proportions of terrestrial and instream contributions at the outlet is validated using sediment sourcing. Finally, results from the simulations used to examine the characteristic scale unit are presented.

6.4.1. Model Validation

In each of the validation cases presented herein, the performance of the model is examined using the r^2 value and/or the mean absolute error (MAE). Per convention, an r^2 value of 1.0 corresponds to a perfect agreement between the observed and simulated fluxes whereas an r^2 value of 0.0 shows no agreement. The value indicates the proportion of the variability in observed fluxes that can be predicted with the model.

The correlation coefficient, r, is determined herein as follows:

$$r = \frac{\sum_{j=1}^{n}(o_j-\bar{o})(s_j-\bar{s})}{\sqrt{\sum_{j=1}^{n}(o_j-\bar{o})^2 \sum_{j=1}^{n}(s_j-\bar{s})^2}} \quad (15)$$

where j is a counter, n is the number of data points, O is the observed flux, S is the simulated flux, and $\bar{O}$ and $\bar{S}$ are the average observed and simulated fluxes of the event, respectively.

The mean absolute error (MAE) is determined as:

$$MAE = \frac{\sum_{j=1}^{n}|o_j-s_j|}{n} \quad (16)$$

A small value of MAE suggests a good correspondence between model prediction and observed fluxes, whereas a large value suggests poor correspondence.

6.4.1.1. Terrestrial Fluxes

Figure 6.7 provides a comparison of measured and simulated runoff and sediment fluxes from experimental runs on three of the plots that were examined. Other validation results from the exercises have also been presented in *Abban et al*. [2016]. A summary of the r^2 and MAE values in each case, along with the simulated times to runoff initiation, is presented in Table 6.3 below.

Overall, there was very good agreement between the observed and simulated runoff data, with r^2 values ranging between 0.7-0.87. Although the agreement between the observed and simulated sediment fluxes was not as good as that for runoff, it was generally acceptable, falling between 0.39-0.65. The model performed best when predicting the variability in sediment fluxes on the rill-interrill plot with the steepest gradient, and poorest when predicting the variability in sediment fluxes on the vegetated plot. On the contrary, the MAE was largest when predicting sediment fluxes on the rill-interrill plot with the steepest gradient, and smallest when predicting sediment fluxes on the vegetated plot. The above trends are expected since the fluxes on the steep rill-interrill plot are two orders of magnitude larger than those on the vegetated plot (2×10^{-3} kg/s vs. 2×10^{-5} kg/s, respectively). Thus, one would expect stochastic effects relative to the mean flux to be more pronounced on the vegetated plot, but the magnitude of the deviation in fluxes to be less on the vegetated plot. Since the model predicts mean trends and does not directly simulate stochastic effects, its ability to simulate the observed variance in fluxes is expected to be poorer for smaller fluxes, but the error is expected to be smaller, which is the case above.

Table 6.3: Model validation results for terrestrial fluxes

Plot	r^2		MAE		Time to runoff (mins)	
	Runoff	Sediment*	Runoff	Sediment*	Observed	Simulated
1	0.87	0.65	1.25×10^{-5}	0.55×10^{-3}	1.8	3.7
2	0.70	0.49	0.64×10^{-5}	0.11×10^{-3}	4.2	12.0
3	0.82	0.39	0.73×10^{-5}	0.01×10^{-3}	3.0	8.4

* r^2 value was calculated excluding outlier shown in the plot.

Plot 1: Net fluxes on rill-interrill surface plot with residue at 8.5% slope

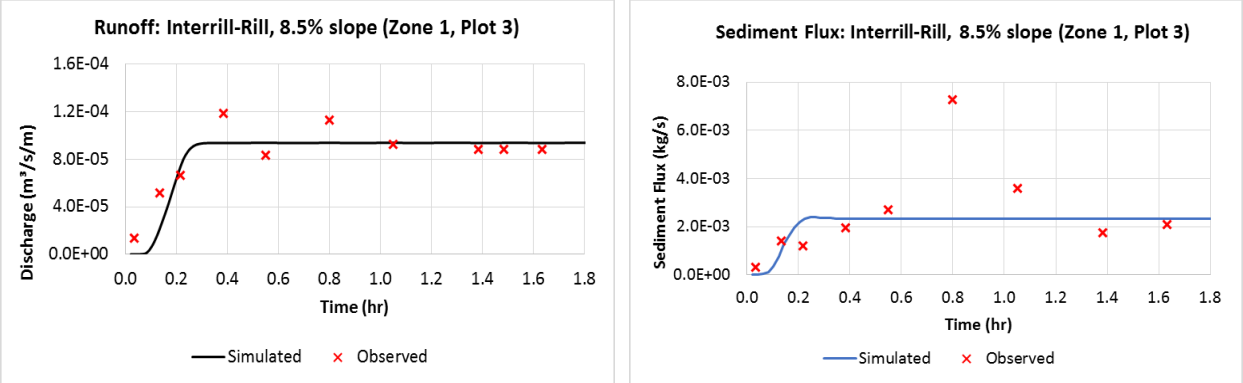

Plot 2: Net fluxes on rill-interrill surface plot with residue at 2.5% slope

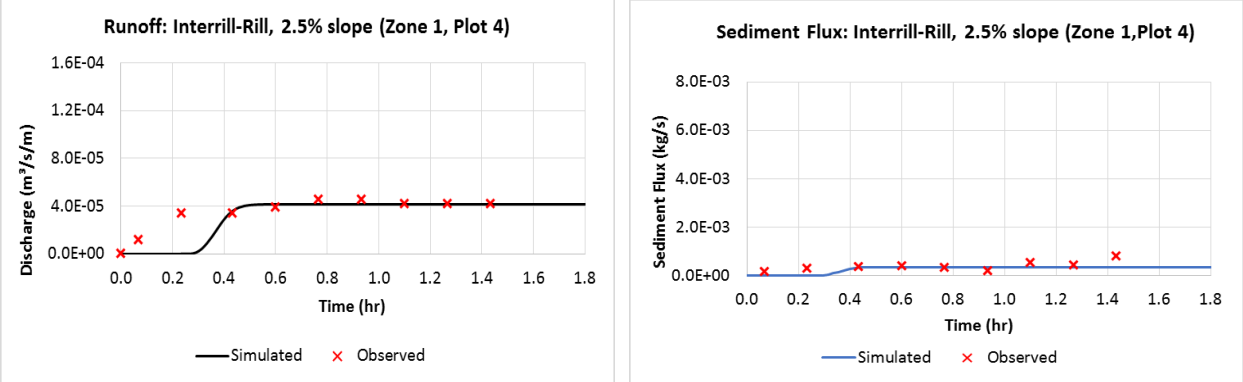

Plot 3: Net fluxes on vegetated surface plot at 15.4% slope

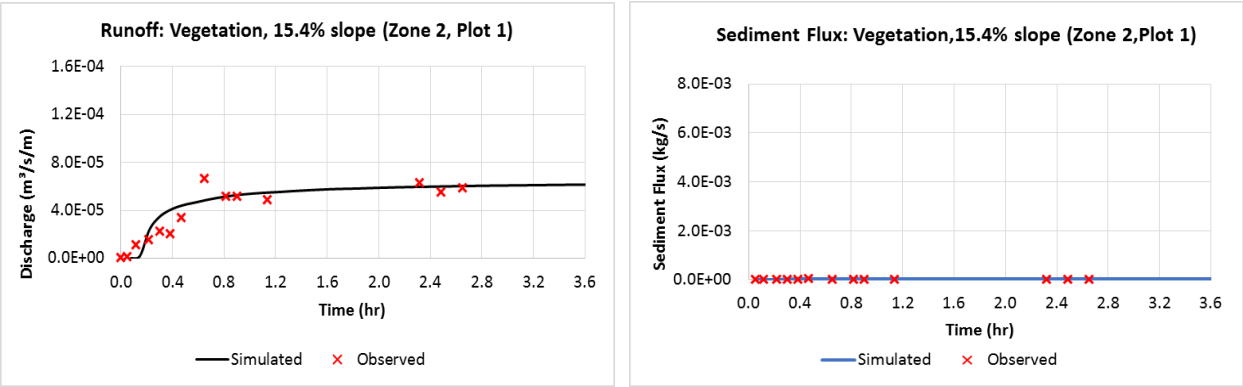

Figure 6.7: Flow and sediment fluxes measured at plot outlet

A comparison between the modeled and simulated times to runoff suggests that the model tends to over-predict the time to runoff initiation by a factor of up to 3, although the differences are on the order of minutes. This tendency of the model to over-predict the time to runoff initiation is attributed to a limitation in the WEPP model in the presence of surface roughness elements that prevents it from simulating runoff until all depression storage is filled. Since the depression storage is considered to be a function of both random roughness and hillslope gradient, this explains why the effects are more notable on plot 2 (milder gradient plot, more depression storage) compared to plot 1 (steeper gradient plot, less depression storage). Due to the shorter travel times at the plot scale, the effects of the limitation are expected to be generally more notable when considering fluxes at that scale.

The model's ability to predict overland flow velocities was also assessed on the three plots under steady state conditions. Figure 6.8 compares the simulated and observed velocities. The model performed well in all three cases, with percentage differences between the observed and simulated velocities of 21%, 4.6%, and 18% for plots 1, 2, and 3, respectively.

6.4.1.2.Instream Fluxes

The model's ability to predict flow advection and dispersion within the stream network is examined in Figure 6.9, which compares measured and simulated dye tracer concentrations at different instream locations in SASW under different flow conditions. For each case presented, the specified flow range reflects the natural increase in flow discharge from the dye injection point to the final sampling point (at the watershed outlet). An average dispersion coefficient of

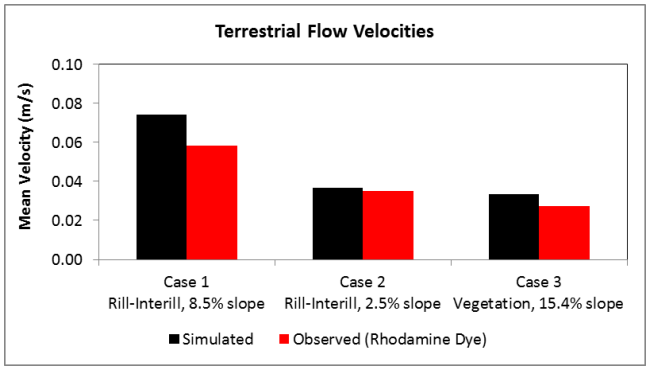

Figure 6.8: Comparison between simulated and observed overland flow velocities

Case 1: Flow discharge range: 0.33-0.90 m³/s

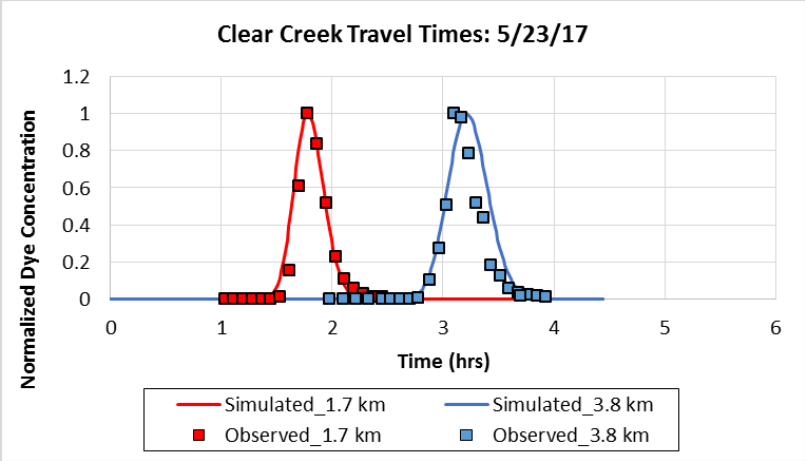

Case 2: Flow discharge range: 0.25-0.80 m³/s

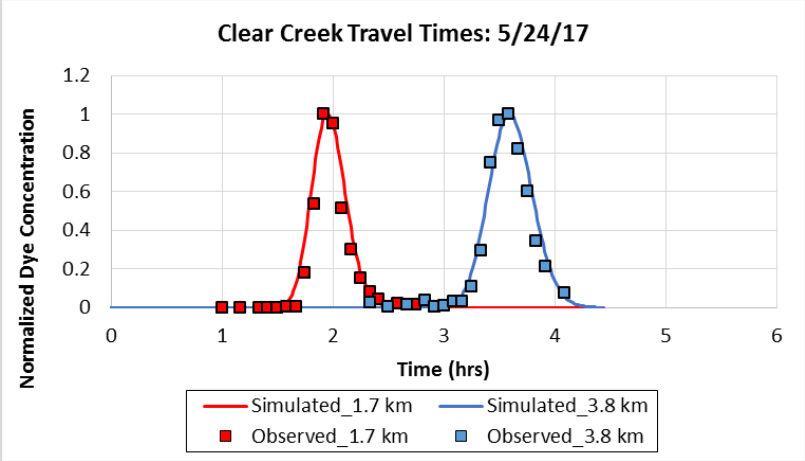

Case 3: Flow discharge range: 0.14-0.62 m³/s

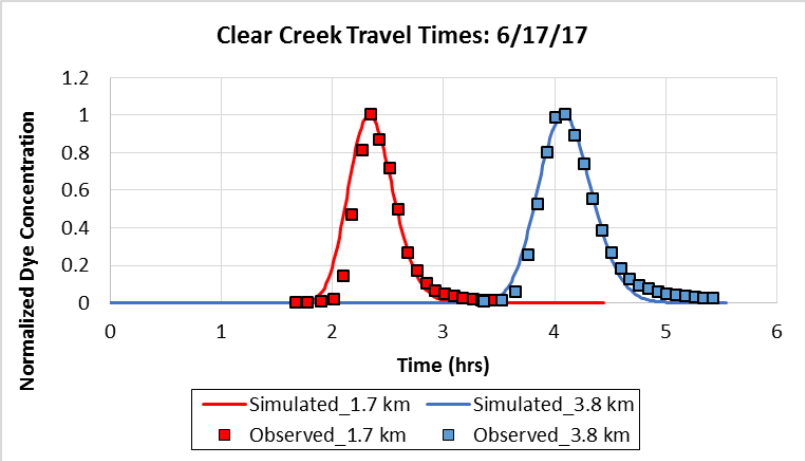

Figure 6.9: Comparison between measured and simulated dye tracer concentrations at different instream locations in SASW under different flow conditions

0.35 m²/s was found to be satisfactory for all the cases. This value matched well with data from other studies within the same flow range (0.001-1 m²/s) [*Shen et al*., 2010].

Table 6.4 below provides a summary of the r^2 and MAE values from the comparison between simulated and measured concentrations. The results suggest an excellent agreement between the predicted and measured concentrations, with r^2 values ranging from 0.89 to 0.98 and MAE values ranging from 0.04 to 0.07. Since over 90% of the normalized sediment concentrations fall between 0.1 and 1, the MAE values indicate minimal error in model predictions. Furthermore, the performance of the model was consistent between the injection point and both of the downstream sampling locations, suggesting overall that the model is able to predict advective-dispersive flows with high confidence in space for the conditions considered.

6.4.1.3. Watershed Fluxes

Figure 6.10 compares observed and predicted flow discharge rates at the outlet of SASW for four different rainfall events that took place in 2007 and 2014. Collectively, these four cases represent different rainfall and land cover conditions in SASW. A summary of the model performance in predicting flow discharge for these cases is presented in Table 6.5.

The model performed very well overall, predicting the general observed trends with r^2 values between 0.52 and 0.87, and MAE values between 1.14 and 4.47. As with the terrestrial fluxes, the larger MAE values at the watershed scale corresponded to the cases with higher flow discharges whereas the smaller MAE values corresponded to the cases with lower flow discharges. Nonetheless, the MAE values in all cases were generally less than 15% of the peak flow discharge, and less than 40% of the average flow discharge.

Table 6.4: Model validation results for instream advection-dispersion

Case	r^2		MAE	
	Sampling Point 1	Sampling Point 2	Sampling Point 1	Sampling Point 2
1	0.93	0.90	0.04	0.07
2	0.96	0.97	0.05	0.05
3	0.89	0.98	0.07	0.04

Case 1: June 22, 2014 rainfall event

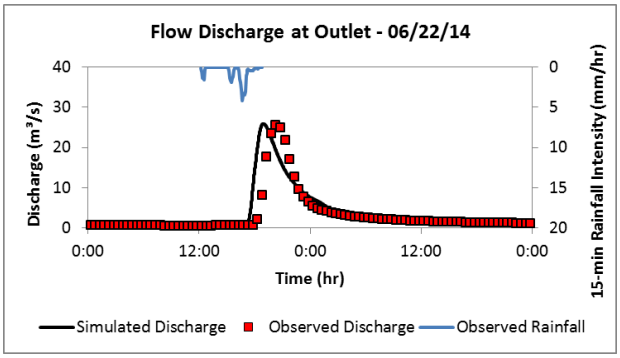

Case 2: June 22, 2007 rainfall event

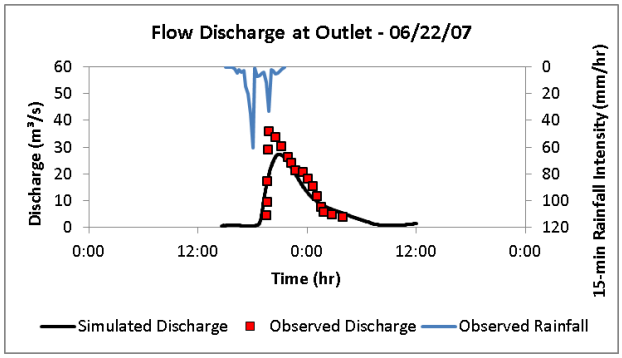

Case 3: July 12, 2014 rainfall event

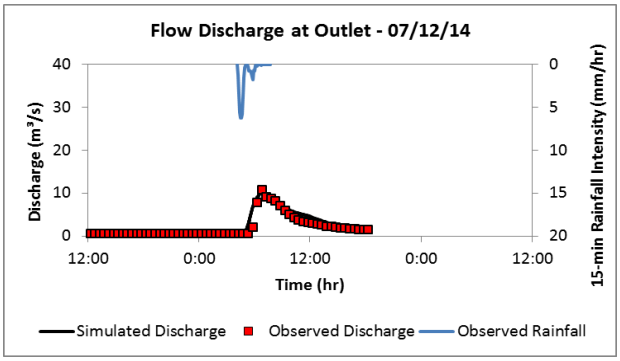

Case 4: September 10, 2014 rainfall event

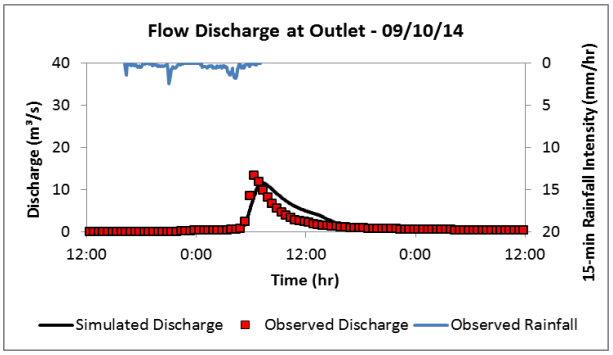

Figure 6.10: Comparison between observed and predicted flow discharge at the SASW outlet

Table 6.5: Model validation results for watershed flow discharge

Case	r^2	MAE
1	0.52	3.15
2	0.73	4.47
3	0.87	1.14
4	0.71	1.83

The model performed the poorest for Case 1, with an r^2 value of 0.52 and an MAE of 3.15, for a storm event that occurred on June 22, 2014. As seen in Figure 6.10, the primary shortcoming in this case was the model's ability to predict the time to peak of the hydrograph; it predicted a peak that occurred approximately 1 hr earlier than the observed peak. This could be due to a number of factors, including the spatiotemporal distribution of rainfall within the 26 km² sub-watershed, which may not be always be sufficiently captured by the rain gauge.

In contrast, there was near excellent agreement between the model predictions and the observed hydrograph for Case 3, which is an event that occurred on July 12, 2014. The r^2 and MAE values in this case were 0.87 and 1.14, respectively, suggesting that the model well replicated the rainfall and land use/land cover conditions for this scenario.

The observed and predicted sediment concentrations for four scenarios are compared in Figure 6.11. The first two cases consider sediment concentrations at the sub-watershed outlet for different storm events, while the last two cases consider sediment concentrations at two different locations within SASW for the same storm event. The events and locations are clearly shown in the figure. The model performance in these cases is also presented in Table 6.6.

Overall, the model was able to capture well the general trends and magnitudes of sediment concentrations, with r^2 values between 0.36 and 0.92, and MAE values between 0.22 and 0.63. Although the MAE values for the sediment concentration predictions were lower compared to values for the flow discharge predictions, the model performed better for the flow discharge predictions in relative terms. This is readily seen in Figure 6.11, where the scatter and differences between the predicted and observed values are more notable compared to the flow discharge values in Figure 6.10. Percentagewise, the sediment concentration MAE values were generally less than 30% of the peak sediment concentration, and also generally less than 56% of the average sediment concentration; these error thresholds are larger than the 15% and 40% noted respectively for the flow discharge.

The least agreement between the predicted and observed concentrations was in Case 2 for fluxes from an event that occurred on July 12, 2014. The r^2 and MAE values for this event were 0.36 and 0.22, respectively. Figure 6.11 indicates that the model was unable to capture the scatter in the observed data, although the general predicted trends were good. The scatter in the data could be due to processes not captured by the model, including local perturbations as a result of bioturbation and/or obstructions (e.g., logs) [*Loperfido et al*., 2010].

Case 1: June 22, 2007 rainfall event, watershed

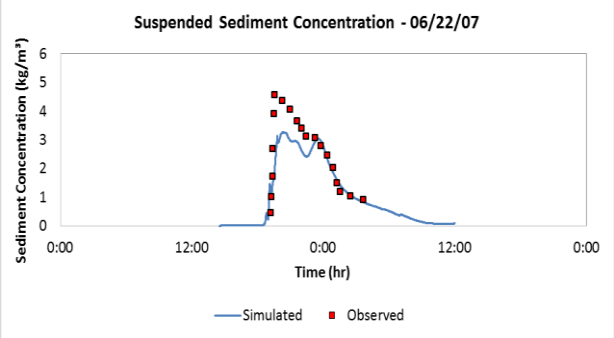

Case 2: July 12, 2014 rainfall event, watershed outlet

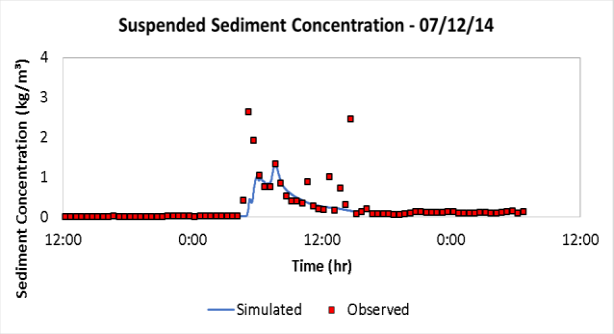

Case 3: June 19, 2007 rainfall event, Maas Site

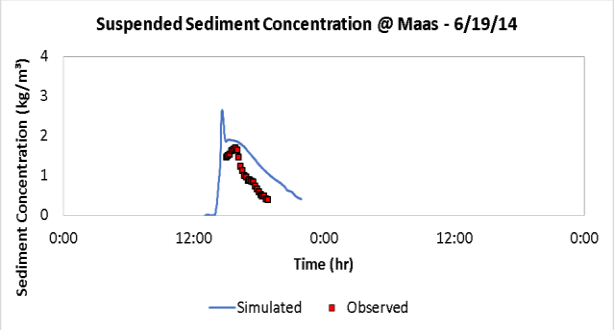

Case 4: June 19, 2007 rainfall event, Church Site

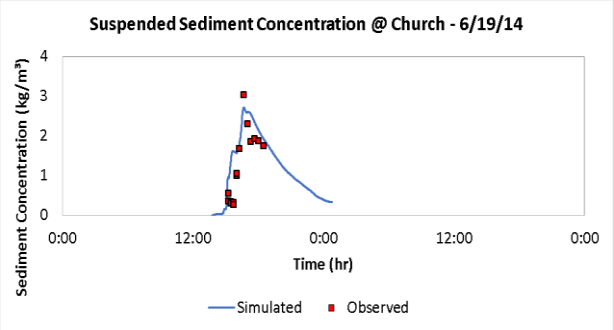

Figure 6.11: Comparison between observed and predicted sediment concentration within SASW (see Figure 6.4 for site locations)

Table 6.6: Model validation results for sediment concentration

Case	r^2	MAE
1	0.60	0.63
2	0.36	0.22
3	0.92	0.48
4	0.76	0.59

Nevertheless, comparing the various cases, not only was the model able to capture the trends in sediment concentration at a single location (i.e. at the outlet) for different storm events (Case 1 vs Case 2), it was also able to capture well the trends at two different locations for the same event (Case 3 vs Case 4), where one location (i.e., the Maas site) was approximately 3.8 km upstream from the other (i.e., the Church site) (these locations are shown on Figure 6.4). Thus, the results highlight the utility of the model for examining net fluxes of sediment (resulting from the processes it simulates) at different spatial locations and temporal moments in SASW.

6.4.1.4. Watershed Source Contributions

Probability density functions (pdfs) of terrestrial and instream sediment source contributions in SASW for June and July 2007, based on observed data, are presented in Figure 6.12. The pdfs were generated from sediment fingerprinting analyses using the Bayesian sourcing model and the tracer signatures of the field samples described in Section 6.3.2. For comparison, model predicted terrestrial and instream contributions for storm events that occurred in June and July of 2007 and 2014 are also shown in Figure 6.12.

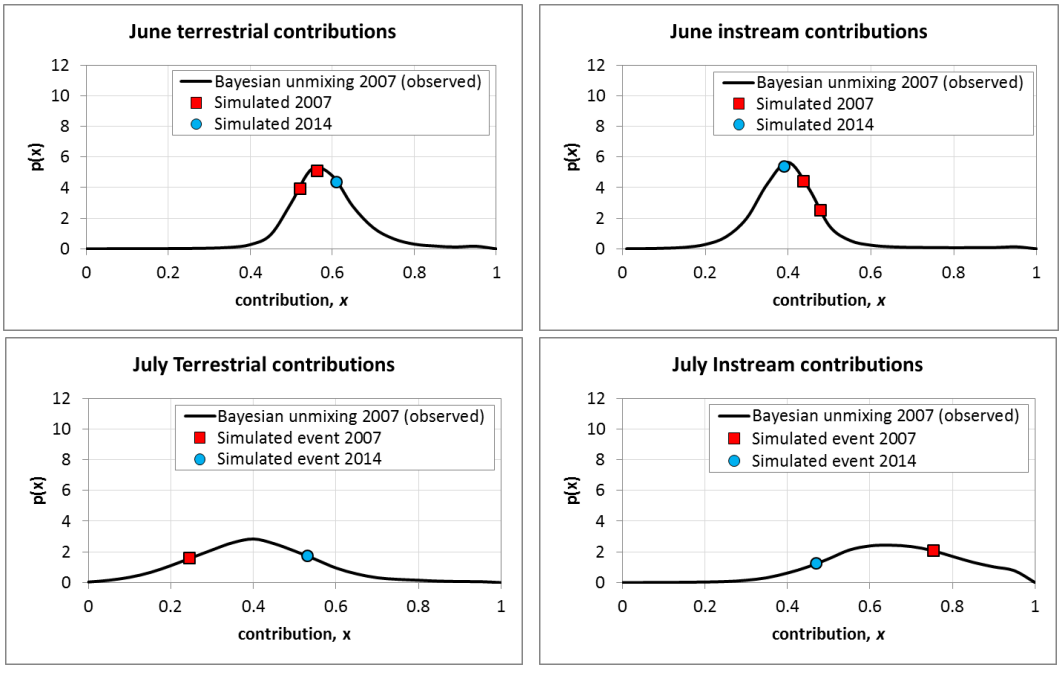

Figure 6.12: Comparison between predicted source contributions and field-based probability density functions of source contributions

As explained by *Abban et al*. [2016], the pdfs represent expected sediment source contributions taking into account uncertainty related various factors, including the origin, travel time, and delivery of material to the collection point (watershed outlet in this case). Hence, for model validation, one would expect the predicted contributions from an event that yields significant erosion to fall within a region of the pdf where the area under the curve is greater than zero, i.e. $p(x) > 0$, where x is the source contribution. To illustrate this, in Figure 6.12, the contribution, x, of terrestrial sources is expected to fall somewhere between 0.3 and 0.9 for all significant events in June of 2007 (see upper right plot).

With the above explanation in mind, it is noted that the 2007 model simulations do indeed predict terrestrial and instream contributions that fall within the expected ranges for June and July 2007 based on the field-driven sediment fingerprinting analysis. Further, the 2014 simulations also seem to behave in a similar fashion as the 2007 simulations. This is to be expected, since overall similar land management practices have been used within the watershed in both years, and the rainfall characteristics were similar for June and July of these two years. Also noteworthy in Figure 6.12 are the spreads of the pdfs and the spreads in predicted source contributions. *Abban et al*. [2016] noted that source contribution pdfs in June in SASW tended to be narrower with higher peaks compared to source contribution pdfs in July, which were more spread out with lower peaks. The narrower pdfs in June were attributed to greater connectivity between sources and the watershed outlet arising from less surface cover and higher storm magnitudes that led to more runoff and erosion, and subsequent delivery of material to the outlet. The increased delivery of material from more widespread regions of the watershed resulted in less uncertainty in source contributions which was reflected in the spread of the pdfs. In terms of modeling, the net effect would be less spread in the predicted contributions from different significant events in June (i.e., they would plot close together), and more spread in the predicted contributions from different significant events in July (i.e., they would plot farther apart). This is what is seen in the plots in Figure 6.12. Thus, not only was the model able to correctly predict the terrestrial and instream contributions, it also appeared to reflect observed trends in connectivity between the sources and watershed outlet in the months of June and July.

6.4.2. Characteristic Scale Unit

The results of the characteristic scale unit analyses for both water and sediment fluxes are presented in Figure 6.13 and Figure 6.14 for the months of June and July, respectively, for the events presented in Table 6.2. The plots in the figures show variations in the specific flow discharge and specific sediment concentration with area. Estimated characteristic scale units for both flow and sediment are also shown with solid blue and red vertical lines, respectively. The vertical axes have the same upper limits as the flow discharge and sediment concentrations are of the same order of magnitude.

Distinct patterns in characteristic scale units are noted for June and July. The results indicate that the characteristic scale unit is not static, but changes with event magnitude and land cover extent. Generally, the characteristic scale units for the June events are larger (mostly > 6 km^2) than the characteristic scale units for the July events (mostly < 6 km^2). As seen in the plots, the flow discharge and sediment concentrations in June are overall higher compared to July due to the larger storm event magnitudes and relatively lower land cover (see Table 6.2 and Figure 6.6).

Overall, it is apparent from Figure 6.13 and Figure 6.14 that the characteristic scale units for flow discharge and sediment concentration can be different based on the approach adopted herein. In June, the characteristic scale unit for sediment was larger than that for flow for five out of the six events that were examined. On the contrary, the characteristic scale unit for sediment in July was smaller or equal to that for flow for five out of the six events that were examined. This difference in trends between the two months is to be expected since flow and sediment responses in June and July are known to be different in SASW [*Papanicolaou and Abaci*, 2008; *Abaci and Papanicolaou*, 2009; *Abban et al.*, 2016]. A further examination of the June trends indicates that the one event for which the characteristic scale unit for sediment was smaller than that for flow was an event whose magnitude was smaller than all the other events examined for that month (see Event 4 for June in Table 6.2). Likewise, for July, the one event for which the characteristic scale unit for sediment was larger than that for flow was an event whose magnitude was larger than all the other events examined for that month (see Event 1 for July in Table 6.2).

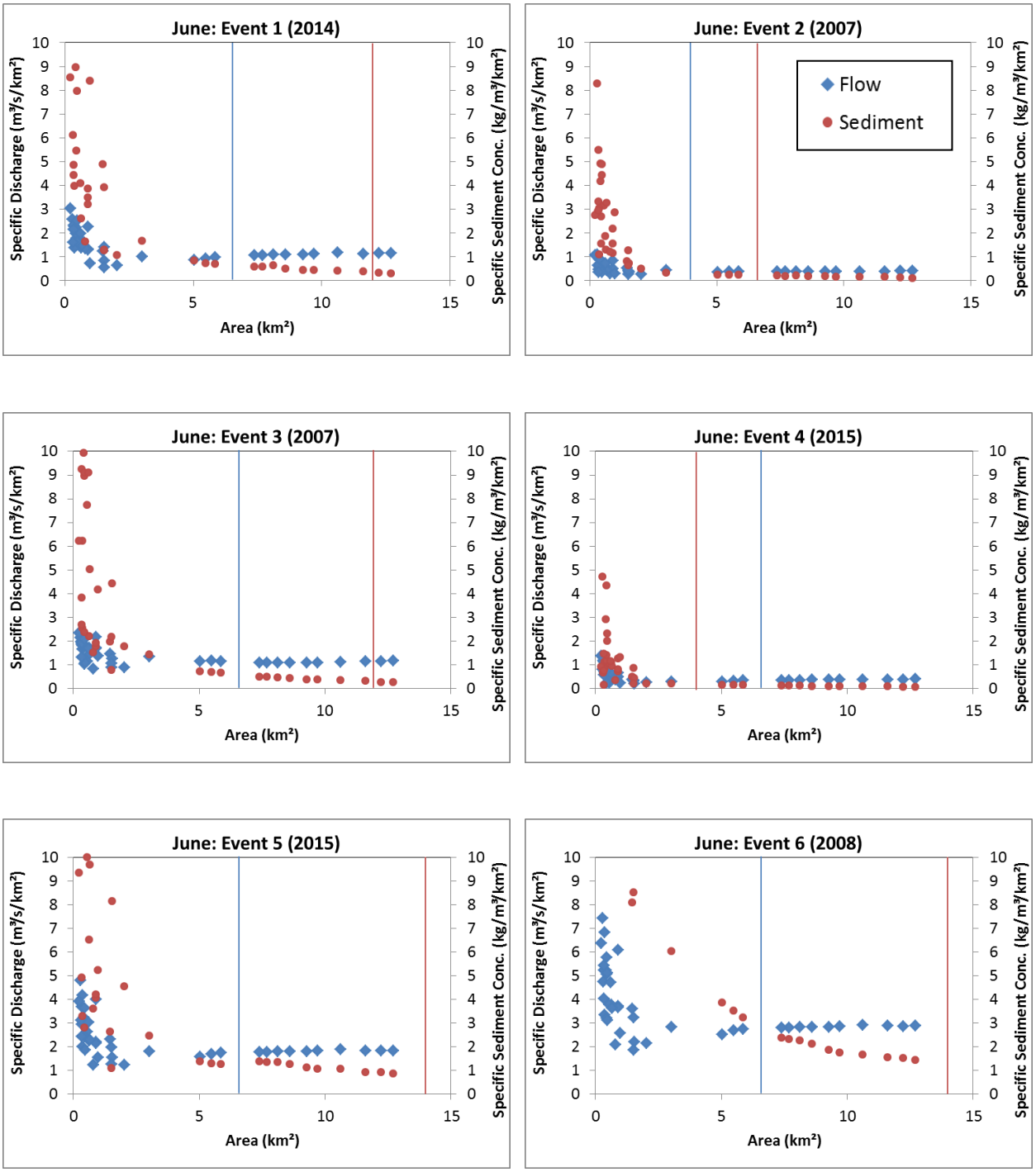

Figure 6.13: Plots of Specific Flow Discharge and Specific Sediment Discharge with Area for June

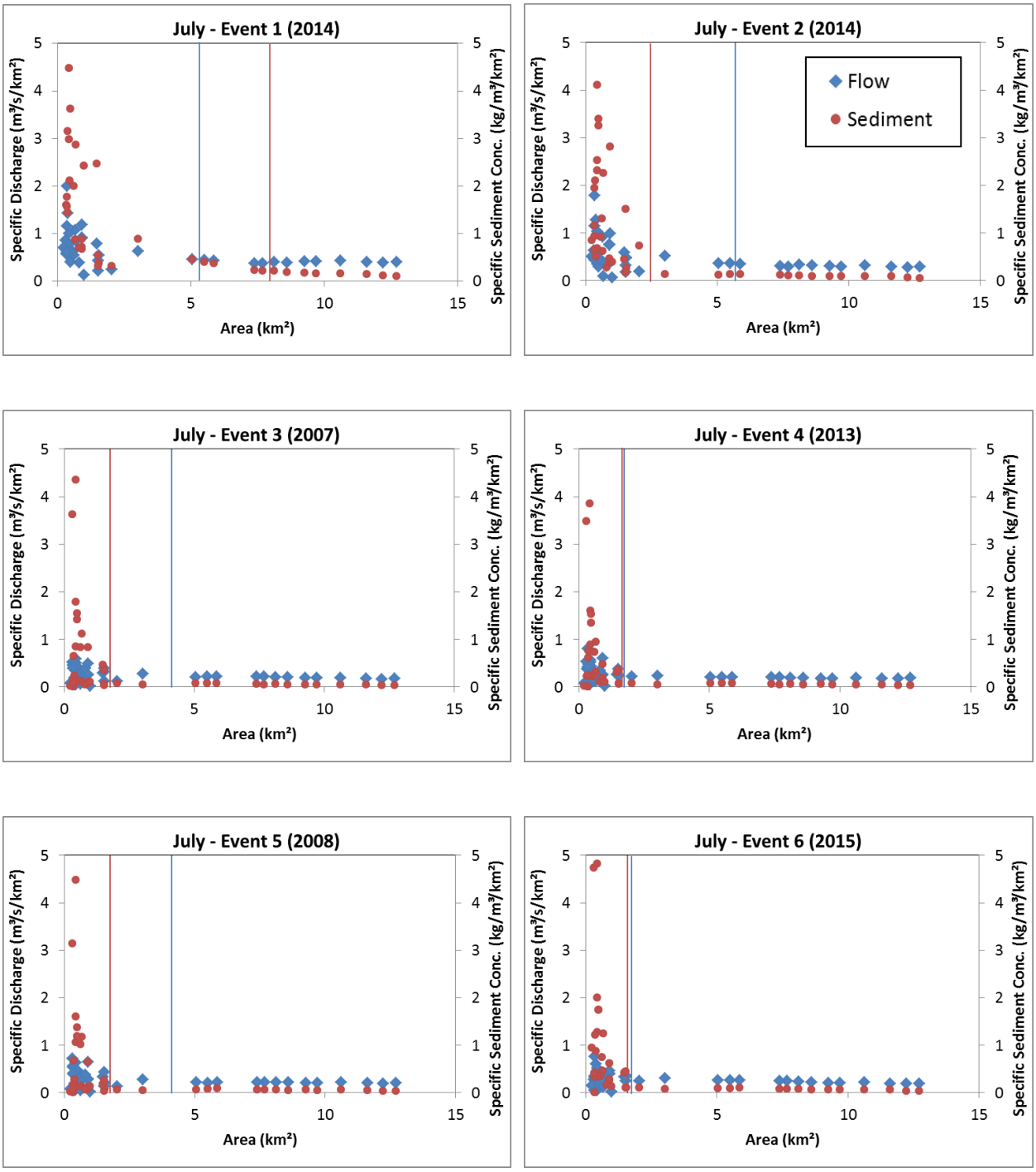

Figure 6.14: Plots of Specific Flow Discharge and Specific Sediment Discharge with Area for July

An examination of the characteristics scale units for sediment in both months reveals an apparent correlation between the characteristic scale unit and the suspended sediment concentration. Events that yielded higher sediment concentration had larger characteristics scale units, whereas events generating lower sediment concentrations had lower characteristic scale units. This observation is true both within and between the two months, and appears to indicate that the combined effects of rainfall and land cover have an impact on the characteristic scale unit through their effects on the net sediment flux.

The trends in characteristic scale unit shown in Figure 6.13 and Figure 6.14 are considered to represent two contrasting behaviors of watershed response in SASW. As alluded to above, and reported by Abaci and Papanicolaou [2009] and Abban et al. [2016], water and sediment fluxes in SASW are generally highest in June when storm event magnitudes are high and the land surface is relatively uncovered. The fluxes in July, on the other hand, are generally low because of lower magnitude events and more extensive land cover that lead to less material transport. These characteristics are known to have led to shifts in terrestrial and instream sediment flux interactions between two endpoints reflective of the sub-watershed dynamics, where terrestrial sources are dominant on one hand (June) and instream sources are dominant on the other (July) [*Wilson et al*., 2012; *Abban et al*., 2016]. Consequently, flux behavior between the endpoints may be examined by considering typical conditions for the two months separately.

6.5. Discussions and Conclusions

A modeling framework to simulate water and sediment flux dynamics in intensively managed landscapes has been presented in this study. The framework takes advantage of modeling advances from other studies related to simulating overland flows, coupling terrestrial and instream fluxes, and sediment fingerprinting in intensively managed landscapes. An extensive field campaign was performed to gather data from terrestrial and instream sources at scales ranging from the plot to the watershed scale for the purposes of framework model validation. The data collected included flow discharge and velocities, and suspended sediment fluxes. Sediment source contribution estimates were also determined using the tracer signatures of insitu and eroded material sampled at the watershed outlet. Model performance metrics such as the MAE and r^2 values were used to assess the absolute error in model predictions and its ability to predict the variance in the observations, respectively. The model performed well

overall for both water and sediment fluxes, though water predictions were generally better than sediment predictions. The model also replicated well the source contributions at the outlet for the two different months examined (June and July), capturing both the relative proportions and range of expected proportions.

The validated modeling framework was then used to examine the existence of a characteristic scale unit for sediment fluxes for typical rainfall and land cover conditions in SASW in the months of June and July. For each month, an ensemble of six events selected from observed rainfall data between 2007 and 2015 were used for the analyses. Characteristic scale units for sediment fluxes were observed for the cases examined. The scale units were, however, not static but changed between events and the two months. This change appeared to be influenced by storm magnitude and extent of land cover. The influence of these parameters on the characteristic scale unit are attributed to their effects on net flow rates (transport) and concentration (amount) of sediment fluxes. Higher flowrates and concentration of material corresponded to larger characteristic scale units, and vice versa.

Considering the results from the event ensembles, in June, most characteristic scale units for sediment were larger than their corresponding scale units for flow except for one event (Event 4), which was the smallest event in terms of storm magnitude. On the contrary, in July, most characteristic scale units for sediment were smaller than the corresponding scale units for flow except for one event (Event 1), which was the largest in magnitude. To better understand why the smallest and largest magnitude events in June and July, respectively, displayed distinct behaviors from the other events in the respective months, the results were also compared against the relative source contributions estimates for each event. These are summarized in Table 6.7 below. The comparison revealed a consistent trend across all the datasets for both months – the characteristic scale unit for sediment was larger than that for flow whenever terrestrial source contributions were dominant and the characteristic scale unit was smaller than that for flow whenever instream source contributions were dominant. A further investigation revealed that the primary difference between fluxes from terrestrial sources and instream sources was the sediment size distribution. As illustrated in Figure 6.15, instream contributions were generally coarser than terrestrial contributions suggesting that sediment size was an important factor affecting the characteristic scale unit for sediment.

Table 6.7: Relative source contributions from terrestrial and instream sources

Event No	June*		July*	
	Terrestrial	Instream	Terrestrial	Instream
1	0.61	0.39	0.53	0.47
2	0.56	0.44	0.25	0.75
3	0.52	0.48	0.25	0.75
4	0.23	0.77	0.22	0.78
5	0.72	0.28	0.03	0.97
6	0.84	0.16	0.15	0.85

*the relative contributions highlighted in red display different trends than the other events of the month

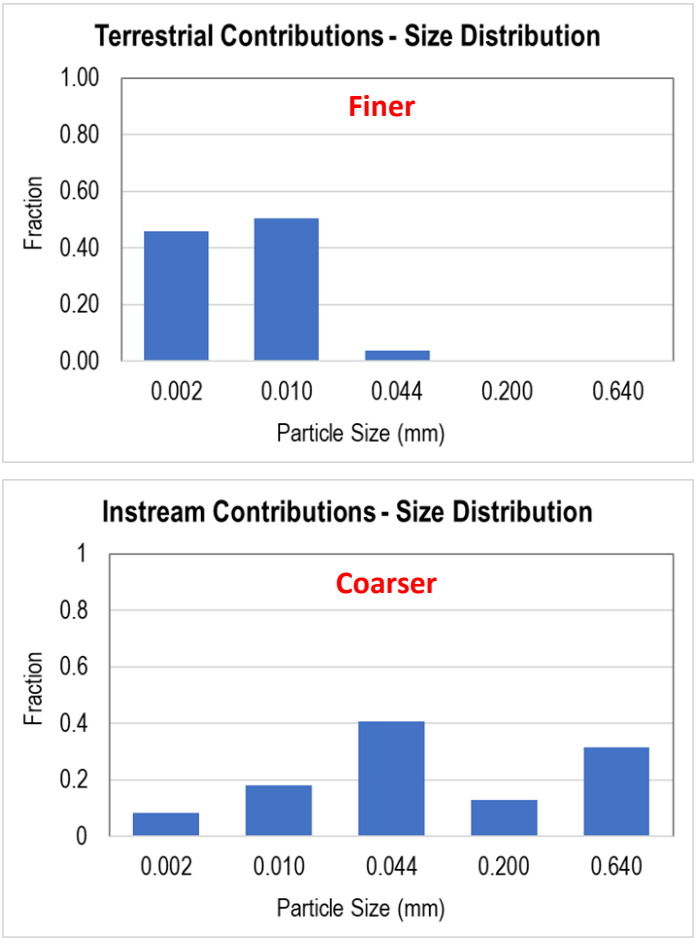

Figure 6.15: Sample of sediment size distribution

To ascertain the role of sediment size, the characteristic scale unit for sediments of different size classes were established and compared for the same storm event. A summary of the findings is presented in Figure 6.16 below. Finer fractions generally had larger characteristic scale units than coarser particles, with the 0.002 mm and 0.01 mm classes having larger characteristic scale units than the 0.044 mm, 0.2 mm, and 0.64 mm classes. The influence of sediment concentration was however apparent in the figure. For the coarser sediment sizes, the 0.64 mm class had a larger characteristic scale unit than the 0.02 mm class, despite it being coarser. This is attributed to the fact that the fraction (concentration) of the 0.64 mm class was larger than the fraction of the 0.02 mm class (see Figure 6.15). Similarly, the 0.01 mm class had a larger characteristic scale unit than the 0.002 mm class despite its coarser size. Again the fraction (concentration) of the 0.01 mm class was larger than the 0.002 mm class.

The effect of sediment size on the characteristic scale unit can be attributed to its effect on the lag or travel distance. Particle sizes that can be transported over longer distances by the flow will require a longer distance to adjust to flow conditions once they are introduced into the flow (i.e. a longer distance for erosion and deposition processes to start balancing out). On the other hand, particle sizes that can only be transported over shorter distances will require much shorter distances to adjust to the flow conditions. The particle travel distance is inversely related to its fall velocity which a function of its weight [*Wu*, 2008]. Coarser, heavier particles will have shorter travel distances compared to finer, lighter particles.

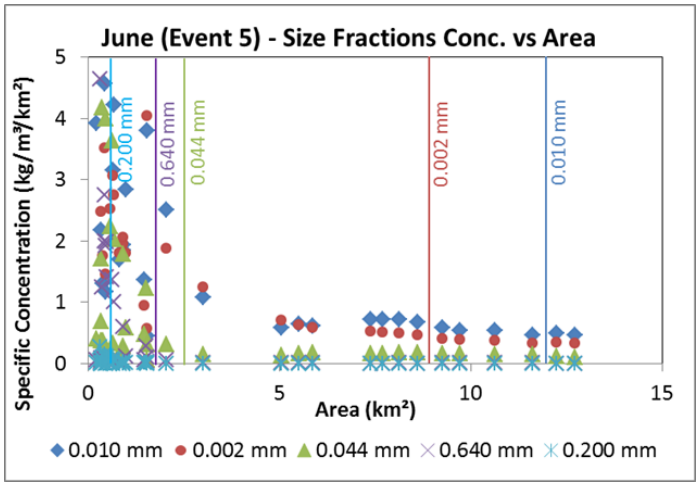

Figure 6.16: Characteristic scale units for different sediment size classes for a June event in SASW

The above effects can be readily inferred from the following steady-state sediment concentration relationship that incorporates spatial lag effects [*Jain*, 1992]:

$$\frac{dC}{dx} = -S_L(C - C_*) \tag{17}$$

where C is the sediment concentration, x is the longitudinal direction, C_* is the transport capacity, and S_L is the spatial lag coefficient. The difference $(C - C_*)$ on the right hand side represents the excess sediment concentration above the transport capacity, whereas the S_L represents the rate, with respect to space, at which the sediment concentration approaches the transport capacity (i.e. equilibrium concentration at which erosion and deposition are balanced out). Using the method of separation of variables and integrating to the location just before equilibrium conditions are attained, the distance to space-invariant conditions, x_*, can be expressed as:

$$\int_0^{x_*} dx = -\frac{1}{S_L}\int_{C_0}^{C_*+\delta} \frac{dC}{(C-C_*)} \tag{18}$$

$$x_* = \frac{1}{S_L}\left[\ln\left(\frac{C_0-C_*}{\delta}\right)\right] \tag{19}$$

where C_0 is the initial sediment concentration and δ is a short distance before equilibrium conditions are attained. S_L may be represented by the relationship [*Chang*, 2008], $S_L = \alpha w_s/q$, where α is a dimensionless coefficient known as the adaptation coefficient, w_s is the particle settling velocity, and q is the flow discharge per unit width. Thus, Equation 19 may be written as follows:

$$x_* = \frac{q}{\alpha w_s}\left[\ln\left(\frac{C_0-C_*}{\delta}\right)\right] \tag{20}$$

Equation (20) shows that the distance to space-invariant conditions is inversely related to the particle fall velocity and directly related to the sediment concentration and flow discharge. Coarser, heavier particles have larger settling velocities and will, thus, adjust to space-invariant

conditions over shorter distances than finer, lighter particles with smaller settling velocities. At a given flow rate, a higher concentration of particular sediment size class will attain space-invariant conditions over a longer distance than a lower concentration of the size class. Likewise, a larger flow rate will lead to space-invariant conditions over a longer distance than a smaller flow rate for a given sediment size class and concentration (and transport capacity).

Equation (20) provides an elementary understanding of how far sediment supply adjusts to space-invariant conditions within a watershed, and identifies basic factors that affect this distance. Since the distance is proportional to the area, the factors identified in the equation also affect the sediment characteristic scale unit, which, as alluded to before, is considered as a representative area at which space-invariant conditions are applicable (statistically). Although the steady state assumption precludes the effects of some factors such as landscape patchiness and unsteadiness of sediment supply that represent heterogeneity, the equation elucidates adjustments within homogeneous segments, which ultimately serve as a first order filter for interactions at larger scales with greater heterogeneity. The factors it identifies are thus primary factors that further interact with landscape heterogeneity and connectivity to dictate the overall value of the characteristic scale unit.

The basic factors identified in Equation (20) assume that sediment concentration introduced into the drainage network is initially larger than the transport capacity. This assumption is valid for the conditions presented above. However, this may not always be the case, and the vice versa (concentration less than the transport capacity) may be true. In this case, the relationship between the distance to space-invariant conditions and sediment concentration will not be the same as above; a higher concentration is expected to yield a shorter distance, whereas a lower concentration is expected to yield a longer distance. The relationship between the distance to space-invariant conditions, the particle settling velocity, and the flowrate, under this condition, however, are not affected and remain the same as above.

The existence of a characteristic scale unit for sediment has two important practical benefits for studying watershed processes and flux responses to anthropogenic activities (as driven by the combined actions of rainfall and land cover). These benefits are depicted in Figure 6.17. First, since statistical representations of landscape properties are valid beyond the characteristic scale unit, it can serve as a representative area that is used as a building block in models for simulating sediment fluxes at larger scales. For a typical building block, one could

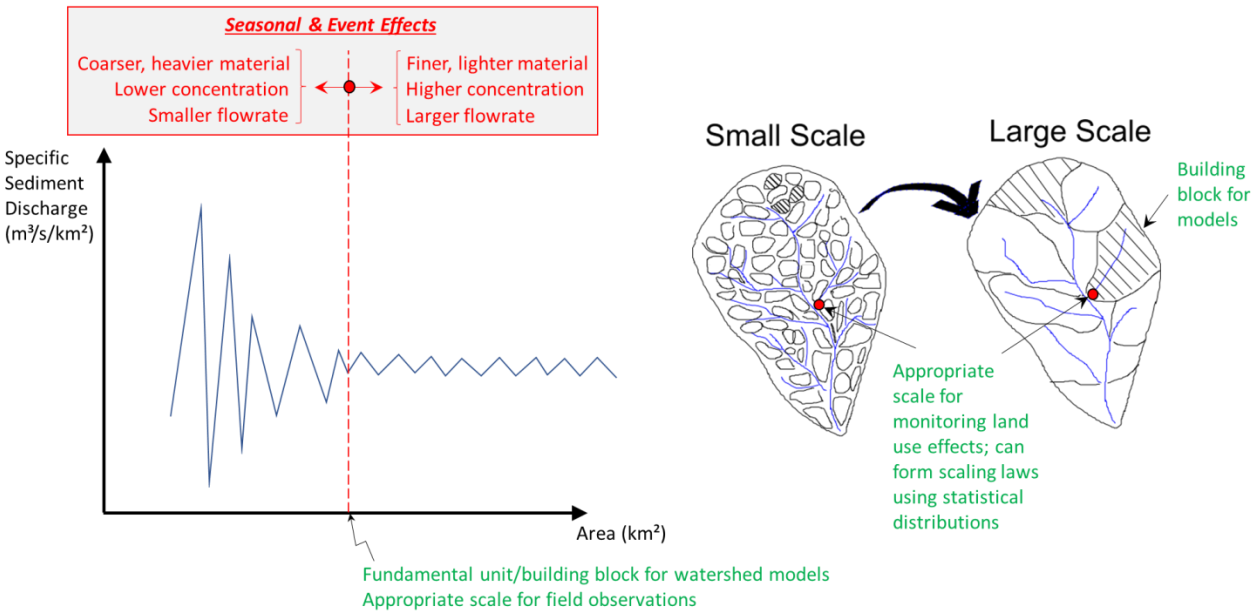

Figure 6.17: Depiction of characteristic scale unit for sediment fluxes and its benefits

establish and utilize sediment flux laws that only rely on statistical properties (e.g., the mean and variance) of all the relevant factors to predict fluxes from the block. Not only does this approach provide a scientifically sound method of accounting for the effects of local heterogeneity in landscape attributes on fluxes at larger scales, the simplification of landscape representation reduces computational requirements tremendously, thereby making it feasible to study flux responses in large-scale systems (watershed to basin scales), where detailed local-scale representations of the landscape would otherwise prohibit cross-scale flux simulations due to limited computational capacity.

The second practical benefit of the characteristic scale unit is that since it offers a scale at which specific sediment fluxes are not affected by local scale variabilities in landscape attributes, and, thus, flux laws can be established to represent mean landscape response, it provides a scale at which field observations should be made for an appropriate assessment of the net effects of anthropogenic activities on mean trends in sediment fluxes. Thus, the characteristic scale unit must be the basic unit used by watershed management for field monitoring of fluxes, assessing best management practice (BMP) design alternatives, and for evaluating the performance of installed BMPs. Since the characteristic scale unit has been found to vary with storm magnitude, land cover, and sediment characteristics, it will have to be

estimated separately for watersheds with different rainfall and landscape characteristics. It must also be established taking into consideration the full range of land uses and design storms applicable to the watershed under consideration.

For the analyses presented herein, the selection and use of typical rainfall and land cover conditions for June and July in SASW were based on the findings of *Abban et al*. [2016] to allow for the evaluation of two contrasting watershed responses covering the range of significant sediment flux dynamics within the watershed. The range of characteristic scale units presented herein is, thus, considered to be representative of the range of event-based dynamics within SASW. As noted above, however, the basic factors affecting the characteristic scale unit (i.e., flowrate, sediment concentration, sediment size characteristics) further interact with landscape heterogeneity and connectivity to ultimately dictate what the final size of the characteristic scale unit will be. Landscape heterogeneity and connectivity (both structural and functional per the definition of *Wainwright et al*. [2011]) affect sediment travel pathways, modes and distances over the course of a season. For example, in SASW, sediment can be transported in pulses over long distances at certain times of the year whereas at other times of the year, they are transported more intermittently over shorter distances [*Abban et al*., 2016]. The different pathways, modes and travel distances lead to memory effects, where sediment travel within the watershed to the outlet may occur over a series of storm events [*Wilson et al*., 2012], depending also on other factors such as the sediment size characteristics. In this case, the characteristic scale unit will not be dictated by a single event, but rather a distinct series of events over a longer time period that also captures the cumulative effects of any changes in land cover that may occur.

Evaluation of the longer term effect of a series of storm events on the characteristic scale unit must necessarily follow an approach that combines field-based observations with a model that has been well-validated for capturing structural and functional connectivity on the landscape over the course of a season and from season to season. In addition to the methods proposed herein, the model validation must incorporate the use of high resolution land surface data, and physical experiments involving tagged sediments of different size classes to determine their travel pathway and distance distributions under different storm event sequences and land cover conditions. The findings from the evaluation of the long-term sediment characteristic scale unit should be used in conjunction with the findings from this study to develop, if possible, a holistic

means of determining the characteristic scale unit for different watershed types – for management purposes – that accounts for uncertainty in its estimate.

References

Abaci, O., and A. N. Papanicolaou (2009), Long-term effects of management practices on water-driven soil erosion in an intense agricultural sub-watershed: monitoring and modelling, *Hydrol. Process.*, *23*(19), 2818-2837.

Abban, B., A.N. Papanicolaou, D. Dermisis, D. Flanagan, and J. Frankenberger (2011), Coupling WEPP and 3ST1D models for improved prediction of flow and sediment transport at watershed scales, Proceedings of the 7th IAHR Symposium on River, Coastal and Estuarine Morphodynamics, Beijing: Tsinghua University, China, 10 pp.

Abban, B., A.N. Papanicolaou, M.K. Cowles, C.G. Wilson, O. Abaci, K. Wacha, K. Schilling, and D. Schnoebelen (2016), An Enhanced Bayesian Fingerprinting Framework for Studying Sediment Source Dynamics in Intensively Managed Landscapes, Water Resources Research, DOI: 10.1002/2015WR018030.

Abban, B., A.N. Papanicolaou, C.P. Giannopoulos, D.C. Dermisis, , K.M. Wacha, C.G. Wilson, and M. Elhakeem (2017), Quantifying the changes of soil surface microroughnessdue to rainfall impact on a smooth surface, Nonlinear Processes in Geophysics, 24:569-579. doi:10.5194/npg-24-569-2017

Abrahams, A.D., A.J. Parsons, and S.-H. Luk (1986), Field measurement of the velocity of overland flow using dye tracing, Earth SurfaceProcesses and Landforms 11: 653 657.

Belmont, P., Kumarasamy, K., Kelly, S.A., Schaffrath, K.R., Beach, T.J. (2014). The cascade of non-stationarity. American Geophysical Union Fall meeting. December 2014. San Francisco, CA.

Brantley, S.L., and M. Lebedeva (2011), Learning to Read the Chemistry of Regolith to Understand the Critical Zone, Annual Review of Earth and Planetary Sciences, 39:387-416.

Conroy W. J., R. H. Hotchkiss, and W. J. Elliot (2006), A coupled upland-erosion and instream hydrodynamic-sediment transport model for evaluating sediment transport in forested watersheds, Transactions of the ASABE, 49(6), 1713–1722.

Cruse, R., D. Flanagan, J. Frankenberger, B. Gelger, D. Herzmann, D. James, W. Krajewski, M. Kraszewski, J. Laflen, J. Opsomer, and D. Todey (2006), Daily estimates of rainfall, water runoff, and soil erosion in Iowa, *J Soil Water Conserv*, *61*(4), 191-199.

Dermisis, D., O. Abaci, A. N. Papanicolaou, and C. G. Wilson (2010), Evaluating grassed waterway efficiency in southeastern Iowa using WEPP, *Soil Use Manage.*, *26*(2), 183-192.

Edwards TK, Glysson GD (1999) Field methods for measurement of fluvial sediment. U.S. Geological Survey Techniques of WaterResources Investigations Book 3, Chapter C2. Reston, VA, USA

Elhakeem, M. and A. N. Papanicolaou (2009), Estimation of the runoff curve number via direct rainfall simulator measurements in the State of Iowa, USA, Water Resources Management, 23, 2455–2473, doi:10.1007/s11269-008-9390-1.

Flanagan D. C., J. E. Gilley, and T. G. Franti (2007), Water Erosion Prediction Project (WEPP): development history, model capabilities and future enhancements, *Trans. ASABE*, *50*(5), 1603–1612.

Fox, J. F., and A. N. Papanicolaou (2007), The Use of Carbon and Nitrogen Isotopes to Study Watershed Erosion Processes, *J Am Water Resour As*, 43(4), 1047-1064.

Fox, J. F., and A. N. Papanicolaou (2008), An un-mixing model to study watershed erosion processes, *Advances in water resources*, *31*(1), 96-108.

Hubbard, E.F., F.A. Kilpatrick, L.A. Martens and J.F. Wilson. 1982. Measurement of time of travel anddispersion in streams by dye tracing. Techniques of water-resources investigations of the U.S. Geological Survey, Book 3 (Applications of Hydraulics), Chapter A9,44 p.

Jencso, K. G., B. L. McGlynn, M. N. Gooseff, S. M. Wondzell, K. E. Bencala, and L. A. Marshall (2009), Hydrologic connectivity between landscapes and streams: Transferring reach-and plot-scale understanding to the catchment scale, Water Resour. Res., 45, W04428, doi:10.1029/2008WR007225

Loperfido, J.V., C.L. Just, A.N. Papanicolaou, and J.L. Schnoor (2010), In situ sensing to understand diel turbidity cycles, suspended solids, and nutrient transport in Clear Creek, Iowa, Water Resources Research, 46:W06525, doi:10.1029/2009WR008293.

Michaelides, K. and J. Wainwright (2008), Internal testing of a numerical model of hillslope-channel coupling using laboratory-flume experiments, Earth Surface Processes and Landforms, 27: 1441-1458.

Olley, J. M. (2002), Organic carbon supply to a large lowland river and implications for aquatic ecosystems, *International Association of Hydrological Sciences Publication* (276), 27-33.

Papanicolaou, A.N., and O. Abaci (2008), Upland erosion modeling in a semi-humid environment via the water erosion prediction project model, Journal of Irrigation Drainage, 134:796-806

Papanicolaou A. N., A. Bdour, and E. Wicklein (2004), One-dimensional hydrodynamic/sediment transport model applicable to steep mountain streams. *J. Hydraul. Res.*, *42*(4), 357–375.

Papanicolaou, A. N., J. T. Sanford, D. C. Dermisis, and G. A. Mancilla (2010), A 1-D morphodynamic model for rill erosion, *Water Resour. Res.*, *46*(9), W09541, doi:10.1029/2009WR008486.

Papanicolaou, A.N., K.M. Wacha, B.K. Abban, C.G. Wilson, J. Hatfield, C. Stanier, and T. Filley (2015), From Soilscapes to Landscapes: A Landscape-oriented Approach to Simulate Soil Organic Carbon Dynamics in Intensively Managed Landscapes, Journal of Geophysical Research: Biogeosciences, 120, DOI: 10.1002/2015JG003078.

Papanicolaou, A.N., B.K.B. Abban, D.C. Dermisis, C.P. Giannopoulos, D.C. Flanagan, J.R. Frankenberger, and K.M. Wacha (2018), Flow Resistance Interactions on Hillslopes With Heterogeneous Attributes: Effects on Runoff Hydrograph Characteristics, Water Resources Research, 54. DOI: 10.1002/2017WR021109.

Shen, C., J. Niu, E.J. Anderson, and M.S. Phanikumar (2010), Estimating longitudinal dispersion in rivers using Acoustic Doppler Current Profilers, Advances in Water Resources, 33: 615-623.

Sloan (2013), Hydrologic impacts of tile drainage in Iowa, MS Thesis, University of Iowa.

Sullivan, P., A. Wymore, W. McDowell et al. 2017. New Opportunities for Critical Zone Science. June 2017 Arlington Meeting for CZ Science White Booklet, Critical Zone Observatories, US NSF National Program.

Sutarto, T., A. N. Papanicolaou, C. G. Wilson, and E. J. Langendoen (2014), Stability Analysis of Semicohesive Streambanks with CONCEPTS: Coupling Field and Laboratory Investigations to Quantify the Onset of Fluvial Erosion and Mass Failure, J Hydraul Eng, 140(9).

Van Meter, K.J., N.B. Basu, J.J. Veenstra, and C.L. Burras (2016), The nitrogen legacy: emerging evidence of nitrogen accumulation in anthropogenic landscapes, Environmental Research Letters, 11(3).

Wainwright, J., L. Turnbull, T.G. Ibrahim, I. Lexartza-Artza, S.F. Thornton, R.E. Brazier (2010), Linking environmental regimes, space and time: interpretations of structural and functional connectivity, Geomorphology, 126: 387–404.

Wilson, C. G., A. N. T. Papanicolaou, and K. D. Denn (2012), Partitioning fine sediment loads in a headwater system with intensive agriculture, J Soil Sediment, 12(6), 966-981.

Wood, E. F., M. Sivapalan, K. Beven, and L. Band (1988), Effects of spatial variability and scale with implications to hydrologic modeling, J. Hydrol., 102, 29-47.

Woods, R., M. Sivapalan, and M. Duncan (1995), Investigating the representative elementary area concept: an approach based on field data, Hydrological Processes, 9: 291-312.

Wu, W.M. (2008), Computational river dynamics. Taylor & Francis Group, London.

Chapter 7

Conclusions and Future Work

7.1. Conclusions

This study has developed and validated a modeling framework for simulating event-based flow and sediment dynamics in intensively managed landscapes. The model has been applied to the South Amana Sub-watershed, IA, to establish the existence of a characteristic scale unit at which the specific sediment discharge is not significantly affected by local-scale variability in landscape attributes. The study has also identified three basic factors that affect the characteristic scale unit, namely the flow rate, sediment concentration, and sediment size. To achieve the overarching goals, several specific objectives were undertaken from the plot to the sub-watershed scale with significant outcomes. These outcomes are summarized as follows:

- Plot Scale. The study findings suggest that landscape surfaces with microroughness less than 5 mm can undergo an increase in roughness when subject to rainfall action. Further, a surface undergoing roughness increase or decrease under rainfall action will approach a limiting threshold where the surface roughness ceases to change significantly. This threshold needs to be incorporated in existing models. The findings are illustrated in Figure 7.1, which plots the ratio of the final to initial random roughness against the initial random roughness for selected studies in intensively managed landscapes.

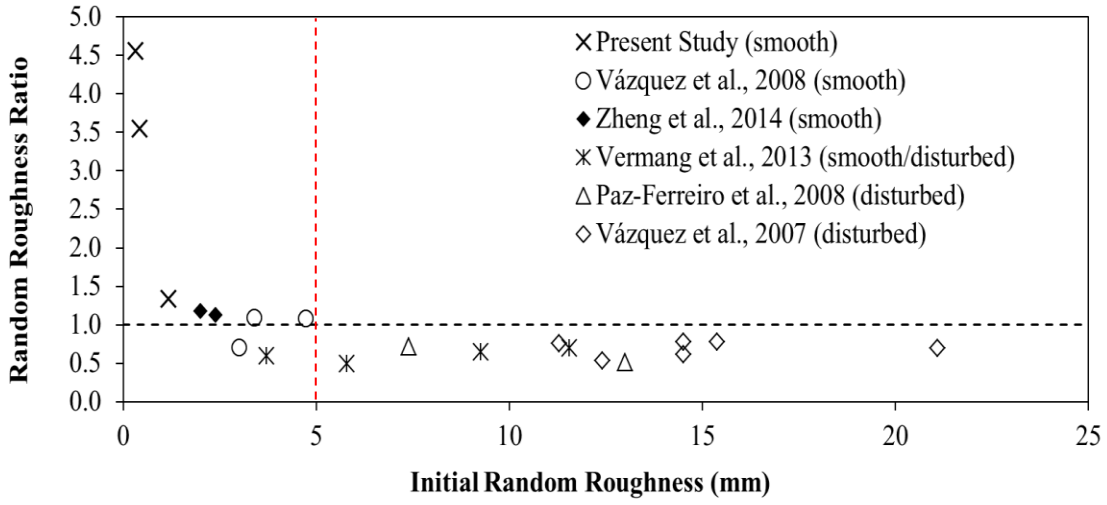

Figure 7.1: Trends in surface roughness evolution from various studies

- Hillslope Scale. The study results highlight weaknesses of the space/time-invariant flow resistance assumption used in many existing models, and demonstrate that assumptions on landscape terrain characteristics exert a strong control on the shape and magnitude of hydrographs, with deviations reaching 65% in the peak runoff when space/time-variant resistance effects are ignored in some cases. An examination of the influence of particle grains, isolated roughness elements, and vegetation on overland flow revealed the existence of threshold storm magnitudes and hillslope gradients beyond which the resistance effects of these landscape attributes on the peak stream power were negligible. The threshold can be used as practical means for determining the effective length of best management practices such as grassed water ways. The threshold can also be used as a guide for determining appropriate model complexity when simulating fluxes. This is depicted in Figure 7.2 using two zones. Below the threshold (Zone I) space-time variant (dynamic) resistance representation of landscape attributes is needed for simulations and above the threshold (Zone II) the space-time invariant resistance assumption can be used. Other findings from the study for the examined site suggest that changes in land cover from vegetation to a bare surface has a larger impact on overland flow than profile curvature effects, with estimated increases in peak runoff rates of up to 133% due to land cover change compared to 16% due to profile curvature change.

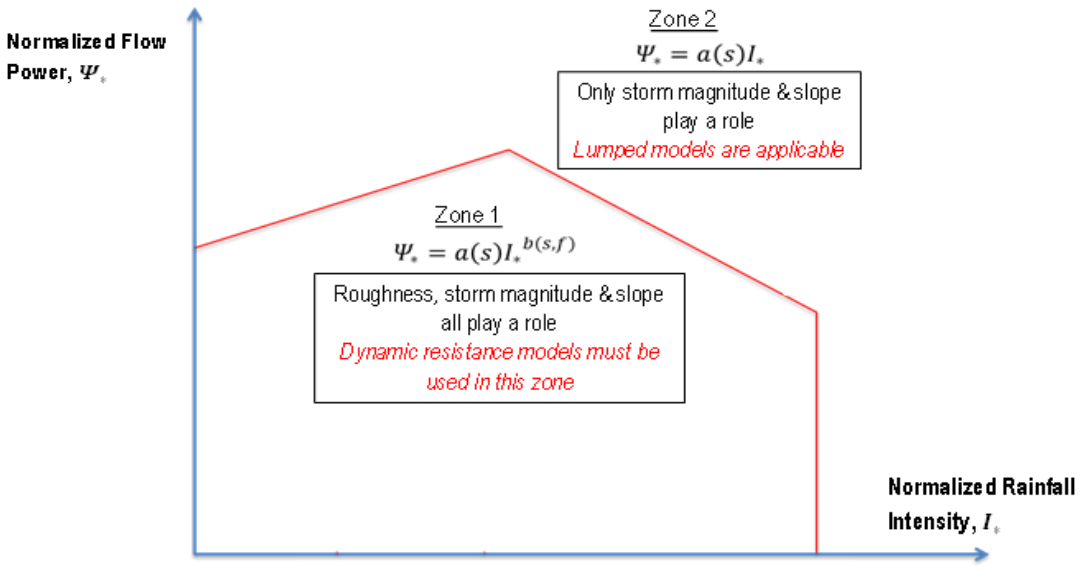

Figure 7.2: Conceptual representation of roughness effects

- Sub-watershed Scale. Two key stochastic parameters, α and β, were introduced into a Bayesian sediment fingerprinting model to reflect the spatial origin attributes of sources and the time history of eroded material delivered to the watershed outlet. Together, these two parameters account for landscape heterogeneity effects in intensively managed landscapes by accounting for variabilities in source contributions, their pathways, delivery times and storage within the watershed. By incorporating the parameters, the fingerprinting model was able to capture important trends in sediment flux behavior over the course of a typical growing season at the study site. The study revealed that terrestrial sources tend to contribute the most eroded material in the months of May and June, whereas instream sources tend to contribute the most from July onwards. Further, the model showed that in June, high hydrologic forcing combined with lower cover creates a "piston" effect where action (flow) creates reaction (transported fluxes) with minimal delay and less intermittency in transported material to the watershed outlet. On the contrary, in July, a lower storm magnitude and greater protection of the surface by vegetation cover leads to less mobilization of material. The resistance offered by the vegetation promotes more deposition and reduces sediment transport times/delivery rates to the watershed outlet. The two months thus represent contrasting watershed behavior that stems from the combined action of rainfall and land use (see Figure 7.3 below).

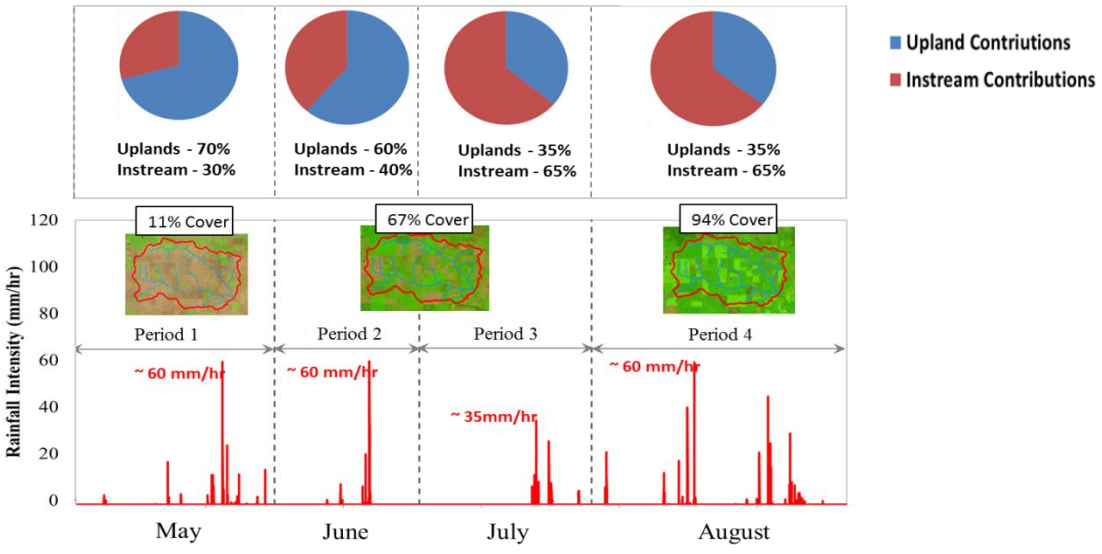

Figure 7.3: Intra-seasonal changes in sediment source contributions in South Amana, IA.

The study performed herein was premised on two hypotheses. The first hypothesis was that continued human modification of the landscape has affected the connectivity between terrestrial and instream domains, significantly altering (in a non-linear fashion) the travel times and net fluxes of water and sediment through the drainage network compared to undisturbed conditions. It was hypothesized that continued modification is maintaining the system in a state of disequilibrium with intra-seasonal patterns in fluxes that are regulated by the collective action of land use and rainfall; patterns that would otherwise be absent without human intervention. The findings presented in Chapters 2 to 6, and summarized above, confirm the notion that human action has significantly altered material travel times and net flux amounts, and is maintaining the system in a state where human-induced intra-seasonal patterns in fluxes exist, regulated by the collective action of land use and rainfall.

The second hypothesis was that there exists a characteristic scale unit where the specific sediment discharge is not significantly affected by local-scale variability in landscape and hydrologic properties, and at which statistical representations of watershed properties may be used to predict sediment fluxes. This characteristic scale unit for sediment was hypothesized to differ from that for specific flow discharge due to differences in travel times and processes involved. The findings in Chapter 6 confirm the existence of the characteristic scale unit for the specific sediment discharge described above. The results also confirm that the scale unit can indeed be different from that for the specific flow discharge. For the study conditions examined, the specific sediment discharge scale unit tended to be larger than that for specific flow discharge whenever finer, lighter material was being transported material. On the other hand, it tended to be smaller whenever coarser, heavier material was being transported. Overall, three important factors that were found to affect the characteristic scale unit was the sediment size, sediment concentration, and the flow rate. The effects of these factors are depicted in Figure 7.4.

Two practical benefits of the characteristic scale unit have also been identified and illustrated in Figure 7.4. The first practical benefit is that it can serve as a representative area that is used as a building block in models for simulating sediment fluxes at larger scales. Spatial averaging of landscape attribute effects is permissible within this building block such that the attributes may be represented using statistical distributions. The second benefit is that it provides a watershed monitoring scale at which field observations can be made to reliably assess the net effects of anthropogenic activities, and mitigation measures such as BMPs, on sediment fluxes.

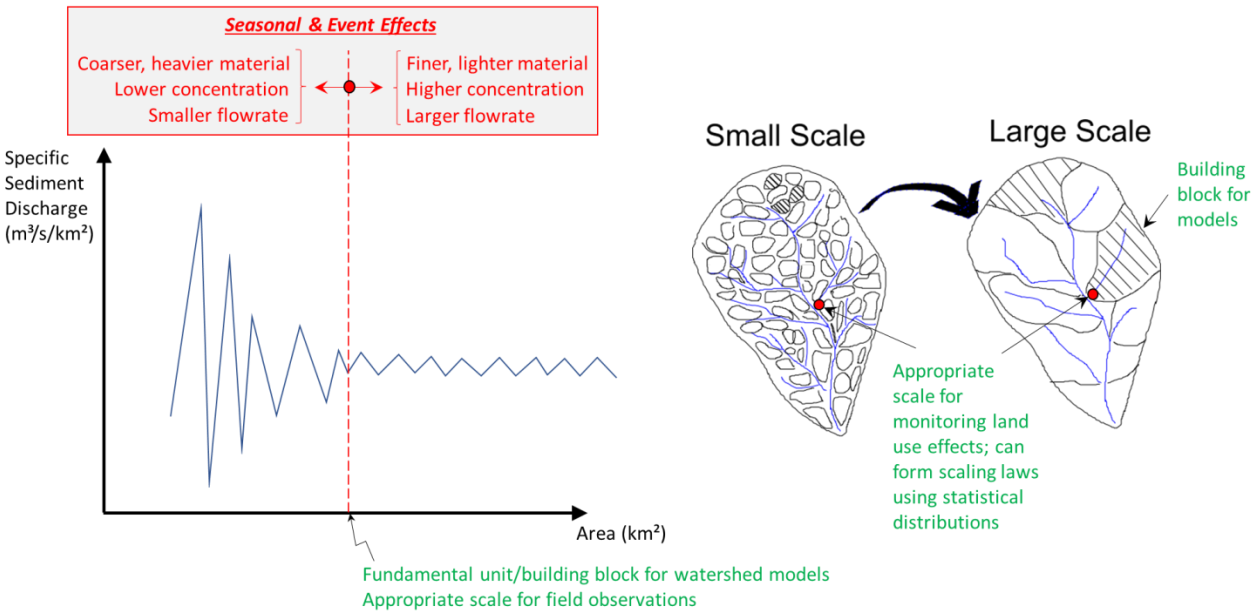

Figure 7.4: Depiction of characteristic scale unit for sediment fluxes and its benefits

7.2. Future Work

A modeling framework for simulating water and sediment fluxes on an event basis has been developed and presented in this dissertation. The development of the framework considered processes at plot, hillslope, and sub-watershed scales. Whilst advances were made at each of these scales to enable the development and use of the framework to establish the existence of the characteristic scale unit for sediment fluxes, the study only provides an assessment of the characteristic scale unit on an event basis and its behavior under conditions that are considered to reflect end members of the combined action of land use and rainfall. Further studies are needed to examine the evolution of the sediment characteristic scale unit over longer time periods as dictated by the interplay between event-based dynamics and seasonal dynamics. These studies should follow the approach of *Papanicolaou et al.* [2015] in simulating the trajectory of fluxes as affected by the different modes of sediment transport, storage, and delivery to the watershed outlet. The evaluation of longer term sediment flux dynamics using the model presented herein will require further validation of its ability to represent sediment flux pathways and connectivities on the seasonal scale. This should involve the use field experiments to establish high resolution land surface digital elevation models of the study area from which flow pathway distributions can be developed. The flow pathway distributions should then be

used as the basis for field connectivity and travel time/distance experiments, involving the use of tagged sediments of different size classes, to monitor sediment travel and resting times for sequences of storm events over the course of a season and from season to season (see virtual velocity concept by *Papanicolaou et al*. [2002]). The field observations should then be used to validate the model's ability to replicate terrestrial and instream travel and resting time distributions over the course of a season and from season to season.

Longer term simulations may also require further modeling advances at different scales. At the plot scale, studies are needed for developing a model for surface roughness evolution that can predict both increase and decrease in surface roughness depending on the initial conditions. For this, the exact mechanisms leading to increase in roughness under smooth surface condition need to be established. The studies must also consider the implications of sealing and soil water retention characteristics of the soils under sealing to the evolution [*Saxton and Rawls*, 2006]. In addition, they must consider the role of successive storm events on the evolution. Physical processes that have to be examined include compression and drag forces from the raindrop impact on the soil, angular displacement due to rainsplash, aggregate fragmentation, and differential swelling [*Warrington et al*., 2009; *Rosa et al*., 2012; *Fu et al*., 2016].

At the sub-watershed scale, it was determined that the role of tiles on fluxes during a storm event was relatively minimal compared to mean flow discharges, even though roughly 94 tile outlets were present in the sub-watershed. Field observations of tile flows at the study site suggested peak flow rates on the order of 0.01 m^3/s per tile (on average). Thus, the net tile flow rates were generally less than 5% of the peak event flow discharges along the channel network. However, for long term seasonal fluxes, the role of tiles may be more important as they are known to maintain continuous flow discharge over the course of a season. Water and sediment flux analyses over seasonal time frames should therefore take tile contributions into account.

References

Fu, Y., Li, G., T. Zheng, B. Li, and T. Zhang (2016), Impact of raindrop characteristics on the selective detachment and transport of aggregate fragments in the Loess Plateau of China, *Soil Science Society of America Journal, 80*, 1071, doi:10.2136/sssaj2016.03.0084.

Papanicolaou, A. N., D. Knapp, and K. Strom (2002), Bedload Predictions by Using the Concept of Particle Velocity: Applications, Hydraulic Measurements and Experimental Methods Specialty Conference (HMEM), Estes Park, Colorado, United States.

Papanicolaou, A. N., K. M. Wacha, B. K. Abban, C. G. Wilson, J. L. Hatfield, C. O. Stanier, and T. R. Filley (2015), From soilscapes to landscapes: A landscape-oriented approach to simulate soil organic carbon dynamics in intensively managed landscapes, *Journal of Geophysical Research: Biogeosciences, 120*, 2375–2401, doi:10.1002/2015JG003078, 2015b.

Paz-Ferreiro, J., I. Bertol, and E. V. Vázquez (2008), Quantification of tillage, plant cover, and cumulative rainfall effects on soil surface microrelief by statistical, geostatistical and fractal indices, Nonlinear Processes in Geophysics, 15, 575–590. doi:10.5194/npg-15-575-2008.

Rosa, J. D., M. Cooper, F. Darboux, and J.C. Medeiros (2012), Soil roughness evolution in different tillage systems under simulated rainfall using a semivariogram-based index, *Soil and Tillage Research, 124*, 226–232, doi:10.1016/j.still.2012.06.001.

Saxton, K. E. and W. J. Rawls (2006), Soil water characteristic estimates by texture and organic matter for hydrologic solutions, *Soil Science Society of America Journal, 70*, 1569, doi:10.2136/sssaj2005.0117.

Vázquez, E. V., R. G. Moreno, J. G. V. Miranda, M. C. Díaz, A. S. Requejo, J. Paz-Ferreiro, and A. M. Tarquis (2008), Assessing soil surface roughness decay during simulated rainfall by multifractal analysis, *Nonlinear Processes in Geophysics, 15*, 457–468, doi:10.5194/npg-15-457-2008.

Vermang, J., L. D. Norton, J. M. Baetens, C. Huang, W. M. Cornelis, and D. Gabriels (2013), Quantification of soil surface roughness evolution under simulated rainfall, *Transactions of the ASABE, 56*, 505–514, doi:10.13031/2013.42670.

Warrington, D. N., A. I. Mamedov, A. K. Bhardwaj, and G. J. Levy (2009), Primary particle size distribution of eroded material affected by degree of aggregate slaking and seal development, *European Journal of Soil Science, 60*, 84–93, doi:10.1111/j.1365-2389.2008.01090.x.

Zheng, Z. C., S. Q. He, and F. Wu (2014), Changes of soil surface roughness under water erosion process: Soil surface roughness under water erosion, *Hydrological Processes, 28*, 3919–3929, doi:10.1002/hyp.9939.

Vita

Benjamin Abban was born in Accra, Ghana, to James and Cecilia Abban. He received his elementary education from the Christ the King International School and Maseru English Medium Preparatory School in Ghana and Lesotho, respectively. He attended high school at the St. Peters Senior High School in Nkwatia, Ghana, and on completion was adjudged the overall best student and best science student in the country in the Senior Secondary School Certificate Examination by the West African Examination council. He represented his high school in the National Science and Math Quiz and was a quarter finalist. He received B.Sc. and M.Sc. degrees in Civil Engineering from the Kwame Nkrumah University of Science and Technology (KNUST), Ghana, and the University of Cape Town, South Africa, respectively. He was honored with the Unilever Best Engineering Student Award for graduating at the top of his class in the College of Engineering at KNUST. Prior to pursuing his PhD degree, he worked for four years as a consulting engineer for Aurecon in South Africa, where he performed hydrologic and hydraulic analyses of riverine flows and hydraulic structures, as well as the design of water supply and drainage systems. He was also involved in the design and development of several water resources software, one of which was for managing environmental flow releases from the Berg River Dam. His research interests include upland erosion processes, watershed dynamics and scaling laws, knickpoint development and migration, and local scour around bridge piers and abutments. He is also interested in computational modeling of river networks, as well as the use of various sensor technologies such as Radio Frequency IDs for monitoring land surfaces changes and sediment fluxes. He is a National Science Foundation IGERT Fellow and has a Graduate Certificate in Geoinformatics from the University of Iowa. He has received several other scholarships and awards, including the NASA Iowa Space Grant Consortium Scholarship and the University of Tennessee's Chancellor's Citation for Extraordinary Professional Promise. He is a member of the American Geophysical Union, the American Society of Civil Engineers, the International Association of Hydro-Environment Engineering and Research, and the American Water Resources Association.